AD NUMBER

ADA209166

NEW LIMITATION CHANGE

TO

Approved for public release, distribution unlimited

FROM

Distribution authorized to U.S. Gov't. agencies and their contractors; Administrative/Operational Use; Apr 1989. Other requests shall be referred to Office of Naval Research, 800 North Quincy Street, Arlington, VA 22217-5660.

AUTHORITY

ONR ltr, 5 Jun 1989

(4)

HUGHES
AIRCRAFT COMPANY
ELECTRO-OPTICAL & DATA SYSTEMS GROUP

AD-A209 166

FINAL REPORT FOR THE PERIOD
25 SEPTEMBER 1985 THROUGH 24 APRIL 1989

HIGH TEMPERATURE ADHESIVE SYSTEMS

DTIC
ELECTE
JUN 1 2 1989
S **D**
D cg

PREPARED FOR
OFFICE OF NAVAL RESEARCH
ARLINGTON, VIRGINIA

HIGH TEMPERATURE ADHESIVE SYSTEMS

Final Report for the Period
25 September 1985 through 24 April 1989

April 1989

Contract N00014-85-C-0881

Prepared by:

E. H. Catsiff, T. K. Dougherty, W. E. Elias,
D. J. Vachon, G. Angsten, and R. W. Seibold
Materials Technology Laboratory
Technology Support Division
Electro-Optical & Data Systems Group

W. G. Knauss and S. Shimabukuro
Graduate Aeronautical Laboratories
California Institute of Technology

K. M. Liechti
Department of Aerospace Engineering
and Engineering Mechanics
University of Texas at Austin

Prepared for:

R. W. Seibold
Program Manager

E. B. Holst, Manager
Materials Science Department

CONTENTS

i

CONTENTS   (Cont'd)

CONTENTS (Cont'd)

FIGURES (Cont'd)

TABLES

1. INTRODUCTION AND SUMMARY

1.1 INTRODUCTION

Projected requirements for future high-performance jet engine, missile, and fighter aircraft structures will necessitate extensive use of high temperature structural adhesives. For example, many advanced jet engine and tactical aircraft components will need to perform for hundreds of hours at 700°F (371°C) and above. For advanced air-to-air tactical missiles and air-launched stand-off missiles, composite airframe structures capable of maintaining strength for short periods (minutes) at 1000°F (538°C) and above will be needed. Other needs for adhesives capable of performing at high temperatures include bonding of structures   extended range cruise missiles, bonding of specialty materials for stealth applications, and, potentially, joining of aerospace plane structures.

The critical need for an easily processible, tough polymer-based adhesive capable of meeting these performance parameters cannot be satisfied through implementation of state-of-the-art high temperature polymeric materials. Although polymers capable of such performance exist, none of them exhibit adequate toughness nor can they be processed using practical temperature/pressure cycles. Examples include polybenzimidazoles (PBIs), polyphenylquinoxalines (PPQs), polybenzothiazoles (PBTs), polybisbenzimidazobenzo-phenanthrolines (BBBs), etc. The persistent problem is that the solubility, flow, gel time, and melting temperature of such linear and branched heteroaromatic polymer molecules are inadequate to achieve suitable processibility. Development of polymer systems possessing both ultrahigh thermal stability and good processibility, while maintaining a high level of toughness, will represent a much needed technological breakthrough.

Under this program, a comprehensive technical effort was undertaken with the goal of developing high-temperature adhesive systems with inherent processibility and toughness. The approach was to perform a multidisciplinary integrated research effort involving a combination of polymer chemistry, moisture diffusion analysis, and fracture mechanics to

tailor, characterize, and qualify tough adhesive systems for bonding to titanium and ferrous alloys. Performance goals for the adhesive systems included the ability to withstand extended duty cycles at high temperature (450° - 700°F or 232° - 371°C) while remaining viable under hot-wet and cold-dry conditions. Keywords (adhesives; polymer chemistry) (кт)

The polymer chemistry effort employed novel methods of synthesis to develop appropriate polymer-ceramic systems, and was spearheaded by polymer chemists at the Hughes Aircraft Company. The principal investigators at Hughes were Dr. K. S. Y. Lau for early phases of the program and Dr. E. H. Catsiff for later phases. Messrs. T. K. Dougherty and W. E. Elias, and Dr. D. J. Vachon contributed substantially to the polymer chemistry effort. The moisture diffusion analysis furthered the understanding of solvent diffusion into structural adhesives and was performed by Prof. W. G. Knauss and S. Shimabukuro at the California Institute of Technology. The mechanics effort involved the development of test methods and a data base for determining adhesion failure mechanisms under severe environments and was spearheaded by Prof. K. M. Liechti at the University of Texas at Austin. The contributions of Prof. W. P. Weber, University of Southern California, who provided valuable consultation in the area of polymer chemistry, are acknowledged. R. W. Seibold served as the Hughes program manager.

This final report summarizes progress from 25 September 1985 through 24 April 1989.

1.2 SUMMARY

1.2.1 Polymer Chemistry (Hughes Aircraft Company)

A hard block-soft block approach to obtaining a toughened polymer-ceramic adhesive was undertaken. Toughenable hard blocks (i.e., with silanol end groups) based on heterocyclic precursors, particularly incorporating the hexafluoroisopropylidene ("6F") moiety, were explored. Bisbenzimidazoles containing 6F groups were prepared, and silanol-containing end-groups were incorporated, but purification of these products proved extremely difficult. Model (non-6F) benzimidazoquinazolines also proved difficult to purify at the stage of silanol introduction, while an alternate route to 6F-containing

benzimidazoquinazolines demonstrated ring-closure problems. Benzoxazoles containing 6F groups were the most promising of these hard block-soft block moieties but were also difficult to purify at the silanol stage. An alternative route to silylation also posed ring-closure problems. Although these problems appeared solvable with sufficient efforts, another approach, employing phthalocyaninosiloxane-containing tougheners, appeared to offer a simpler route to the desired adhesives. Following this second route, polymers were made by bisureido monomer chain extension and by hydrosilation chain extension. Standard sol-gel (silanol polycondensation) was shown to provide polymeric intermediates, but considerable siloxane chain rearrangement also occurred, interfering with structure control. Potentially more stable moieties (tetraphenylphthalocyanino-trisiloxane) were identified, and routes to preferentially avoid catalysis of chain rearrangement were also examined. These hard-block synthetic procedures, based on standard sol-gel technologies, yielded highly foamed, hard, brittle, but thermogravimetrically stable polymer-ceramic materials. Lap-shear joint specimens adhered to FPL-etched aluminum but were mechanically weak because of porosity resulting from volatiles generation and internal stresses. Recommendations for further work are presented in Section 2.9.

1.2.2 Moisture Diffusion in Adhesives (California Institute of Technology)

Reliable structural analysis of bonded joints over long time periods requires a better understanding of the environmental effects that may contribute to bond failure. One particular area of importance is how moisture effects the properties of the polymeric material that comprises the adhesive. Moisture diffusion into adhesives may be complicated by coupling between mechanical stresses and moisture concentration. It is this area that we have addressed.

Early in the program we developed a model for the diffusion of small molecules in a polymeric material. This model was based on a conceptual picture of the molecular processes that could drive the diffusion process, but the actual description is entirely in phenomenological terms. The underlying idea that couples the diffusion problem to the stress analysis problem is that osmotic pressure develops as the moisture diffuses into the

polymer. This pressure can aid the diffusion process, along with the concentration gradient of the diffusant, but over time it will relax due to the viscoelastic nature of the adhesive. Further, the diffusant alters the so called free volume of the polymer. The free volume is factored into certain viscoelastic constitutive laws to alter the time scale of the material response functions. Due to the complexity of the resulting set of nonlinear differential equations, a numerical solution was attempted.

Early work in numerically solving the governing equations used the idea of finite differences to frame the differential equations into a set of equations that could be programed in a computer. The finite difference program developed could solve a class of problems but it also had a few numerical difficulties. The work then shifted into using the technique of finite elements to solve the equations. A program called FEAP (finite element analysis program) was employed and only needed a subroutine that describes the process to be modeled. Most of the work with FEAP consisted of developing a diffusion subroutine that was general enough to accommodate immediate implementation of any changes to our mathematical model.

We believe that we can now solve the transient-fully coupled diffusion problem. The program has been partially tested using both elastic and simple viscoelastic material properties. We are currently testing the program to examine for any numerical instabilities that can lead to erroneous results. It is important in terms of the reliability of the numerical solutions to try and fully test the program. To evaluate our mathematical model, results from experiments will be used to both evaluate the model's material parameters and to also check the validity of the model itself.

Previous experimental work on the sorption of moisture into an adhesive (3M's AF-163-2M) showed that the stress state indeed affected the diffusion process. Another set of similar experiments was planned in an attempt to better quantify the diffusion parameters. New specimens were made of the unscrimmed version of this adhesive. It should be noted that work with this unscrimmed adhesive proved to be very difficult, and a major portion of the research program was spent in trying to manufacture new specimens that were basically void free. Two groups of specimens have been tested in both a humid environment and by full immersion in distilled water. It

appears that the moisture ingression into this epoxy system can be represented by a Fickian process. Numerical results show that if the environment does not cause considerable relaxation to occur, any pressure effects on the diffusion process can be interpreted as a variable coefficient Fickian process. We believe that this is happening with our epoxy-water system.

Both phases, analytical and experimental, of the research program have not progressed as far as we had hoped. Nevertheless, we feel that the progress that has been made has shown that our ideas on moisture diffusion in polymers are valid and warrant continuation of this research.

At the request of DARPA and ONR, characteristics of bonding titanium using LARP-TPI adhesive are being evaluated. The test results and a discussion will be sent as a supplement to this report at a later date.

1.2.3 Fracture Analysis of High Temperature Adhesives (University of Texas at Austin)

The overall objective of this work has been to develop methods for determining the constitutive behavior and fracture properties of high temperature adhesives in-situ. The methods were to be developed with a sensitivity to providing more direct feedback to the formulation of new adhesives and surface preparations. The more direct feedback would be due to the fact that the properties derived from the measurements would have direct application to the design process instead of being qualitative comparisons, as is generally the case in current practice. In order to achieve these objectives, the stress states in constitutive property specimens should be pure and uniform and the fracture modes in fracture property specimens well characterized and understood. In addition, it was felt that the methods to be developed should be as simple to use as possible in order to encourage general use and should furthermore make use of compact specimens so that new formulations could be tested directly.

For determining the constitutive behavior of the adhesive, the main emphasis has been placed on determining the stiffness and strength in shear, although the most favorable specimen geometry developed to date could also be used for more general stress states. The current emphasis on stiffness and strength should not preclude the use of the specimens for the

determination of time dependent properties. The approach that was taken in developing a suitable specimen was to compare the stress distributions in napkin ring, cone-and-plate and stiff adherend specimens under shear, bond-normal and thermal loadings. The stress distributions were determined from finite element analyses with particular attention being placed on bimaterial corners. It was found that a slight rounding of adherends, particularly in the case of the stiff adherend specimen, eliminated stress concentrations, even along the interface. Test methods were developed for using the stiff adherend specimen to determine the stiffness and strength of FM-300. The results have been encouraging in the sense that the shear strength measured in this way was higher than the manufacturer's values and that the fracture surfaces were highly ridged, indicating shear failure. The specimen geometry and alignment procedure are relatively complex, and steps are now being taken to reduce these difficulties.

Since the fracture mode in cracked adhesively bonded joints can vary considerably, and criteria can vary from one adhesive to another, methods have been developed for determining the pure mode I and mode II fracture toughnesses as well as an intermediate, mixed-mode value. The wide range of mode mix has been provided by very similar laminated beam specimens, that can be cut from the same laminated plate, but which are loaded differently. The mode I, mode II and mixed-mode fracture toughnesses of FM-300 have been determined using double cantilever (DCB), end-notched flexure (ENF) and mixed-mode flexure (MMF) specimens respectively. The values determined by the DCB and MMF specimens were consistent, whereas there was a greater degree of scatter in the mode II (ENF) fracture toughnesses. Part of the variation has been initially attributed to relatively large plastic zones that are interacting with the central load point. The conclusions were based on elastoplastic finite element analyses and deflections of photoresist grids, techniques that will be further refined for validation purposes. DCB and ENF specimens were used to determine the room temperature and high temperature fracture toughness of titanium/FM-36 and titanium/LARC-TPI joints.

2.0 POLYMER CHEMISTRY

2.1 POLYMER CHEMISTRY APPROACH

The objective of our effort was to develop adhesive polymer systems which possess ultrahigh thermal stability and good processibility while maintaining a high level of toughness. Toughening by modification of ultrahigh temperature resins represented the crux of the challenge. Results of current research have demonstrated that the property requirements of toughness and ultrahigh temperature stability are difficult to achieve in a single material.

To address the problem of toughening, incorporation of elastomer domains in the resin represented the state-of-the-art approach. This requires the integration of molecularly tailored polymerizable branch units into the polymer backbone as pendent or end groups. Examples or such units are silyl alkoxides and silyl triacetates, which can be polymerized to form a siloxane/silicate domain during cure, and can be converted to a polymer-ceramic material.

Provision of elastomer domains requires the tailoring of a backbone flexible enough to function as a toughener, yet resistant to degradation caused by thermally-induced chain motion. The polysiloxane chain is more thermooxidatively stable than the carbon-carbon chain; it is also more flexible and may require some constraint. Incorporation into a polymer-ceramic material promised to be relatively straightforward.

Two general approaches were pursued to synthesize suitable polymer-ceramic materials. One of the two approaches reached the stage of preparing some preliminary specimens of polymer-ceramic materials. This entailed initial preparation of phthalocyanino-siloxane difunctional monomers, oligomers, and polymers. Specifically, two such difunctional monomers were synthesized and fully characterized. The polymer-ceramic material specimens prepared from these phthalocyaninosiloxane compounds exhibited a good level of thermooxidative stability, as determined by isothermal gravimetric analysis.

The second approach that was examined in parallel involved development and modification of some selected ultrahigh-temperature-resistant heterocyclic chemical systems. Heterocyclic ring structures not only possess high temperature resistance, but also have good adhesive properties. In particular, heterocyclic

precursors containing the hexafluoroisopropylidene (6F) group
(specifically, 6F-benzimidazoles, 6F-benzimidazoquinazolines, and 6F-
benzoxazoles) were selected on the basis of their apparent ease of
synthesis compared to others. The 6F-benzoxazoles appeared to be the
most promising. Some earlier technical problems in benzoxazole ring
closure and organolithium metallation were resolved. However,
purification and characterization problems persisted.

In general, the synthetic difficulties encountered with the
heterocyclic systems were more severe than expected. In every case,
the technical impasse was related to the sensitivity of substituent
groups on the heterocyclic nucleus to the reactivity of the chemical
system. Consequently, model study results could not always be
directly extrapolated to real system applications. Subtle
modifications of procedures were generally required.

In the following three sections (2.2, 2.3, and 2.4), the second
of these two general approaches is discussed. These three sections
are devoted to compounds based on benzimidazole, benzimidazo-
quinazoline, and benzoxazole, respectively. Sections 2.5 and 2.6 are
devoted to the first general approach, i.e., preparation of polymer-
ceramic material from phthalocyaninosiloxane compounds.

2.2 BENZIMIDAZOLE-BASED COMPOUNDS

Among the heterocyclic systems investigated were those
containing benzimidazole nuclei in the polymer chain. The essential
monomer for preparation of benzimidazole compounds is the tetraamino
compound V, whose synthesis was accomplished (Reference 1) by the
route shown in Figure 2-1. The various reactions shown in the figure
are detailed in Table 2-1.

Compound V was converted in low yield to the bisbenzimidazole VI
by reaction with 3-bromobenzaldehyde because of incomplete formation
of the imidazole ring. Using the same reaction conditions (Reference
2), compound V with 4-ethynylbenzaldehyde (Reference 3) and N-phenyl-
1,2-diaminobenzene with 3-bromobenzaldehyde yielded the expected
benzimidazole derivatives VII and VIII, respectively (Table 2-2).
Attempts were made to synthesize compounds IX and X from compound V,
but the yields were very low, and it was very difficult to isolate
and purify the compounds. As a consequence, efforts were shifted to
other heterocyclic systems.
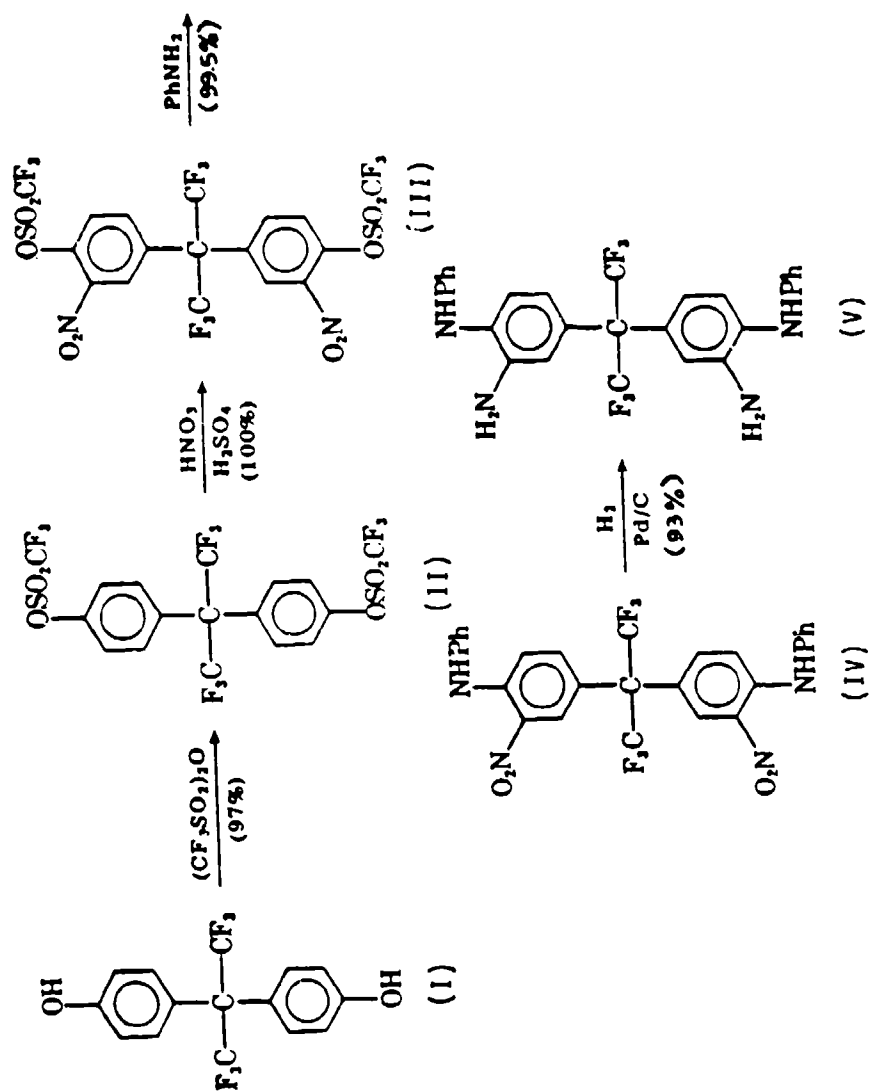
Figure 2-1. Preparation of Bis(N-phenylbenzimidazole) Precursor

TABLE 2-1

SUMMARY OF COMPOUNDS PERTAINING
TO BENZIMIDAZOLE-BASED OLIGOMERS

(I - V)

Compound	Synthesized From	Reaction Condition	Yield	Characterization	Comments
I R_1=OH R_2=H	Commercially available	--	--	---	Better grade materials are available from American Hoechst
II R_1=OSO$_2$CF$_3$ R_2=H	I	(CF$_3$SO$_2$)$_2$O[a] CH$_2$Cl$_2$,-78°C,4h	97%	mp 98°C IR[b] 890 NMR[c] δ 7.01(m)	Confirmed with reference spectra
III R_1=OSO$_2$CF$_3$ R_2=NO$_2$	II	HNO$_3$(90%) H$_2$SO$_4$ 100°C,4h	100%	mp 130-131°C IR 1530,1360, . 890 NMR δ 7.80-8.17(m)	Confirmed with reference spectra
IV R_1=NHPh R_2=NO$_2$	III	PhNH$_2$, THF, reflux, 17h	100%	mp 160-161°C IR 3360,1530,1360 MS m/e 576,512 NMR --	Confirmed with reference spectra
V R_1=NHPh R_2=NH$_2$	IV	5% Pd/C, H$_2$ CH$_3$CH$_2$OH 25°C,17h	93%	mp 178-180°C IR 3380 NMR (acetone-d$_6$) δ 2.90(s), 6.35-7.42(m)	Confirmed with reference spectra

a   Trifluoromethanesulfonic anhydride (bp 78-82°C, density 1.81) was made from
    trifluoromethanesulfonic acid (3M commercial product) and phosphorus pentoxide.

b   IR - Only important absorptions (in wavenumbers) are included here.

c   All NMR's were taken using CDCl$_3$ as solvent, unless indicated otherwise; chemical
    shift values are given in ppm downfield from tetramethylsilane internal standard.
    Multiplicities: s = singlet, bs = broad singlet, t = triplet, q = quartet,
    m = multiplet.

TABLE 2-2

BENZIMIDAZOLE-BASED OLIGOMERS
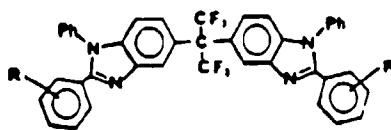
(VI, VII, IX, X)

Compound	Synthesized From	Reaction Condition	Yield	Characterization	Comments
VI R = Br meta	V	**3**-BrC$_6$H$_4$CHO Na$_2$S$_2$O$_5$, CH$_3$CH$_2$OH, H$_2$O reflux 24h	Low Yield	Poor spectra. characteristics	Incomplete for- mation of benzi- midazole ring
VII R = C≡CH para	V	4-HC≡C-C$_6$H$_4$CHO Na$_2$S$_2$O$_5$, CH$_3$CH$_2$OH, H$_2$O reflux, 24h	93%	mp 265°C IR 3500, 2120 NMR ---	Confirmed with reference spectra; validated proce- dure
VIII	NH$_2$ / NHPh / Br-CHO	Na$_2$S$_2$O$_5$, CH$_3$CH$_2$OH, H$_2$O reflux, 24h	60%	mp 124-125.5°C IR 1625 NMR δ 6.50-8.80 Uncharacter- istic absorp- tions	Model reaction for calibrating reaction condi- tion
IX R= RO-Si-OR / OR	V	Low yield, difficult to isolate and purify.			
X R= CH$_3$/Si/OH / H$_3$C	V	Low yield, difficult to isolate and purify.			

2.3 BENZIMIDAZOQUINAZOLINE-BASED COMPOUNDS

The second heterocyclic system investigated was based on benzimidazoquinazolines. These are derived from 2-(2-amino-phenyl)benzimidazole, a commercial product. This can be synthesized, if necessary, from 1,2-diaminobenzene and a 2-nitrobenzoic acid derivative, followed by reduction of the nitro group. The conversion to the silylated compound XIV is detailed in Figure 2-2.

A 10-gram scale bromination reaction successfully converted monomer XI to the mono-bromo derivative XII, which was fully characterized. The position of the bromo group was established by nuclear magnetic resonance (NMR) spectrometry (Figure 2-3, upper spectrum). However, a subsequent larger scale reaction resulted in incomplete bromination.

The reaction of XII with 3-bromobenzaldehyde yielded the dibromobenzoimidazoquinazoline compound XIII, which has been fully characterized.

The subsequent organolithium reaction with XIII presented some difficulties in achieving a homogeneous solution. Further effort was undertaken to introduce the hexafluoroisopropylidene (6F) group into these functionalized monomers. Thus, the bromobenzaldehyde reactant for the synthesis of XIII would be replaced with the 6F-containing aldehydes XVI and XVII (Figure 2-4). Both key intermediates, XVI and XVII, have been successfully synthesized. While both XVI and XVII required the use of the high-purity dibromo precursor XV, XVII also necessitated more stringent control of reaction conditions. Early attempts had resulted in impure XVI and XVII contaminated with polymeric impurities due to the presence of I in the dibromo compound XV. However, further recrystallizations of XV from methanol can provide highly pure XV with a melting range of less than 1°C. Experiments using the aldehyde intermediates XVI and XVII to prepare compounds XVIII and XIX have not been successful. The products were found to be quite soluble in nitrobenzene solvent (which also functions as an oxidant), rendering isolation very tedious and difficult. Efforts with this series of compounds were terminated because of more success with others. Table 2-3 summarizes the results in this series.
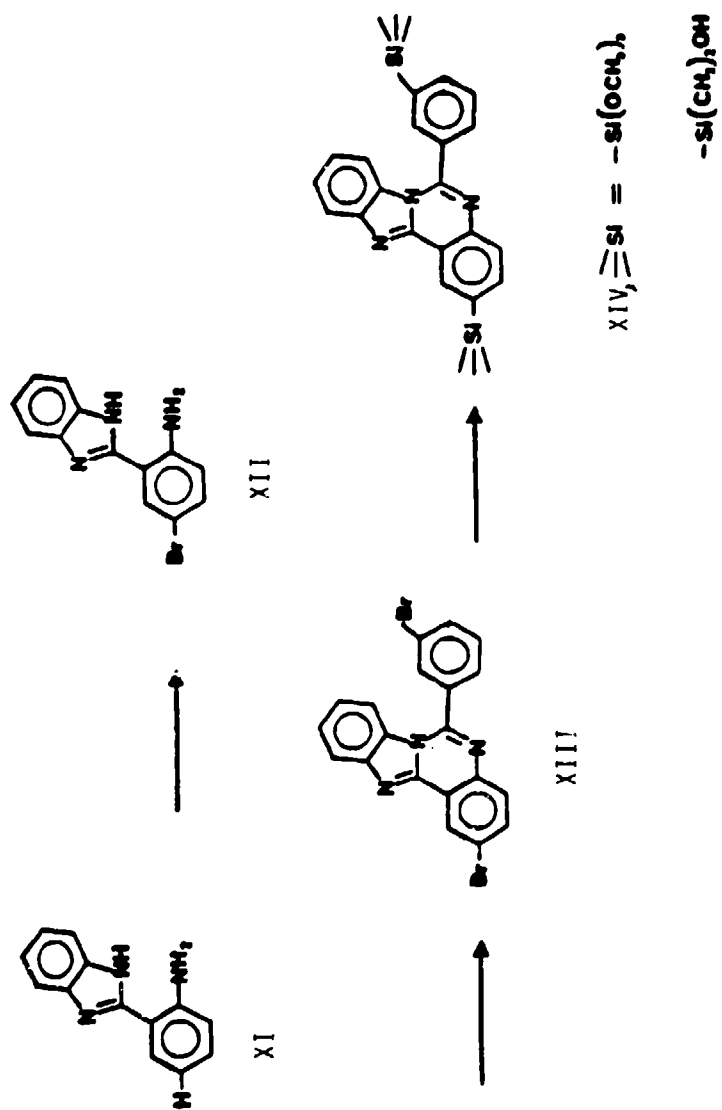
Figure 2-2. Synthesis of Silylated Benzimidazoquinazolines
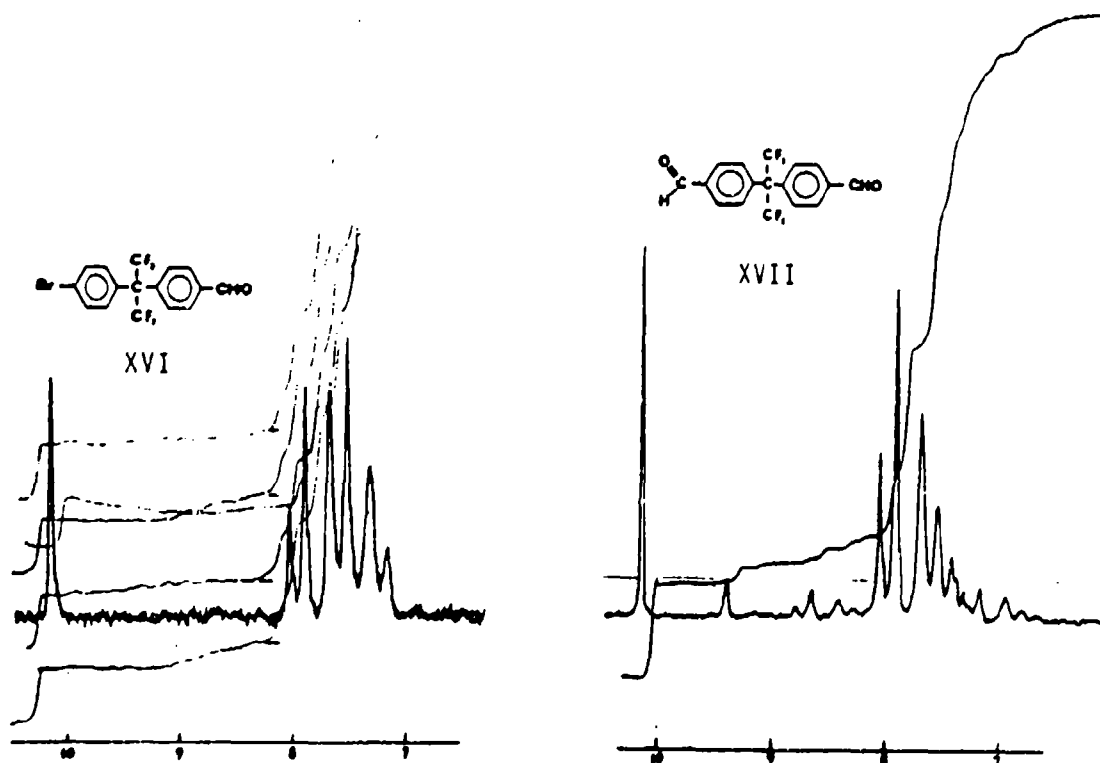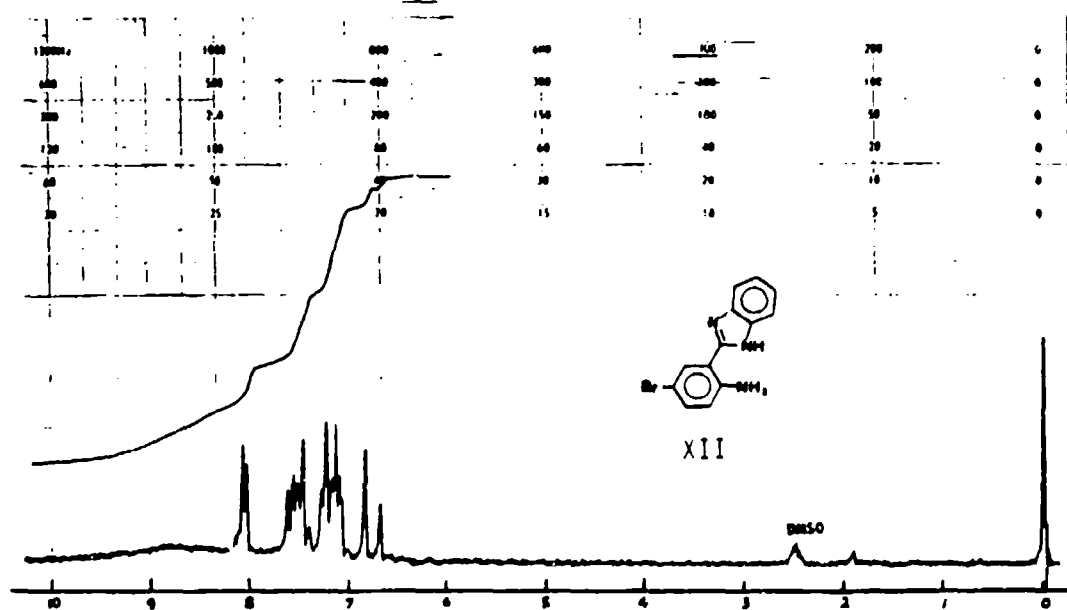
Figure 2-3. NMR Spectra of Three New Compounds.
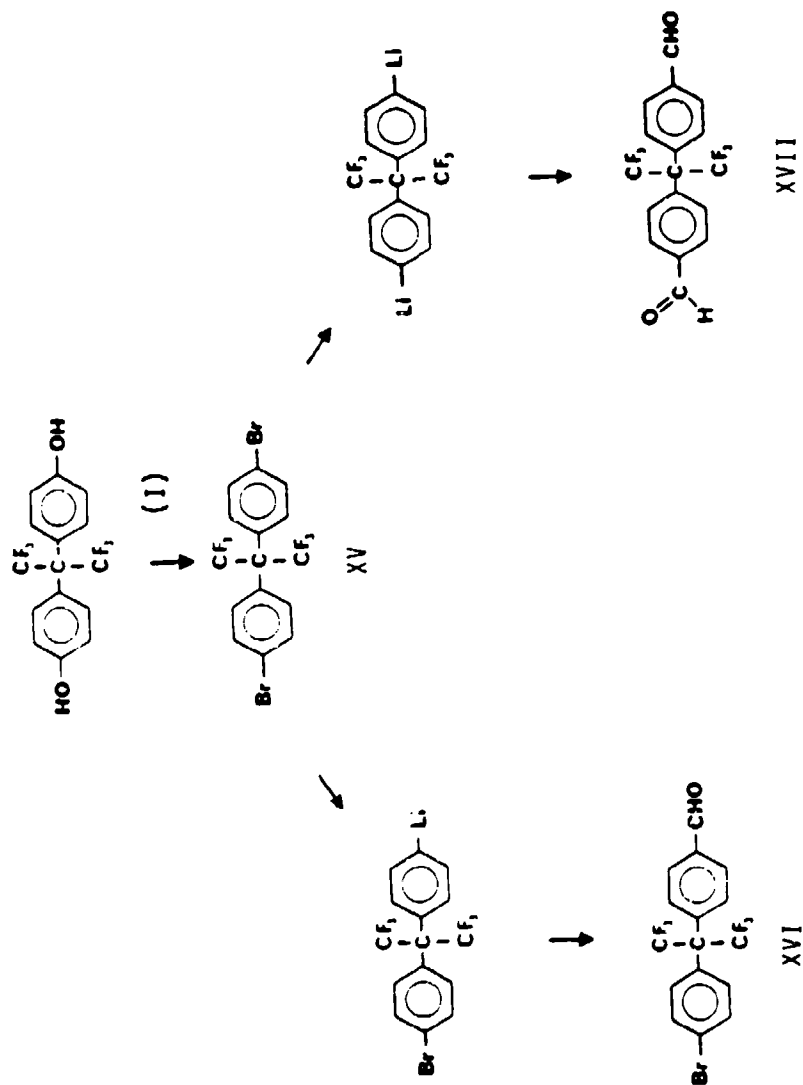
Figure 2-4. Preparation of Two Key Ingredients, 2-(4-Bromophenyl)-2-(4-formylphenyl)hexafluoropropane and 2,2-Bis(4-formylphenyl)-hexafluoropropane

TABLE 2-3

SUMMARY OF COMPOUNDS PERTAINING TO
BENZIMIDAZOQUINAZOLINE-BASED OLIGOMERS
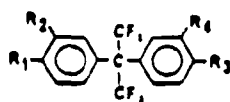
(XV, XVI, XVII, XX, XXI)   (XI, XII)

(XIII)

Compound	Synthesized From	Reaction Condition	Yield	Characterization	Comments
XV $R_1, R_3 = Br$ $R_2, R_4 = H$	I	$Ph_3P \cdot Br_2$ 300-320°C	78%	mp 75-77°C IR 1590,1495, 818 NMR δ 7.15,7.30 7.46,7.61(q)	Reaction yield is a function of starting material purity
XVII $R_1, R_3 = CHO$ $R_2, R_4 = H$	XV	1) BuLi(2 eq.) THF, -78°C 2) HC-N(CH$_3$)$_2$ ‖ O	57%	mp 122-128°C IR --- NMR δ 7.50-8.15(q), 10.2(s)	New compound; impure XV was found to lead to drastically lowered yields
XVI $R_1 = Br$ $R_3 = CHO$ $R_2, R_4 = H$	XV	1) BuLi(1 eq.) THF, -78°C 2) HC-N(CH$_3$)$_2$ ‖ O	30%	mp 90-93°C IR --- NMR δ 7.15-8.15 (2 overlapping q's) 10.2(s)	New compound; impure XV led to very low yields
XVI	XV	Grignard method	---	---	Reactions did not occur under this condition
XX $R_1, R_3 = H$ $R_2, R_4 = CHO$	3,3'-isomer of XV	1) BuLi(2 eq.) THF, -78°C 2) HC-N(CH$_3$)$_2$ ‖ O	57%	bp 170-175°C/0.01 torr IR 2740,1710, 1140-1260 NMR δ 7.20-820(m), 10.40(s)	These are literature data; actual preparation of this compound was not carried out under this program

2-10

TABLE 2-3 (Cont'd)

Compound	Synthesized From	Reaction Condition	Yield	Characterization	Comments
XXI R_1, R_3=H R_2=Br R_4=CHO	3,3'-isomer of XV	1) BuLi(1 eq.) THF, -78°C 2) $H\overset{\text{O}}{\underset{}{\text{C}}}$-N(CH$_3$)$_2$	58%	bp 130-135°C/0.1 torr IR 2740,1710,1140-1260 NMR δ 7.10-8.10(m), 10.00(s) MS m/e 410,412	These are literature data; actual preparation of compound was not carried out under this program
XI R=H	Commercial product from Aldrich	---	---	---	---
XII R=Br	XI	Br$_2$,CH$_3$CO$_2$H	76%	mp 269-271°C IR 3225, 1600, 1590,866 NMR (DMSO-d$_6$) (See Figure 2-3) MS m/e 289,287	New compound
XIII R_1=Br R_2=H R_3=Br	XII	3-BrC$_6$H$_4$CHO C$_6$H$_5$NO$_2$	50%	mp 268-270°C IR 3077,1621,1587 NMR -- MS m/e 453,374,293	Confirmed with reference spectra
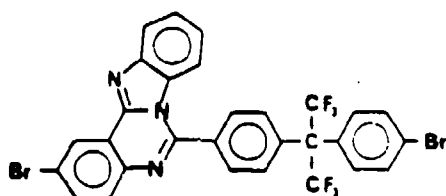
XVIII
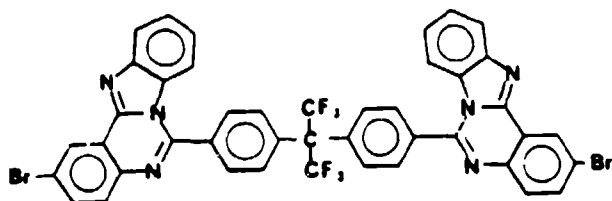
XIX

2.4 BENZOXAZOLE-BASED COMPOUNDS

The third heterocyclic system investigated was based on benzoxazoles. For this series, the necessary monomer was 2,2-bis(3-amino-4-hydroxyphenyl)hexafluoropropane (XXII), which was synthesized by simultaneous hydrogenolysis and hydrogenation of III, itself prepared as shown in Figure 2-1. Since that time, XXII has become commercially available (Hoechst Celanese Corp., Central Glass Company).
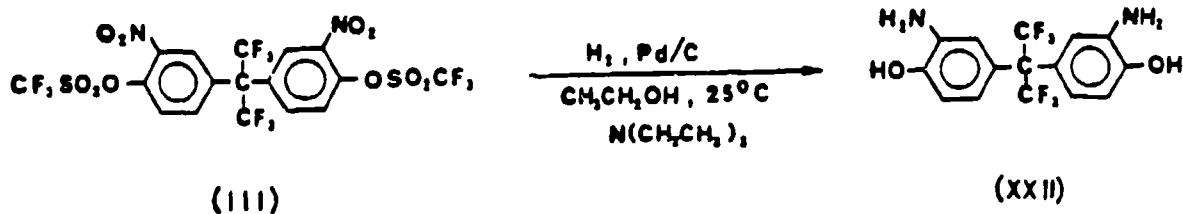
Several methods have been reported for the synthesis of benzoxazole structures. None appeared to be efficient (References 4, 5). Preliminary model experiments (Table 2-4) indicated that using a suitable liquid reactant such as methyl benzoate, which also served as the solvent for the other reactant, 2-aminophenol, led to a good yield of 2-phenylbenzoxazole. Esters of bromobenzoic acid were therefore evaluated as suitable reaction partners for XXII.

Methyl 4-bromobenzoate was prepared from the corresponding acid in 93 percent yield (mp 79-80°C) (Reference 6). Although the reaction of methyl 4-bromobenzoate with 2-aminophenol proceeded uneventfully, it failed to react with XXII even under severe conditions (200°C, 24 hours). Phosphorus pentoxide-methanesulfonic acid was recently used for the synthesis of benzoxazole rings (References 7-10). This reaction medium served for the synthesis of the model compound 2-(4-bromophenyl)benzoxazole from 2-aminophenol and 4-bromobenzoic acid. The difunctional compound, 2,2-bis(5-[2-(4-bromophenyl)]benzoxazolyl)hexafluoropropane, XXIII, was likewise synthesized with great ease and in good yields.
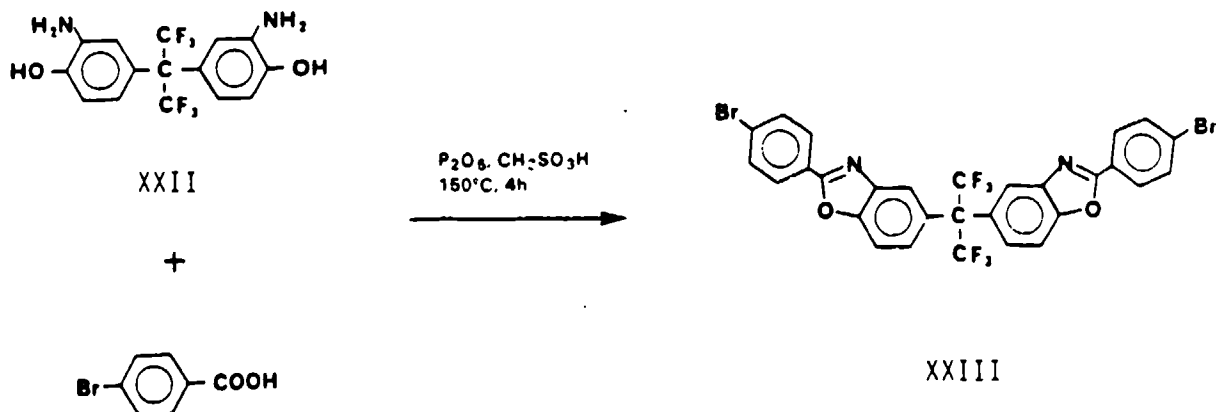
Prior to the conversion of the bromo substituent of XXIII to silyl functionalities, an evaluation of pertinent metallation conditions was undertaken (Table 2-5).

TABLE 2-4

SUMMARY OF COMPOUNDS PERTAINING TO BENZOXAZOLE

XXII

XXIII
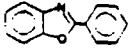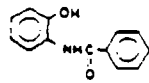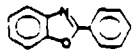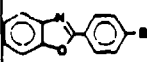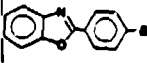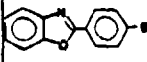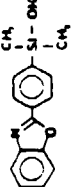
Compound	Synthesized From	Reaction Condition	Yield	Characterization	Comments
XXII	III	H_2, Pd/C, $N(CH_2CH_3)_3$, CH_3CH_2OH, 25°C, 24 h	67%	mp 244-245°C IR 3700-2400, 3430, 3350, 1620, 1520 NMR (Acetone-d_6) 2.63-3.47(bs), 6.37-7.07(m) MS m/e 366	This compound recently became commercially available in kilogram quantities.
(benzoxazole-phenyl structure)	(aminophenol structure) $C_6H_5CO_2H$	200°C 24 h	--	Only identifiable product was (structure)	--
(benzoxazole-phenyl structure)	(aminophenol structure) $C_6H_5CO_2CH_3$	200°C 24 h	85%	mp 102-103°C NMR 7.25-7.90(m), 8.15-3.45(m)	Confirmed by Beilstein data
(bromophenyl-benzoxazole structure)	(aminophenol structure) $4\text{-}BrC_6H_4CO_2CH_3$	m-cresol 200°C, 24 h	0	--	--
(bromophenyl-benzoxazole structure)	(aminophenol structure) $4\text{-}BrC_6H_4CO_2CH_3$	200°C, 24 h	36%	See next entry	Neat reaction hampered by sublimation of starting materials.
(bromophenyl-benzoxazole structure)	(aminophenol structure) $4\text{-}BrC_6H_4CO_2H$	P_2O_5, CH_3SO_3H, 150°C, 4h	86%	mp 158°C NMR 8.0-8.2(m,2H) 7.2-7.6(m,6H) IR OK	Difficult to recrystallize
XXIII	XXII $4\text{-}BrC_6H_4CO_2CH_3$	200°C, 24 h	--	Only identifiable compounds in reaction mixture were starting materials	--
XXIII	XXII $4\text{-}BrC_6H_4CO_2H$	P_2O_5, CH_3SO_3H, 150°C, 4h	90%	mp 214°C NMR 7.3-8.3(m) IR 1600, 1480, 1250, 1230, 1200, 883, 810	Easily recrystallized from acetone

TABLE 2-5

SUMMARY OF METALLIZATION STUDIES IN TETRAHYDROFURAN

$$ArBr + R \cdot Li \xrightarrow[-30°]{THF} \xrightarrow{\underset{CH_3-SiCl_2}{\overset{CH_3}{|}}} \xrightarrow{H_2O} Ar-\underset{CH_3}{\overset{CH_3}{\underset{|}{\overset{|}{Si}}}}-OH$$
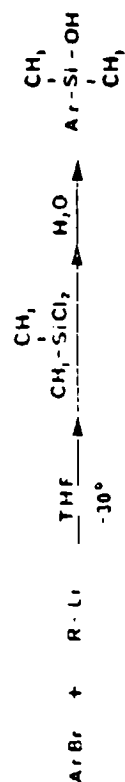
Substrate	Metallization Reagent	Reaction Conditions	Products after Quenching with (CH₃)₂SiCl₂ and Aqueous Workup	Yield	Characterization	Comments
	sec-Butyllithium (1 eq.)	THF -30°C	1:1 mixture of	<50%	NMR	Contains starting material
	sec-Butyllithium (2 eq.)	TH 30°C		67% crude yield	NMR	Not crystalline
	t-Butyllithium (2 eq.)	THF -30°C		<30% Purified by column chromatography	NMR	Excess base caused hydrolysis of benzoxazole ring
	t-Butyllithium (1 eq.)	THF -30°C	and starting material	<30% Obtained pure after column chromatography	NMR	Further experiments to be run at -78°C and with 1.5 equivalents of alkyllithium

Solubility studies of compound XXIII indicated that tetrahydrofuran would be required as the solvent. Tertiary-butyllithium was found effective in the metallation of the model compound 2-(4-bromophenyl)benzoxazole. Although two equivalents of the alkyllithium reagent is required in most metallation reactions in order to stabilize the metallated species in solution (Reference 11), the presence of excess t-butyllithium in the metallation reaction of 2-(4-bromophenyl)benzoxazole had caused hydrolytic ring opening of the benzoxazole. Stoichimetric control was therefore a stringent requirement.

The silanols (Figure 2-5) derived from the metallation of 2-(4-bromophenyl)benzoxazole and the difunctional monomer XXIII posed difficulties in purification and characterization. The problems were partially traceable to the difficulty of stoichiometric control of metallation reagent, resulting in undesirable aromatic alkylation and heterocyclic ring opening side reactions. Another source of technical difficulty was the formation of siloxane appendages and polysiloxane chains and rings during the hydrolytic work-up step that followed the quenching of the lithiated intermediate with excess dichlorodimethylsilane. Such formation of polysiloxane chains and rings always occurs in the hydrolytic transformation of dichlorodimethylsilane.

A new approach was deemed necessary. A logical alternative reagent for silanol is silicon hydride (hydridosilane). Oxidative conversion of the silicon-hydrogen bond to the silanol has been reported (Reference 12):
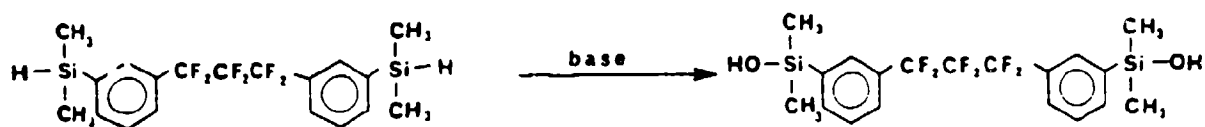
Two variations of utilizing the dimethylsilyl group are possible. In one variation, the dibromo derivative XXIII can be derivatized to a bis(dimethylsilyl) derivative prior to oxidation to the silanol product XXIV. The second variation entails the formation of the bis(dimethylsilyl) derivative directly from compound XXII by forming the oxazole ring with 4-(dimethylsilyl)benzoic acid (XXV).
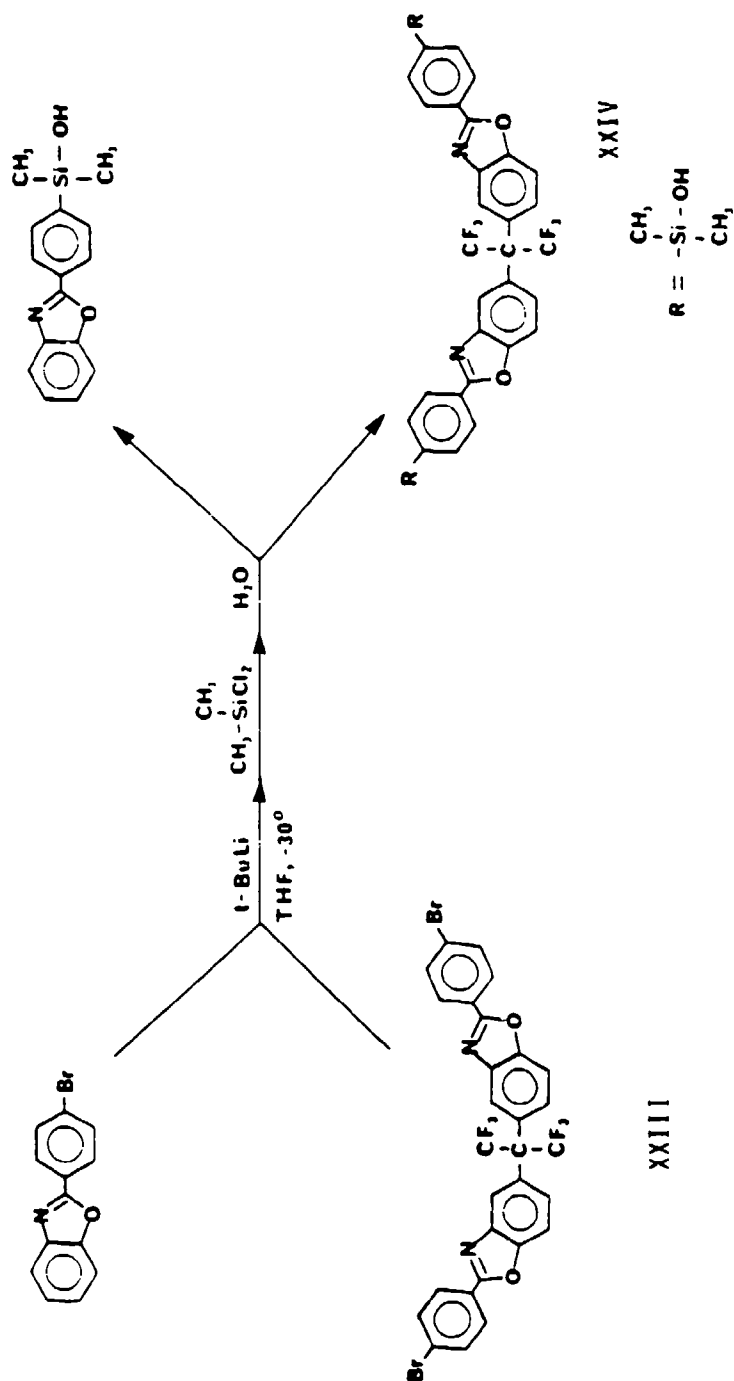
Figure 2-5. Synthesis of Disilanols of 2-(4-Bromophenyl)benzoxazole and 2,2-Bis(5-[2-(4-bromophenyl)]benzoxazolyl)hexafluoropropane, XXIII, via t-Butyllithium Metallation.

Synthesis of 4-(dimethylsilyl)benzoic acid was accomplished by a classical Grignard reaction (Reference 13). The purified yield of 44% was considerably better than that of the literature preparation. The silicon-hydrogen bond has well-defined and unambiguous infrared and NMR characteristics which provide easy monitoring of the reactions of XXV.

$$H-\underset{\underset{CH_3}{|}}{\overset{\overset{CH_3}{|}}{Si}}-\text{C}_6\text{H}_4-\text{COOH}$$
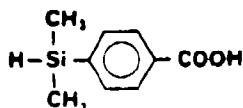
XXV

Table 2-6 summarizes the reactions of compound XXV in comparison to other substrates. Neither the azeotropic distillation method nor the phosphorus pentoxide-methanesulfonic acid method was suitable for compound XXV. NMR results from the experiments revealed the destruction of the dimethylsilyl group under those reaction conditions.

N,N-Dicyclohexylcarbodiimide (DCC) has been known to effectively promote amide bond formation in peptide chemistry (Reference 14). As an efficient dehydration agent, it has been applied to the development of polyisoimide technology. DCC did not effect a reaction between 2-aminophenol and 4-dimethylsilylbenzoic acid (Table 2-6). In the presence of 0.25 equivalent of trifluoroacetic acid, formation to yield an amide product XXX took place. An encouraging result was that the NMR signal of the silicon-hydrogen bond persisted through the reaction. Since cyclization to the benzoxazole ring did not take place, a second step would be needed. Further work would require the isolation of XXX and development of methods for its cyclization.

$$\text{2-aminophenol} \quad + \quad H-\underset{\underset{CH_3}{|}}{\overset{\overset{CH_3}{|}}{Si}}-\text{C}_6\text{H}_4-\text{COOH} \quad \xrightarrow[\text{THF, }\Delta]{\text{DCC, 0.25 TFA}} \quad \text{XXX}$$

XXV   XXX
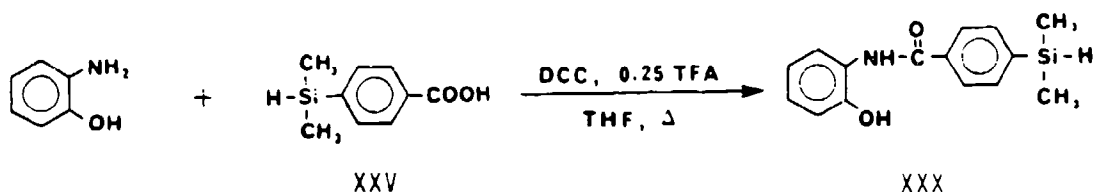
TABLE 2-6

BENZOXAZOLE RING CONSTRUCTION USING

4-DIMETHYLSILYLBENZOIC ACID (XXV) AND OTHER SUBSTRATES
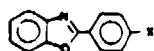
XXVI: X = H
XXVII: X = Br
XXVIII: X = Si(CH₃)₂H
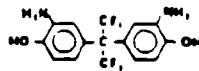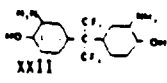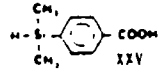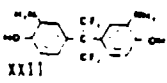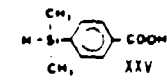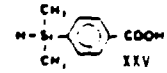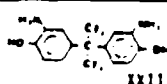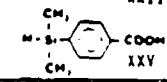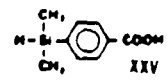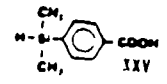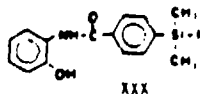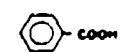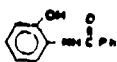
XXII
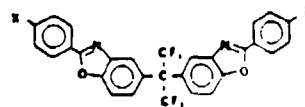
XXIII: X = Br
XXIX: X = Si(CH₃)₂H

Description of Synthesis Method	Reactants	Reaction Product	Reaction Conditions	Yield	Comments
Direct Synthesis	(2-aminophenol) NH₂, OH; C₆H₅COOH	XXVI	200°C, 24h	0	Only identifiable product was (o-hydroxyphenyl benzamide structure)
Direct Synthesis	(2-aminophenol) NH₂, OH; H-Si(CH₃)₂-C₆H₄-COOH XXV	XXVIII	200°C, 24h	-	Not attempted in view of futile model experiment.
Synthesis via Ester Derivative	(2-aminophenol) NH₂, OH; C₆H₅COOCH₃	XXVI	200°C, 24h	85%	mp 102-103°C, NMR, IR
Synthesis via Ester Derivative	(2-aminophenol) NH₂, OH; Br-C₆H₄-COOCH₃	XXVII	200°C, 24h	36%	mp 158°C, NMR, IR
Synthesis via Ester Derivative	HO-C₆H₃(CH₃)-C(CF₃)₂-C₆H₃(CH₃)-OH XXII; Br-C₆H₄-COOCH₃	XXII	200°C, 24h	0	Only starting materials were recovered.
Synthesis via Ester Derivative	(2-aminophenol) NH₂, OH; H-Si(CH₃)₂-C₆H₄-COOCH₃	XXVIII	200°C, 24h	-	Not done.
PPMA Method	(2-aminophenol) NH₂, OH; Br-C₆H₄-COOH	XXVI	P₂O₅, CH₃SO₃H 150°C, 4h	86%	mp 158°C, NMR, IR

TABLE 2-6. (Continued)

Description of Synthesis Method	Reactants	Reaction Product	Reaction Conditions	Yield	Comments
PPMA Method	XXII (structure); Br—⟨⟩—COOH	XXIII	P_2O_5, CH_3SO_3H 150°C, 4h	90%	mp 214°C NMR 18
PPMA Method	(structure); XXV (structure)	XXVIII	P_2O_5, CH_3SO_3H 150°C 4 - 38h	0	NMR indicated loss of SiH absorption.
PPMA Method	XXII (structure); XXV (structure)	XXIX	P_2O_5, CH_3SO_3H	–	Not attempted in view of futile model experiment.
Azeotropic Distillation Method	(structure); C_6H_5COOH	XXVI	Toluene 120°C	–	Benzene cannot be a substitute for toluene as the azeotropic solvent.
Azeotropic Distillation Method	(structure); XXV (structure)	XXVIII	Toluene 120°C, 12h	0	NMR showed loss of SiH absorption.
Azeotropic Distillation Method	XXII (structure); XXV (structure)	XXIX	Toluene 120°C	–	Not attempted in view of futile model experiment.
DCC Method	(structure); XXV (structure)	XXVIII	R—N=C=N—R ($R=C_6H_{11}$)	0	Only starting materials were recovered.
DCC Method	(structure); XXV (structure)	XXVIII	R—N=C=N—R ($R=C_6H_{11}$) 0.25 eq. CF_3CO_2H	–	Only product was (structure XXX). No ring closure. NMR showed intact SiH function
DCC Method	(structure); ⟨⟩—COOH	XXVI	R—N=C=N—R ($R=C_6H_{11}$) 0.25 eq. CF_3CO_2H	–	Only product was (structure). No ring closure.

2.5 PHTHALOCYANINOSILOXANE COMPOUNDS

The phthalocyanines have been known to impart ultrahigh temperature stability to resins that contain them. Based on isothermal aging studies, phthalocyanine-containing polyimides (Reference 15) can be considered as potentially useful 700°F (371°C) resins. The silicon-phthalocyanine polymer, in particular, can be readily synthesized in large quantities and has high molecular weight (References 16, 17) (Figure 2-6).

The phthalocyaninosiloxane polymer resins are especially attractive because of their structural similarities to high temperature silane-type coupling agents and silicate networks produced by sol-gel polymerization. Phthalocyaninosiloxane polymers selected for evaluation included both high molecular weight materials and oligomers with appropriate pendent groups.

The route chosen to make the phthalocyaninosiloxane monomers involved converting phthalonitrile to 1,3-diiminoisoindole (XXXI) (Reference 18), which could then be condensed to the phthalocyanine ring system. Dichloro(phthalocyanino)silicon (XXXII) is the starting material for subsequent phthalocyanine compounds XXXIII through XXXVI.

	R
XXXII	-Cl
XXXIII	-OH
XXXIV	$-O-\underset{\underset{Ph}{\mid}}{\overset{\overset{CH_3}{\mid}}{Si}}-O-\underset{\underset{Ph}{\mid}}{\overset{\overset{CH_3}{\mid}}{Si}}-OH$
XXXV	$-O-\underset{\underset{Ph}{\mid}}{\overset{\overset{CH_3}{\mid}}{Si}}-Cl$
XXXVI	$-O-\underset{\underset{Ph}{\mid}}{\overset{\overset{CH_3}{\mid}}{Si}}-OH$

M = Si

R = CH$_3$, C$_6$H$_5$

Figure 2-6. Phthalocyaninosiloxane Polymers

1,3-diiminoisoindole
XXXI
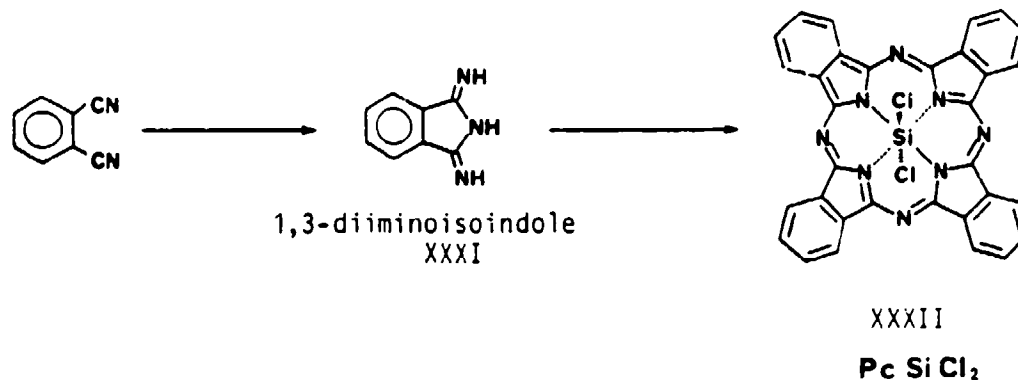
XXXII
Pc Si Cl₂

As shown in Table 2-7, previously reported direct synthesis of XXXII from phthalonitrile with excess tetrachlorosilane or stoichiometric amounts of hexachlorodisiloxane resulted in low yields of 7 and 23.6 percent, respectively (Reference 19). Subsequent improvement via the intermediate compound XXXI was achieved. Compound XXXI can be routinely synthesized and possesses long shelf life.

In this laboratory, the synthesis of XXXI was carried out routinely in 100-300 gram lots and generally in 72 percent yield (Table 2-8). The conversion of XXXI to dichloro(phthalocyanino)-silicon (XXXII) was evident from the formation of intense blue-purple color in the reaction mixture. Filtering the reaction mixture at a temperature above 180°C turned out to be a critical laboratory technique. Microcrystalline blue-purple solids were obtained in yields comparable to literature reports. In an earlier experiment, the temperature of the reaction mixture was allowed to go below 180°C, whereupon filtering was virtually impossible, probably due to the precipitation of other extremely fine particles. An extended waiting period was needed to allow coagulation to occur, and the product appeared to be less crystalline. Although it was not possible to ascertain the purity of the latter batch by IR or NMR, its purity was questionable due to the fact that the subsequent hydrolytic conversion to the dihydroxy derivative afforded low yields

TABLE 2-7

SUMMARY OF LITERATURE METHODS FOR
DICHLORO(PHTHALOCYANINO)SILICON, XXXII
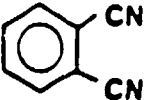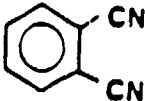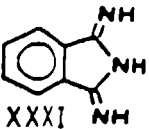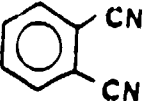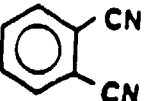
Compound	Synthesized From	Reaction Condition	Yield	Characterization	Comments
XXXII		$SiCl_4$ (xs) quinoline 220°C, 2h	7%	Combustion Analysis IR	Ref. 19
XXXII		$Cl_3SiOSiCl_3$ quinoline 219°C, 4h	23.6%	IR	Ref. 19
XXXI		$NaOCH_3$ CH_3OH Reflux, 3h	43%	mp 195-196°C	Ref. 18
XXXII	XXXI	$SiCl_4$ (xs) quinoline 219°C, 0.5h	71.7%	IR	Ref. 18
XXXI		$NaOCH_3$ CH_3OH reflux, 3h	50%	mp 192-196°C	Ref. 16
XXXII	XXXI	$SiCl_4$ (xs) quinoline 219°C, 0.5h	58.7%	Combustion Analysis	Ref. 16
XXXII	XXXI	$SiCl_4$(xs) NBu_3 tetralin reflux, 2h	80%	Combustion Analysis IR	Ref. 1⁻

TABLE 2-8

SUMMARY OF PHTHALOCYANINE-RELATED COMPOUNDS

XXXI

XXXII — XXXVI

Compound	Synthesized From	Reaction Condition	Yield	Characterization	Comments
XXXI	(benzene-1,2-dicarbonitrile)	NaOCH₃, CH₃OH, Reflux, 3h	72%	m.p. 192-194	Comparable to Ref.16, 18
XXXII R=Cl	XXXI	SiCl₄(xs), Quinoline, 219°C, 0.5h	67%	IR OK mp >300°C	Comparable to Ref.18; filtering must be carried out at 180°C
XXXIII R=OH	XXXII	NaOH(aq.), Pyridine, Reflux, 1h	95%	IR OK NMR - not soluble mp >280°C	Dried at 100°C over P₂O₅ for next reaction
XXXIV R=	XXXIII and	1. Pyridine, triethylamine 25°C, 168h 2. Dioxane, pyridine, H₂O, 25°C, 18h	36%	NMR showed the correct compound containing other siloxane impurities	Soluble in common solvents including hexane; did not crystallize after column chromatography
XXXV R=	XXXIII and	Pyridine, Triethylamine, 70°C, 40h	50% (purified yield)	250 MHz FT-NMR indicated high purity	Recrystallized from toluene; FT-NMR was mandatory for characterization due to low solubility in common deuterated solvents
XXXVI R=	XXXV	Dioxane, Pyridine, 25°C, 18h	Not determined	250 MHz FT-NMR IR OK	Low solubility necessitated FT-NMR; hydrolysis under this condition was incomplete
XXXV R= Literature Data	XXXIII and	Pyridine, Triethylamine, 25°C, 192h	72.2% (crude yield)	mp 292-3°C IR OK Combustion analysis No NMR	--
XXXVI R=	XXXV	Dioxane (25), Pyridine (1), Water (1), 25°C, 18h	98.9% (crude yield)	mp 380°C IR OK Combustion analysis No NMR	The hydrolysis had not gone to completion; NMR needed for more accurate determination of purity and yield

(ca. 18 percent). In comparison, using crystalline dichloro-
(phthalocyanino)silicon, XXXII, for the hydrolysis reaction gave
virtually quantitative yields of dihydroxy(phthalocyanino)silicon,
XXXIII (Table 2-8).

The alternative method for the synthesis of XXXII, using tri-n-
butylamine and tetralin as co-solvents, did not proceed as claimed
(Reference 17). It is apparent that both a higher boiling medium and
a more polar environment are essential.

Conversion of dihydroxy(phthalocyanino)silicon, XXXIII, to
siloxane derivatives XXXIV and XXXV was achieved (Figure 2-7).
Although XXXIV had good solubility in common organic solvents, it was
difficult to recrystallize. Purification was accomplished by the
more tedious column chromatographic technique, which makes efficient
preparation of polymer-grade material difficult. The other
chlorosiloxane derivative XXXV was synthesized and purified by
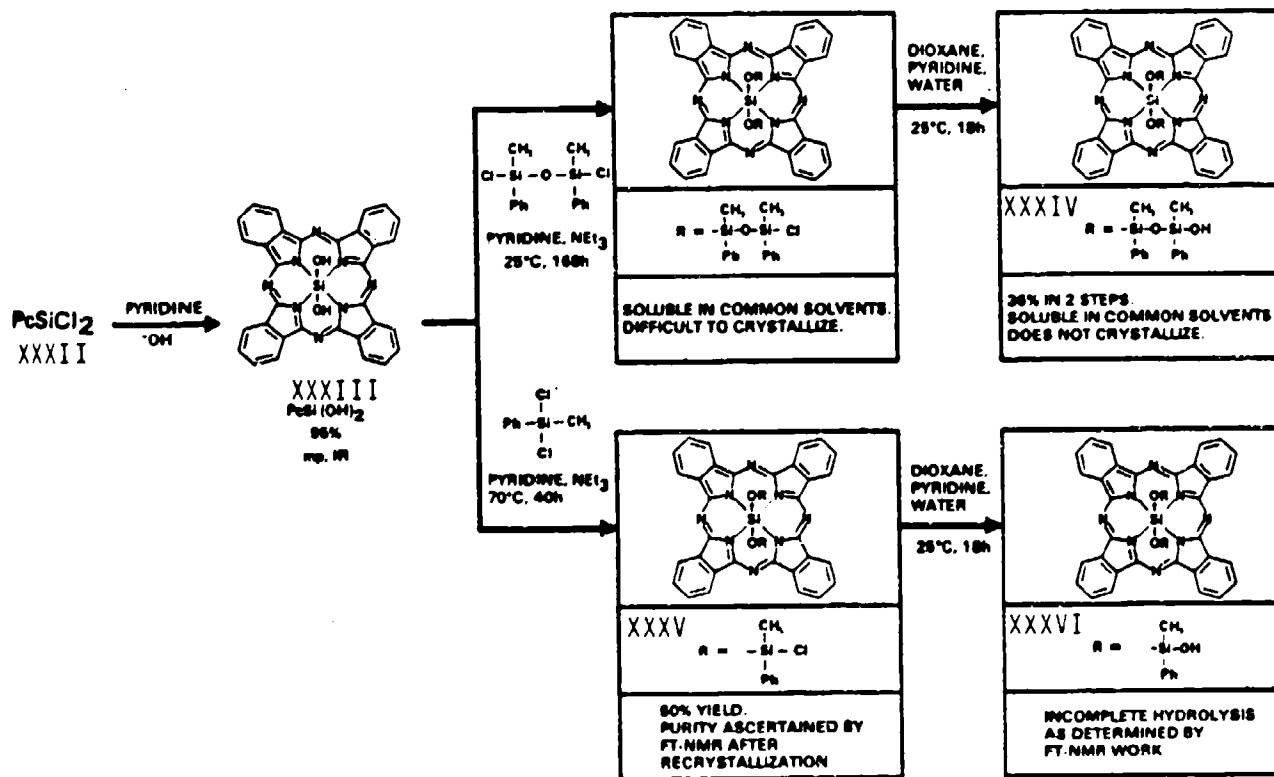
Figure 2-7. Siloxanes from Dihydroxy(phthalocyanino)silicon, XXXIII

recrystallization.   The low solubility in deuterated solvents
necessitated the use of Fourier Transform Nuclear Magnetic Resonance
(FT-NMR) Spectrometry analysis.   The NMR spectrum demonstrated the
purity of the compounds.   The advantage of FT-NMR spectrometry in
terms of sensitivity is illustrated in Figure 2-8.   The physical
characteristics of the subsequent hydrolysis product did not agree
with the literature (Reference 17).   Hydrolysis carried out in strict
adherence to the literature conditions led to incomplete conversion.
FT-NMR analysis showed the prominent presence of unreacted starting
material amid the product.   The presence of unreacted starting
material, however, did not cause problems for subsequent application
to sol-gel polymerization studies.   The unreacted silicon-chlorine
bonds likely underwent hydrolysis under the sol-gel conditions.

The need for pure compound XXXVI for construction of high
molecular weight phthalocyaninosiloxane polymer led to a modification
of the procedure used.   A successful optimization of the hydrolysis
of compound XXXV to XXXVI was achieved by refluxing XXXV in aqueous
pyridine and dioxane for 72 hours.

Preliminary sol-gel polymerization results were encouraging.
After the sol-gel polymerization reaction and stepwise drying over a
gradual temperature gradient, the specimens were cured at 300°C for
24 hours.   A high level of thermo-oxidative stability was
demonstrated by isothermal gravimetric analysis (ITGA) at 400°C in
air (Figure 2-9).   A scale-up synthesis of dihydroxy(phthalo-
cyanino)silicon, XXXIII, was then completed so that more materials
could be made available.

Despite the thermal and thermo-oxidative stability demonstrated
by these phthalocyaninosiloxane polymer-ceramic materials (PCMs),
they suffered from brittleness.   The most promising route to enhanced
toughness required the synthesis of high molecular weight polymer
(Figure 2-10) for use as a second-phase toughening elastomer.   The
synthesis of the required bisureidosiloxane compound, XXXVII, is
illustrated in Figure 2-11.   As shown in Figure 2-10, the soluble
phthalocyaninotrisiloxanediol(XXXVI) was chain extended with
bisureidotetramethyldisiloxane (XXXVII) to form a polymer with the
repeating unit XXXVIII.   The isolated product had reduced viscosity
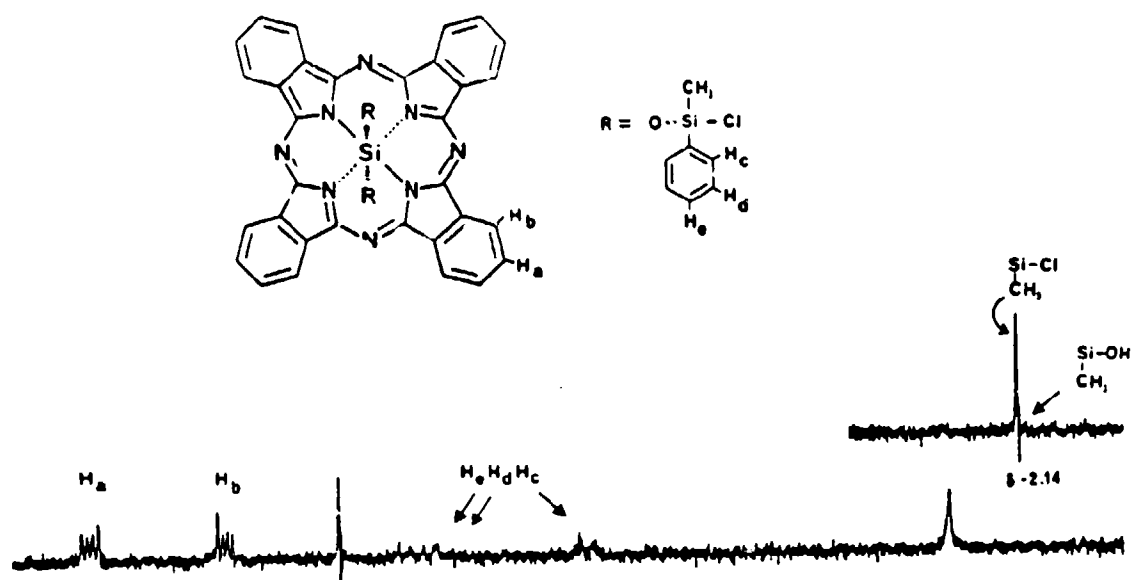
a. Continuous Wave Scan NMR Spectrum
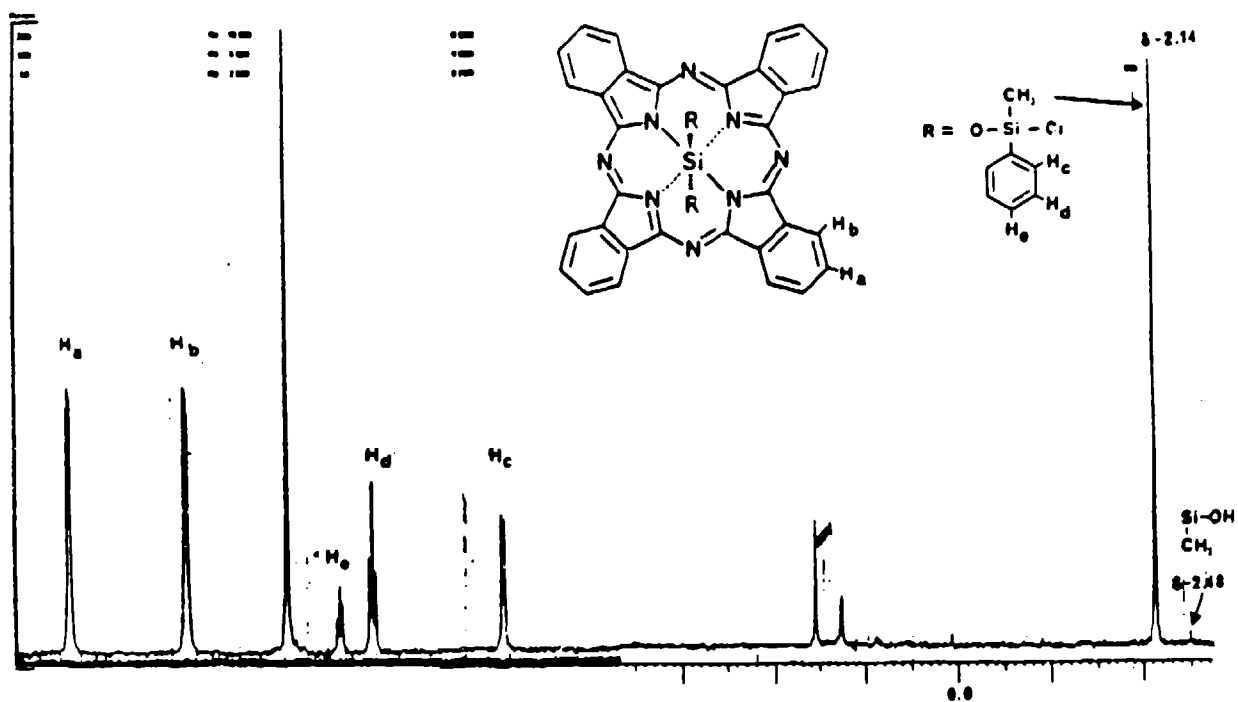
b. Fourier Transform NMR Spectrum

Figure 2-8. NMR Spectra of (Phthalocyanino)silicon Derivative XXXV.

2-28
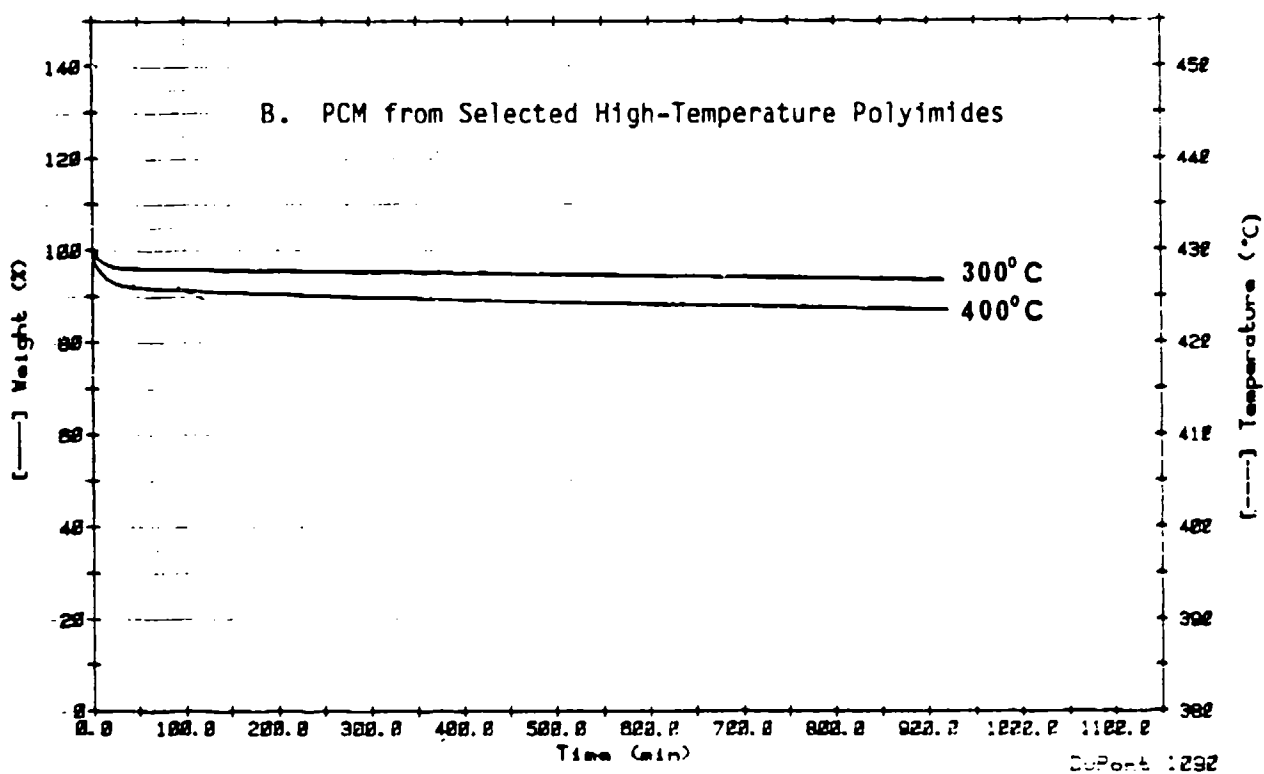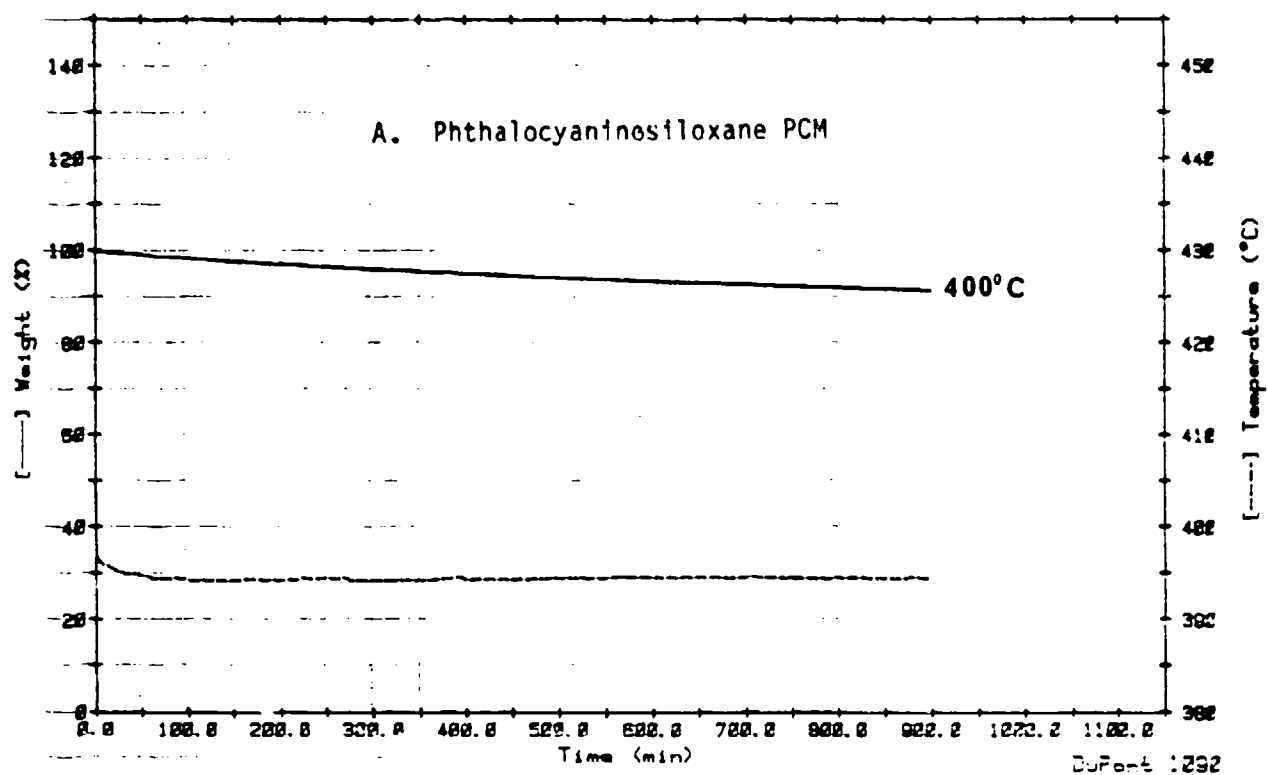
Figure 2-9. Isothermogravimetric Analyses of Polymer-Ceramic Materials (PCMs)
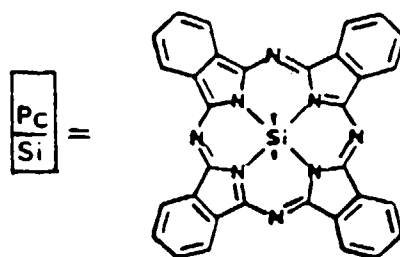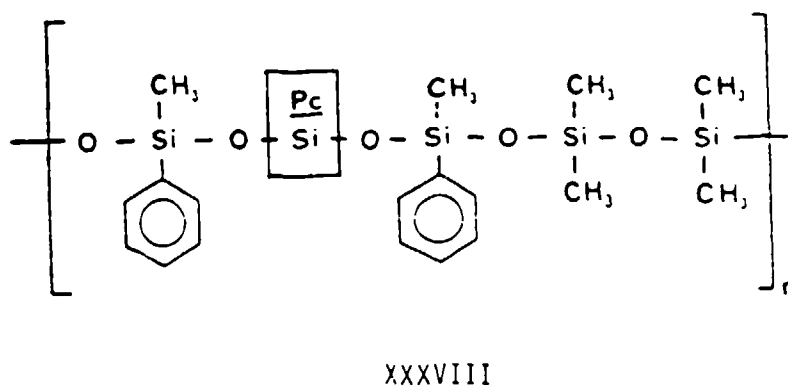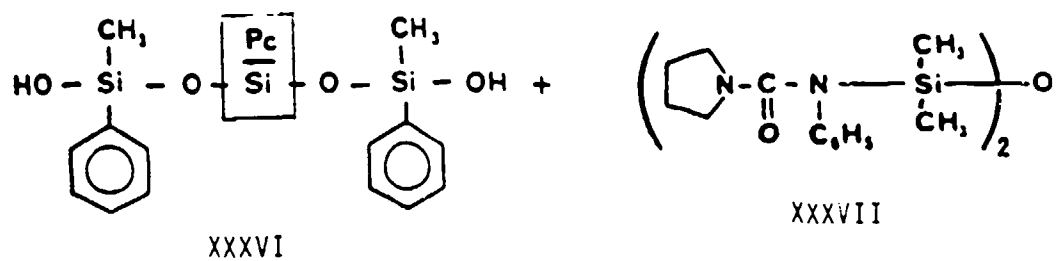
Figure 2-10. Increased Molecular Weight by Chain Extension of Phthalocyaninosiloxane Polymers.

$$\left(Cl-\underset{CH_3}{\overset{CH_3}{Si}}\right)_2 O \ + \ 2 \ \bigcirc NH \ \xrightarrow{\text{TEA}} \ \left(\bigcirc N-\underset{CH_3}{\overset{CH_3}{Si}}\right)_2 O$$

$$\Big\downarrow C_6H_5NCO$$

$$\left(\bigcirc N-\underset{O}{\overset{\|}{C}}-\underset{C_6H_5}{\overset{|}{N}}-\underset{CH_3}{\overset{CH_3}{Si}}\right)_2 O$$
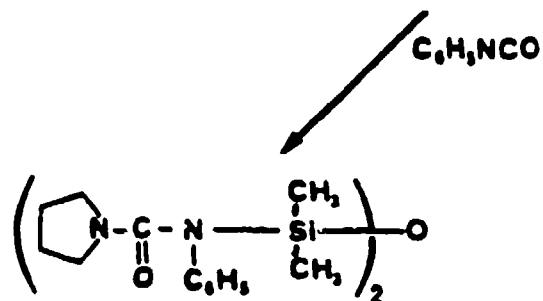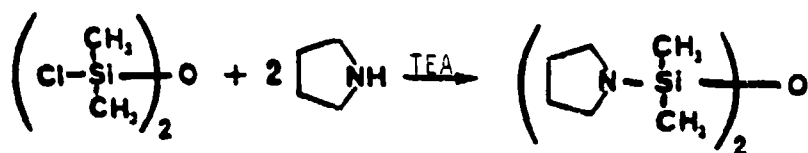
XXXVII   TEA = Triethylamine

Figure 2-11. Typical Synthesis of Bisureidosiloxane.

TABLE 2-9

PHTHALOCYANINOSILOXANE   POLYMERS

	N6305-9	Literature (A)
R.V.(B)	0.12	0.10
P_N(C)	≥ 6	14
P_N(F)	8-9	---
T_G	125-130°C(D)	100°C(E)

(A) "Compound IV", Reference 17

(B) Reduced viscosity in chloroform at RT, 2 g/100 mL

(C) By integration of NMR $Si-CH_3$ resonances

(D) Small endotherm by DSC, possibly T_M

(E) Softening point

(F) GPC estimate

of 0.12 in chloroform and P_n (number-average degree of polymerization) of at least 6, determined by ^{1}H nuclear magnetic resonance (NMR) of the methyl groups on the Si adjacent to the phthalocyaninosiloxane moiety, following Davison and Wynne (Reference 17). An independent determination of P_n, based on end-group counting by NMR of the hydrogens in the phthalocyanine ring, also supported this value. Gel permeation chromatography (GPC) of the polymer in dichloroethane was routine, and showed a heterogeneity index (ratio of weight-average to number-average molecular weight, M_W/M_n) of 1.7, close to the value expected for a linear condensation polymer. As a quasicalibration procedure for the GPC, the monomer XXXVI was also chromatographed. Since repeating unit XXXVIII has ten Si-O bonds, while XXXVI has six, it was assumed that the "polystyrene equivalent weight" (PSEQ) of XXXVIII was 10/6 that measured for the principal peak of XXXVI. On this basis, the PSEQ M_n found for the polymer was equivalent to a P_n of 6.6, gratifyingly close to the NMR-based values. (It is important to note that there are 5 Si-O chain units in the repeating unit of XXXVIII, so the chain length at a P_n of 6.6 is actually 33 Si-O chain units.) A more detailed analysis of the molecular size of XXXVI, based on standard bond lengths and angles (Reference 20) suggests that the measured PSEQ at M_n for polymer corresponded to P_n 8.5, a value still compatible with the NMR measurements. Table 2-9 compares our poly XXXVIII with Davison and Wynne's "polymer IV" of the same structure.

A possible second method to enhance toughening of the phthalocyanine materials was through the incorporation of a unique diarylsilane-based siloxane oligomer, XXXIX (Figure 2-12). The oligomer XXXIX was a resinous material as synthesized. It was isolated during an intermediate stage of sol-gel processing, as described subsequently (Section 2.6.1.1), and the properties obtained are given in Table 2-10, in Section 2.6.1.2.

2.6 SOL-GEL PREPARATION OF POLYMER CERAMIC MATERIALS

Incorporation of suitable organosubstituted polysiloxanes into sol-gel preparations has been somewhat sketchily described in the literature (References 21-27). As is also true with wholly inorganic sol-gel preparations (References 28-30), ratio of reactants (water,
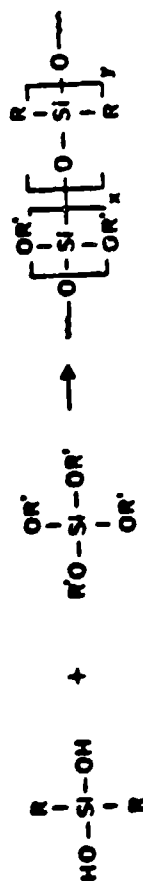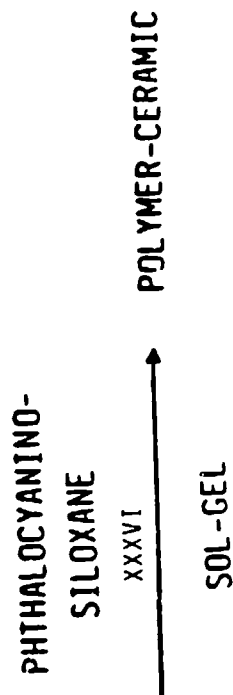
Figure 2-12. Toughening of Phthalocyaninosiloxanes through Incorporation of a Unique Diarylsilane-based Siloxane to Reduce Cross-link Density of Inorganic Component.

silicate esters, siloxanediols;, catalyst (acid or base), and solvent composition (ethanol/toluene, THF, diglyme) all contribute to control of the molecular architecture (cross-link type and frequency) and backbone sequencing, which play a major role in governing the properties of the resultant product.

This conventional sol-gel pathway was later supplemented by a hydrosilation approach. Both pathways are described subsequently.

2.6.1   The Conventional Sol-Gel Pathway

In the conventional sol-gel approach to preparation of silicate glasses, tetraalkoxysilanes (e.g., tetramethyl orthosilicate, TMOS) are hydrolyzed, and resulting silanols condense, eliminating water, to form silicate bonds in a tight three-dimensional network. In order to provide organically modified silicate glasses, silanol-containing organic molecules may be incorporated, so that the condensation reaction will link these into the silicate network. Both preformed siloxane polymers (e.g., hydroxyl-terminated polydimethylsiloxane) and simple silanediols and disilanols have been reported (References 21-27) as starting materials.

2.6.1.1   Sol-Gel Polymerization Of Phenylceramer Compositions

"Phenylceramer" compositions were prepared using diphenylsilanediol (DPSD) in a hydrolyzing solution of TMOS or tetraethyl orthosilicate (TEOS). The initial thrust was to establish preparative control over this approach to polymer-ceramic products, in the absence of the less tractable Pc/Si moieties. The latter could then be introduced as partial replacement for the diphenylsilanediol. Initial preparations used excess water and base catalysis. Subsequently, lower ratios of water to TMOS were adopted, and acid catalysis was also explored.

Phenylceramer polymerizations were undertaken using not only the DPSD monomer but also a commercially available oligomer, poly(diphenylsiloxane) or PDPS, degree of polymerization (DP) about six. With the latter starting material, phase separation became a problem after relatively brief reaction between PDPS

oligomer and partially hydrolyzed TMOS. Temperature elevation in glyme solvent accelerated the onset of phase separation; it did not appear to increase the miscibility of the two phases. The water content of these preparations was set at "50% stoichiometry"; i.e., there were half as many water molecules as there were hydrolyzable methyl groups in TMOS. This 1 .io was expected to promote linear enchainment of the resulting dimethoxysilanediol (Reference 29) rather than a 3-dimensional network or cross-linked structure.

Base-catalyzed DPSD/TMOS preparations at various degrees of "water stoichiometry" and different ratios of TMOS to DPSD gave no phase separation problems in suitable solvents. Even after apparently thorough cure, however, they appeared to be readily soluble in acetone. Inorganic sol-gel literature (Reference 28) shows that base catalysis favors rapid condensation of partially hydrolyzed TMOS to tight clusters, whereas the acid-catalyzed process favors formation of "overlapped" linear chain-extended oligomers, which can be converted thermally to a cross-linked polymer in a subsequent reaction.

Phenylceramer was prepared with acid catalyst, at an equimolar ratio of diphenylsilanediol to TMOS, with "50% stoichiometry" of added water. A leathery/rubbery solid intermediate-stage copolymer, presumably composed of diphenylsiloxane and dimethoxysiloxane units, corresponding to XXXIX, was obtained. This copolymer was examined by differential scanning calorimetry (DSC), thermogravimetric analysis (TGA), and Rheometrics dynamic spectrometry (RDS). DSC showed it to have a Tg about 5°C, and there was a small endotherm at about 160°C, with a marked exothermic shift in baseline at 175-300°C. TGA showed that this shift corresponded to a mass loss of about 10%. In DSC, such a mass loss could be seen as an apparent decrease in heat capacity (C_p), since less heat would be needed to raise the temperature of the smaller mass; this probably accounts for the apparent exothermic baseline shift. Continued TGA (non-oxidative) to higher temperatures showed a total mass loss of 35-38% by 700°C, with little further loss up to 1000°C.

RDS cure analysis of the intermediate-stage copolymer showed that, on heating above 100°C, the copolymer became quite fluid;

viscosity fell to less than 3 poises. There was a small transient rise in viscosity at 135-150°C, but it fell again to about 3 poises, and foaming could be seen. On subsequent holding at 166°C, viscosity began to rise steadily, and after an hour at this temperature, an apparent gel point (by RDS analysis) was reached. Continued aging at this temperature brought about marked increase in network formation, to the apparent level of a lightly cross-linked rubber. When the temperature was then further raised, the apparent cross-link level increased, although RDS machine artifacts contributed to the apparent stiffness of the material. During this high-temperature (180-350°C) treatment, the material between the platens appeared capable of supporting tension. After this postcure and cooling, the remaining material was brittle and glassy and contained large bubbles. Because of easy crack formation in this bubble-filled brittle glass, the platens did not cohere.

2.6.1.2 Sol-Gel Phenylceramer Polymerization Using Phthalocyaninosiloxane Monomer

As a route to investing polysiloxanes with the thermal stability of the phthalocyanine ring, phthalocyaninosiloxanes were synthesized with hydroxyl terminal groups to participate in the sol-gel condensation. The simplest molecule phthalocyaninosilanediol [dihydroxy(phthalocyanino)silicon](XXXIII), was too insoluble to use, so it was converted (Section 2.5) to 1,5-dimethyl-1,5-diphenyl-3-phthalocyaninotrisiloxane-1,5-diol (XXXVI).

The acid-catalyzed equimolar-ratio phenylceramer preparation was modified by replacing 20% of the diphenylsilanediol with an equal number of moles of XXXVI.

The "solids" content and HCl concentration were kept at 30% and 0.014 N, respectively. The reaction time needed to reach a resinous product was much shorter than with the simple phenylceramer (4 hours instead of 16). The resulting resin hardened to a brittle "blue glass" at room temperature.

This glass was examined by DSC, TGA, NMR, and RDS. DSC showed a Tg about 45°C. TGA weight loss was 3% at 150°C; it continued

steadily to 14% at 525°C, then increased sharply to 26% at 700°C, where a near plateau ensued to above 850°C. RDS cure study showed that the glass softened somewhat at 80°C; at 102°C it was soft enough to become sticky. At 110°C, the material was fluid enough to overflow the platens and form threads, although the viscosity was over 1000 poises. Foaming may have begun at 149°C; above 150°C the viscosity began to rise steadily, peaking near 200°C. From 200°C to about 240°C, apparent viscosity fluctuated. Above 240°C the force needed to deform the material began to rise sharply, and the behavior appeared to become more elastic. At 275°C, the forces generated had become so large it was necessary to discontinue the test. The cured material was quite brittle and flaky when cool; like some base-catalyzed phthalocyanine-containing sol-gel preparations, it adhered somewhat to the untreated aluminum platens. The properties of these two types of "phenylceramers" are compared in Table 2-10.

Based on the thread-forming behavior, an attempt was made to advance a portion of this "blue glass" by brief thermal treatment at 180°C. Visual observation during this process indicated that the glass had already advanced somewhat during the three weeks it had been kept at room temperature. Skinning over of the molten surface was observed also. Two simple lap shear joints were manually prepared using FPL-etched aluminum (1" x 5") substrates (1" sq. overlap).

The advanced melt was quite viscous, but reasonably well aligned joints were obtained. These were cured for 2 hours at 180°C, and appeared to adhere/cohere well enough to permit handling. One lap joint was then postcured 1.5 hours at 350°C. The two pieces separated on handling, leaving very brittle residues on both pieces. The non-postcured joint remained handleable for a few days, but also broke cohesively under moderate flatwise tension. The fail re surface showed essentially contiguous bubbles from one edge to the other. A few bubbles extended to the substrate surface, but overall the cured glass adhered moderately well to the etched metal surface.

NMR spectrometry of the soluble "blue glass" stage showed that the phenylmethylsiloxane moieties that were adjacent to the phthalocyaninosiloxane group in starting monomer XXXVI had been

2-37

TABLE 2-10

CERAMER PROPERTIES

Diphenylsiloxane Ceramer	Phenylceramer with 20% "PC Monomer"
Resinous/leathery at RT	"Blue glass" brittle at RT
T_g 10°C	T_g ~45°C
Stored in freezer	Stored at RT
Liquid (very fluid) at 150-165°C	Liquid at 110°C
	Viscous, thread-forming melt
Advances/cures at 167-170°C	Advances at 150-240°C
Still foams, emits volatiles	Much volatiles during cure

virtually completely (97%) replaced by diphenylsiloxane moieties. Some of the phenylmethylsiloxane could be detected in the next position (i.e., two Si-O units away from the Pc ring). Presumably there were also some phenylmethylsiloxane groups elsewhere in the chain, but they would not be readily distinguished by NMR spectrometry.

The most reasonable mechanism for this rearrangement is acid-catalyzed interchange of Si-O bonds. If this process were random, the initial ratio of diphenylsilanediol to phthalocyanino-trisiloxanediol would result in only 67% replacement, so clearly there was a driving force, either kinetic or thermodynamic, and most probably of steric origin, favoring the replacement. Whatever the mechanism, such an effect may also be expected when preformed polymer, e.g., poly-XXXVIII, is incorporated (for toughening) into the phenylceramer sol-gel preparation. This might well result in scrambling of the preformed polymer block, making it more difficult to control the block length (and hence the toughening effect) in the cured polymer.

Conceivably this replacement of one siloxane moiety by another could be repressed if the chain sequence around the phthalocyanino-siloxane group were sufficiently stable. The diphenylsiloxane moiety adjacent to the Pc/Si group might well be that stable. With this in mind, dihydroxy(phthalocyanino)silicon (XXXIII) was reacted with diphenyldichlorosilane under conditions that had been successful in preparing 1,5-dichloro-1,5-dimethyl-1,5-diphenyl-3-phthalocyaninotrisiloxane (XXXV), but no analogous tetraphenyl-substituted compound could be isolated by crystallization. Accordingly, this line of investigation was set aside.

Another approach to control of the unwanted interchange of siloxane moieties was based on the concept (Reference 31) that interchange and polymer chain extension may be promoted by different aspects of the polar catalyst used (e.g., one by degree of acid ionization, the other by polarizability of the anion). Several acids other than hydrochloric acid were substituted in the conventional sol-gel preparation, using about the same acidity and reactant concentrations. ^{1}H NMR spectrometry was used to follow the rate of

interchange. The rate of polymer condensation or advancement was
inferred from the viscosity of the solution or the isolated product;
in a few cases, gel permeation chromatography (GPC) was also used to
estimate how much advancement had occurred. The results of these
studies are shown in Table 2-11. Clearly there were distinguishable
differences among the catalysts between the promotion of interchange
and the promotion of polymer formation. Of the acids examined, none
promoted chain extension rapidly without promoting interchange as
well. In the absence of any reliable guides (Reference 31) to the
catalyst attributes needed to promote desirable reaction paths,
pursuit of this line of investigation would require an Edisonian
approach. It, too, was set aside.

2.6.2 Hydrosilation Sol-Gel Pathway

To avoid the sensitivity of silicon-oxygen bonds to strong acids
and bases, a metal-catalyzed hydrosilation reaction between silanes
(i.e., Si-H bonds) and silanols may provide an alternate route to
stable organo-substituted siloxane/silicate networks (Reference 32).
The fundamental reaction step is illustrated in Figure 2-13 for a
monofunctional silane and a silanol. Difunctional silanes or
siloxanes and silanediols or disilanols would provide linear
polymers, while phenylsilane, which is trifunctional, would be a
potential cross-linking site. In addition to the neutral catalyst,
another advantage of hydrosilation is the much smaller volume change
associated with the reaction, since the mass loss of the
polycondensation is so much less (per bond formed) than in the water-
eliminating autocondensation of silanols to siloxanes.

Diphenylsilanediol and the Pc/Si monomer XXXVI were usable
disilanols. In addition to the commercially available silanes shown
in Figure 2-14 (phenylsilane (XLV), 1,1,3,3-tetramethyldisiloxane
(XLVI), and 1,1,3,3,5,5,7,7-octamethyltetrasiloxane (XLVII)), two Pc-
containing silanes were prepared by addition of dimethylchlorosilane
to XXXVI and XXXIII to give the new compounds XLVIII and XLIX (Figure
2-15), as described in the Appendix.

Several hydrosilation catalysts were tried with various reactant
combinations. Although dibutyltin dilaurate was effective with a
polysilane-PDMS cross-linking reaction, it did not promote
hydrosilation with XLVIII or XLIX and diphenylsilanediol. Results

TABLE 2-11

EFFECTS OF ACID CATALYST CHANGES IN Pc-PHENYLCERAMER

CATALYST	DEGREE OF SILOXANE EXCHANGE	RATE/DEGREE OF ADVANCEMENT
Hydrochloric Acid (Standard)	Nearly Complete	High Degree
Trifluoroacetic Acid	None	Little
Acetic Acid	Rapid	Not Noted
Methanesulfonic Acid	Complete	Some
p-Toluenesulfonic Acid	Much	Not Noted
Phosphoric Acid	Little	Not Noted
Sodium Hydroxide	Unknown	Much; Condensed to Microgel

$$R_3Si-OH \ + \ R'_3Si-H \ \xrightarrow[-H_2]{Metal} \ R_3Si-O-SiR'_3$$
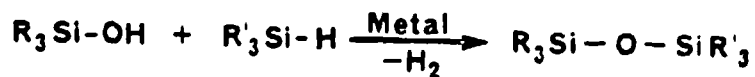
Figure 2-13. Fundamental Hydrosilation Reaction.

Figure 2-15. *Phthalocyanine-containing Silane Monomers.*
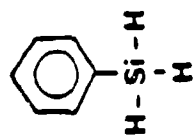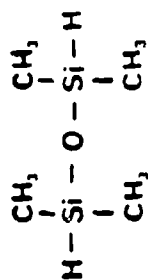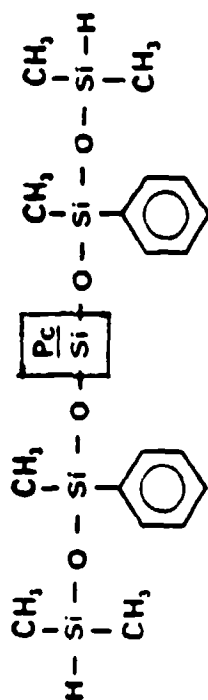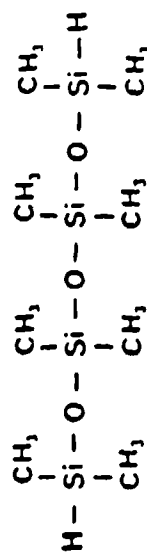
XLVIII
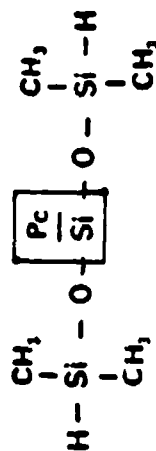
XLIX

Figure 2-14. *Commercially Available Silane Monomers.*

XLVI

XLVII

XLV

with this and other (noble metal) catalysts are summarized in Table 2-12. One example of high-polymer formation was found, but it was accompanied by extensive rearrangement of the siloxane backbone. In this example (Figure 2-16), the acidic catalyst H_2PtCl_6 was employed; it may well have catalyzed rearrangement. In addition, enough heat was necessary to induce reaction so that dehydrative polycondensation of diphenylsilanediol (to PDPS) could have generated free H_2O, also facilitating siloxane backbone rearrangement.

In summary, the hydrosilation pathway did not prove to be free of backbone rearrangements, perhaps because the active catalysts were insufficiently neutral.

2.6.3 Additional Sources of Possible Instability

Statements in related literature imply that some additional sources of possible thermal instability need to be addressed. One of these appears to be specific to the transition noble metal catalysts (platinum, iridium, and rhodium), when used to promote the Si-H/silanol reaction: all other groups on the hydride-containing Si atom may also be exchanged, leading to extensive redistribution of the siloxane backbone at moderate temperatures (Reference 33). Increased selectivity for the desired exchange type was reported for oxide-supported catalysts. The reported findings did not establish whether the scope of this extensive exchange reaction is limited to molecules containing the moiety $H-SiR_2-O-SiR_2-H$. If so, only XLVI need be disqualified from the group of silane-functional molecules in Figure 2-15. However, the authors also postulated that R_2SiH_2 and $RSiH_3$ (e.g., XLV) were particularly unstable in their reaction conditions. If true, this would necessitate design of a more suitable cross-linking site for use in this pathway.

A more general thermal instability may be inferred for phthalocyaninosiloxanes from Kenney's report (Reference 34) of "the migration of entire siloxy end groups during the reaction" in 20 hours at 300°C under vacuum. These were groups initially bonded to the Pc/Si moiety; at least 3 percent of the input end groups were recovered in molecules to which they could have migrated only after scission of this bond. Such a rate of Pc/Si-O bond breakage would preclude 300°C (572°F) service, unless it can be ascribed to

2-43

TABLE 2-12

EFFECTS OF HYDROSILATION CATALYSTS IN POLYMER FORMATION

CATALYST	REACTION	REARRANGEMENT
Dibutyltin Dilaurate	Little or None	None
Wilkinson's Catalyst (Rhodium)	Some; Oligomer Formation	Low Temp: Little 260°C: Complete
Neutral Catalyst (Platinum Complex) (Divinyltetramethyldisiloxane)	Some; Oligomer Formation	Some; Increasing with Time/Temp.
Chloroplatinic Acid (Octanol Complex)	Some	Extensive
Chloroplatinic Acid (THF or Toluene)	Variable; Oligomer to High Polymer (>30,000)	Extensive

XLIX
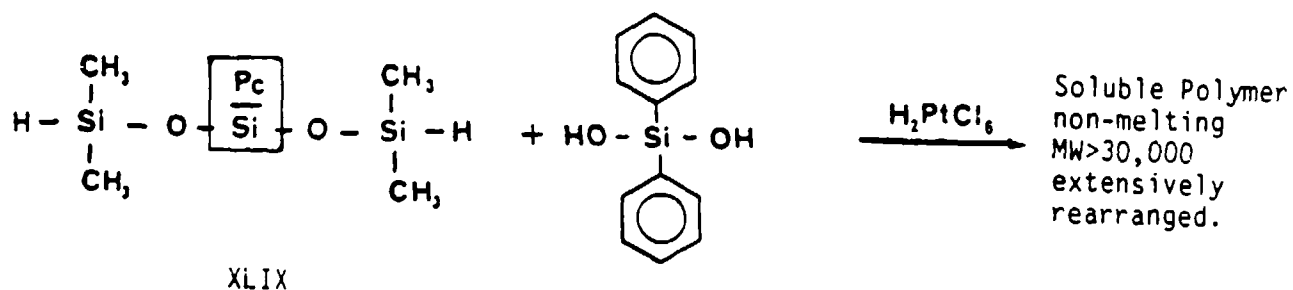
Figure 2-16. High Polymer by Hydrosilation Reaction.

peculiarities of the particular input molecule that Kenney used (specifically, to the absence of a sterically protecting group on one side of the Pc/Si ring).

2.7 ALTERNATIVE APPROACHES

However formed, it is likely that a polysiloxane backbone containing a sequence of more than three $-SiR_2-O-$ units (where R may be alkyl, phenyl, or free vinyl) will be susceptible to chain shortening (or chain scission) with loss of cyclotri- or cyclotetrasiloxane at high temperatures (References 35, 36). Interruptions in the polysiloxane backbone are presumably needed to avert this instability. The massive phthalocyaninosiloxane moiety may act as one such interruption, raising the temperature of thermal breakdown (TGA weight loss) noticeably higher than that of conventional polysiloxanes, though not as much as did the stiff and massive carborane moiety (Reference 37).

A general concept for creating such interruptive moieties is shown in Figure 2-17: react XXXII with a bis(dimethylsilanol) so as to produce a longer-chain bis(dimethylsilanol) that can be incorporated into a sol-gel polymer ceramic composition or into a block copolymer with short polysiloxane moieties.

Two readily available bis(dimethylsilanols) are shown in Figure 2-18. As noted, L is commercially available, while LI is a proprietary product of Hughes IR&D Programs. Other Hughes proprietary products are also available. Thus XXXII and L would give LII (Figure 2-19).

$$\text{Cl} - \boxed{\frac{\text{Pc}}{\text{Si}}} - \text{Cl} \;+\; 2 \quad \text{HO} - \underset{\underset{\text{CH}_3}{|}}{\overset{\overset{\text{CH}_3}{|}}{\text{Si}}} - \text{R} - \underset{\underset{\text{CH}_3}{|}}{\overset{\overset{\text{CH}_3}{|}}{\text{Si}}} - \text{OH} \quad \longrightarrow$$

XXXII

$$\text{HO} - \underset{\underset{\text{CH}_3}{|}}{\overset{\overset{\text{CH}_3}{|}}{\text{Si}}} - \text{R} - \underset{\underset{\text{CH}_3}{|}}{\overset{\overset{\text{CH}_3}{|}}{\text{Si}}} - \text{O} - \boxed{\frac{\text{Pc}}{\text{Si}}} - \text{O} - \underset{\underset{\text{CH}_3}{|}}{\overset{\overset{\text{CH}_3}{|}}{\text{Si}}} - \text{R} - \underset{\underset{\text{CH}_3}{|}}{\overset{\overset{\text{CH}_3}{|}}{\text{Si}}} - \text{OH}$$
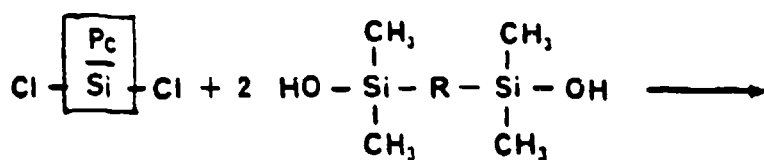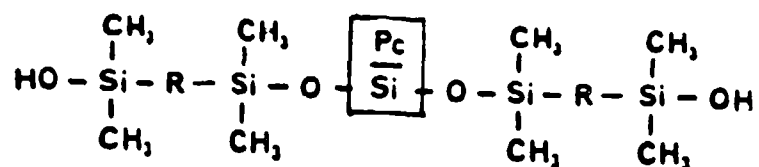
Figure 2-17. Proposed Synthesis of "Interruptor" Phthalocyaninosiloxanes.

Commercially Available

$$\text{HO} - \underset{\underset{\text{CH}_3}{|}}{\overset{\overset{\text{CH}_3}{|}}{\text{Si}}} - \bigcirc\!\!\!\!\!\bigcirc - \underset{\underset{\text{CH}_3}{|}}{\overset{\overset{\text{CH}_3}{|}}{\text{Si}}} - \text{OH}$$

L

Proprietary

$$\text{HO} - \underset{\underset{\text{CH}_3}{|}}{\overset{\overset{\text{CH}_3}{|}}{\text{Si}}} - \bigcirc\!\!\!\!\!\bigcirc - \underset{\underset{\text{CF}_3}{|}}{\overset{\overset{\text{CF}_3}{|}}{\text{C}}} - \bigcirc\!\!\!\!\!\bigcirc - \underset{\underset{\text{CH}_3}{|}}{\overset{\overset{\text{CH}_3}{|}}{\text{Si}}} - \text{OH}$$
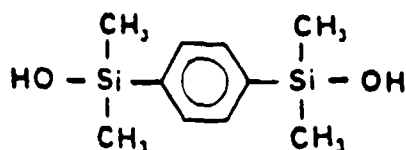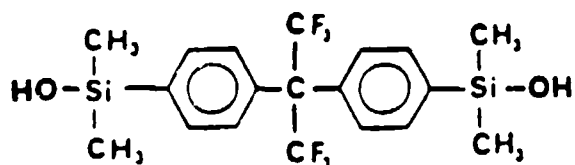
LI

Figure 2-18. Available Bis(silanols).

XXXII L

Figure 2-19. Synthesis of a Specific "Interruptor".

LII

Figure 2-20. Potentially Stable
Phthalocyaninosiloxane.

LIII

2-47

2.8 CONCLUSIONS

Polymer-ceramic materials were made that had thermogravimetric stability but were hard and brittle. They were somewhat adherent to etched aluminum substrates; internal stress and volatiles generation during cure led to cohesive failure of the non-toughened material when applied in a simple lap joint.

The goal of a 371°C (700°F) maximum service temperature remained elusive, and may be unrealistic, given the limitations of carbon-carbon chemistry and the propensity of siloxane chains to rearrange. Nevertheless, indications were found that more stable structures could be defined.

From the standpoint of a hard block - soft block approach to toughening, stable "soft" blocks based on siloxane chains need to be assembled. Stability, in this situation, includes resistance to rearrangement. The phthalocyaninosiloxane unit alone may not be sufficiently stable, but the bulkier tetraphenylphthalocyanino-trisiloxane moiety may show promise, as well as other interruptor groups in the chain. The siloxane rearrangement is subject to catalysis during the sol-gel polymerization; selectivity of catalysts to reduce exchange during polymerization appeared to be possible, also. This was true of both the silanol polycondensation and the hydrosilation routes to siloxane chains.

"Hard" blocks may comprise heterocyclic polymer moieties of the kind envisaged in the original approach (benzimidazoles, benzimidazoquinazolines, and benzoxazoles), as well as the three-dimensional silicate (ceramic) structure resulting from the sol-gel reactions.

Routes to synthesis of the heterocyclic precursors proved more difficult than had been anticipated, but many of the problems were overcome, and success seems possible with sufficient further effort. Difficulties that were encountered involved purification of the silanol-containing heterocyclic moieties. Some alternative routes to the final silylation were explored, and some promise was shown.

Thermal/oxidative stability of these heterocyclic moieties to about 316-343°C (600-650°F) is a possible limiting factor. These heterocyclic hard blocks should be less brittle and respond better to toughening than the wholly inorganic hard blocks.

The direct products of the sol-gel reactions, i.e., the silicate three-dimensional structures, appeared to be stable, although it is

unclear whether microblocks (e.g., assemblies of relatively few Si-O tetrahedra) may be subject to the same kinds of rearrangements as the siloxane chains. If so, they should also respond favorably to selective catalysis during sol-gel reactions.

Overall, a maximum service temperature goal of 316-343°C (600-650°F) may prove more realistic for these materials.

2.9 RECOMMENDATIONS

The lines of investigation recommended for further inquiry are given in an order selected to permit early decisions on routes that may provide simple solutions, while allowing more far-ranging studies of the more complex approaches, if needed.

1. Establish whether the 1,1,5,5-tetraphenyl-3-phthalocyanino-trisiloxane-1,5-diol (LIII) can be prepared (Figure 2-20), and whether it can provide a sufficiently stable siloxane chain to avoid the rearrangements noted in Section 2.6.1.2.

2. Prepare LII and analogous compounds from XXXII and L or LI and establish whether such molecules can provide a sufficiently stable siloxane chain.

3. Based on modern hard/soft acid-base theoretical considerations, select candidate catalysts for the TMOS-based sol-gel process (Section 2.6.1.2) and evaluate in the model system utilizing XXXVI and diphenylsilanediol. Include solvent variations and additions of such "drying control additives" as formamide (Reference 30).

4. Using as a model system XLVIII and diphenylsilanediol, determine whether an active, neutral chloroplatinate catalyst can be found, in order to produce high polymer without rearrangement. Also try other noble-metal complexes and supported catalysts.

2.10 REFERENCES

1. K. S. Y. Lau, A. L. Landis, W. J. Kelleghan, and C. D. Beard, _J. Polym. Sci., Polym. Chem. Ed._, 20, 2381(1982).

2. H. F. Ridley, R. G. W. Spickett, and G. F. Timmis, _J. Heterocyclic Chem._, 2, 453(1965).

3. K. S. Y. Lau, W. J. Kelleghan, R. H. Boschan, and N. Bilow, _J. Polym. Sci., Polym. Chem. Ed._, 21, 3009(1983).

4. B. Gordon III, R. J. Kumpf, and P. C. Painter, _Polym. Prepr._, 26(1), 146(1985).

5. H. Vogel and C. S. Marvel, _J. Polym. Sci., Polym. Lett. Ed._, 511(1961).

6. C. A. Buechler and D. E. Pearson, _Survey of Organic Synthesis_, Vol. 1, Wiley-Interscience, New York, 1970, p. 806.

7. P. E. Eaton, G. R. Carlson, and J. T. Lee, _J. Org. Chem._, 38, 4071(1973).

8. M. Ueda and T. Kano, _Makromol. Chem., Rapid Commun._, 5, 833(1985).

9. M. Ueda, _Makromol. Chem., Rapid Commun._, 6, 271(1985).

10. M. Ueda, H. Sugita, and M. Sato, _J. Polym. Sci., Polym. Chem. Ed._, 24, 1019(1986).

11. Professor Richard Chamberlain, U. C. Irvine, private communication.

12. W. J. Patterson and D. E. Morris, _J. Polym. Sci., A-1_, 10, 169(1972).

13. F. Mareš, P. Neudörfl, Z. Plzák, and V. Chvalovský, _Coll. Czech. Chem. Commun._, 35, 2324(1970).

14. L. F. Fieser and M. Fieser, _Reagents for Organic Synthesis_, I, 233(1967).

15. B. N. Achar, G. M. Fohlen, and J. A. Parker, _J. Polym. Sci., Polym. Chem. Ed._, 20, 2773(1982); _ibid_, 2781(1982).

16. C. W. Dirk, T. Inabe, K. F. Schoch, Jr., and T. J. Marks, _J. Amer. Chem. Soc._, 105, 1539(1983).

17. J. B. Davison and K. J. Wynne, _Macromolecules_, 11, 186(1978).

18. M. K. Lowery, A. J. Starshak, J. N. Esposito, P. C. Krueger, and M. E. Kenney, _Inorg. Chem._, 4, 128(1965).

19. R. D. Joyner and M. E. Kenney, _Inorg. Chem._, 1, 236(1962).

20. F. A. Cotton and G. Wilkinson, _Advanced Inorganic Chemistry_, Wiley-Interscience, New York, 1962, pp 93, 104.

21. H. Schmidt and B. Seiferling, <u>Materials Research Society Symp. Proc.</u>, <u>73</u>, 739(1986).

22. H. K. Schmidt, <u>Polymer Preprints</u>, <u>28(1)</u>, 102(1987).

23. H. Schmidt, H. Scholze, and G. Tunker, <u>J. Non-Cryst. Solids</u>, <u>80</u>, 557(1986).

24. G. L. Wilkes, B. Orler, and H.-H. Huang, <u>Polymer Preprints</u>, <u>26(2)</u>, 300(1985).

25. H.-H. Huang, R. H. Glaser, and G. L. Wilkes, <u>Polymer Bulletin</u>, <u>28(1)</u>, 434(1987).

26. H.-H. Huang, B. Orler, and G. L. Wilkes, <u>Polymer Bulletin</u>, <u>14</u>, 557(1985).

27. C. S. Parkhurst, W. F. Doyle, L. A. Silverman, S. Singh, M. P. Andersen, D. McClurg, G. E. Wnek, and D. R. Uhlmann, <u>Materials Research Society Symp. Proc.</u> <u>73</u>, 769(1986).

28. C. J. Brinker, K. D. Keefer, D. W. Schaeffer, R. A. Assink, B. D. Kay, and C. S. Ashley, <u>J. Non-Cryustalline Solids</u>, <u>63</u>, 45(1984).

29. S. Sakka and K. Kamiya, <u>Materials Science Research</u>, <u>17</u>, 83(1984).

30. L. L. Hench and G. Orcel, <u>J. Non-Crystalline Solids</u>, <u>82</u>, 1(1986).

31. D. R. Uhlmann, private communication.

32. W. P. Weber, private communication.

33. M. D. Curtis, <u>J. Polym. Sci. Polym Symp.</u> <u>70</u>, 107(1983).

34. T. R. Janson, A. R. Kane, J. F. Sullivan, K. Knox, and M. E. Kenney, <u>J. Am. Chem. Soc.</u>, <u>91</u>, 5210(1969).

35. R. L. Merker and M. J. Scott, <u>J. Polym. Sci., Part A</u>, <u>2</u>, 15(1964).

36. L. W. Breed, R. L. Elliott, and M. E. Whitehead, <u>J. Polym. Sci., Part A-1</u>, <u>5</u>, 2745(1967).

37. K. J. Wynne, private communication.

APPENDIX

The preparation of most of the compounds discussed previously has been described succinctly in Tables 2-1 through 2-6 and 2-8. Several preparations are described more fully below.

1. 1,5-Dimethyl-1,5-diphenyl-3-phthalocyaninotrisiloxane-1,5-diol (XXXVI).

The hydrolysis of PcSi(OSiMePhCl)$_2$(XXXV) was monitored very precisely by utilizing Fourier transform nuclear magnetic resonance (FT-NMR) spectrometry techniques. The partially hydrolyzed soluble XXXV (19.5 g) was placed in a 500 mL round-bottom flask along with 250 mL of dioxane, 10 mL of pyridine, and 10 mL of water. The reaction mixture was magnetically stirred, and aliquots were periodically removed and added to water. The resulting precipitate was filtered and dried, and examined by FT-NMR. The reaction takes 46 hours, and quenching should be done at completion, as side reactions occur which appear to involve hydrolysis of the PcSi-OSi bond. (Evidence for this was a very small NMR signal around 0.0 ppm in the final NMR spectrum.) After 46 hours, the flask contents were poured into water (1.5 L), filtered, washed with 300 mL water, and dried at 80°C in vacuo using P$_2$O$_5$ desiccant. The yield of soluble XXXVI (NMR-pure) was 19.6 g (100%).

2. 1,3-Bis(1-pyrrolidinyl)tetramethyldisiloxane

Ethyl ether (300 mL) was placed in a 500 mL round-bottom flask along with pyrrolidine (50 g, 0.70 mole) and triethylamine (100 mL). Dichlorotetramethyldisiloxane (50 g, 0.246 mole) was added to this solution kept at 0°C over a period of 1 hr. The reaction mixture was allowed to warm to room temperature and was stirred for 1 hr. The milky white slurry was then filtered via Schlenk technique (the product was very hydrolytically unstable), and distilled. The fraction boiling at 114-116°C at 2 torr was collected as product: 50 g. (75% yield; GC shows 98+% purity). IR (NaCl plates): 2980, 1260, 1110, 1070, 1040, 800. ^{1}H NMR (CD$_2$Cl$_2$):3.1(m, 8H), 1.95(m, 8H), 0.50(s, 12H).

3. 1,3-Bis(N-phenyl-N'-tetramethyleneureido)tetramethyldisiloxane (XXXVII).

Ethyl ether (250 mL) was placed in a 1 L round-bottom flask, along with 1,3-bis(1-pyrrolidinyl)tetramethyldisiloxane (50.0 g, 0.18 mole). To this was added at 0°C freshly distilled phenyl isocyanate (40 mL, 0.37 mole, in 50 mL ethyl ether). The use of large syringes and septa was most helpful in handling the large quantities of air-sensitive reagents. The reaction mixture was stirred at room temperature overnight. The large amount of product was filtered via Schlenk technique and dried in vacuo. It was impossible to analyze this material by GC as it did not have the requisite thermal stability. The solid was placed in a dry box and transferred to a tared bottle. The yield of white crystalline solid was 83.7 g (90%), m.p. 116-118°C.

^{1}H NMR (CDCl$_3$):7.6-7.0 (m, 10H), 3.05 (m, 8H), 1.80 (m, 8H), 0.60 (s, 12H). IR (CCl$_4$): 2970, 2880, 1680, 1630, 1592, 1400, 1260, 1070.

4. 2,2-Bis(5-[2-(4-bromophenyl)]benzoxazolyl)hexafluoropropane (XXIII)

A mixture of p-bromobenzoic acid, (2.1 g, 0.12 mole) 2,2-bis(3-amino-4-hydroxyphenyl)hexafluoropropane (XXII, 1.83 g, 0.05 mole) and 25 mL of phosphorus pentoxide-methanesulfonic acid solution was heated to 150°C for 4 hours, cooled, and poured into 200 mL of ice-cold 5% sodium hydroxide solution. The resulting precipitate was filtered, dissolved in hexane-dichloromethane solution, and dried over anhydrous sodium sulfate. The mixture was filtered and evaporated to give a tan solid (2.0 g, 90% yield). A portion of this was chromatographed (hexane-dichloromethane on silica gel) to give an analytical sample. The amorphous solid had undetermined melting point(s) but was pure and of the correct structure as determined by IR (no carbonyl) and NMR. Benzoxazole oligomers are well known to exhibit liquid crystalline behavior. IR(KBr):1595, 1470, 1250, 1230, 1198, 1138, 1070, 1010, 830, 810, 730. ^{1}H NMR (CDCl$_3$):8.05 (d, 4H, J=8.6 Hz), 7.90 (s, 2H), 7.64 (d, 4H, J=8.6 Hz), 7.52 (d, 2H, J=8.8 Hz), 7.26 (d, 2H, J=8.8 Hz); ^{13}C-NMR(CDCl$_3$) 163.33. 150.64, 141.99, 132.31, 130.35, 129.04, 127.46, 124.5 (q, 2C, J(C,F)=287.4 Hz), 126.75, 125.52, 122.54, 110.31, 64.57 (septet, J(C,F)=25.6 Hz).

5. **1,1,5,5-Tetramethyl-3-phthalocyaninotrisiloxane (XLIX)**

Dihydroxyphthalocyaninosilicon (24.8 g, 0.0432 mole) in a dry 500 mL round-bottom flask was treated with a solution of 300 mL of dry pyridine and 60 mL of dry tributylamine. Dimethylchlorosilane (16.3 g, 0.170 mole) was added to the vigorously stirred reaction mixture, and stirring was continued under nitrogen for 8 days at room temperature. The mixture was filtered and the solid product was dissolved in 1.6 L of boiling toluene. This solution was filtered and the filtrate was cooled and let stand 48 hours. The crystalline product was filtered off, washed with cold toluene, and dried under vacuum. The yield of 19.2 g was 64 percent of the theoretical. The product was characterized by proton NMR and IR spectrometry.

6. **1,1,3,7,9,9-Hexamethyl-3,7-diphenyl-5-phthalocyaninopentasiloxane XLVIII)**

1,5-Dimethyl-1,5-diphenyl-3-phthalocyaninotrisiloxane-1,5-diol (7.6 g), dissolved in 150 mL of anydrous pyridine, was treated with dimethylchlorosilane (25 mL, 0.23 mole). The mixture was stirred under nitrogen for 2 days at room temperature, and was then filtered. The filtrate was evaporated to dryness *in vacuo*. The yield of 9.3 g was 93 percent of the theoretical. ^{1}H NMR(CDCl$_3$): 9.535(m, 16H), 6.6, 6.29, and 4.83(arom, 9.4H), 2.94(m, 1.5H), -1.06(m, 11H), -2.59(s, 6H). IR (NaCl plates): 3580, 3080, 2920, 2105.

7. **Sol-Gel Reactions**

7.1 **Sample K2359-96-1 (EC677)**

Diphenylsilanediol (3.0 g) was placed in a 50 mL round-bottom flask, along with 2.0 g of tetramethoxysilane, 3 mL of toluene, 3 mL of ethanol, 5.0 mL of water, and 0.5 mL of 5% aqueous NaOH. The mixture was stirred and refluxed for 2 hr. The mixture began refluxing as both a solid and two liquid phases. During the reflux period it became two clear liquid phases. The top aqueous layer was discarded and the residue (3.7 g) was labeled, bottled, and submitted for evaluation.

7.2 Sample K2359-96-2 (EC678)

XXXVI (2.0 g) was placed in a 50 mL round-bottom flask, along
with 2.0 g of diphenylsilanediol, 2.0 g of tetramethoxysilane, 3 mL of
toluene, 3 mL of ethanol, 5.0 mL of water, and 0.5 mL of 5% aqueous
NaOH. The mixture was stirred and refluxed for 12 hr. The mixture
did not dissolve or react in the same manner as K2359-96-1 described
above. For this reason the mixture was taken up in 50 mL of glyme and
refluxed 4 hr. At this time the condenser was removed and the mixture
was cncentrated by simple distillation to abojt 8 mL. The residue was
labeled, bottled, and submitted for evaluation.

7.3 Sample K2359-102-B (EC680)

XXXVI (2.0 g) was placed in a 100 mL round-bottom flask, along
with 2.0 g of diphenylsilanediol, 1.0 g of tetramethoxysilane, 50 mL
of glyme, 5.0 mL of water, and 0.5 mL of 5% aqueous NaOH. The mixture
was stirred and refluxed for 12 hr. The mixture was concentrated by
rotary evaporation to about 8 mL. The residue was labeled, bottled,
and submitted for evaluation.

7.4 Sample K2359-102-A (EC679)

XXXVI (4.0 g) was placed in a 100 mL round-bottom flask along
with 1.0 g of tetramethoxysilane, 50 mL of glyme, 5.0 mL of water, and
0.5 mL of 5% aqueous NaOH. The mixture was stirred and refluxed for
12 hr. The mixture was concentrated by rotary evaporation to about 8
mL. The mixture was concentrated by rotary evaporation to about 8 mL.
The residue was labeled, bottled, and submitted for evaluation.

7.5 Sample K2359-106-A

Diphenylsilanediol (3.0 g) was placed in a 100 mL round-bottom
flask, along with 3.0 g of triacetoxysilane, 45 mL of glyme, and 5.0
mL of water. The mixture was stirred and refluxed for 12 hr. The
mixture was concentrated by rotary evaporation to 7.0 g. The residue
was labeled and bottled.

Final Project Report
for the Period
25 September 1985 - 31 January 1989

MOISTURE DIFFUSION IN ADHESIVES

Dr. W.G. Knauss[*]
Sy Shimabukuro[†]

January 1989

Graduate Aeronautical Laboratories
California Institute of Technology
Pasadena, CA 91125

---
[*] Principal Investigator
[†] Graduate Research Assistant.

1 DESCRIPTION OF PROGRESS

This report summarizes the progress that we have made in furthering the understanding of solvent diffusion into structural adhesives. A description of the analytical, numerical, and experimental accomplishments will follow some preliminary remarks motivating this research.

DARPA and ONR have requested that tests on the bond performance of titanium bonded with LARC-TPI. The test results and discussion are not included in this report and will be presented to DARPA and ONR at a later date.

2 PRELIMINARY REMARKS

When bonded joints are subjected to loads the latter are, generally, transmitted from one adherend to the other through a complex path of stresses. These stresses may be due to the geometry of the joint, the applied loads, the manufacturing process (residual stresses), and from the environment itself. In this stress path, concentrations occur usually near the termination of the joint and it is usually these stress concentrations which determine the ultimate load to which a bonded joint can be subjected. Hence the joint termination area is a zone which should receive special attention in the design procedure. We shall see below that this is especially true in connection with the environmental problem of solvent ingression.

Environmental influences must be considered when one examines the suitability of (new) polymers for adhesion purposes. This is true of temperature, especially in a program aimed at developing high temperature adhesives, as well as of solvents which are normally present in an aircraft environment, including particularly, water. While residual stresses develop from the differential contraction of materials during cool-down in the manufacturing process, solvents tend to swell polymers to varying degrees and thus would seem to oppose the effect of the cool-down process. However,

this seems to be is effective only during the first cycle of diffusion. Solvents tend also to plasticize the adhesive lowering the load carrying capability of the joint. Yet, there seems to be no clear picture of how cyclic diffusion and the stresses interact to affect the subsequent bond strength.

When the temperature is raised to or above the boiling point of the solvent a competition arises between its vaporization and diffusion out of the polymer. Vaporization is clearly undesirable since it tends to disintegrate the polymer but it requires a sufficient concentration of solvent to become destructive. Thus it is clear that this failure scenario may depend as much on the rate of diffusion as on the concentration of the solvent present. This failure mode is all the more critical since it would tend to occur in the joint termination region where there are stress and strain concentrations.

Other researchers [11,15,19] have shown that the stress level affects both the rate and final moisture uptake indicating that the bond termination regions are particularly susceptible to solvent ingression. In one limiting case, Fickian diffusion processes occur and is characterized, for a planar geometry, by the solvent's initial mass pickup being proportional to the square root of time. The other limit case is known as Case II diffusion and is characterized by a mass pick-up that is proportional to time. Current theories explain Case II diffusion as being relaxation controlled where the adhesive's internal stresses due to the osmotic pressure drive the solvent flux.

Thus for the safe operation of bonded joints, intended for high temperature use, it is the purpose of this portion of the program to examine the basic question of solvent diffusion as it occurs interactively with the local state of stress in a bonded joint.

3 DIFFUSION MODEL

3.1 General

It is important to discuss how we visualize the diffusion process while our deliberations occur at the molecular level their description will be entirely in phenomenological terms. This approach is based on our firm conviction that an understanding is relatively easy in molecular/mechanical terms, but extremely difficult to represent analytically and realistically for applications to engineering systems. On the other hand, we know from experience quite a bit about how molecular phenomena are representable in terms of phenomenological description.

The underlying idea is that the motion of the diffusion molecules depends on the space (free volume) available to them in the form of vacancies, cavities, or other transport paths, which may be of the same dimensions as the diffusing molecules. Clearly there must be some driving forces which cause the diffusing species to migrate into the polymer. With some thought one can imagine that these forces take the form of a diffusant concentration gradient, pressure gradient on the diffusant due to the polymer, and other chemical forces occurring between the diffusant and the polymer molecules. It is interesting that by considering the thermodynamics of the diffusion process that these driving forces can be derived plus another in the form of the gradient in temperature [17,27].

The situation is complicated by the polymer's constitutive behavior which is currently best described by nonlinear viscoelasticity. The nonlinearity comes about by the introduction of the polymer's intrinsic viscosity. Coupling between diffusion and mechanical response occurs because the intrinsic viscosity is also dependent on the free volume of the polymer. Further indications that we are on the right track is the work by Thomas and Windle [25] which showed that a key element in modelling non-Fickian behavior is the relaxation of mechanical properties that characterizes a

polymer.

Below we will try to explain the physical basis for the driving forces and present a diffusion model which should be able to cover the range from Fickian to Case II diffusion.

3.2 Physical Basis of the Diffusion Driving Forces

3.2.1 Concentration

Consider a diffusant molecule which can be visualized as a "ball". When there are more "balls" bouncing on one side of this particular ball than on the other side, it will experience, on the average, more impacts from the denser pack of balls and move away from it. This view accounts, basically, for the observation that diffusing molecules will move in the direction of the negative gradient of the concentration. The fact that the ball would be expected to move the faster the more impacts it receives per unit time represents the fact that the rate of mass transport is proportional to the size of the concentration gradient [4].

3.2.2 Pressure

The diffusant molecules will also experience forces exerted from the polymer itself. These are not the forces due to chemical potentials between the polymer and diffusant molecules but the forces due to loads caused by the swelling process as diluent penetrates the polymer and/or external loads applied on the polymer. An unbalance of pressure on the "balls" will tend to drive the "balls" from a region of high pressure to that of a low pressure. Thus the solvent molecules move in the direction of the negative of the gradient of pressure. The greater the unbalance of pressure the more likely that the "balls" will move increasing the mass flux of the diluent [4].

3.2.3 Chemical forces

The chemical affinity between the polymer and the solvent molecules will intuitively affect the mass transport rate. This affinity is responsible for the system's desire to draw in solvent on the one hand and to dilate the polymer structure to accommodate as many of the solvent mo' les as there is room. In a simplistic way we may think of this process as the des .e by the solvent molecules to attach themselves to as much surface of the polymer m·,lecules as possible before "the space gets crowded". Similarly, one would expect that if two species repel each other, diffusion should be very difficult. From our interpretation this chemical driving force should be dependent on the solvent concentration and the sign of the term will depend on whether the force is attractive or not [4].

3.2.4 Temperature

From thermodynamics the gradient of temperature should also be included as a driv-ing force. One can visualize that as the solvent "ball" moves in the direction of increasing temperature its sp··ed and subsequent distance traveled will increase and likewise decrease in the direction of a negative gradient. Therefore on the average the "balls" will move in the direction of positive temperature gradient. The effects of a temperature gradient should be minimal due to the large differences in the time scales between heat conduction and molecular diffusion. More importantly the ef-fect of temperature will be increase the average kinetic en··rgy of both the polymer and solvent molecules. This increase in energy will accelerate the process by helping the polymer molecules to reorient themselves to accommodate the diffusant "balls" and by increasing the speed of the "balls" themselves. Therefore the proportionality constants for all the driving forces should be functions of temperature.

We now assume that the all these driving forces contribute independently in an additive manner to the mass flux. The mass flux equation can now be given explicitly

as

$$j = -D\nabla C - K\nabla P + \lambda\nabla T + S \qquad (1)$$

where the j is the mass flux, D is the diffusion coefficient tensor, C the solvent concentration, P the pressure acting on the solvent, T the temperature, and S the chemical affinity driving force function. K and λ are the proportionality tensors for the pressure gradient and temperature gradient driving force functions, respectively.

3.3   Time shift factor

So far we have considered only the time response of the polymer under the attack of diffusion molecules, but we have not yet addressed the fact that the rate of the accommodating and coordinated motion of the molecule segments is influenced by the intrinsic polymer viscosity. This intrinsic viscosity is, in turn governed by the free volume.

The shift factor ϕ which governs the rate of internal molecular viscosity is a function of the temperature history $T(t)$, isotropic stress component τ_{kk} and the diluent concentration C.

The diffusion process is influenced by the time shift factor in the following way: When a diffusant molecule forces the segments of the neighboring polymer chains to move in order for it to pass, this resultant motion is accelerated in proportion to the shift factor. Thus the time for diffusion should be "reduced" by this shift factor according to the relation

$$dt' = \frac{dt}{\phi(T, \tau_{kk}, C)} \qquad (2)$$

which is the same form as normally encountered with viscoelastic behavior. Since the internal material time is "reduced" by the shift factor the mass flux equation 1 must also reflect this and should now be given as:

$$j = \frac{1}{\phi}(-D\nabla C - K\nabla P + \lambda\nabla T + S) \qquad (3)$$

3.4 Diffusion Coefficient

How to predict the functional form of the components, D, of the diffusion coefficient tensor D is one of the current research topics in polymer diffusion today. Einstein's relations [23] for perfect gases or dilute solutions has D inversely proportional to the concentration. Early work by Crank [13] used the mean values of D given by the initial-rates-of-sorption curves for a number of surface concentrations to determine the relationship between D and C. Work by Fujita [14] tries to theoretically define the functional form of D and correlate the required constants with experimental data. More recently Vrentas and Duda [26] try to develop another model for D by considering the self diffusion coefficients of the polymer and diluent. Vrentas and Duda claim to compare favorably to experimental data and succeeded in modelling some behavior not captured by the Fujita model.

3.5 Pressure Coefficient

By assuming that the only driving force on the mass flux is an external pressure and by modelling the mass transfer as a Poiseuille flow one can show that the pressure coefficient can be given as:

$$K = k_o \cdot \frac{\rho_s}{\eta_s} \cdot f^n I \tag{4}$$

Where ρ_s is the density of the solvent, η_s the viscosity of the solvent, and f the free volume fraction raise to some power n. I is the unit tensor. If in addition one recognizes the fact that external pressure is being supported by both the polymer and the solvent the value of K in equation (4) could be modified to:

$$K = k_o \cdot \frac{\rho_s}{\eta_s} \cdot f^n \cdot \frac{\kappa_s(3\kappa + 4\mu)}{\kappa_s(3\kappa + 4\mu f) + 4\kappa\mu(1 - f)} I \tag{5}$$

Where κ and μ are the bulk and shear modulus, respectively and the subscript s denotes the solvent's properties [4].

3.6 Summary of Governing Field Equations

We may now summarize the pertinent equations which govern the diffusion in polymers (in general). These are:

A. Constitutive Behavior:

$$f = f_o + A \int_{-\infty}^{t} \alpha(t' - \xi')dT + B \int_{-\infty}^{t} M(t' - \xi')d\tau_{kk} + \Gamma \int_{-\infty}^{t} N(t' - \xi')dC \quad (6)$$

$$\ln\phi = -\frac{b}{f_o}\frac{f - f_o}{f} \quad (7)$$

$$t' - \xi' = \int_{\xi'}^{t'} \frac{dt}{\phi(T, \tau_{kk}, C)} \quad (8)$$

1. Stress-Strain

$$s_{ij}(\mathbf{x}, t) = \int_{-\infty}^{t} \mu(t' - \xi')de_{ij} \quad (9)$$

$$\varepsilon_{kk}(\mathbf{x}, t) = \int_{-\infty}^{t} \alpha(t' - \xi')dT + \int_{-\infty}^{t} M(t' - \xi')d\tau_{kk} + \int_{-\infty}^{t} N(t' - \xi')dC \quad (10)$$

2. Diffusion

$$\mathbf{j}(\mathbf{x}, t) = \frac{1}{\phi(T, \tau_{kk}, C)}(-D\nabla C - K\nabla P + \lambda\nabla T + S) \quad (11)$$

B. Field Equations

1. Equilibrium

$$\tau_{ij,j} + \chi_i = 0 \quad (12)$$

2. Strain-displacement

$$\varepsilon_{ij} = \tfrac{1}{2}(u_{i,j} + u_{j,i}) \quad (13)$$

3. Mass Conservation

$$\frac{\partial C}{\partial t} + \nabla \cdot \mathbf{j} = 0 \quad (14)$$

where the following definitions apply:

ν_f	$=$	free volume
ν	$=$	total volume
f	$=$	$\frac{\nu_f}{\nu}$ = free volume fraction
f_o	$=$	reference free volume

t	=	time
$\alpha(t)$	=	thermal creep function
$M(t)$	=	mechanical volume creep function
$\mu(t)$	=	shear relaxation modulus
$N(t)$	=	concentration creep function
T	=	temperature
C	=	concentration
$A, B, \Gamma,$	=	proportionality constants
ϕ	=	(instantaneous) shift function
b	=	constant in WLF equation
ξ', t'	=	reduced time
u	=	displacement component
ε_{ij}	=	strain component
e_{ij}	=	deviatoric strain component
τ_{ij}	=	stress component
s_{ij}	=	deviatoric stress component
j	=	mass flux vector
D, K, λ	=	proportionality constants
S	=	Chemical "driving" force
χ_i	=	body force component

4 NUMERICAL WORK

4.1 General

The solution to the field equations that govern the diffusion process in polymers will in general be obtained numerically. Both the coupling of the governing partial differential equations and the nonlinear constitutive behavior necessitate the use of a numerically derived solution. For future reference the diffusion problem will be known as the Diffusion Boundary Value Problem (DBVP) and the stress analysis will be known as the Solid Boundary Value Problem (SBVP). Two separate methods have been applied to perform the numerical analysis, we initially used the method of finite differences, FDM, to solve the one-dimensional diffusion problem by converting the partial differential field equations into its numerical equivalent. Converting the differential equations is straight forward and there exits a large volume of references on the subject. We pursued this area until we had to solve the coupled diffusion-viscoelastic problem, here we ran into a host of numerical problems. At this point, we felt that there may be a better way to solve the problem.

Other researchers here at the California Institute of Technology have been using a program call FEAP (Finite Element Analysis Program) to solve the coupled thermal-viscoelastic problem. As the name of the program suggests the technique of finite elements, FEM, is used to numerically model the governing field equations. The heat conduction problem is very similar to the diffusion problem and we felt that by modifying this program less time would be needed in developing a computer code. Other motives for the change in numerical technique included the fact that FEAP has a tested nonlinear viscoelastic element and if we continued using our finite difference program we would have had to develop and test a nonlinear viscoelastic routine. Meshing or modelling the region of interest is simpler because the finite element method satisfies the field equations within an element thus it is trivial to have

variable sized elements within the region to be analyzed. With finite element it is easy to expand from the one dimensional problems that is used to do parameter studies to the two or three dimensional problems that would be needed to model an adhesive joint. Finally the broader goal of being able to solve the coupled thermal-diffusion-viscoelastic problem can be accomplished once the diffusion problem is solved. Below is a summary of the progress in each of the two techniques.

4.2 Finite Difference Program

The flow chart of the program is shown in figure 1. Due to the nonlinearities, two major iteration loops were incorporated into the program. The first loop insured that the nodal concentration values within a time step converged to some value as governed by the mass conservation equation. This concentration iteration scheme used two numerical schemes; one being an explicit scheme and the other an implicit scheme. The explicit scheme is used as a predictor and provides the intial guess at the start of a time step, and the implicit scheme corrects that guess through a series of iterations. The finite difference molecules for both schemes are shown in figure 2. The iteration halts after the average absolute change for the concentration nodal values between successive iterations is below some tolerance value. The program then proceeds to the next time step.

The second major iteration occurs within each concentration iteration. This iteration insures that the stress and strain values satisfy the constitutive behavior and that equilibrium is satisfied.

Convergence is not necessarily guaranteed in either iteration loop but no problems have occurred in all the test cases examined so far. We feel that this program is capable of solving the coupled diffusion-elastic solid problem where the diffusion coefficient is dependent on the free volume of the solid [6].

The solution using the finite-difference scheme is shown in figure 3. This is a
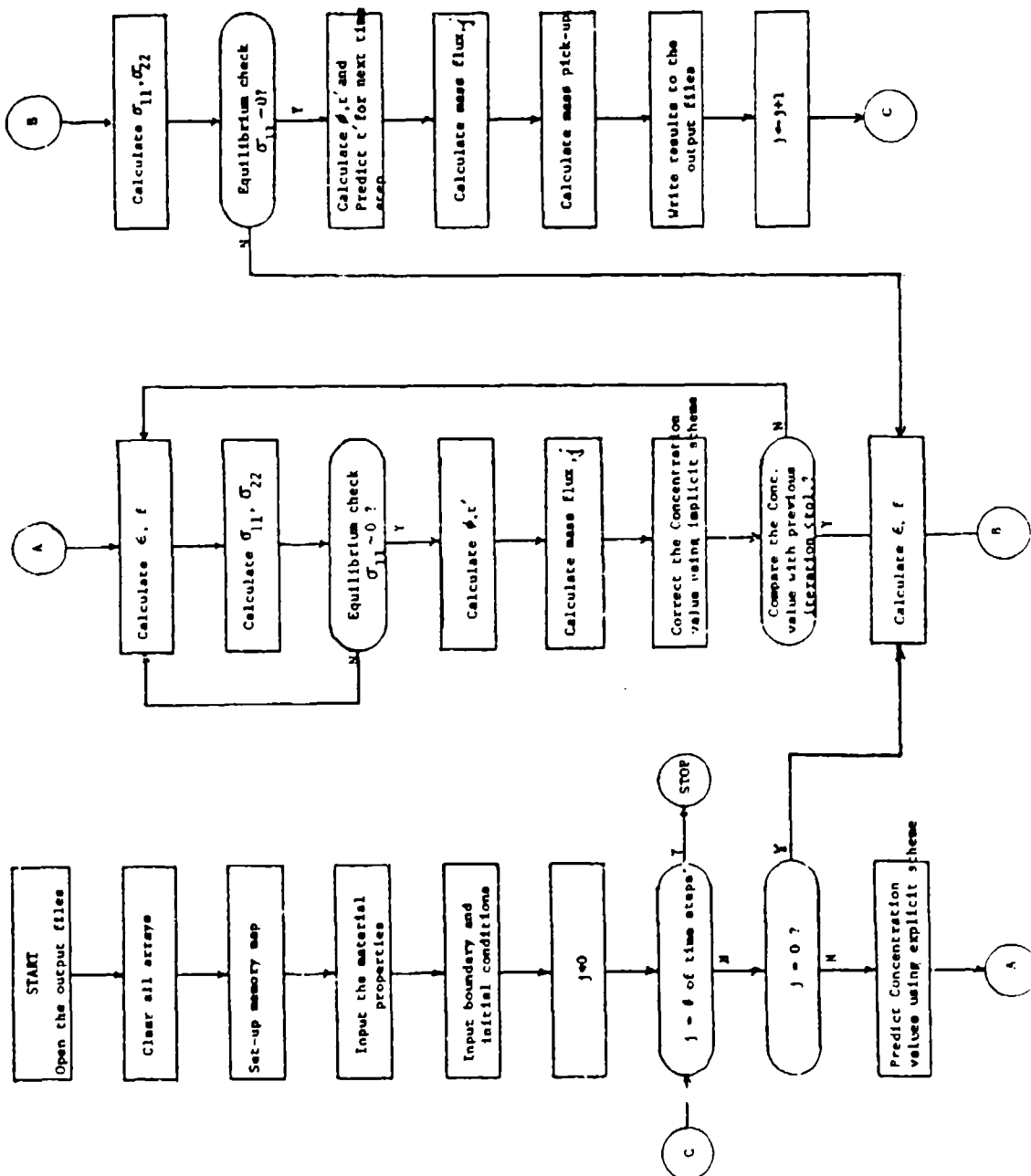
Figure 1: Flow Chart for the Finite Difference Program
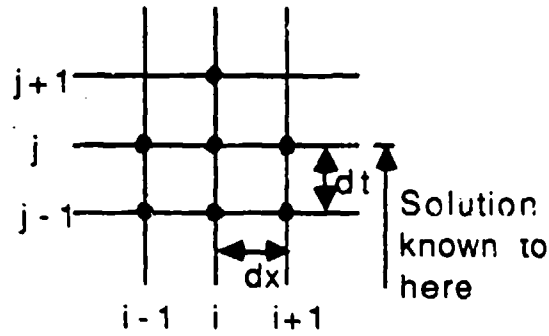
$$C_{i,j+1} = 2C_{ij} - C_{i,j-1} + \frac{\Delta t}{2\Delta x}[J_{i+1,j} - J_{i+1,j-1} + J_{i-1,j-1} - J_{i-1,j}]$$

Explicit molecule
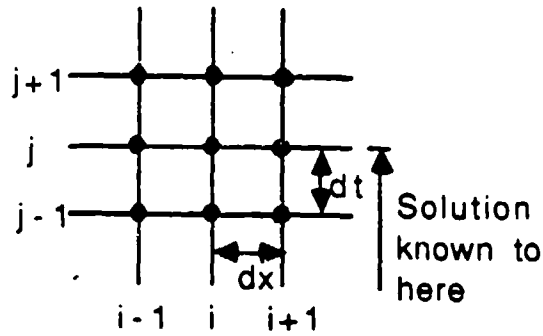
$$C_{i,j+1}^{k+1} = \frac{4}{3}C_{ij} - \frac{1}{3}C_{i,j-1} - \frac{\Delta t}{12\Delta x}[(J_{i-1,j-1} - 4J_{i-1,j} - J_{i-1,j+1}^{k}) - (J_{i+1,j-1} - 4J_{i+1,j} - J_{i+1,j+1}^{k})]$$

Implicit molecule

Figure 2: Finite difference molecules for time integration scheme
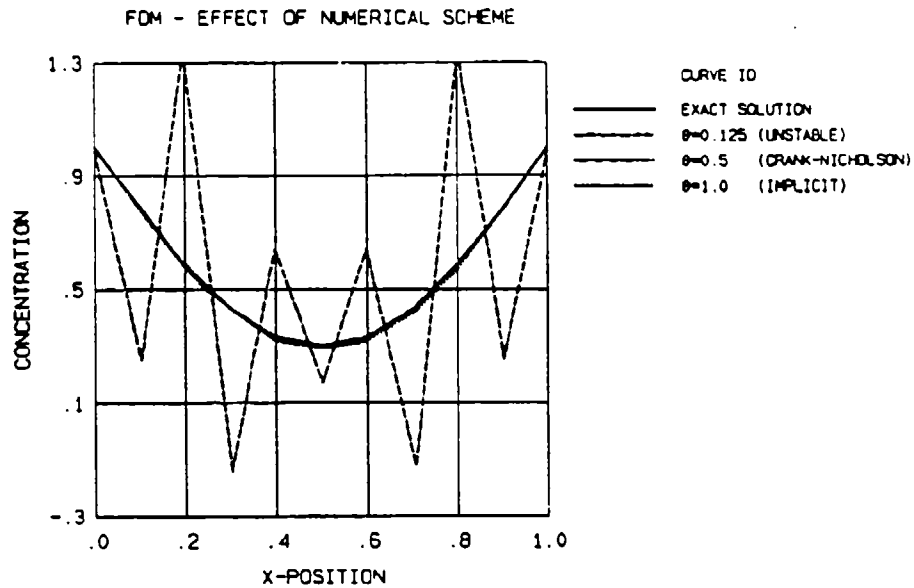
Figure 3: Transient diffusion through a plane sheet $(0 \leq x \leq 1)$, $C(0,t) = C(1,t) = 1.0$, $C(x,0) = 0.0$, at $t = 0.06$

transient solution at time 0.06 through a plane sheet, $0 \leq x \leq 1$, given an initial concentration, $C(x,0) = 0.0$, and boundary concentrations of $C(0,t) = C(1,t) = 1.0$. The diffusion coefficient, D, is equal to 1.0. One of the problems that we have in implementing the finite-difference method is that of numerical instability which can be seen as the oscillating curve in figure 3. Some instability was solved by the time integration scheme that was incorporated but strong restrictions on the time step and mesh size still exist. These restrictions have been shown to be less sever when we incorporated the finite element method.

With the conversion to the finite element method this program can still be used to check the results from the modified FEAP program.

4.3   Finite Element Method

FEAP is a versatile highly modular finite element program that relies on the use of macro commands to accomplish what is needed to solve a problem. There are

commands to define the mesh and input the boundary and initial conditions. After this is done other commands will control how the problem is to be solved. In this way FEAP is easily adapted to solve a host of linear and nonlinear problems. All that is basically required is a routine defining the element stiffness matrix and force vector. The basic finite element formulation for the nonlinear diffusion model can be found in appendix A.

4.3.1 Example test cases

Example test cases for the diffusion problem are shown in figures 4, 5, 6, 7, 8 and 9.

4.3.2 Pressure Smoothing

There are two major problems with coupling the DBVP to the SBVP the first is the problem of consistency between the two solutions and the other is of numerical accuracy. Within each diffusion timestep the new concentration values will be "fed" into the SBVP and a new pressure field is generated that will be "fed" back into the DBVP as part of the iteration updating. A problem with "feeding" the pressure back into the DBVP has to do with the order of the finite element used to generate a solution. We are using a displacement formulation to solve the SBVP thus a linear element which can capture a linear variation in displacement will have a constant pressure state within the element. Likewise, a parabolic element can, at best, have a linear variation of pressure within the element. The concentration enters the SBVP on the same order as the pressure and to maintain a consistent solution it should be a linear field if a parabolic element is used. The DBVP has the pressure entering with the same order as the concentration so if we use a linear element to solve the DBVP a linear pressure field must be used. Hence there is an order mismatch between the two problems.

The pressure field requires the derivatives of the displacements which are most
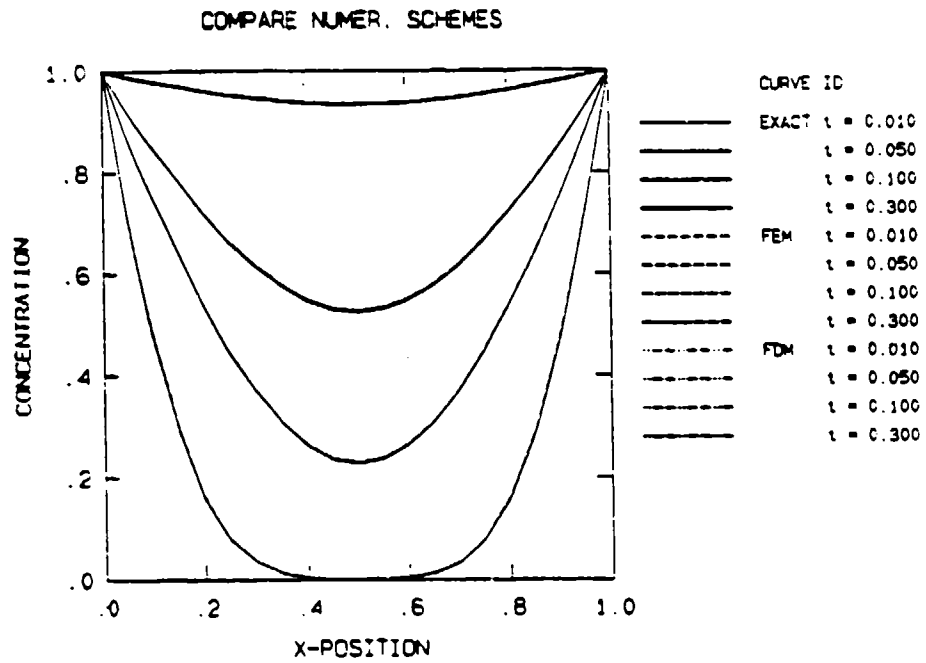
Figure 4: Comparision between FEAP, FDM, and the exact solution for the transient concentration profiles, using $D = 1.0$, boundary conditions $C(0, t) = C(1, t) = 1.0$, and initial condition $C(x, 0) = 0.0$.
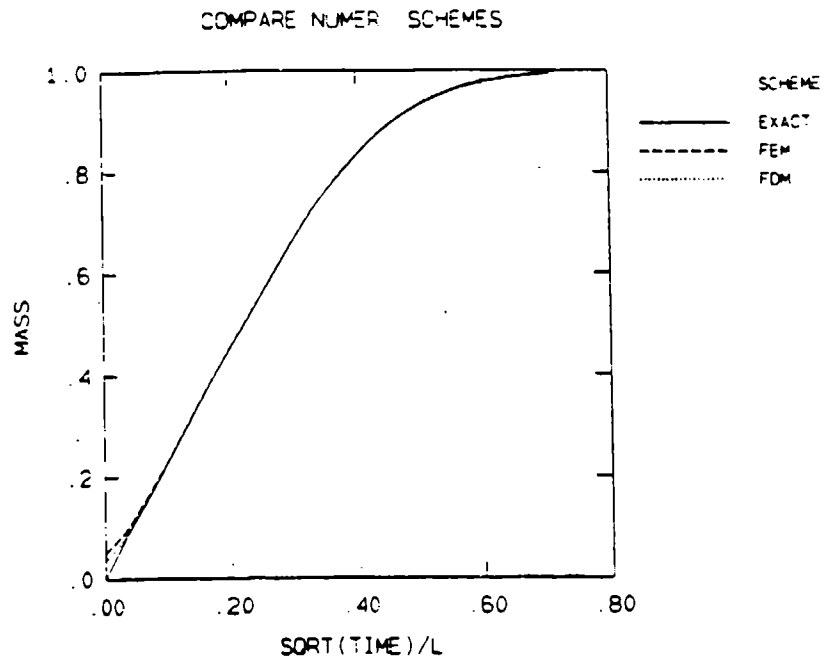
Figure 5: Comparision between FEAP, FDM, and the exact solution for the mass pick-up curve, using $D = 1.0$, boundary conditions $C(0, t) = C(1, t) = 1.0$, and initial condition $C(x, 0) = 0.0$.
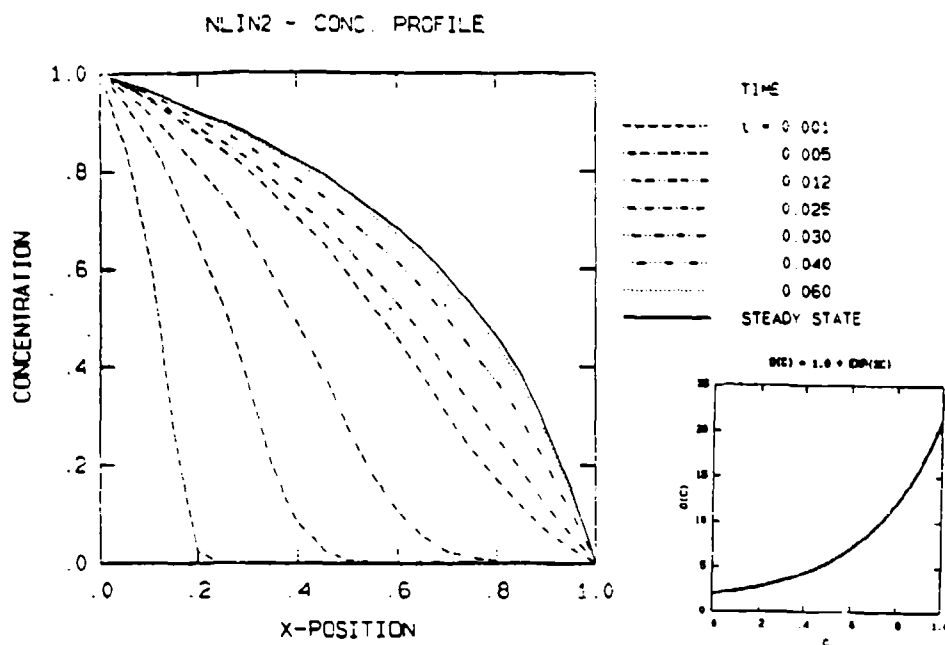
Figure 6: Transient concentration profiles, using $D(C) = 1 + e^{3C}$, $C(0,t) = 1.0$, $C(1,t) = 0.0$, $C(x,0) = 0.0$.
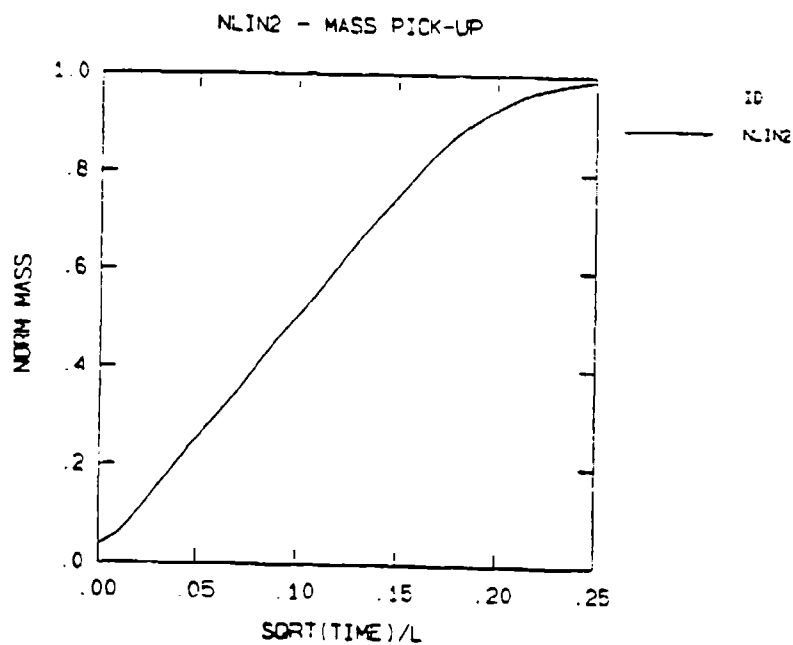
Figure 7: Mass pick-up curve, using $D(C) = 1 + e^{3C}$, $C(0,t) = 1.0$, $C(1,t) = 0.0$, $C(x,0) = 0.0$.
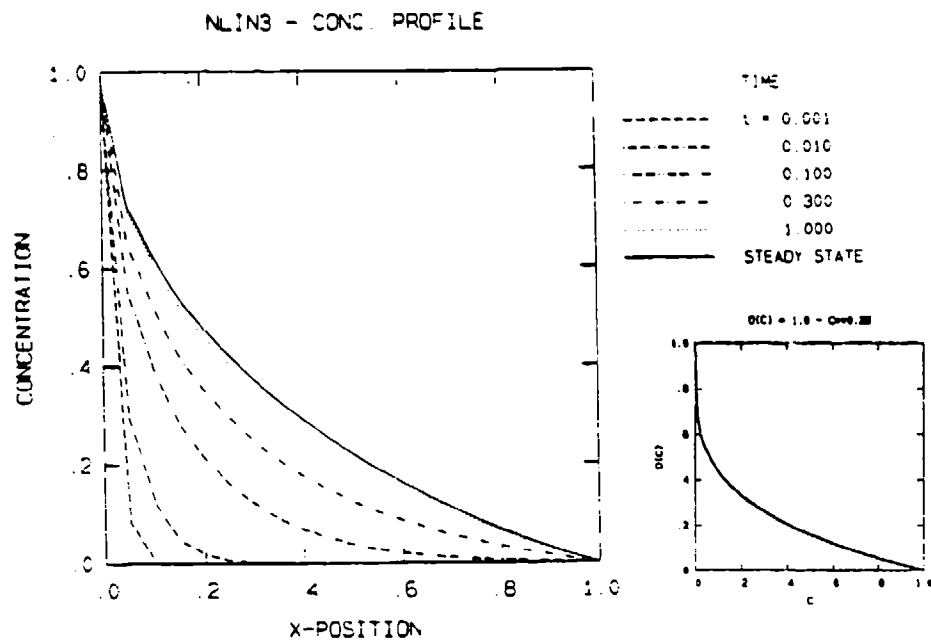
Figure 8: Transient concentration profiles, using $D(C) = 1 - C^{0.25}$, $C(0,t) = 1.0$, $C(1,t) = 0.0$, $C(x,0) = 0.0$.
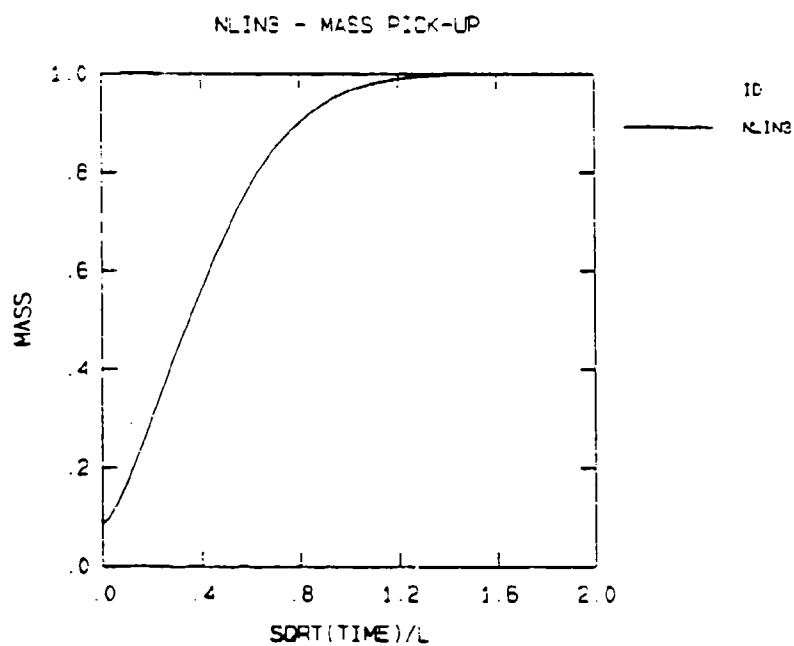
Figure 9: Mass pick-up curve, $D(C) = 1 - C^{0.25}$, $C(0,t) = 1.0$, $C(1,t) = 0.0$, $C(x,0) = 0.0$.

accurate when computed at the element's Gauss points. Unfortunately, in order to "feed" the pressure back into the DBVP the pressure values are needed at the element's nodes. To achieve this and to maintain accuracy we used a smoothing procedure that is described by Hinton and Campbell [16]. This technique allows us to take the pressure values at the element's Gauss points and to smooth them globally to the element's nodal points.

Two schemes were evaluated to see which would give us the best solution results. One scheme used a linear element to solve the SBVP and the pressure was smoothed using a linear element and the other scheme was to use a parabolic element with a linear smoothing element. The results are shown in figures 10, 11 and 12 where the derivatives of the smoothed pressure values are calculated and compared to an exact solution. As the mesh was refined the linear-linear element failed to converge to the proper solutions whereas the parabolic-linear elements did. From this work we felt that the best way to couple the SBVP and DBVP is to solve the SBVP using parabolic elements and smooth the pressure field using a linear element. The DBVP will then be solved using a linear element to maintain the consistency requirement.

4.3.3 Semi-coupled Problems

There were two classes of semi-coupled problems that we addressed. One being where the DBVP creates a pressure field but the pressures do not "feed" back into the DBVP. A solution of this type are shown in figures 13, 14, 15 and 16. It should be noted that the concentration profile and mass pick-up curves are the same as a diffusion only case. The material properties are taken to be elastic.

The other semi-coupled problem can be visualized as a region that is initially prestressed and then the DBVP is solved. The concentration is not allowed to affect the stress field. Numerical simulation for the steady-state solutions show no differences, within plotting accuracy, between the simulation and the exact analytical

LINEAR-LINEAR PRESSURE SMOOTHING
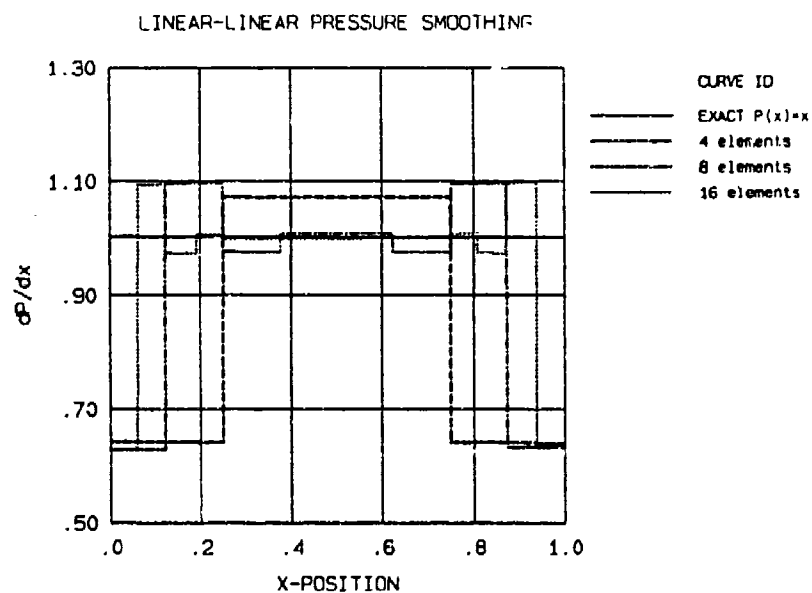
Figure 10: SBVP solved using linear elements and smoothed using linear elements. The exact pressure field is linear, $P(x) = x$.

PARABOLIC-LINEAR PRESSURE SMOOTHING
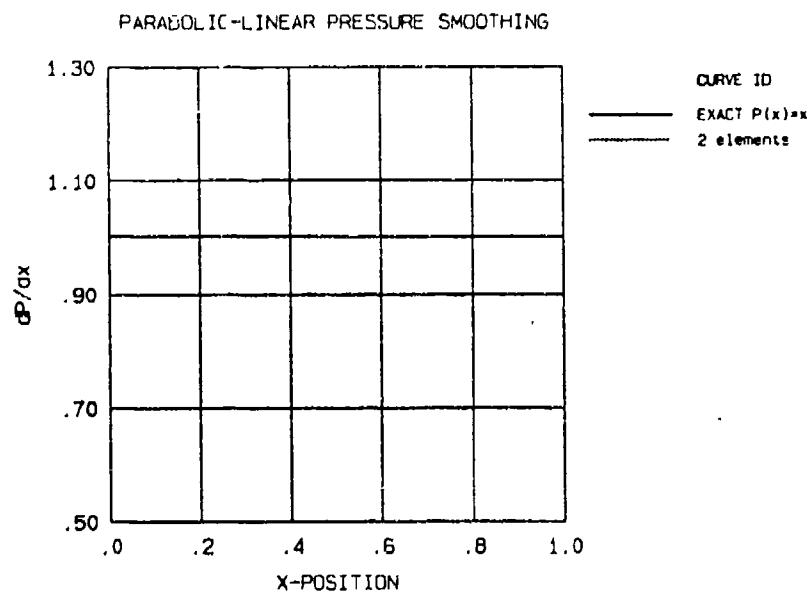
Figure 11: SBVP solved using parabolic elements and smoothed using linear elements. The exact pressure field is linear, $P(x) = x$.
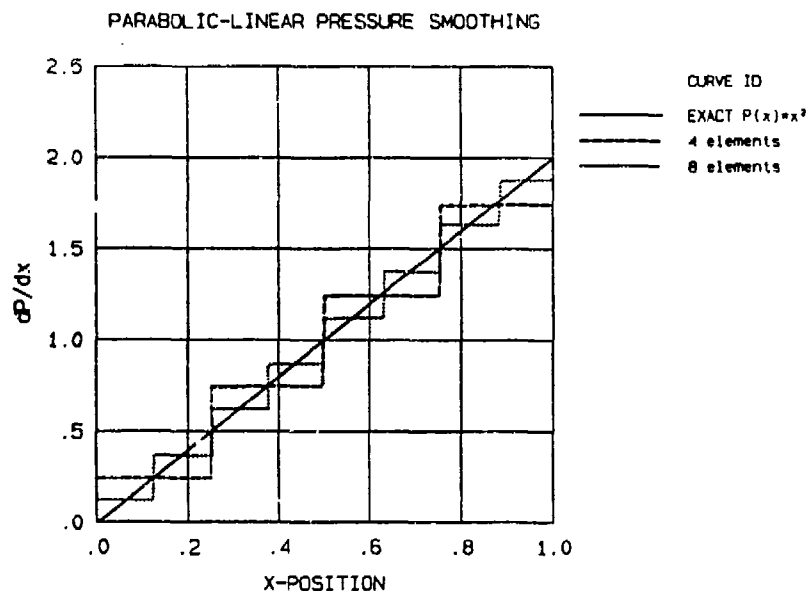
Figure 12: SBVP solved using parabolic elements and smoothed using linear elements. The exact pressure field is parabolic, $P(x) = x^2$.

solutions.

4.3.4 Coupled Problem Test Cases

We are currently looking at test cases for the coupled problem. For an elastic body several solutions have been attempted and seem to indicate the results that we expect. The boundary conditions, figure 17 represent bonded joint where the adherends are much stiffer than the adhesive. The elastic properties have been normalized such that for $C(1,t) = C(-1,t) = 1.0$ the pressure would be for TEST5 $P(1,t) = P(-1,t) = 1.0$ and for TEST6 $P(1,t) = P(-1,t) = 0.5$. From figure 18 the results look Fickian and an averaged diffusion coefficient would well model such a process. This is important since it shows that the moisture transport may not be Fickian yet a Fickian model could be used. Thus experimental data on polymers far below and above the glass transition region may have hidden a pressure forcing response.

CONC. - 1-D STRAIN, SEMI-COUPLED
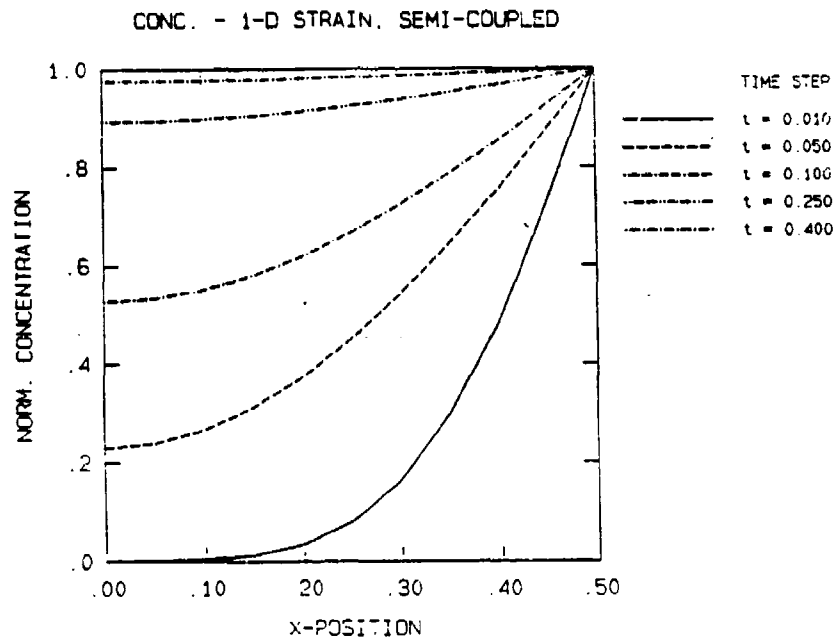
Figure 13: Semi-coupled concentration profile for $D = 1.0$, $C(-1,t) = C(1,t) = 1.0$, $C(x,0) = 0.0$

MASS PICK-UP - 1-D STRAIN, SEMI-COUPLED
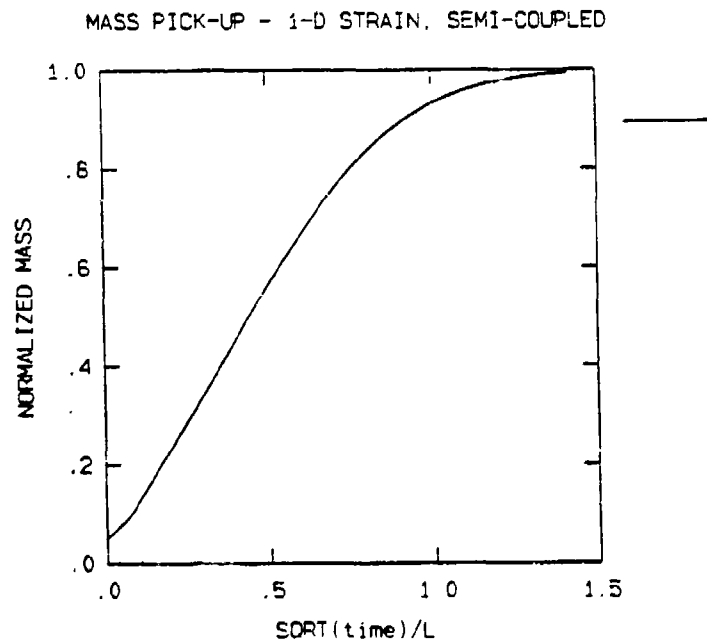
Figure 14: Semi-coupled mass pick-up for $D = 1.0$, $C(-1,t) = C(1,t) = 1.0$, $C(x,0) = 0.0$

STRAIN XX - 1-D STRAIN, SEMI-COUPLED
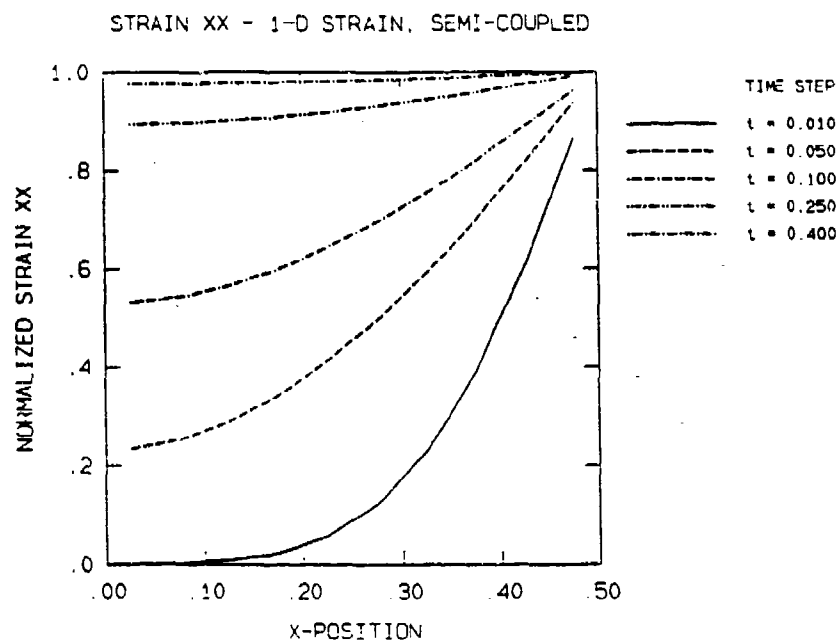
Figure 15: Semi-coupled strain profile for the above concentration profile

STRESS YY - 1-D STRAIN, SEMI-COUPLED
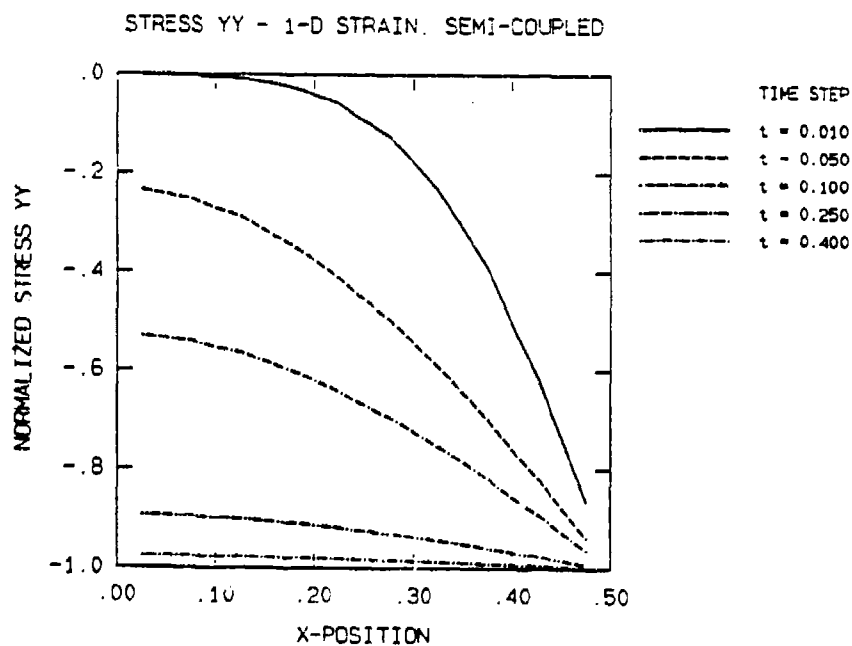
Figure 16: Semi-coupled stress profile for the above concentration profile

3-24
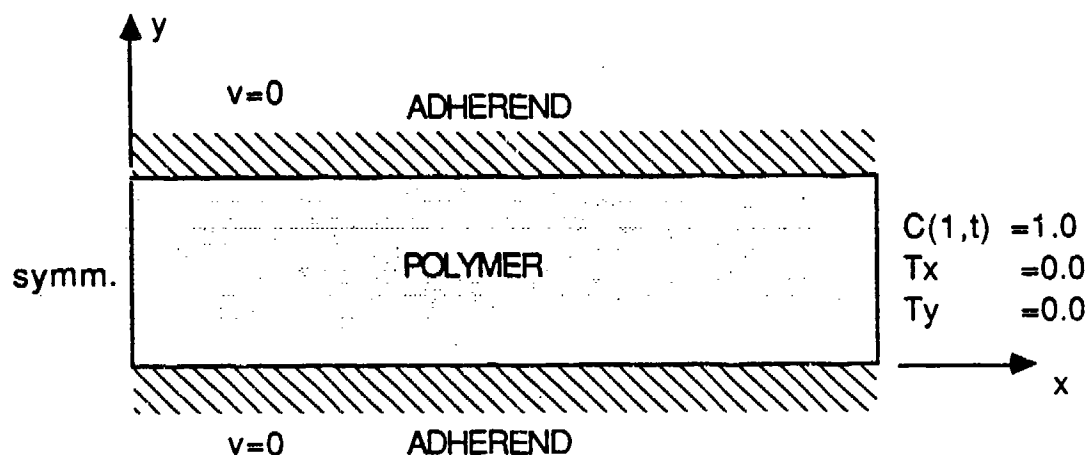
Figure 17: Boundary conditions for fully coupled problem

We are currently looking at the effects of rate relaxation using simple viscoelastic material properties. An example of a particular solution is shown in figure 19. The viscoelastic response is such that the pressure at the $P(1,t)$ decays from 1.0 to 0.5. The reason that no effect can be seen is that the rate of decay is on the order of the diffusion process.

4.4 Future work

It has been shown that Case II diffusion occurs when the pressure term begins to dominate the mass flux equation [25]. We hope to explore this limiting case but numerical instabilities have occurred. We are now working to find a stable scheme.

Once a viable working numerical scheme has been developed we can then apply our ideas on diffusion process to model experimental data.

COUPLED MASS PICK-UP

CURVE ID
FICKIAN (D=2.0)
TEST5 (P(1,t)=1.0)
TEST6 (P(1,t)=0.5)
FICKIAN (D=1.0)
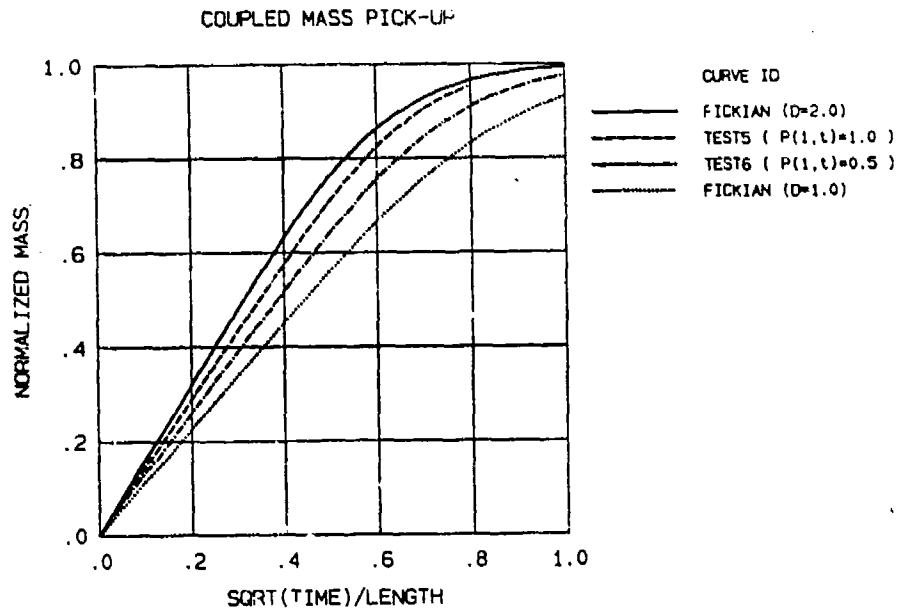
Figure 18: Fully coupled mass profile for $P(1,t) = 1.0$, $P(1,t) = 0.5$ as compared to Fickian diffusion

MASS PICK-UP

CURVE ID
TEST5 (ELASTIC)
TEST6 (ELASTIC)
TEST7 (VISCOELASTIC)
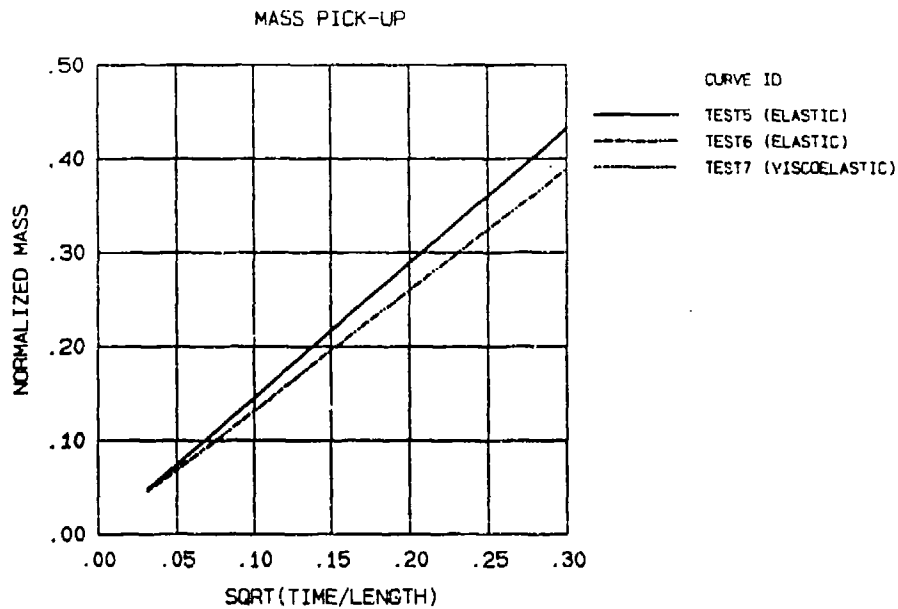
Figure 19: Fully coupled mass profile for simple viscoelastic response as compared to elastic response.

5   EXPERIMENTAL WORK

5.1   General

The stress state within a polymer has been shown for a given polymer–solvent system to affect both the rate of diffusion and the final concentration level. Previous work by other researchers [15] was basically done on "dogbone" polymer specimens exposed to a solvent after being loaded in uniaxial tension. Compressive load data was nonexistent due to the specimen geometry. We felt that by using a different specimen geometry the effects of both compressive and tensile stress states could be examined. The specimen geometry would be a thin layer of polymer applied onto a substrate impervious to the solvent that would be used in the experiment. Bending a strip of the bilayered specimen would thus load the polymer in tension or compression depending on which side of the substrate the polymer was applied. The convex side would load the polymer in tension while the load on the concave side would be compressive. If the polymer was thin "enough" with respect to the overall thickness then the through-the-thickness strain variation could probably be neglected. Differences in the graphs of weight gain versus time for the various strain states would indicate the strain dependence of the diffusion process.

The ability to plot the profile of the concentration curve throughout the polymer as it evolves through time would give a better indication of the diffusion process. This type of measurement can be done by using methods similar to what Long and Richman [18] or Mills, Palmstrom and Kramer [20] used. Unfortunately, we do not possess the equipment needed to use their methods. An alternate way of generating a concentration distribution curve maybe to use optical techniques but due to problems encountered with specimen preparation for the weight gain tests we did not fully explore this option.

5.2 Preliminary Testing

A preliminary test using the bilayered technique was done to check the feasibility of the method. Specimens were manufactured using an epoxy based structural adhesive produced by 3M called AF-163-2M. The adhesive was chosen because we had a supply on hand at the start of the program. The nominal thickness of the adhesive after curing was about 1.0mm and the substrate was a 0.8mm thick aluminum plate. A 150 X 150mm bilayered plate was manufactured and 4 - 35 X 150mm strips were cut from the plate. Aluminum foil was glued to the ends of the specimens where the loads were applied to protect the adhesive from moisture intrusion. See figure 20. The specimens were loaded to different strain levels by using a four-point loading device, see figure 21. The specimens were placed into an environmental chamber set at 30°C and 90% R.H. and the results of the experiment are shown in figure 22.

The results of the test showed that the method was sensitive enough to detect changes in the rate of diffusion with the load levels applied. One can see that qualitatively a higher tensile stress tended to accelerate the diffusion process whereas a compressive stress retarded the rate. A power law was fitted to the data of the form

$$M(t) = Kt^\alpha \tag{15}$$

or of the form

$$M(t) = Dt^{\frac{1}{2}} \tag{16}$$

The resulting coefficients are shown in table 1. Note that the exponent α is nearly equal in all cases and that it is greater than 0.5, which is what α would be for a purely Fickian process. This maybe interpreted as an indication that other transport processes are occurring within the polymer. The monotonic dependence on strain that K and D exhibit indicates that the final equilibrium value is strain dependent reinforcing our idea that the free volume of the polymer plays a large role in the diffusion process.
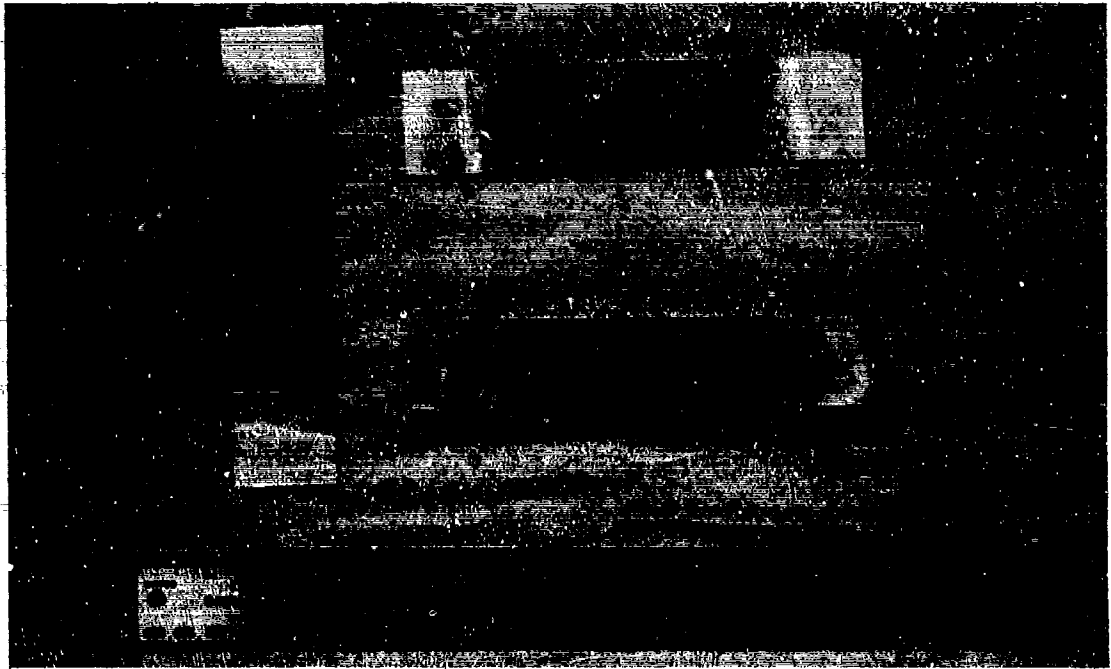
Figure 20: Preliminary test specimen
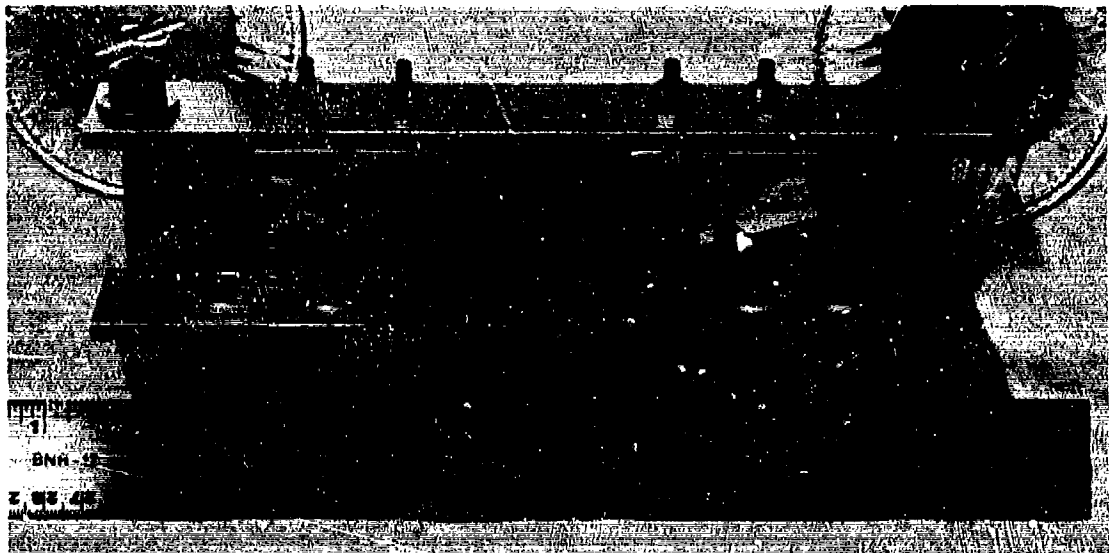
Figure 21: Preliminary test loading device with specimen
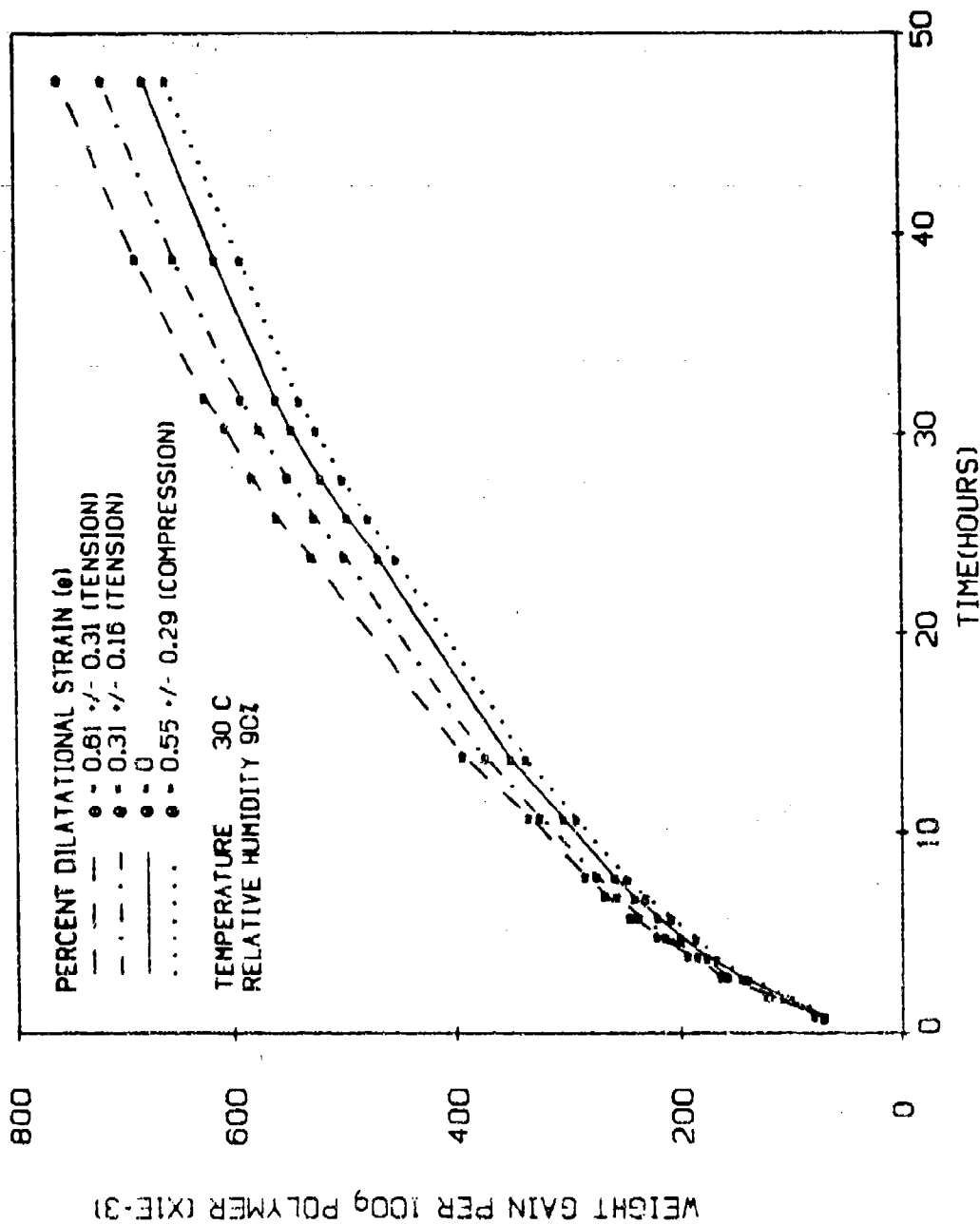
Figure 22: Preliminary test results. Plot of weight gain versus time for various load levels.

% STRAIN	K	α	D
0.55 (COMP)	0.0775	0.560	0.0934
-	0.0808	0.558	0.0969
0.31 (TENS)	0.0859	0.558	0.1027
0.61 (TENS)	0.0871	0.569	0.1080

Table 1: Curve fitting results for the preliminary test

5.3 Modifications to the Test Method

After evaluating the results several changes were made in order to better quantify the results. In the preliminary experiment the mean strain variation throughout the polymer was on the order of $\pm 50\%$. To decrease the strain variation several factors needed to be considered the most important being the total weight and the expected weight gain that could be accurately measured. We chose to increase the thickness of the aluminum substrate by a factor of ten which decreases the mean strain variation to about $\pm 5\%$ [5].

The increase in thickness created a problem on how to bend the aluminum substrate to load the polymer. We decided that by plastically deforming the aluminum beam the substrate would not only protect one side of the polymer from the solvent but would also be loading the polymer too. The plastic deformation was accomplished by using a four-point loading device inserted in a hydraulic press see figure 23. The loading plastically deformed the specimens to a desired radius of curvature. Figure 24 depicts the relative displacement device that was built to facilitate the measurements needed to calculate the applied strains on the adhesive due to the plastic deformation of the aluminum substrate [5].

The adhesive used in the initial test contained scrim material that may have influenced the diffusion results. We felt that it would be advantageous in terms of
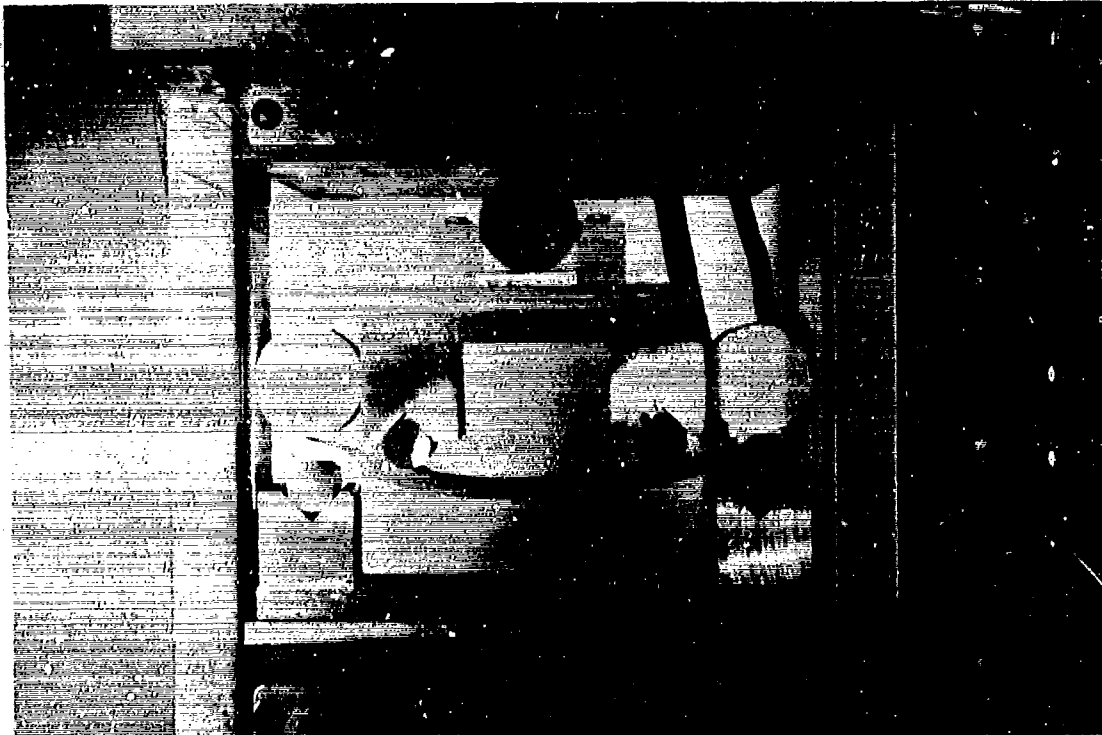
Figure 23: Four point loading device with the hydraulic press
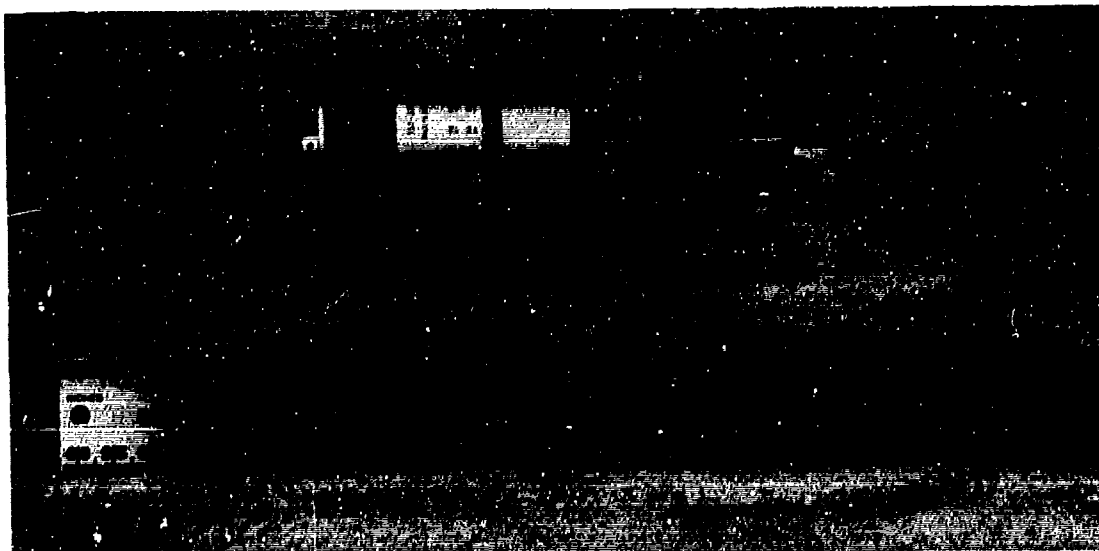
Figure 24: Relative displacement measuring device
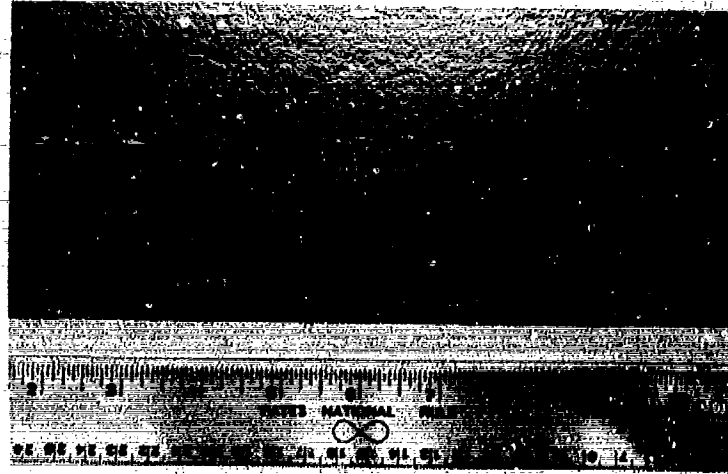
Figure 25: Specimen voids that occur during manufacturing.

modelling and analysis to use the unscrimmed version of the adhesive, AF-163-2U. Attempts to produce specimens using the unscrimmed adhesive resulted in an adhesive layer that contained numerous defects in the form of bubbles or voids, see figure 25 Several plausible explanations for this are that the scrim material provides some alternate paths that allowed any volatile gases to escape or that the scrimmed and unscrimmed material were at different stages of precuring which will affect the amount of volatiles released during the curing process. Whatever the reasons finding a method to minimize the void formation during the curing process was time consuming. After many months of trial and error a combination of vacuum bagging, external pressure, curing time, led us to a set of specimens that, though not perfect, were testable. Several specimen strips underwent a surface analysis to quantify if any surface contamination occurred during the manufacturing process. Specifically we were worried that the release film used in the curing process may have transferred to the adhesive's surface. This work was performed by the chemistry laboratory at Hughes and their report is attached as appendix B. The test indicated that there is no release film on the surface of the adhesive but there maybe some silicone contami-

nation. We are assuming that since we used the same curing method and storage for all of the specimens that these surface analysis tests provide a good representation of our specimens in general.

The specimens were dried by placing them in a vacuum desiccator at 50°C. After 100 days a weight loss in most of the specimens could still be detected and a question of exactly what was being outgassed arose. A qualitative chemical analysis of the outgas material performed during the early part of December 1987 was inconclusive to whether the material consisted of various monomers, solvents, or water. A gas trap collected a yellowish residue and a clear fluid. The yellowish residue was insoluble in pentane and was thought to be the yellow primer material that was used. Not enough of the clear fluid was collected to determine if it was miscible in pentane or at what the freezing temperature was but the fluid was thought to be water.

5.4 Modified Tests

5.4.1 General Procedure

Two groups of specimens, labelled I and J, were exposed to moisture. Group I underwent a single cycle of sorption at T=~50°C, +90%R.H. and desorption under vacuum at room temperature,T=~20°C. Group J underwent two cycles the sorption and desorption, the first cycle was sorption at full immersion in distilled water, T=~50°C and desorption under vacuum at room temperature, T=~20°C. The second cycle was fully immersed in distilled water,T=~50°C but the desorption occurred under vacuum at T=~50°C.

The two groups were placed in an environmental chamber that controlled the temperature and humidity to 50±0.1°C, 90±10%R.H., respectively. Group I was placed on a rack and group J was placed in trays of distilled water. The chamber broke down after 800 hours of testing after which both groups were then placed in a vacuum desiccator at room temperature. The sorption and desorption curves

showed a permanent weight gain that we may attribute to corrosion of the aluminum substrate. For the second sorption cycle we used a temperature bath to minimize the temperature variation during the experiment, see figures 26,27. The specimens were placed in the temperature bath using a double boiler configuration in which the tray holding the specimens was filled with distilled water and then immersed in the water bath. This limited the temperature variation in the tray to approximately $\pm 2°C$ versus the 10°C variation that occurred when the specimens were in the environmental chamber. The double boiler configuration also allows us to test the water to detect if any chemical leaching of the specimens occurred.

To calculate the average diffusion coefficient using two methods, one proposed by Crank [13] and the other by Choji and Karasawa [12]. Both methods, assumes a constant diffusion coefficient for the Fickian model and appears to give similar diffusion coefficient values, but the Choji and Karasawa's method allows one to predict the final mass gain/loss while Crank's method requires the final mass gain/loss values. It should be pointed out that the values shown are average diffusion coefficients and that several experiments must be conducted at varying humidity levels to define the concentration dependence of the diffusion coefficient. It should also be noted that the mass loss/gain are normalized by the volume.

These cyclic sorption and desorption experiments indicate that several problems not initially considered should before need to be taken into account. Below are the results and discussion of the experiments.

5.5 Discussion of Results

5.5.1 Sorption 1, Groups I,J

The initial sorption curves for groups I and J are shown in figures 28, 29, 30 and 31. The nonlinear initial mass pick-up versus the square root of time indicate, es-
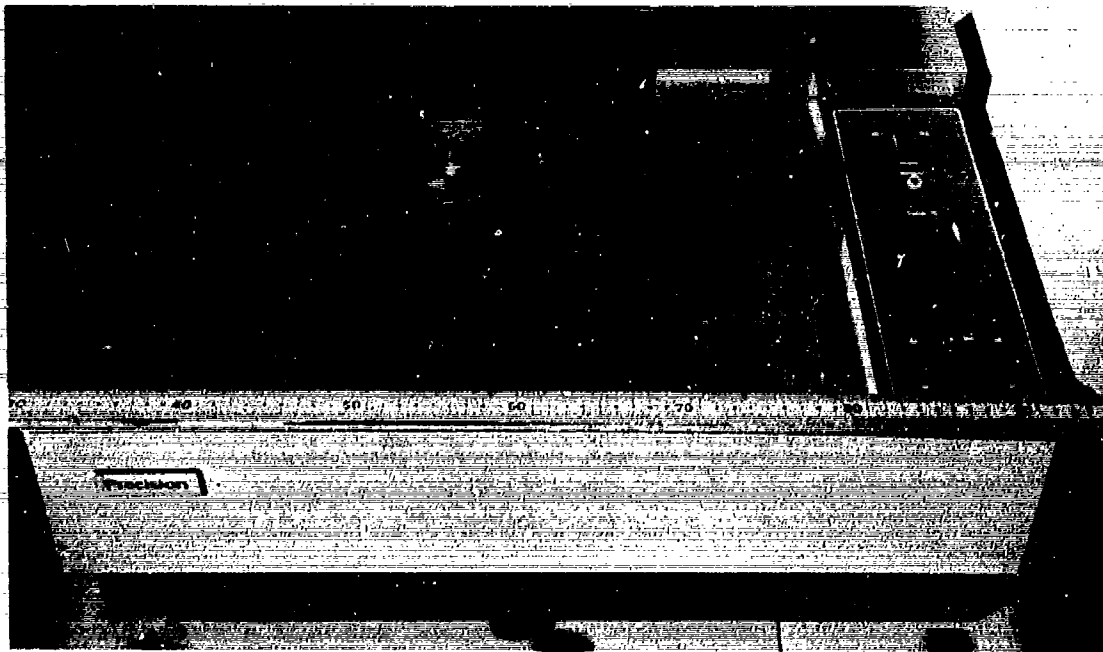
Figure 26: Temperature bath with cover.
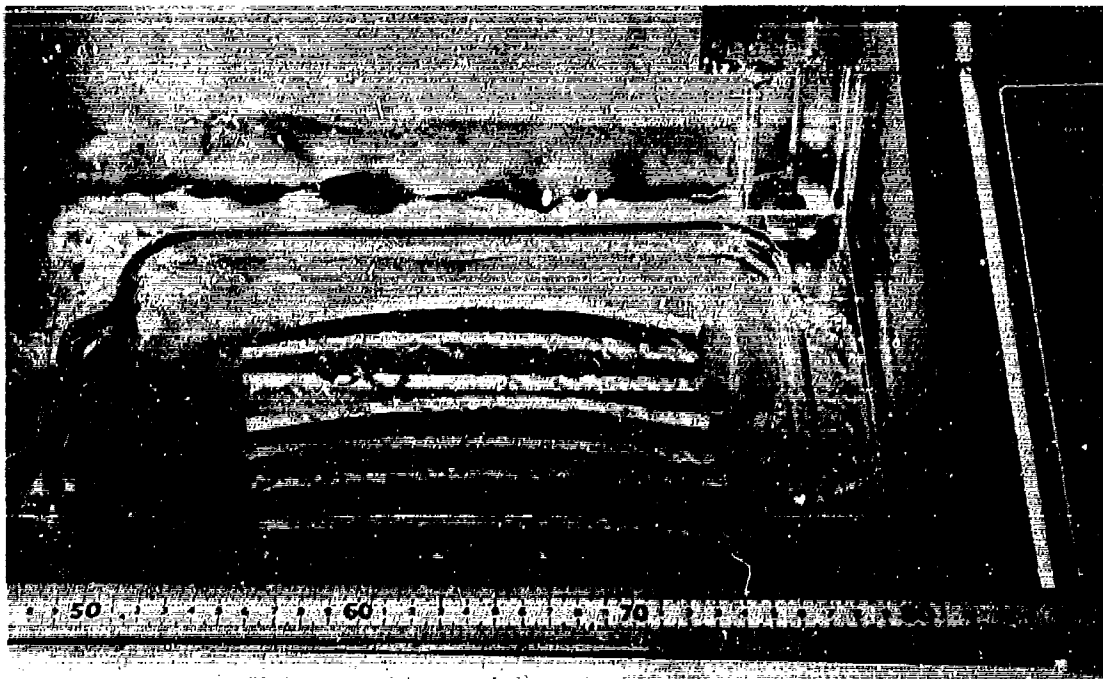
Figure 27: Specimens in temperature bath.

pecially for group J, non-Fickian transport processes. We later concluded that the non-Fickian behavior was probably due to corrosion of the aluminum substrate and will be discussed later in the report. Since the curves were clearly non-Fickian we did not try to reduce the data using either Crank's or Choji and Karasawa's method.

5.5.2 Desorption 1, Groups I,J

The desorption results are shown in figures 32 and 33. The initial linearity of the data when plotted versus the square root of time suggested that a Fickian process maybe able to describe the results, see figures 34 and 35.

From figures 36 and 37 there appears to be a slight correlation between the diffusion coefficient and mechanical strain levels. Although the increase both in compression and in tension maybe due due to damage incurred upon loading of the adhesive. A slight concentration dependence maybe inferred from figures 38 and 39 where the diffusion coefficient increases with concentration. Figures 40 and 41 shows that the final mass loss appears to increase with increasing tensile strains but compressive strains have little effect.

By using the calculated diffusion coefficients and final mass pick-up values a numerical desorption curve can be generated. A comparison between the experiments and the numerical solutions are represented by figures 42 and 43 for the specimens I5 and J3, respectively. Both methods seemed able to provide the correct parameters as to simulate the desorption experimental data quite well using a constant diffusion coefficient Fickian process. The method of Choji and Karasawa consistently tended to underpredict the final mass loss for all the specimens while Crank's method overshot the bend of the curves. These tendencies which could indicate that some other transport processes maybe occurring.
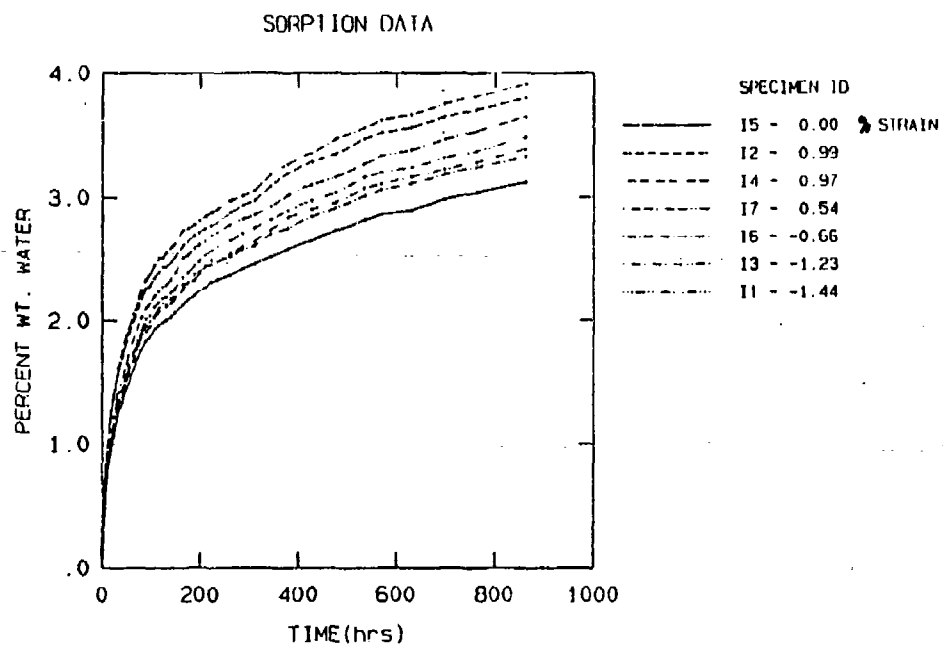
Figure 28: Sorption data for specimen group I plotted versus time.
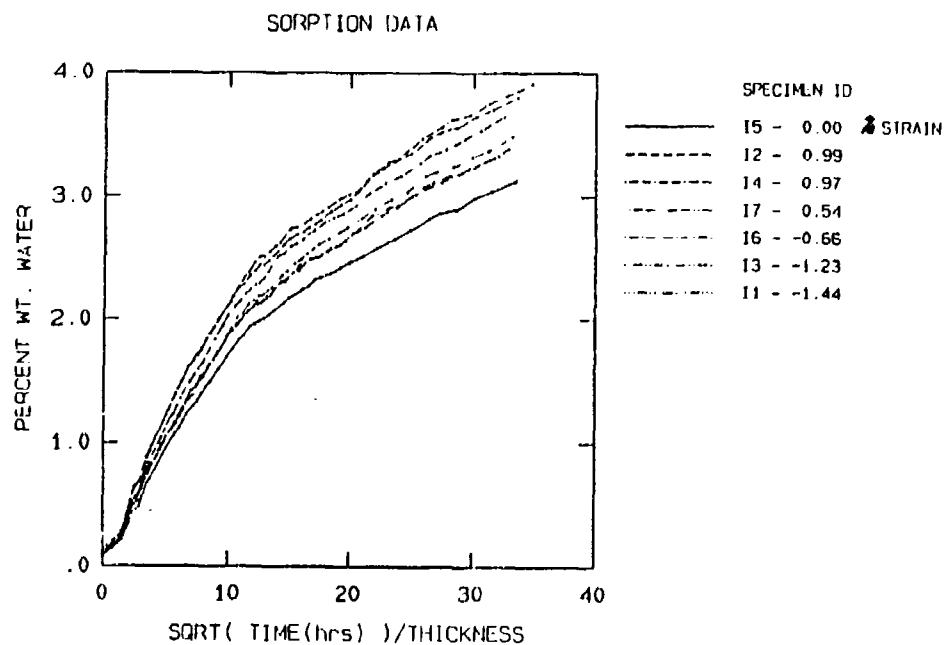
Figure 29: Sorption data for specimen group I plotted versus the square root of tin e.
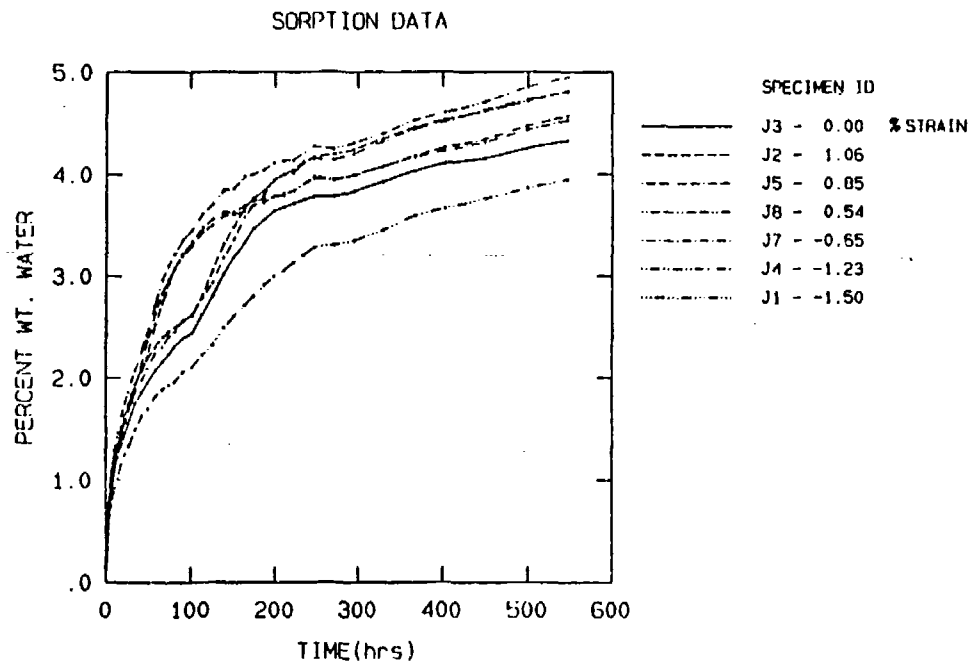
Figure 30: Sorption data for specimen group J plotted versus time.
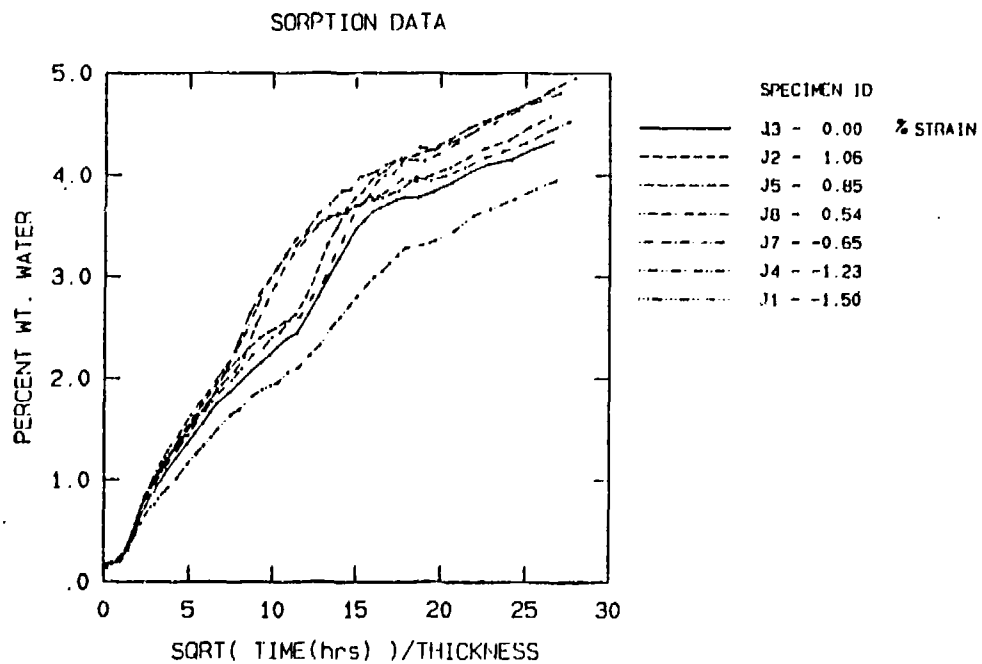
Figure 31: Sorption data for specimen group J plotted versus square root of time.

I - DESORPTION DATA
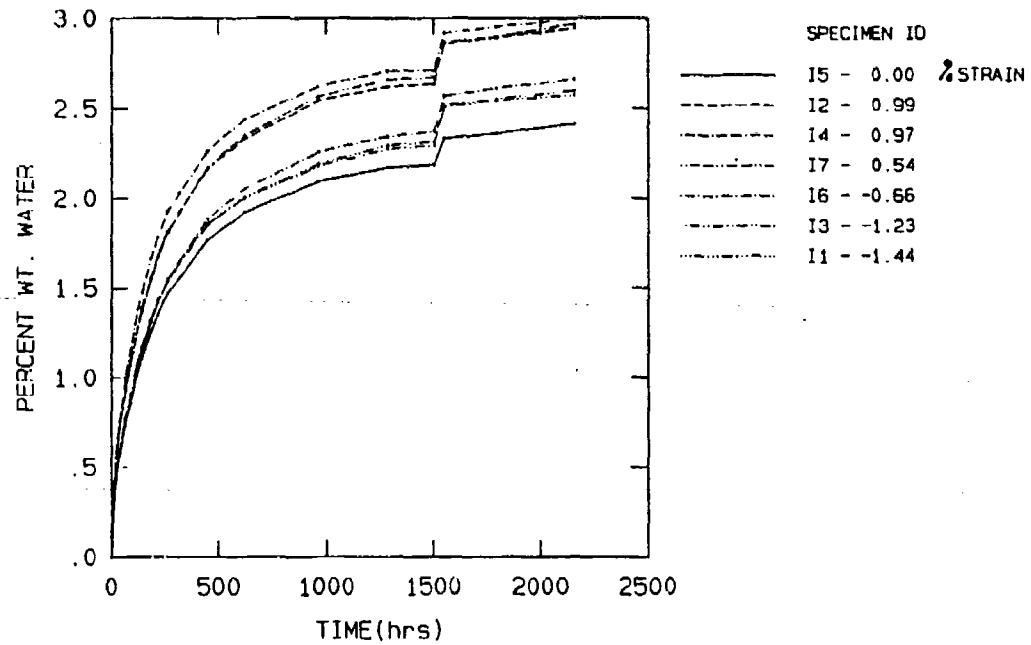
Figure 32: Desorption data for specimen group I plotted versus time. The sudden jump in weight loss near the 1500 hour mark is when the temperature was raised from 20 to 50°C.

J - DESORPTION DATA
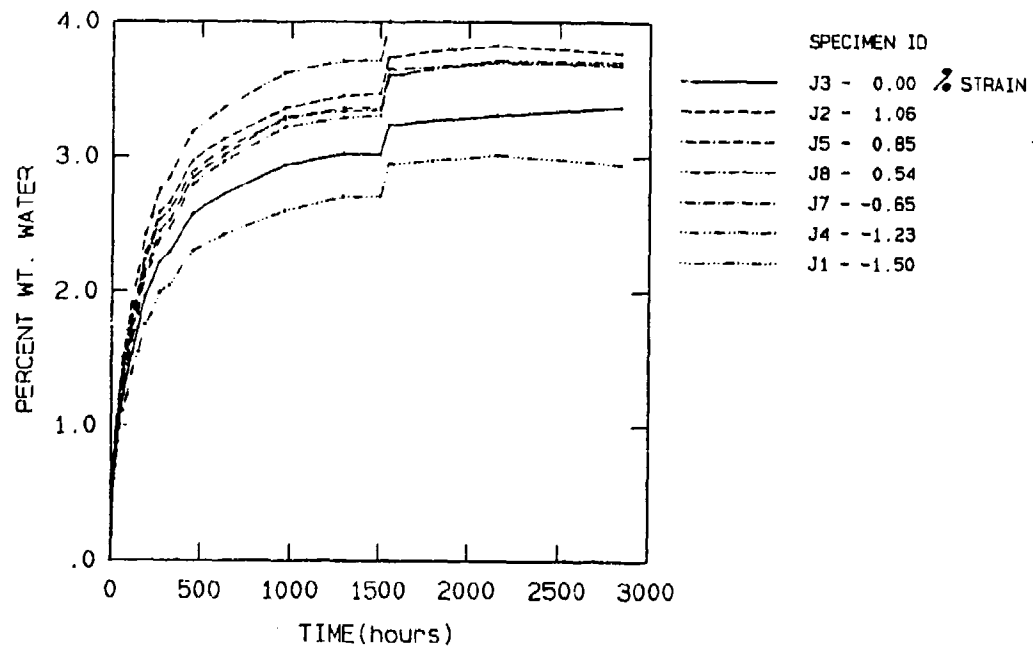
Figure 33: Desorption data for specimen group J plotted versus time. The sudden jump in weight loss near the 1500 hour mark is when the temperature was raised from 20 to 50°C.

I - DESORPTION DATA
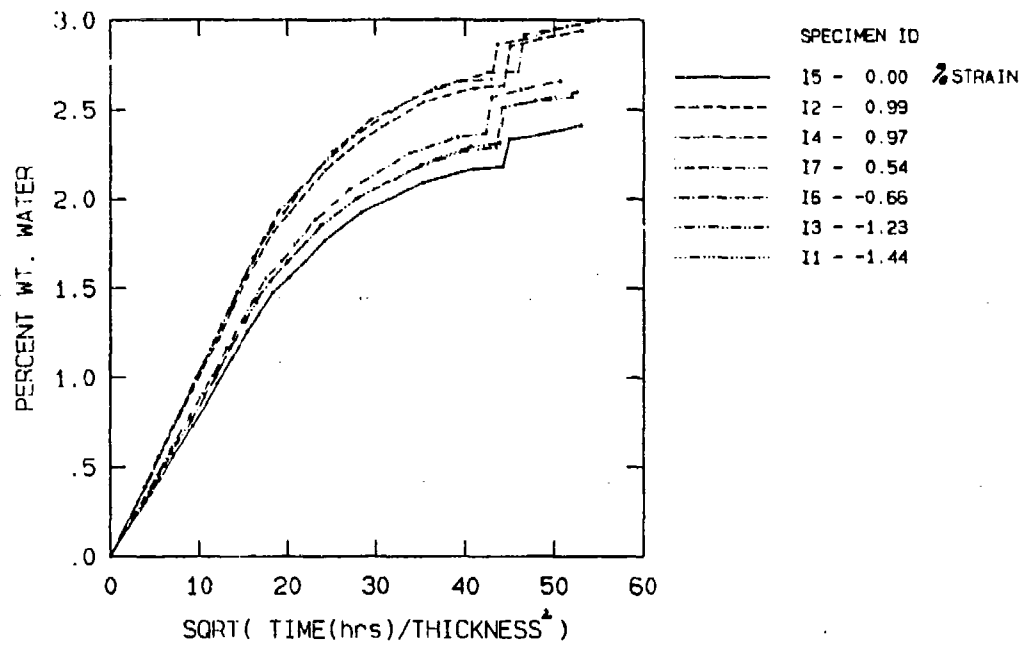
Figure 34: Desor tion data for specimen group I plotted versus the square root of time.

J - DESORPTION DATA
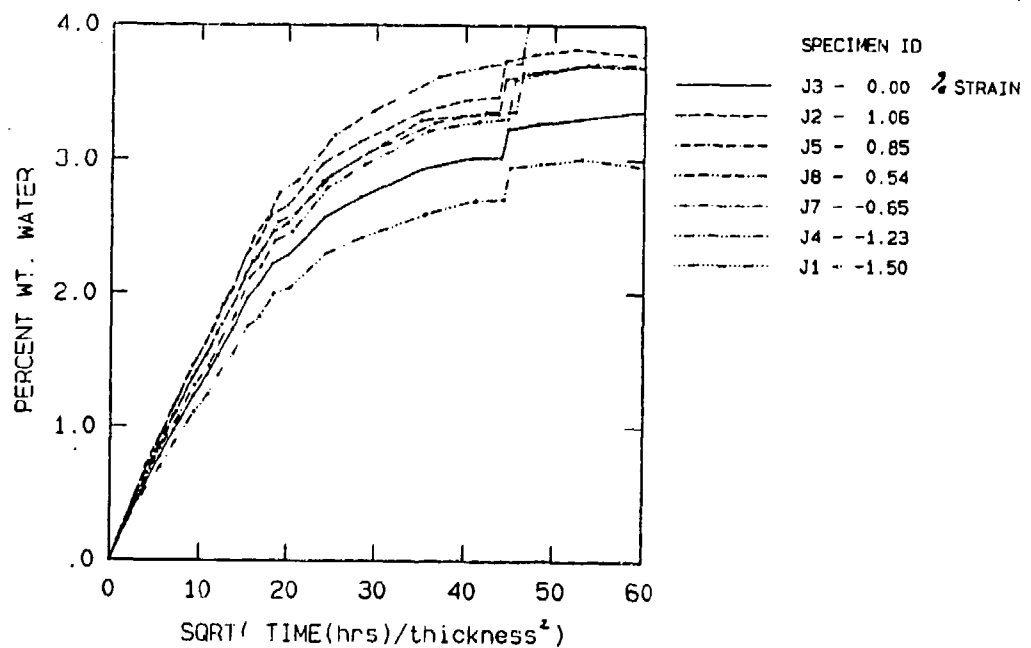
Figure 35: Desorption data for specimen group J plotted versus the square root of time.
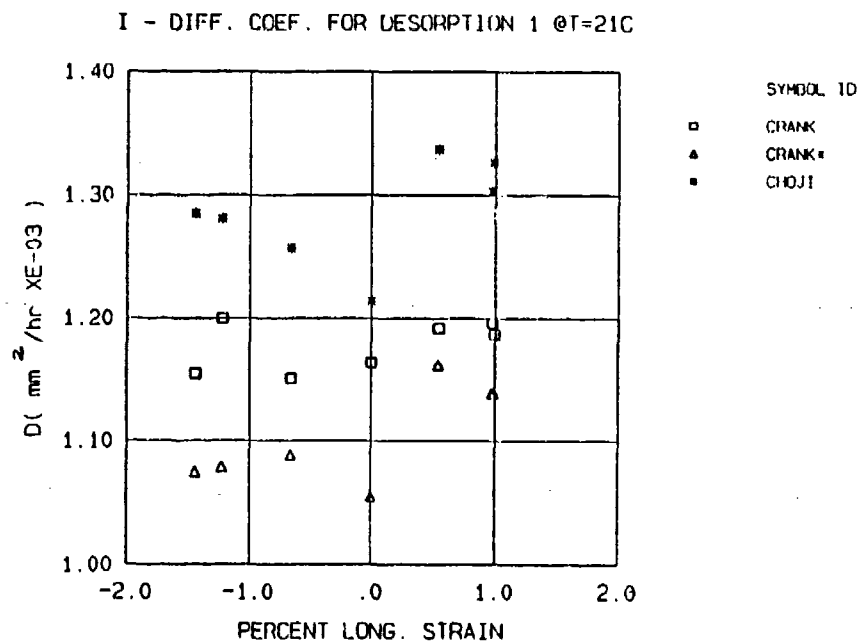
Figure 36: Average diffusion coefficient versus longitudinal strain for group I, Desorption 1.
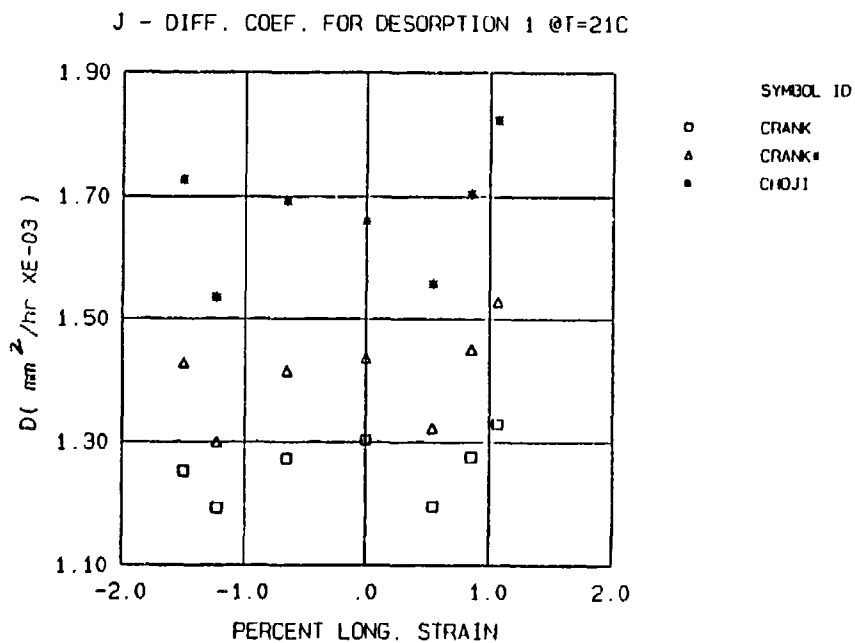
Figure 37: Average diffusion coefficient versus longitudinal strain for group J, Desorption 1.

I - DIFF. COEF. FOR DESORPTION 1 @T=21C
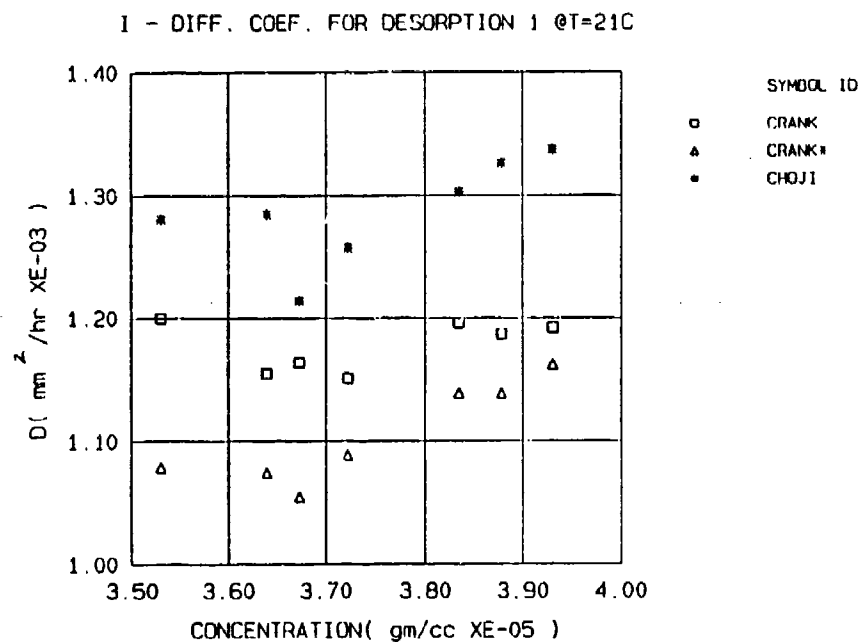
Figure 38: Average diffusion coefficient versus initial concentration for group I, Desorption 1.

J - DIFF. COEF. FOR DESORPTION 1 @T=21
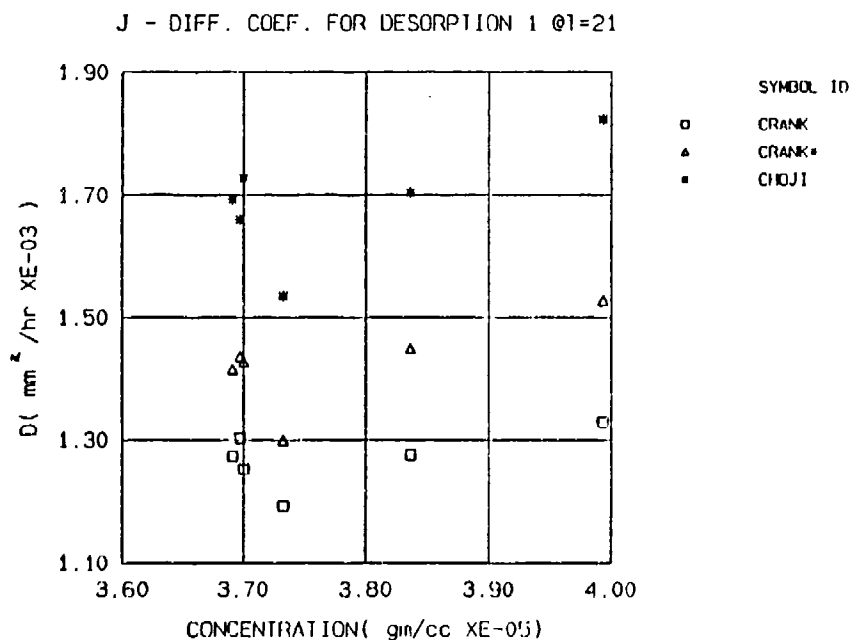
Figure 39: Average diffusion coefficient versus initial concentration for group J, Desorption 1.

I - MASS LOSS FOR DESORPTION 1
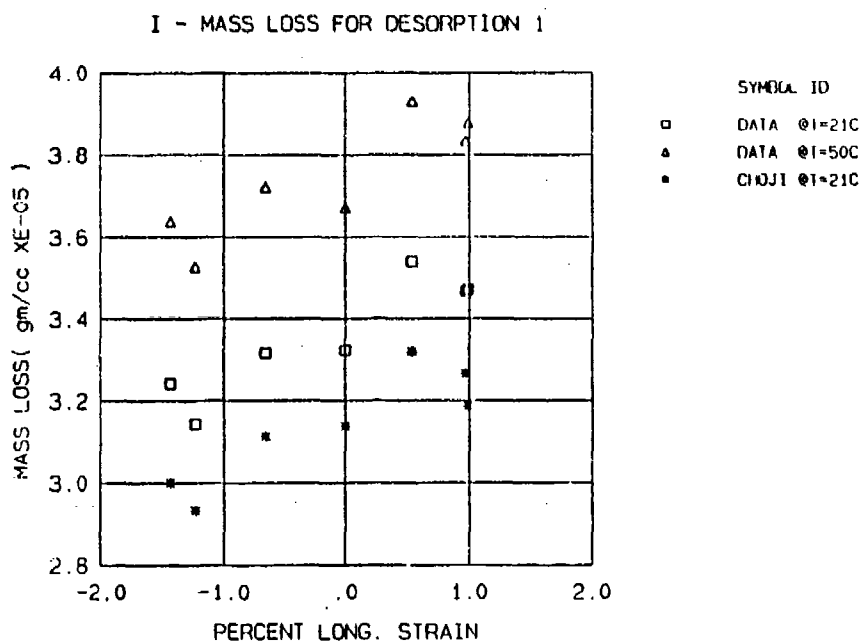
Figure 40: Final percent mass pick-up, mass(final) /polymer mass for group I, Desorption 1.

J - MASS LOSS FOR DESORPTION 1
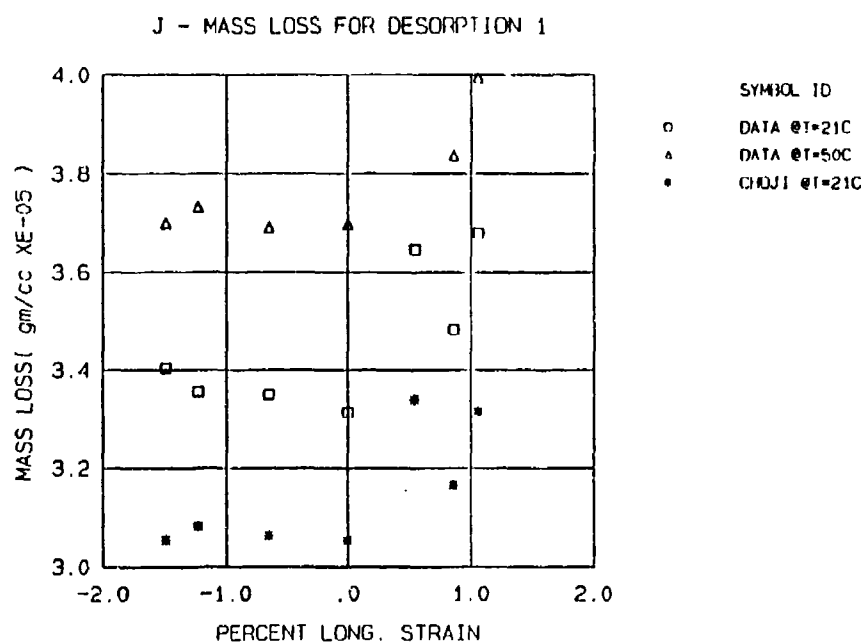
Figure 41: Final percent mass pick-up, mass(final) /polymer mass for group J, Desorption 1.

I5 - DESORPTION 1 COMPARISON

CURVE ID
—— I5 DATA
------ CRANK D = 1.16E-3
-·-·-·- CRANK D = 1.06E-3
············ CHOJI D = 1.21E-3
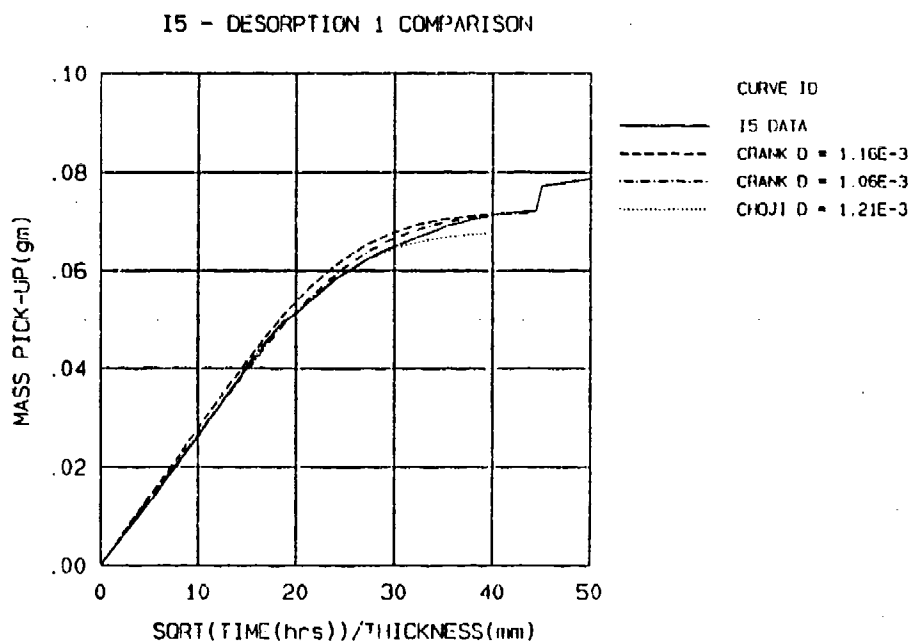
Figure 42: Comparison between desorption experimental data and numerical Fickian diffusion results for specimen I5.

J3 - DESORPTION 1 COMPARISON

CURVE ID
—— J3 DATA
------ CRANK D = 1.30E-3
-·-·-·- CRANK D = 1.44E-3
············ CHOJI D = 1.66E-3
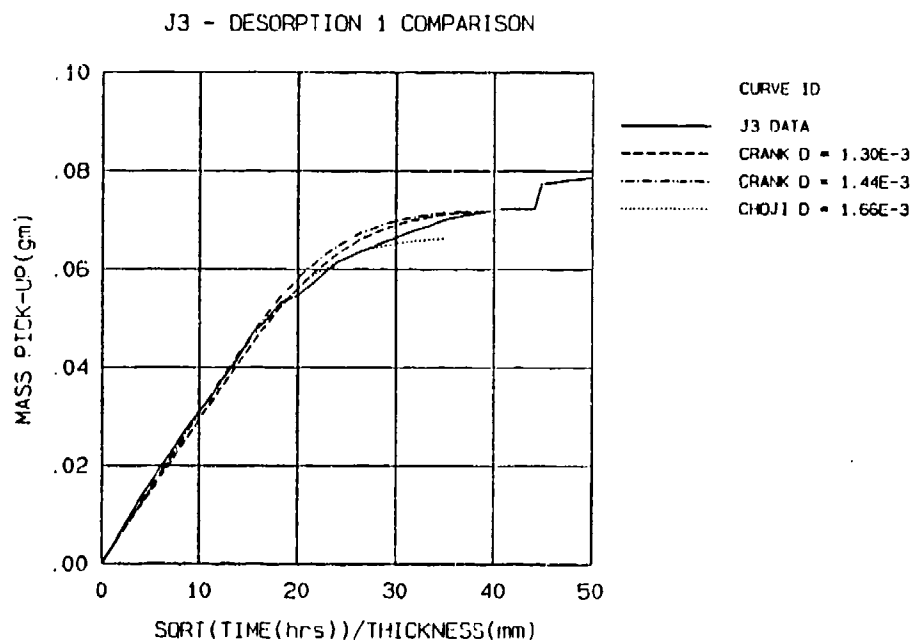
Figure 43: Comparison between desorption experimental data and numerical Fickian diffusion results for specimen J3.

5.5.3 Sorption 2, Group J

In figure 44, the resorption mass pick-up curves again looked initially Fickian and a similar data analysis was performed as that described in the desorption section. Time constraints forces us to include only the the Crank method results. The diffusion coefficient, and final mass pick-up curves are depicted in figures 45 and 46, respectively. There does not appear to be any correlation between the the strain and the diffusion coefficient, but the mass pick-up does appear to increase with increasing strain value.

Figure 47 shows a comparison between the numerically derived solution using the constant average diffusion coefficient and the resorption experimental results.

5.5.4 Desorption 2, Group J

As in the first cycle the initial linearity of the data when plotted versus the square root of time suggested that a Fickian process maybe able to describe the results.

From figures 48 there appears to be a slight correlation between the diffusion coefficient and mechanical strain levels. Unlike the first cycle the compression strain data tended to decrease with increasing compressional strain except at high strains. The tensile response was the same in both cases. It should be noted that the coefficient values here are about four times greater that the first cycle indicating a temperature dependence since the first cycle was at 20°C and the second at 50°C. We would be hard pressed to infer a concentration dependence on the diffusion coefficient from figure 49 but for the mid-concentration region there does appear the same dependence as shown before. Figures 40 and 41 shows that the final mass loss does appear to increase with increasing tensile strains but compressive strains have little effect.

Again by using the calculated diffusion coefficients and final mass pick-up values a numerical desorption curve can be generated. The results are similar to the first cycle and will not be repeated here
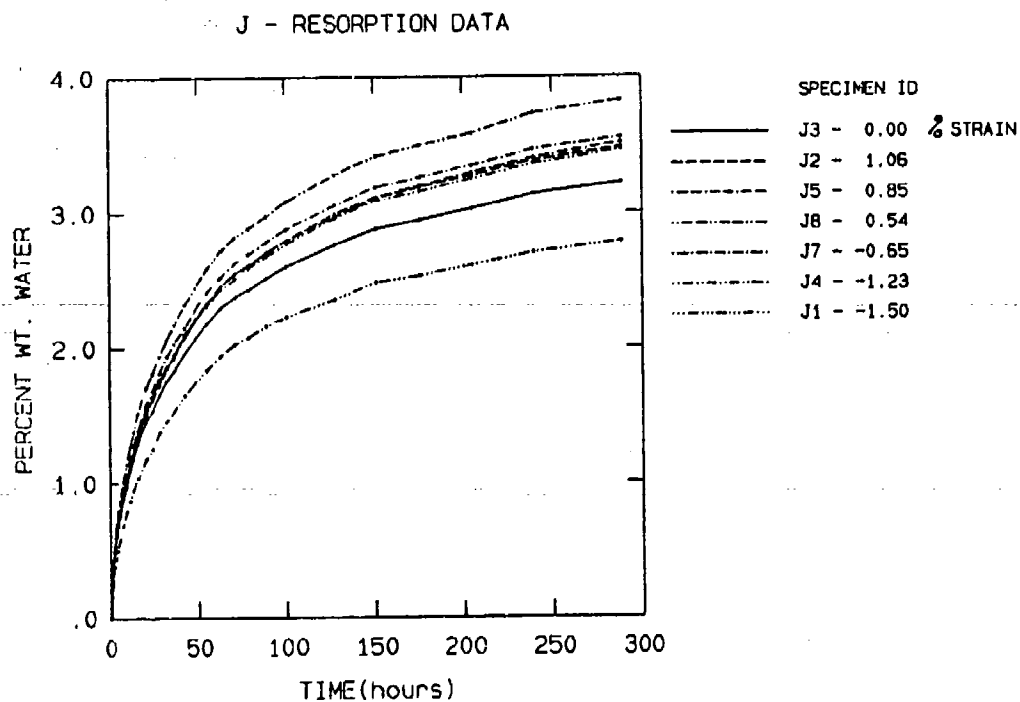
J - RESORPTION DATA

Figure 44: Resorption data for specimen group J plotted versus time.

AVG. DIFF. COEF. VS STRAIN - RESORP.
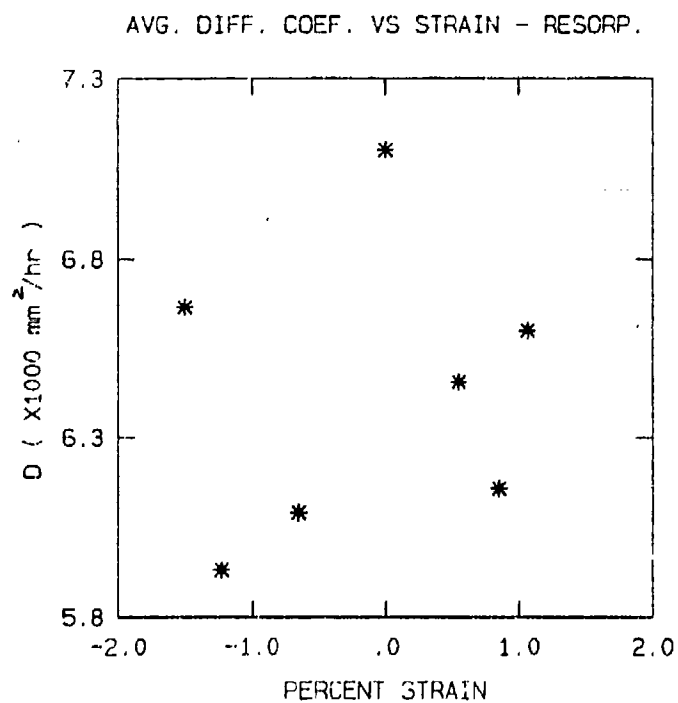
Figure 45: Resorption-average diffusion coefficient for group J at 50°C.

MASS PICK-UP VS STRAIN - RESORPTION
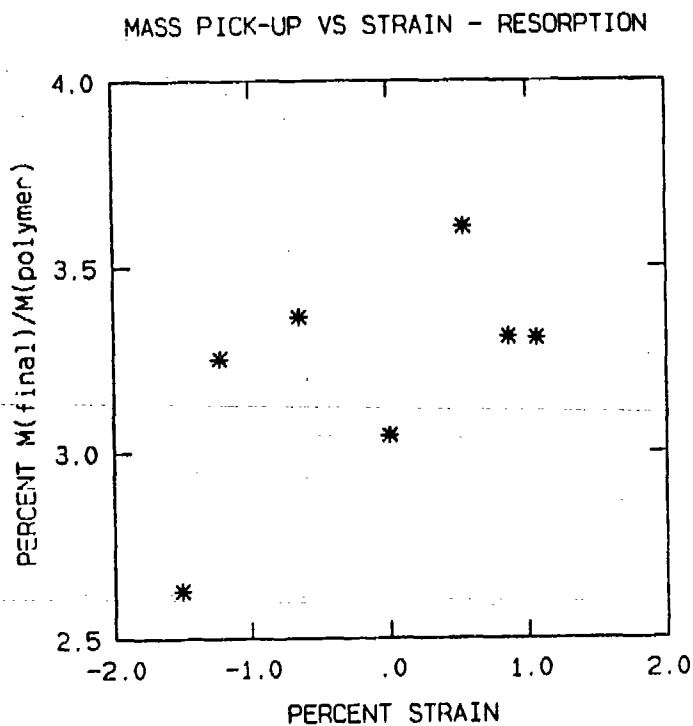
Figure 46: Resorption-final percent mass pick-up, mass(final)/polymer mass for group J.

COMPARISON BETWEEN NUMER./EXPER.
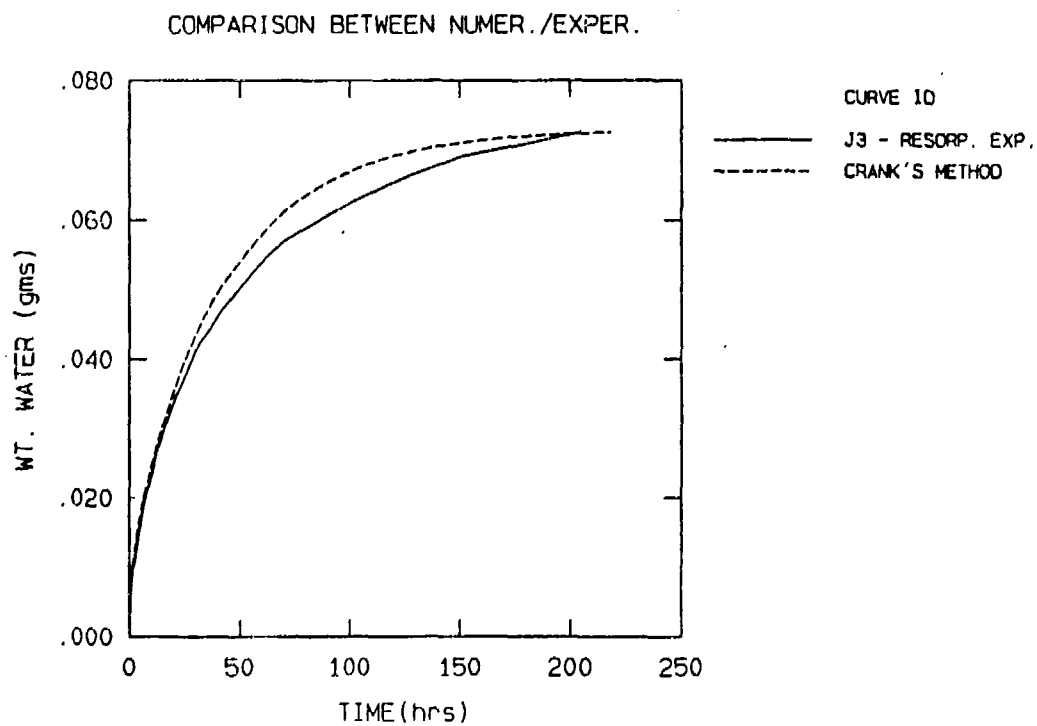
Figure 47: Comparison between resorption experimental data and numerical Fickian diffusion results for specimen J3.

J - DIFF. COEF. FOR DESORPTION 2 @T=50C
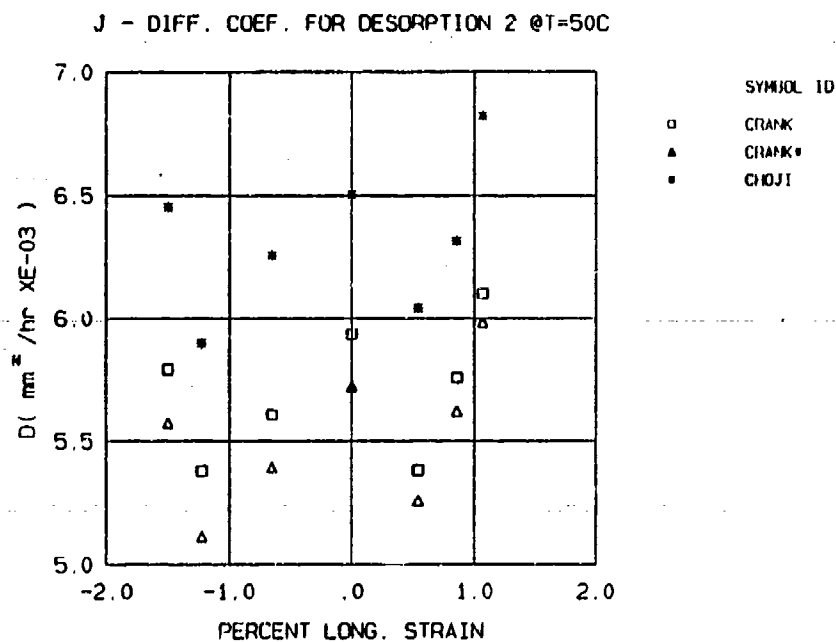
Figure 48: Average diffusion coefficient versus longitudinal strain for group J, Desorption 2.

J - DIFF. COEF. FOR DESORPTION 2 @T=50C
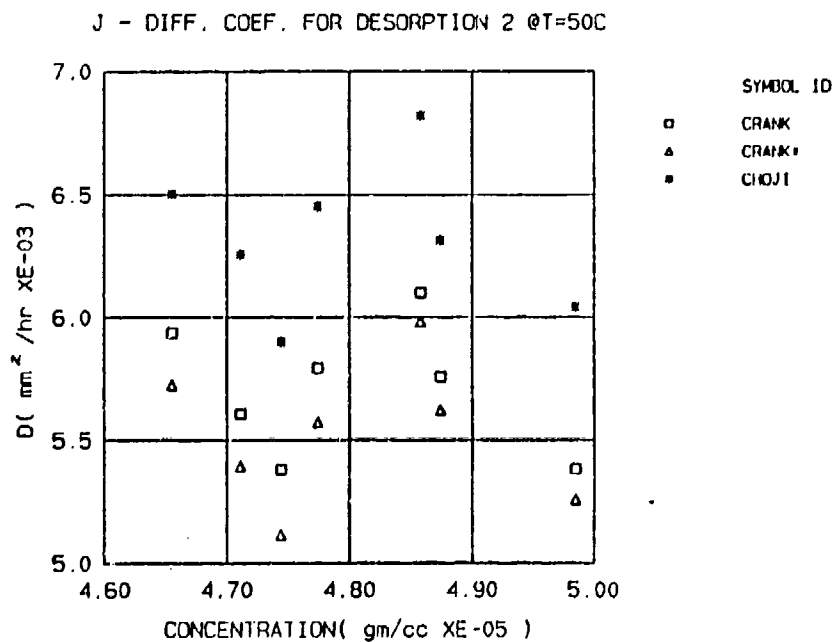
Figure 49: Average diffusion coefficient versus initial concentration for group J, Desorption 2.

J - MASS LOSS FOR DESORPTION 2
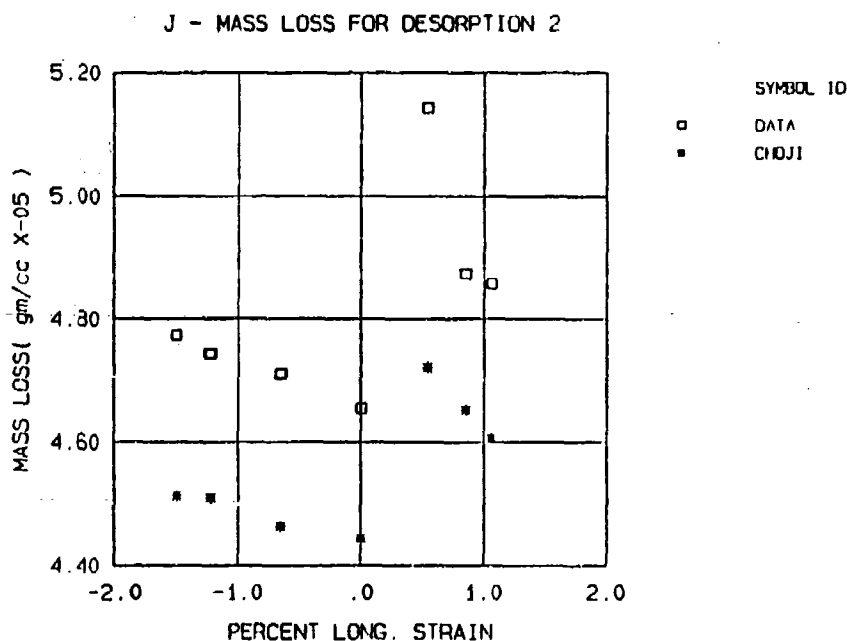
Figure 50: Final percent mass loss, mass(final) /polymer mass for group J, Desorption 2.

5.6   Attempts to Characterize Anomalies in the Data

5.6.1   Oxide Formation on Aluminum Substrate

Figure 51 shows the complete first cycle for specimen I. Note that the final weight never returns to the initial weight. To explain this phenomenon we included as a control, an aluminum bar included to test if the aluminum substrate's is contributing to the measured weight gain. The large weight gain exhibited by the plain aluminum bar seem to indicate that an oxide layer was forming on the bar's surface, see figure 52. This weight gain would obviously affect the data analysis and could elucidate the unusual results exhibited in the first sorption mass pick-up curve. As time progressed the oxide formation slowed explaining why the resorption curves tended to fit a Fickian behavior since the mass gain due to a surface oxide growth was small compared to the water gain of the polymer. The fact that a Fickian process represents the desorption curves also indicates that the anomalous weight gain during the sorption processes maybe due to an oxide formation, since the storage of the specimens in a vacuum

3-50

desiccator would inhibit the formation surface oxides.

5.6.2 Spalling of the Adhesive

After the second cycle the surface of the J specimens appeared lighter in color than the control specimens that have yet to be tested. Microscopic examination indicated that the surface of the test specimens have crazed appearance and that in some areas spalling of the adhesive took place.

Figure 53 is a picture of a virgin specimen magnified ~60 times. The rough surface is probably due to the cover plate that impressed its surface feature onto the adhesive during the curing process. Figure 54 is the surface of a tested specimen again magnified about 60 times. The initial roughness can still be seen but the dominate feature are the large light areas. These light areas are actually places where the adhesive has spalled off the surface or fracture patterns just below the surface.

This observation has two immediate drawbacks; we have now lost some adhesive and the comparison of data between cycles becomes more qualitative and may explain the different behavior between the diffusion coefficient between the two sorption-desorption cycles that group J encountered. The apparent lack of permanent weight gain between the start and finish of the second cycle, now maybe due to the weight gain due to oxide formation it offset by the weight loss of the bulk adhesive. The second is that the transport process of a solvent through a fractured surface is vastly different from the kinetic for normal Fickian diffusion and currently our model cannot handle this process.

On the otherhand it shows that moisture diffusion can contribute to that could lead to adhesive failure and this behavior should be looked at in more detail.
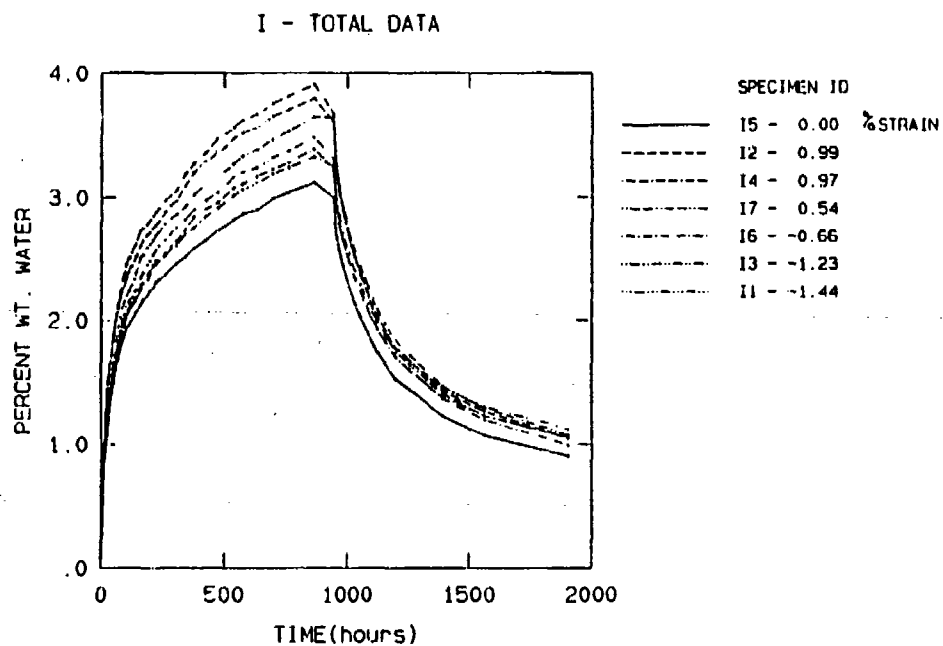
Figure 51: Sorption and desorption of specimen I
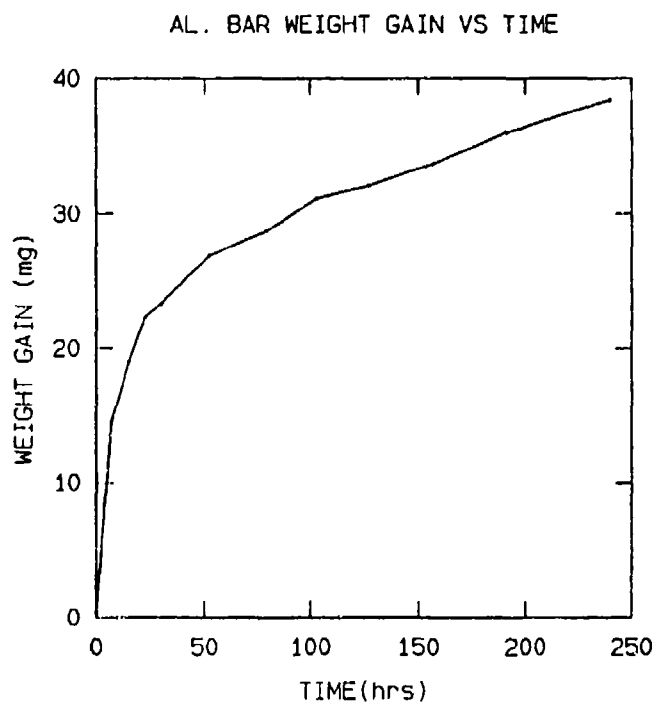
Figure 52: Mass gain of aluminum bar exposed to water bath at 49.7°C.

Figure 53: Surface of virgin specimen, magnified ~60X
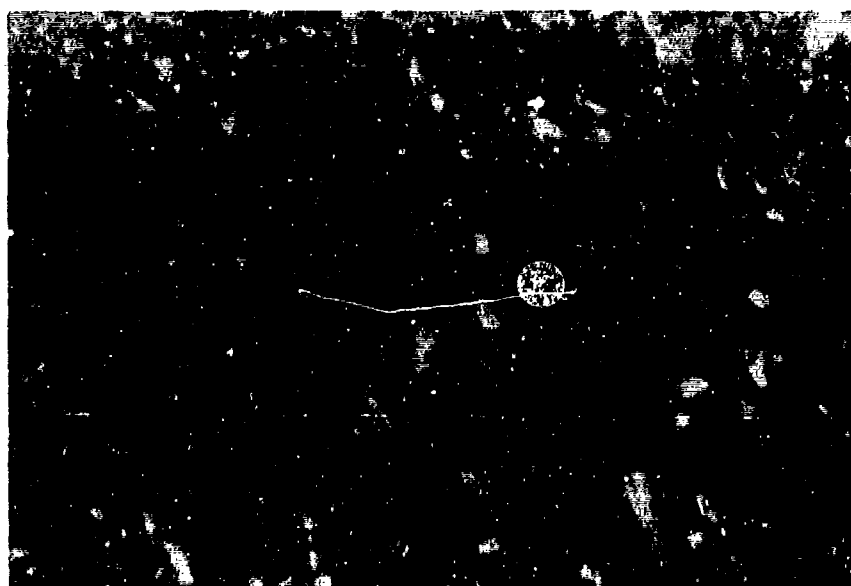
Figure 54: Surface of Tested specimen, J2, magnified ~60X

5.6.3 Reanalysis of Adhesive Strain Measurements

All the results shown above were compared to the longitudinal strain of the adhesive. Actually a better way to have presented the data is by the dilatational strain since this should be related to the free volume. The difference is due to, for the elastic region, Poisson's effect which has the transverse strains opposing the longitudinal strains resulting in a dilatational strain that is lower than the longitudinal strain. The problem is compounded by the fact that we are loading the beam into the plastic region and little is known about the the relationship between the transverse and longitudinal strain. Analytical solutions proved to be intractable, leaving either numerical or experimental results to provide such a relationship. We chose to pursue the latter.

Biaxial strain gages were mounted onto both the top and bottom of aluminum beams, see figures 55, 56, and the beams were then loaded in the same manner that the test specimens were.

The results are shown in figures 57, 58, 59 and 60.

From figure 60 the residual apparent Poisson's ratio are significantly different from the elastic value of 0.33. Compressional strains tend to reflect little change but tensile strain reduce the elastic value to about 0.20.

These results reduce the dilatational region that we can examine without damaging the adhesive since increasing longitudinal strains does not proportionally increase the dilatation strains by the same amount.

5.7 Other Adhesive Systems

Two other adhesives were looked at as possible substitutes for the AF-163-2U. They were Shell's EPON 815 cured with methane diamine and a two part epoxy developed by the NADC. An initial test of the EPON 815 system showed that it was easy to use.
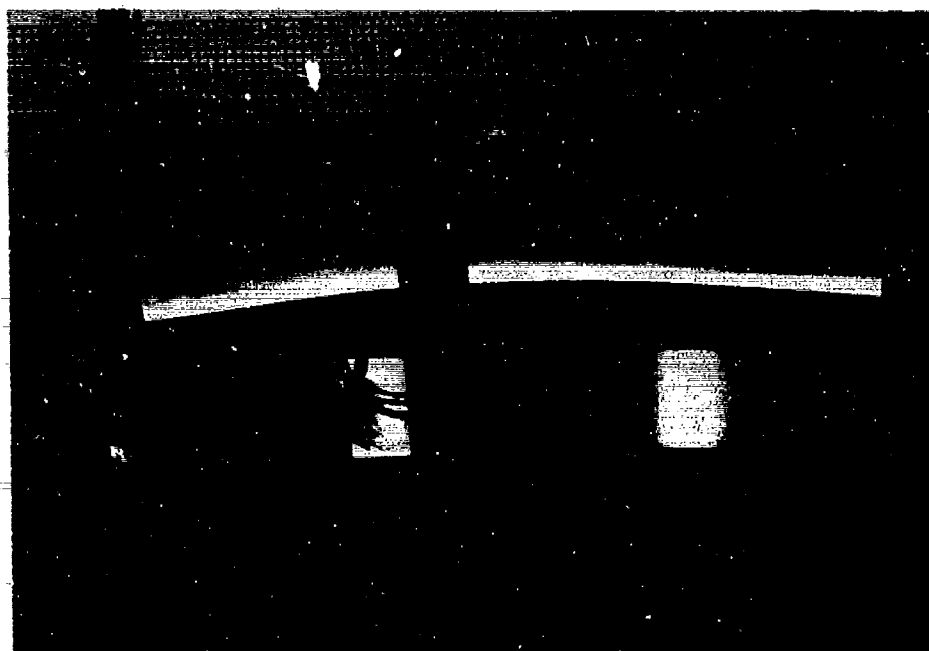
Figure 55: Bent aluminum beams with strain gages mounted
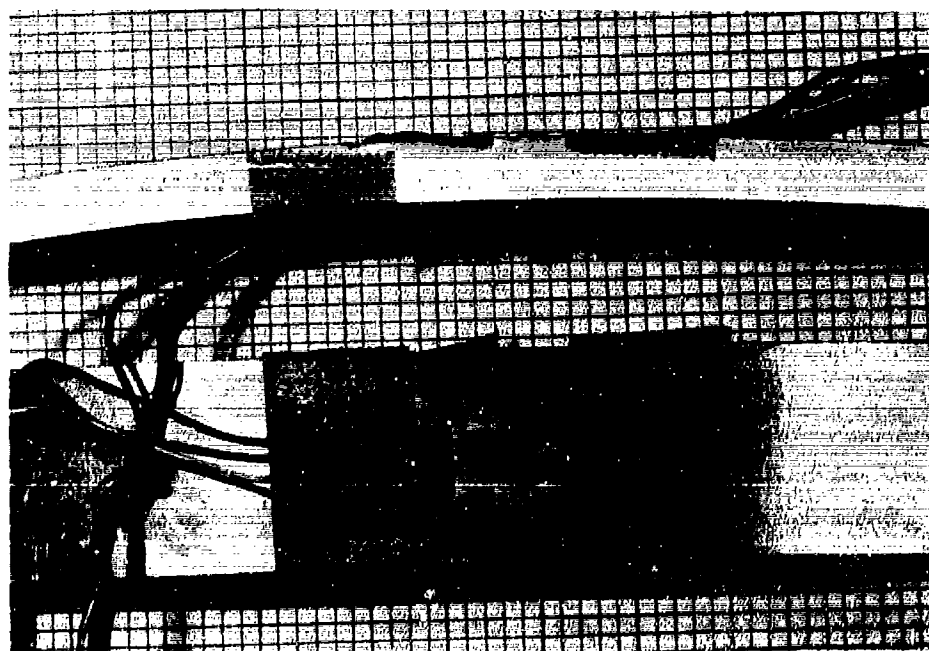
Figure 56: Close-up of biaxial strain gage used.

B1 - LOAD VS LONG. STRAIN
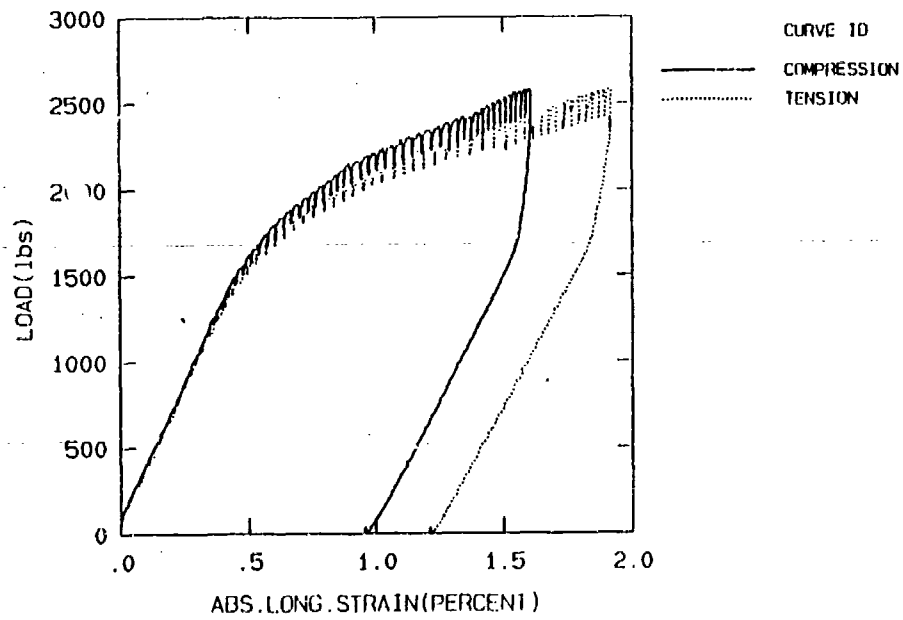
Figure 57: Load versus longitudinal strain

B1 - TRANS. VS LONG. STRAIN
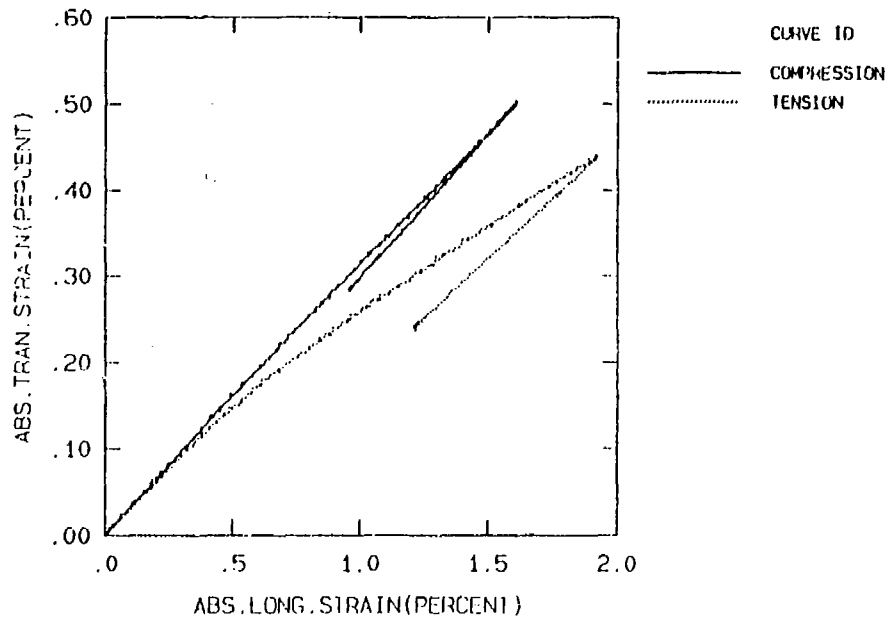
Figure 58: Transverse strain versus longitudinal strain

B1 - POISSON'S RATIO VS LONG.STRAIN
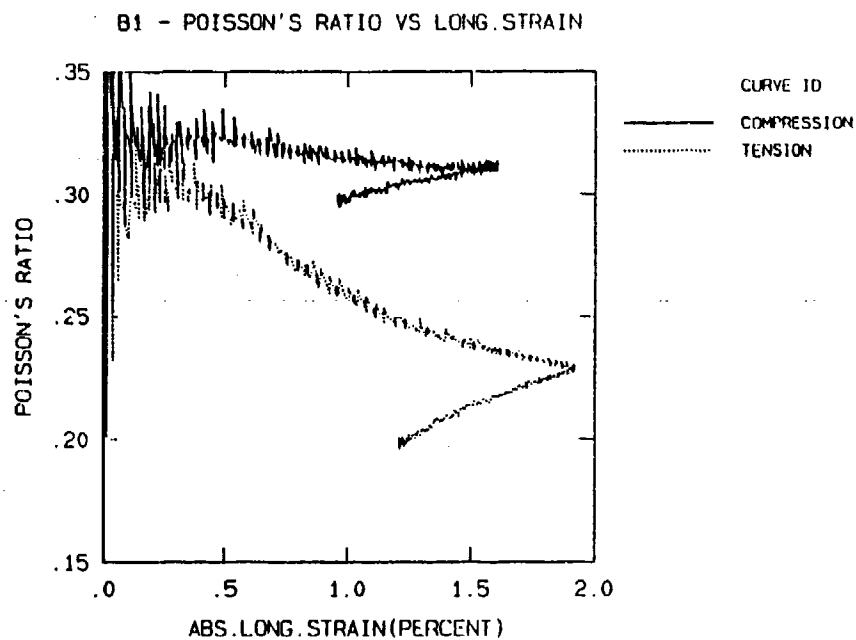
Figure 59: Apparent Poisson's ratio versus longitudinal strain

POISSON'S RATIO VS RESIDUAL STRAIN
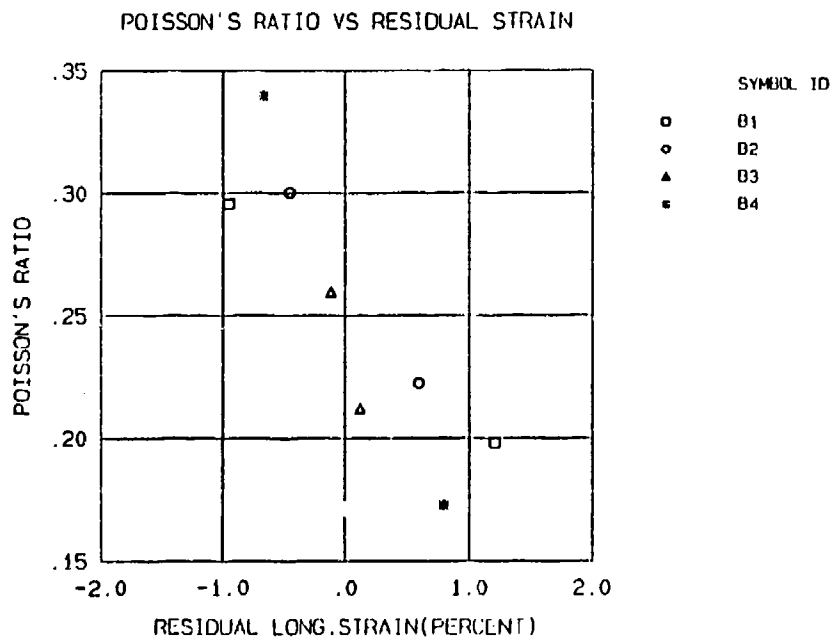
Figure 60: Residual Poisson's ratio versus residual longitudinal strain

The relatively low viscosity made it easy to mix, pour, and by applying a vacuum any trapped air bubbles effervesce easily. The cured adhesive was brittle and did not appear to adhere to the aluminum substrate. It was suggested that various flexiblizers and a different surface preparation may help to solve these problems but they have not yet been tried.

The literature from the NADC describes the adhesive as "a bisphenol A epoxy resin (Shell Epon 828) modified by prereaction with a carboxy terminated butadiene rubber (B.F. Goodrich CTBN 1300X8). Amine curing agents were used."[21] The problem with this system was the high viscosity of the two parts. Mixing introduced trapped air bubbles but unlike the EPON 815 a vacuum could not draw the bubbles out. The people at the NADC suggested numerous ways to minimize the problem but the bubbles still remained. Another method, not yet tried, is to use a centrifuge to force the bubble out of the adhesive.

5.8 Other Techniques

We explored the idea of using the change in the index of refraction to determine the shape of the concentration curve though the polymer. Work done by Robinson[24] showed that a method based on this physical phenomena could work. Instead of following the method of Robinson we tried to measure the change in refraction angle as the laser passed through the polymer sample. An initial test of PMMA-Cyclohexane,2-methyl pentane showed that the change in the angle of refraction was to small to be measured. The crude test set-up may have also contributed to this fact. If a change could be detected subsequent analysis would have yielded information that was also an average of the solvent concentration throughout the polymer and thus yield no new information to what could be inferred by the mass pick-up method. The use of optical techniques would have required us to measure very accurately the relation between the solvent concentration and the index of refraction.

Even in the method used by Robinson this was a very serious limitation. Another limitation would be that optical techniques require transparent adhesives.

References

[1] "High Temperature Adhesive Systems", Quarterly Management Report,
Number 1, for the period ,October-December, 1985;
Contract No. N00014-85-C-0881 for ONR and DARPA

[2] "High Temperature Adhesive Systems", Quarterly Management Report,
Number 2, for the period January-March, 1986;
Contract No. N00014-85-C-0881 for ONR and DARPA

[3] "High Temperature Adhesive Systems", Quarterly Management Report,
Number 3, for the period April-June, 1986;
Contract No. N00014-85-C-0881 for ONR and DARPA

[4] "High Temperature Adhesive Systems", Quarterly Management Report,
Number 4, for the period July-September,1986;
Contract No. N00014-85-C-0881 for ONR and DARPA

[5] "High Temperature Adhesive Systems", Quarterly Management Report,
Number 5, for the period October-December, 1986;
Contract No. N00014-85-C-0881 for ONR and DARPA

[6] "High Temperature Adhesive Systems", Quarterly Management Report,
Number 1, for the period January-March, 1987;
Contract No. N00014-85-C-0881 for ONR and DARPA

[7] "High Temperature Adhesive Systems", Quarterly Management Report,
Number 7, for the period April-June, 1987;
Contract No. N00014-85-C-0881 for ONR and DARPA

[8] "High Temperature Adhesive Systems", Quarterly Management Report,
Number 8, for the period July-September,1987;
Contract No. N00014-85-C-0881 for ONR and DARPA

[9] "High Temperature Adhesive Systems", Quarterly Management Report,
Number 9, for the period January-March,1988;
Contract No. N00014-85-C-0881 for ONR and DARPA

[10] "High Temperature Adhesive Systems", Quarterly Management Report,
Number 10, for the period April-June,1988;
Contract No. N00014-85-C-0881 for ONR and DARPA

[11] "High Temperature Adhesive Systems", Intrim Report,
for the period September,1985-January,1988;
Contract No. N00014-85-C-0881 for ONR and DARPA

[12] Choji, N., and Karasawa, M.
"Diffusion Coefficients From Initial Sorption Data"
J. Poly. Sci., Vol.15, (1977) pp.1309-1313

[13] Crank, J.
Mathematics of Diffusion
Oxford University Press, London 1956

[14] Fujita, H.
"Diffusion in Polymer-Diluent Systems"
Fortschr. Hochpolym.-Forch., Bd.3, (1961) S.1-47

[15] Gillat, O. and Broutman, L.J.,
"Effect of an External Stress on Moisture Diffusion and Degradation in a
Graphite-Reinforced Epoxy Laminate"
ASTM STP 658, (1978) pp.61-83

[16] Hinton, E. and Campbell, J.S.
"Local and Global Smoothing of Discontinuous Finite Element Functions
Using a Least-Squares Method" Int. J. Numer. Meth. in Eng., Vol.8, (1974)
pp.461-480

[17] Lefebvre, D.R., Dillard, D.A., Ward, T.C.

"A Model for the Diffusion of Moisture in Adhesive Joint; Part I: Governing Equations" Paper submitted to the J. Adhesion Sci.

[18] Long, F.A. and Richman, D.

"Concentration Gradients for Diffusion of Vapors in Glassy Polymers and Their Relation to Time Dependent Diffusion Phenomena"

J. Am. Chem. Soc., Vol.82, No.3, (1960) pp.513-519

[19] Neumann, S. and Marom, G.

"Prediction of Moisture Diffusion Parameters in Composite Materials Under Stress"

J. Comp. Mat., Vol.21, (1987) pp.68-80

[20] Mills, P.J., Palmstrom, C.J., and Kramer, E.J.

"Concentration Profiles of Non-Fickian Diffusants in Glassy Polymers by Rutherford Backscattering Spectrometry"

J. Mat. Sci., Vol.21, (1986) pp.1479-1486

[21] Crabtree, D.J.

"Adhesives for Field Repair of Graphite/Epoxy Composite Structures."

Report No. NADC-79286-60, NOV. 1981

[22] Neumann, S. and Marom, G.

"Free-volume Dependent Moisture Diffusion Under Stress in Composite Materials"

J. Mat. Sci., Vol. 21, (1986) pp.26-30

[23] Prigogine, I.

Thermodynamics of Irreversible Processes, 3rd Edition

Interscience

[24] Robinson, C.

"Interferometric Studies in Diffusion I. Determination of Concentration Distributions"

Proc. Roy. Soc. A, Vol.204, pp.339-359

[25] Thomas, N.L., and Windle, A.H.

"A Theory of Case II Diffusion"

Polymer, Vol. 23, (1982) pp.529-542

[26] Vrentas, J.S., and Duda, J.L.

"Molecular Diffusion in Polymer Solutions"

AIChE J., Vol. 25, No. 1 (1979) pp.1-24

[27] Wietsman, Y.

"Stress Assisted Diffusion in Elastic and Viscoelastic Materials"

A Finite Element Formulation for the Non-Fickian Diffusion Model

A.1 Element formulation

The general diffusion equation we chose to numerically solve, ignoring temperature and chemical effects, is given below:

$$\frac{\partial C}{\partial t} - \nabla \cdot (D\nabla C + CK\nabla P) = 0 \tag{17}$$

where D and K are material property tensors that may depend on the concentration C.

Applying the method of weighted residuals, we first multiply equation 17 by a weighting function W and integrate over the domain, V. This gives:

$$\int_V W\frac{\partial C}{\partial t}dV - \int_V W\nabla \cdot (D\nabla C + CK\nabla P)dV = 0 \tag{18}$$

Using Green's theorem on the second term of transforms equation 18 to the following weak form:

$$\frac{\partial}{\partial t}\int_V WCdV + \int_V \nabla W \cdot D\nabla CdV + \int_V \nabla W \cdot CK\nabla PdV - $$
$$\int_B W(D\nabla C + CK\nabla P) \cdot ndB = 0 \tag{19}$$

where B is the boundary of the domain and n the unit outward normal vector to the boundary.

Assuming that equation 18 holds over each individual element we divide up the domain V into elements and approximate the concentration value within the element e, C^e, by:

$$C^e = \langle N^e \rangle \{C\}^e \tag{20}$$

where $\langle N^e \rangle$ is the vector of shape functions relating the nodal concentration vector $\{C\}^e$ to C^e. Following Galerkin's method the weighting functions W are chosen to be the same as the shape functions.

Assembling the appropriate terms we obtain the element matrices and vectors:

$$[C]^e = \int_{V^e} \{N^e\} \langle N^e \rangle dV^e \tag{21}$$

$$[K]^e = \int_{V^e} [B^e]^T [D][B^e] dV^e \tag{22}$$

$$[G]^e = \int_{V^e} [B^e]^T [K][B^e]\{P\}^e \langle N^e \rangle dV^e \tag{23}$$

$$\{f_q\}^e = \int_{B_q^e} q_n \{N^e\} dB_q^e \tag{24}$$

$$\{f_c\}^e = [K]^e \{\text{vector of 0 and specified } C \text{ values}\} \tag{25}$$

where $[B^e]$ contains the derivatives of the shape functions, and q_n the normal solvent flux across the boundary B_q^e.

The integration can be numerically performed, we used the Gauss quadrature method on a parent element which is then mapped onto the desired domain.

The element matrices are then assembled to form a global matrix equation which can be represented as:

$$[C]\{\dot{C}\} + [K+G]\{C\} = -\{f_q\} - \{f_c\} = \{f\} \tag{26}$$

A.2 Material Nonlinearity

In general, the matrices $[K]$ and $[G]$ are dependent on the concentration value C and an iteration scheme must be used to converge to a particular solution. A common method used is the Newton-Raphson technique which can be illustrated by considering the steady-state form of equation 26:

$$[K(C) + G(C)]\{C\} = -\{f\} \tag{27}$$

Applying Newton-Raphson we get for the kth iteration:

$$[K_T(C^k) + G_T(C^k)]\{\Delta C^k\} = \{f\} - [K(C^k) + G(C^k)]\{C^k\} \tag{28}$$

3-65

where the individual element matrices are given by (in 2-D):

$$[K_T]_{ij}^e = [K]_{ij}^e + \int_{V^e} [\frac{\partial N_i^e}{\partial x} \frac{\partial D_{11}}{\partial C^e} \frac{\partial N_n^e}{\partial x} C_n^e N_j +$$
$$\frac{\partial N_i^e}{\partial y} \frac{\partial D_{22}}{\partial C^e} \frac{\partial N_n^e}{\partial y} C_n^e N_j] dV^e \qquad (29)$$

$$[G_T]_{ij}^e = [G]_{ij}^e + \int_{V^e} [\frac{\partial N_i^e}{\partial x} \frac{\partial F_{11}}{\partial C^e} \frac{\partial N_n^e}{\partial x} P_n^e N_j N_m^e C_m^e N_j^e +$$
$$\frac{\partial N_i^e}{\partial y} \frac{\partial F_{22}}{\partial C^e} \frac{\partial N_n^e}{\partial y} P_n^e N_j N_m^e C_m^e N_j^e] dV^e \qquad (30)$$

$$\{C^{k+1}\} = \{C^k\} + \{\Delta C\} \qquad (31)$$

it has been assumed for simplicity that D and K can be represented as diagonal matrices.

A.3 Time integration scheme

If the matrix $[C]$ is assumed to be independent of concentration then the time integration scheme shown below can be used to solve equation 26. The updating procedure is as follows:

$$\{C(t + \Delta t)\} = \{C(t)\} + [(1 - \gamma)\{\dot{C}(t)\} + \gamma\{\dot{C}(t + \Delta t)\}]\Delta t \qquad (32)$$
$$\{C^{k+1}(t + \Delta t)\} = \{C^k(t + \Delta t)\} + \{\Delta C^k\} \qquad (33)$$

The programmed equation can be represented as:

$$[C/\Delta t + \gamma[K_T(C^k(t + \Delta t)) + G_T(C^k(t + \Delta t))]]\{\Delta C^k\} =$$
$$\gamma\{f(t + \Delta t)\} + (1 - \gamma)\{f(t)\} + [C/\Delta t - (1 - \gamma)[K(C(t)) + G(C(t))]\{C(t)\} -$$
$$[C/\Delta t + (1 - \gamma)[K(C^k(t + \Delta t)) + G(C^k(t + \Delta t))]\{C^k(t + \Delta t)\} \qquad (34)$$

where $[K_T]$ and $[G_T]$ are as previously defined.

APPENDIX B

G. Angsten

Hughes Aircraft Company

ADHESIVE SURFACE ANALYSIS

B.1 Procedure

The following samples were received for study:

A. AF-163-2U epoxy adhesive from 3M,

A sheet of Airtech Wrightlon 4600 release film (used to produce this sample),

B. The same 3M adhesive using Wrightlon 4500 as the release film,

A sheet of Wrightlon 4500,

C. The same adhesive using Tedlar as the release film,

A sample of American Cyanamid FM 73U modified epoxy using Tedlar as the release film,

A sample of Tedlar provided by Hughes.

A variety of means were used to determine if any residual release agent remained on the surface of the cured adhesive. The first attempts used the Attenuated Total Reflectance (ATR) technique to examine the surface layer of the epoxy. Although spectra were obtained of the films without a problem, the hard, uneven surface of the epoxies did not provide enough surface contact to produce spectra.

Attempts were then made to examine the surface of the resins by light sanding with very fine silicon carbide paper. The powder removed was scanned by diffuse reflectance and compared to material removed from deeper within the sample.

Solvent washes using carbon tetrachloride and hexane were made from controlled areas of samples A and B. The non-volatile residues were then examined for the presence of the appropriate release film. Blank runs were made to determine the contribution to the residues from the solvents and glassware.

Since the films were only partially soluble, another approach was used to remove the material from the surface. Powdered KCl was rubbed over the surface with a spatula and then examined by diffuse reflectance and transmittance.

B.2 Results

A number of the more useful spectra obtained are attached.

B.3 Sample A

The Wrightlon 4600 release film was found to be a type of polypropylene. Since the only peaks in this spectrum (Fig. 1) are the C-H bending and stretching modes, it is more difficult to identify this material in the epoxy background than it is for the other three samples. The spectrum obtained from the subtraction of the base epoxy background (Fig. 2) from the surface powder did not show a detectable level of hydrocarbon residue (Fig. 3).

A hexane wash of the surface was evaporated and the residue examined. The spectrum (Fig. 4) obtained is attached and is of a crosslinked methyl silicone. Since no silicone was found in the release film, it is presumably due to a contaminant picked up in either the original process or in subsequent processing of the sample. A blank run was made on the glassware and solvent used. Its spectrum (Fig. 5) is attached and clearly shows hydrocarbon and possibly a small amount of a silicone. The blank shows no resemblance to that obtained from the sample however, which appears to be from a silicone rubber or adhesive.

B.4 Sample B

Spectra were obtained from sanded (Fig. 6), washed (Fig. 7) and KCl rubbed sections of the adhesive. None showed a significant residue. A slight amount of hydrocarbon found in the wash is attributable to the blank. The release film was found to be a polyvinyl fluoride (Fig. 8), essentially the same as the Tedlar used in sample C.

3-68

B.5 Sample C

At this point, the KCl rub method was felt to be the most effective and was the only sampling technique used on the two adhesives.

The spectrum obtained from the FM 73U (brown) is attached (Fig. 9) and indicates the presence of what is probably silicone. Although there are similarities to the C-F peaks in the 1100 and 1040 cm region, the shape matches better to that of a silicone. Reproducing the baseline in the background and reference is a problem in reflectance, but the major peaks around 1100 and 1040 cm are clear, and a shoulder is seen at 1260 cm, also indicating silicone.

No contaminants could be detected on the 3M (purple) sample.

B.6 Conclusion

Residues from the release film are not detectable by FTIR. If any residues are present, they are probably less than a few hundred Angstroms thick. ESCA or Auger would be able to determine if any of the fluorocarbon films are present at this level.

There appeared to be some silicone contamination of the adhesives, at least in the A and probably also in the C samples. Although silicone was the likely identity of the residue found on the FM 73, there was some possibility that it was actually the polyvinyl fluoride.
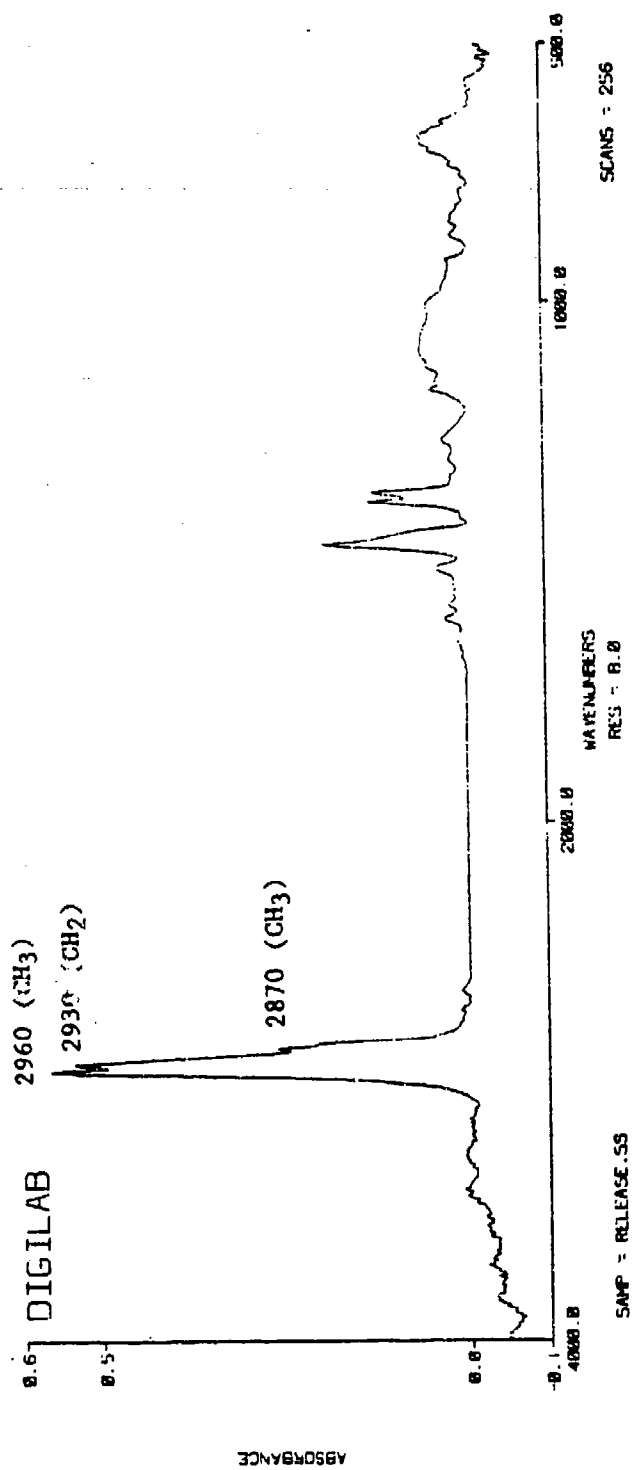
Figure 1. Release Film For Sample A
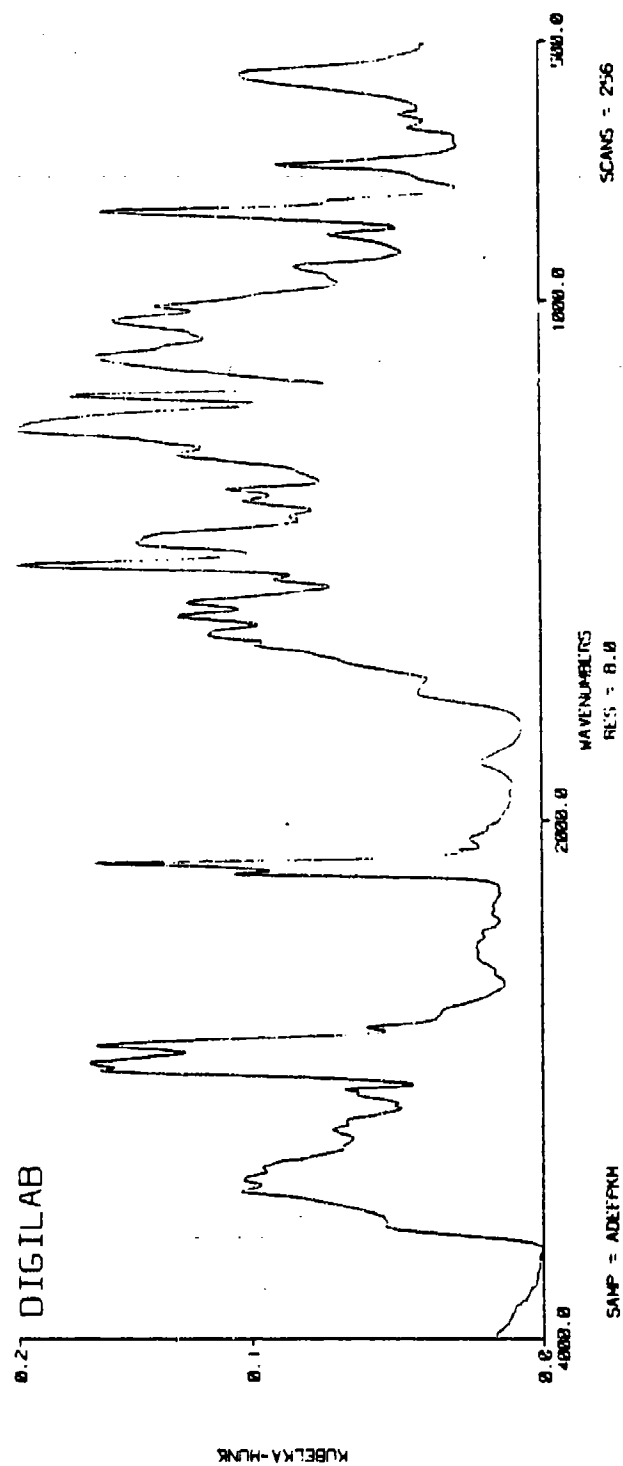
Figure 2. Adhesive A By Diffuse Reflectance
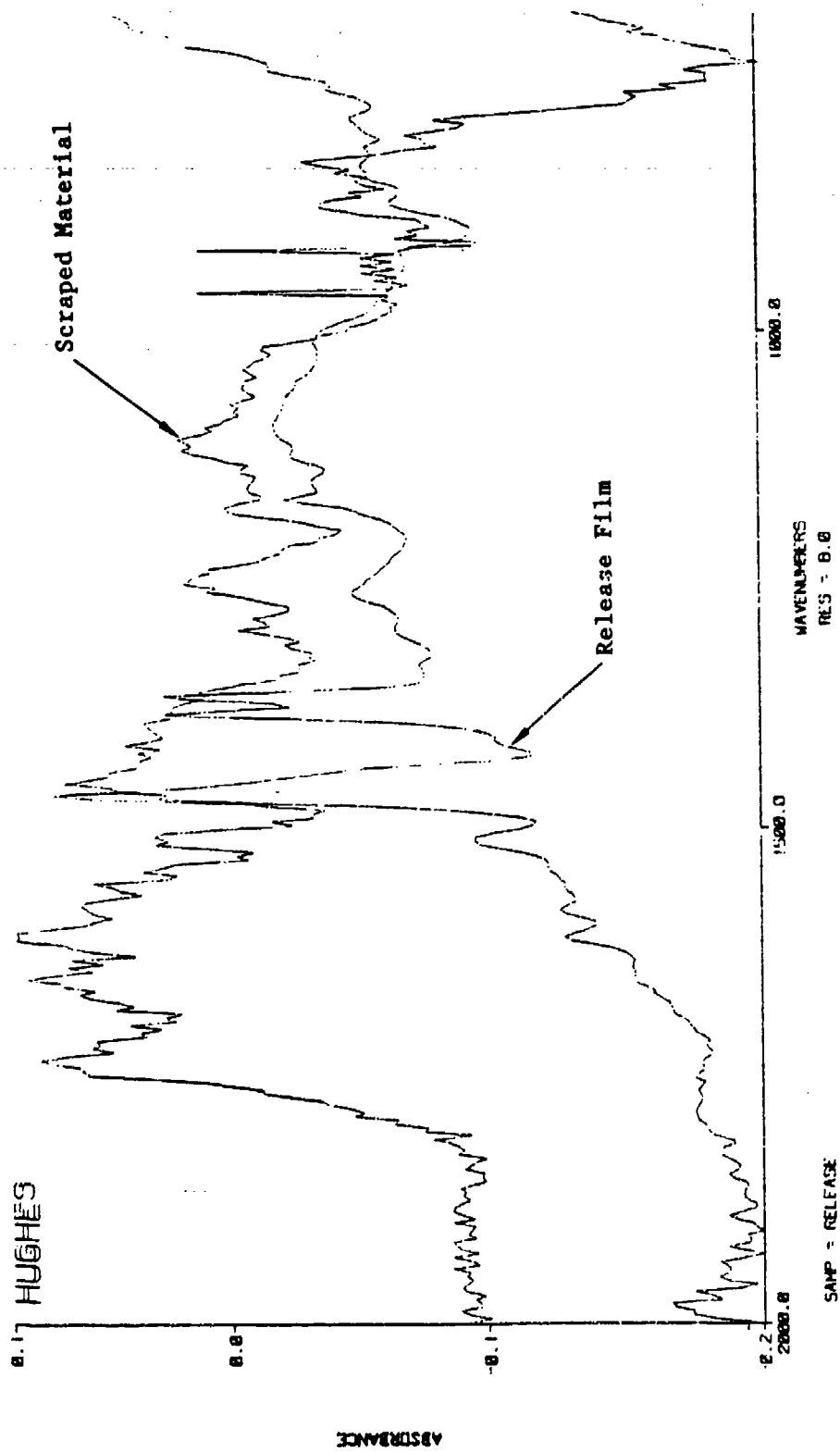
Figure 3. Scraping of Adhesive A
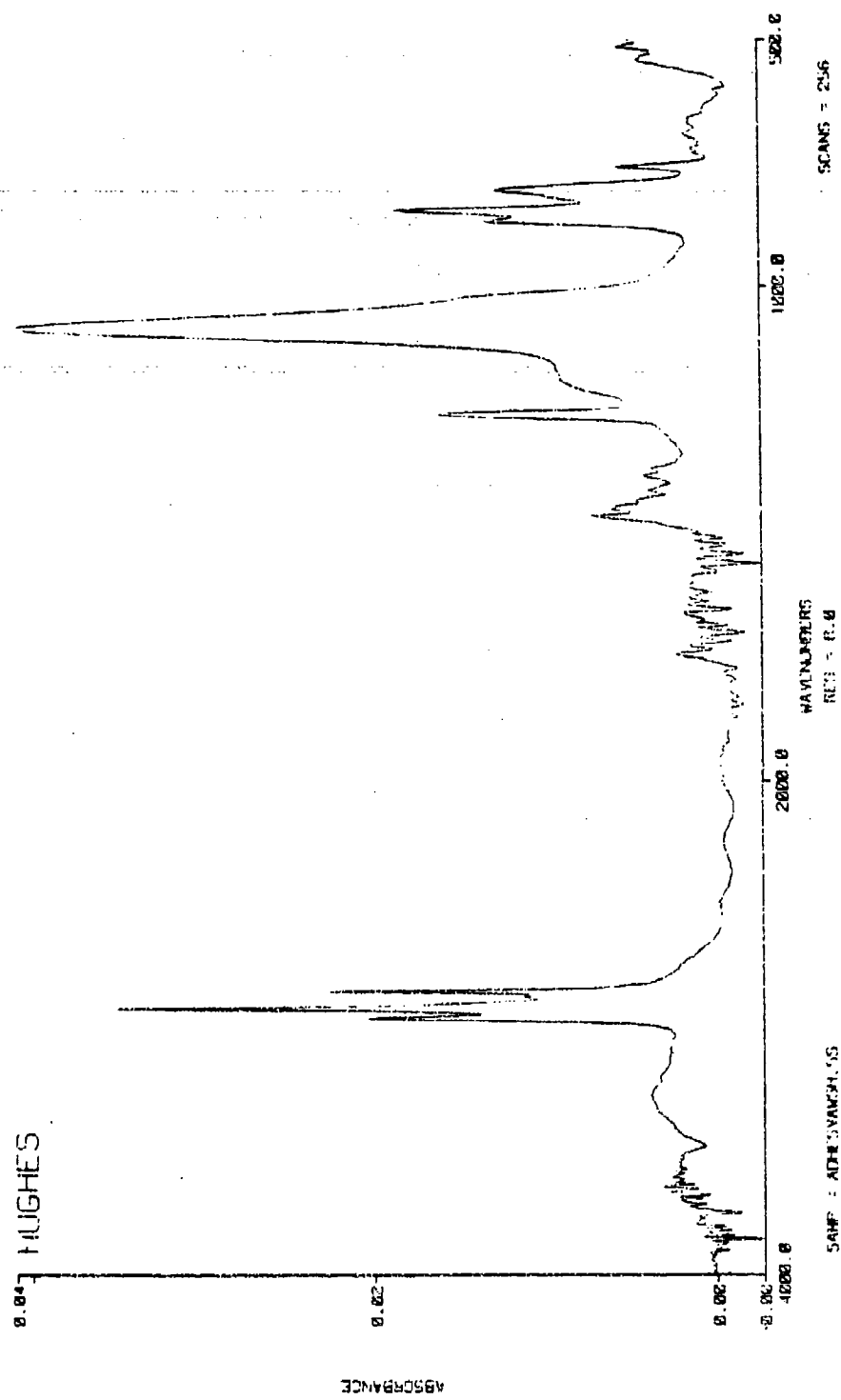
Figure 4. Hexane Wash of Adhesive A

Large Block
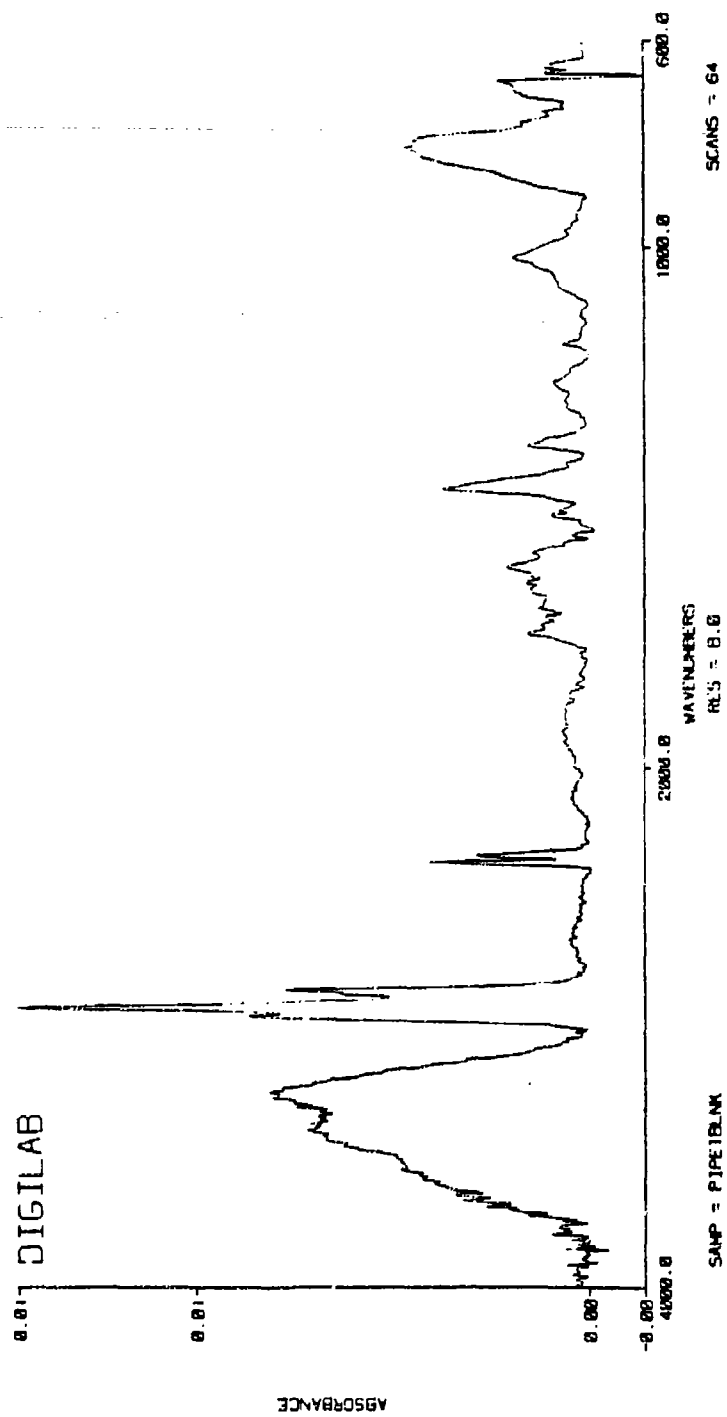
Figure 5. Blank Produced Using Hexane, Pipette, Beaker
and Capillary
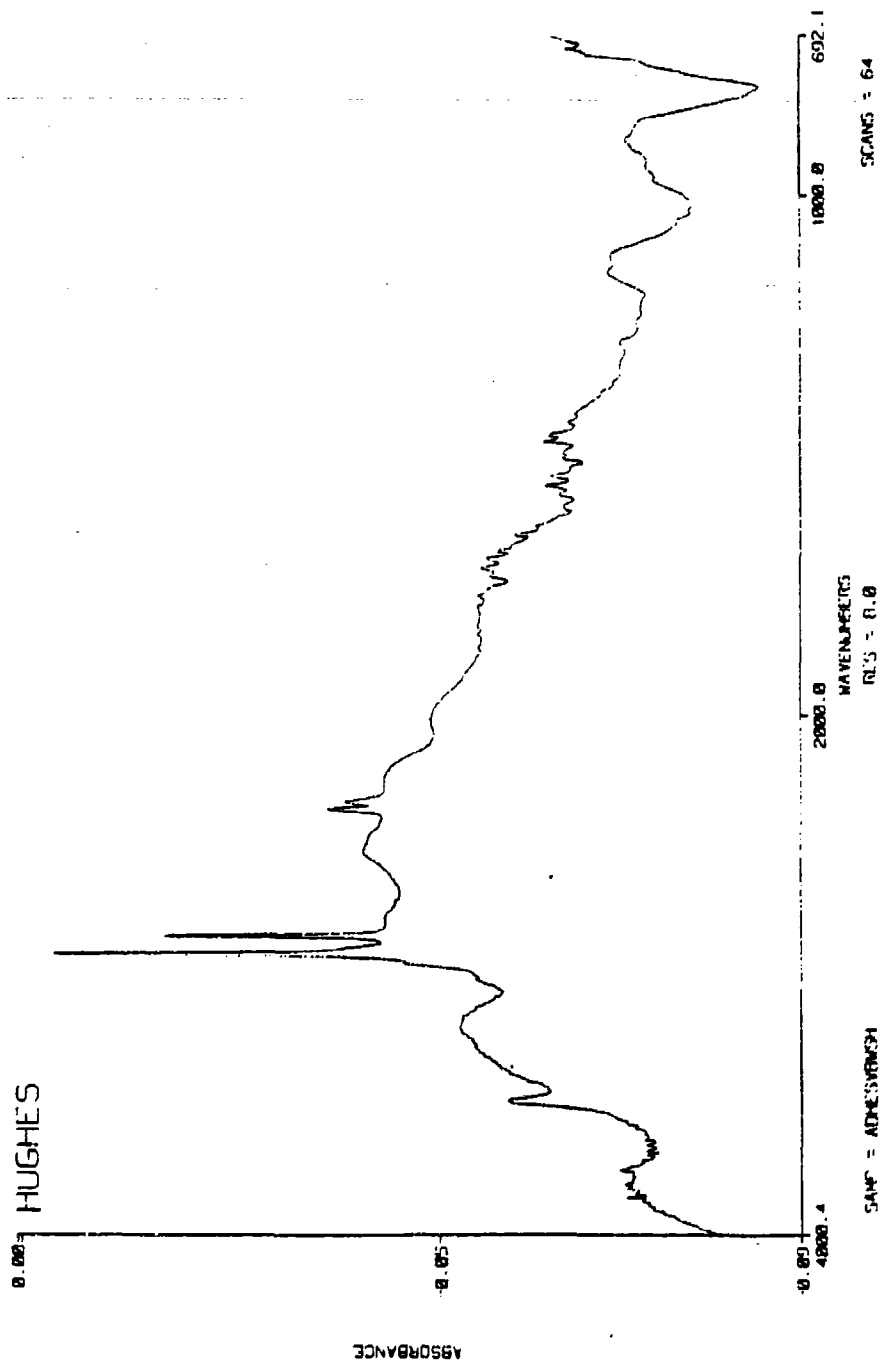
Figure 6. Wash of Adhesive B
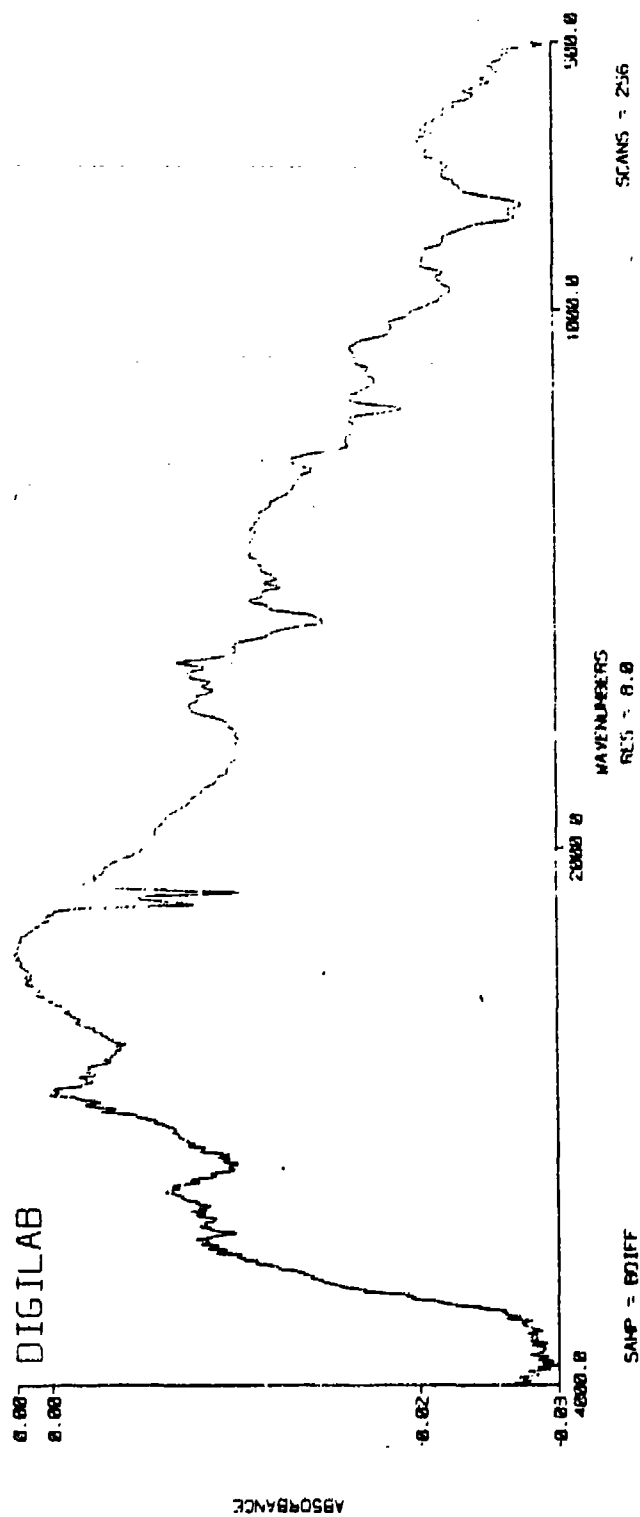
Figure 7. Subtraction of Base Material From
Surface of Adhesive 3
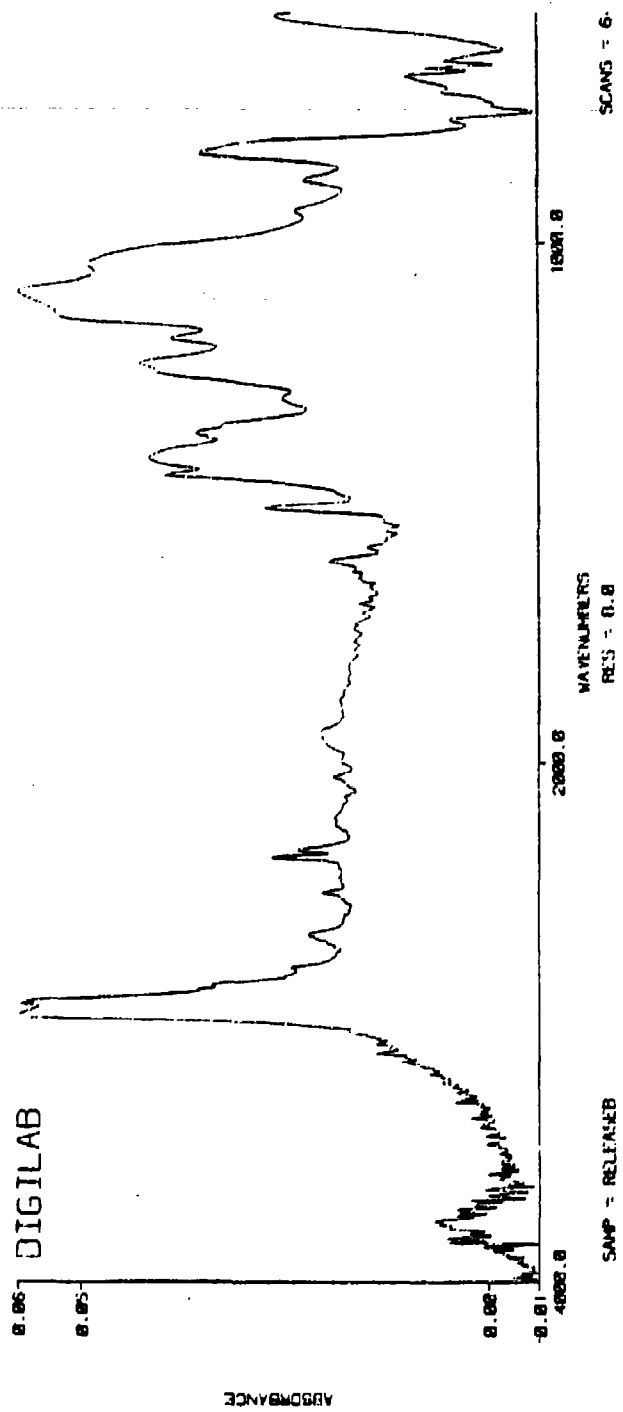
Figure 8. Release Material B By ATR
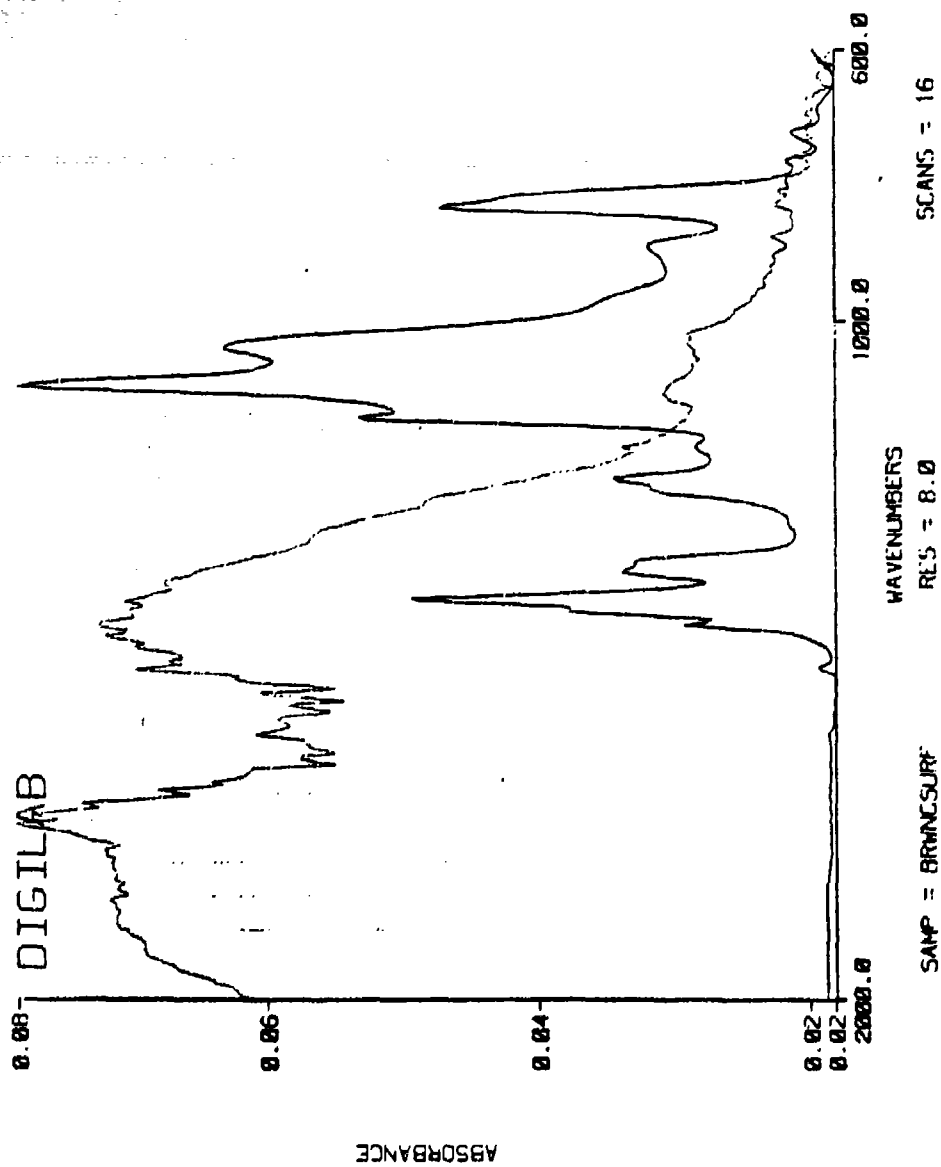
Figure 9. KCl Rub of FM 73U Surface

Fracture Analysis of High Temperature Adhesives

Final Report
by
K. M. Liechti

Engineering Mechanics Research Laboratory Report

EMRL 89/1

Submitted to:
Hughes Aircraft Company
El Segundo, CA 90245

The Department of Aerospace Engineering and Engineering Mechanics
The University of Texas at Austin
Austin, TX 78712

January 1989

1. Introduction

Structural adhesives are being used more and more for joining primary structure. It is therefore important to be able to design such structures in a rational way. This requires that the constitutive and fracture properties be derived from meaningful tests in which the stress states and failure mechanisms are well understood. The purpose of this ongoing study is to develop simple tests that can be used to determine the stiffness, strength and fracture properties of structural adhesives. The tests will be used in a quantitative manner to compare adhesive formulations and surface preparations. The work has developed along two fronts: tests to determine stress-strain behavior and tests to determine mixed-mode fracture behavior. Progress in each area is now described separately in Sections 2 and 3.

2. Constitutive Behavior

The main strength of adhesives is their ability to transmit shear and so many tests for determining the constitutive behavior are oriented towards shear properties such as stiffness, strength and relaxation modulus or creep compliance. The most commonly used specimen for adhesive shear strength has been the simple lap shear joint. However, the stress state in the adhesive is complex and nonuniform and so the meaning of the strength values obtained in this way may be questioned. In order to obtain a more pure and uniform shear stress state Frazier [1] proposed that adherends be thickened so that peel stresses be reduced. Guess et al. [2] compared the stress distributions in the standard and thick adherend lap joints and confirmed the reduction in peel stresses. More recently, Arcan [3] has considered the stiff adherend specimen, an adaptation of a specimen [4] previously proposed for the pure shear testing of homogeneous specimens. A finite element analysis revealed a further reduction in stress concentration over the thick adherend lap shear specimen. However, unless special modifications are made, stress concentrations will always exist at the sharp bond terminations in tensional shear specimens and torsional shear specimens such as the napkin ring [5] and cone and plate geometries [6] have been more promising.

In the present study, the adhesives under investigation will have to be cured at 700°F and residual stresses will be important. The most desirable geometry will be the one that produces the most uniform residual stress state. Since stress concentrations will usually exist at sharp bimaterial corner, the main focus of the work will be to consider how adherend edges can be modified in order to reduce such concentrations. A second consideration in developing the specimens has been the characterization of adhesives under more general stress states

so that multiaxial yield criteria can be examined. Since such stress states will be generated in part by bond normal loads, the geometry of the adherend edges will again be important. On a more practical note, the thin adhesive bondlines require that specimen alignment in testing is crucial. For example, a 0.001 inch bond normal displacement due to misalignment would produce 10% normal strains across a 0.010 inch bondline. Again, such strains are likely to be magnified at the adherend edges unless special precautions are taken. If they are taken, scatter in strength data under shear loadings is likely to be reduced.

With these objectives in mind, stress analyses of napkin ring, cone and plate and stiff adherend specimens have been conducted under shear, bond normal and thermal loadings. Various modifications to adherend edges have been considered through refined finite element analyses of local regions. The most promising geometry was fabricated and tested to yield values of shear stiffness and strength of a structural adhesive.

2.1 Stress Analysis

The stress analysis was conducted using the finite element codes VISTA and TEXPAC-NL (for torsional loading). The aluminum adherends and FM-300 adhesive were considered to be elastic ($E = 68.95$ and 2.32 GPa, respectively; $\nu = 0.33$ and 0.4, $\alpha = 54$ and $167 \mu m/m/°C$, respectively). Each joint and its modifications are now considered separately.

Napkin Ring Specimen

The stress state in the adhesive layer of a napkin ring specimen (Fig. 1) under torsional loading is one of pure shear which increases linearly with radial distance from the center of the ring. However, because the radial thickness of the adhesive layer is small, the shear stress can be considered to be constant, making the specimen attractive for the determination of shear properties. It should be noted that some structural adhesives can withstand 80-100% shear strain. Under such conditions normal stresses are likely to be introduced and the uniformity and purity of the stress state can no longer be taken for granted. When bond-normal loading of the napkin ring specimen was considered, large stress concentrations were found (Fig. 2) due to the sharp, 90°bimaterial corners formed by the adhesive and adherends at the free surfaces of the specimen. In some early work Williams [7] showed that plates having angular corners with one edge free and the other clamped exhibited no stress concentration for angles less than approximately 60°. If the adherends are considered rigid with respect to the adhesive, then these results suggest that some modifications could

Flat Adherends

Upper Adherend

Adhesive

$2t$

Z

r

Lower Adherend

$R_i = 23.8$ mm
(0.9375 in.)
$R_o = 25.4$ mm
(1.000 in.)
$2t = 0.127$ mm
(0.010 in.)

R_o

R_i

Upper Adherend

Adhesive

t

r

Rounded Adherends

Z,w

R

r,u

$2t$

R_i

R_o
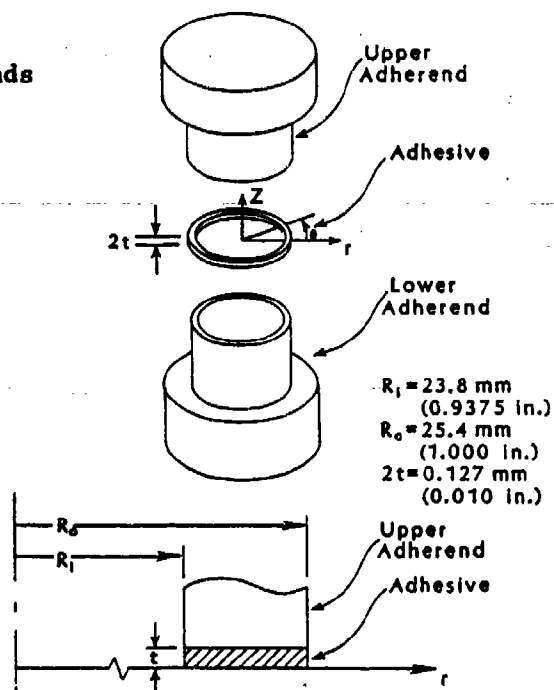
FIG. 1   Napkin Ring Specimen
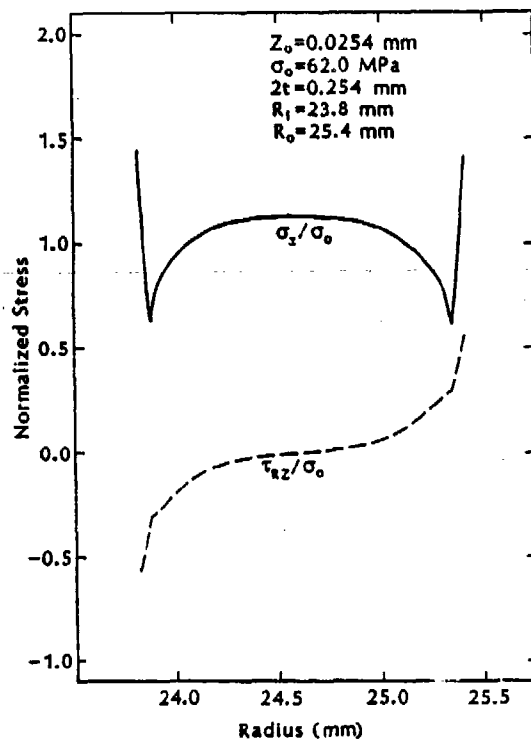
FIG. 2   Napkin Ring Specimen Under Bond-Normal Loading
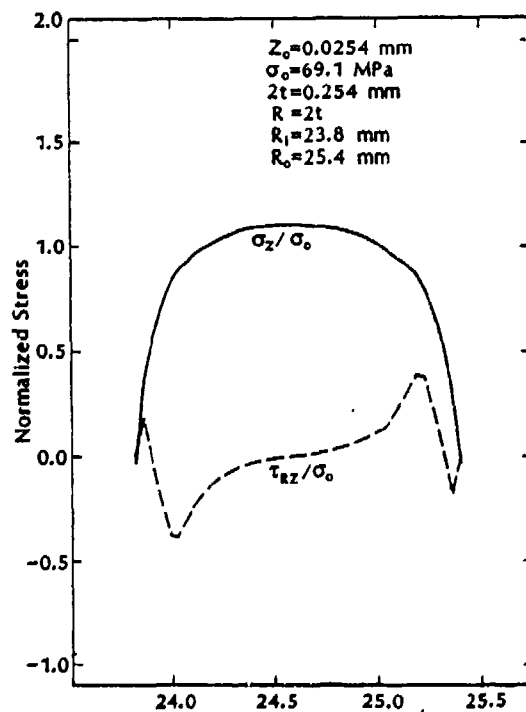
FIG. 3   Napkin Ring Specimen With Rounded Adherend Under
Bond-Normal Loading

4-5

be made to the edges of the adhesive or adherends. The one that was considered here was to round the adherends (Fig. 1b), making the angle between the adhesive and adherends essentially zero. Various rounding radii R, were considered and stress concentrations were gradually reduced and finally eliminated (Fig. 3) for $R = 2t$, the axial thickness of the adhesive layer. However the stress state is not one of purely normal stresses as some shear is excited towards the edges. The residual stress state due to thermal cool down from cure temperature is shown in Figure 4 for a napkin ring specimen with rounded adherends. Even with rounding, stress concentrations were induced near the edges. The rounding also introduced slight peaking in the shear stress under torsional loading while bevelling of the adherends was less beneficial under all loadings [8].

Cone and Plate Specimen

The cone and plate specimen (Fig. 5) has recently been proposed as another torsional shear specimen [6]. A closed form solution based on the assumption of rigid adherends indicated that the cone and plate geometry should provide a mor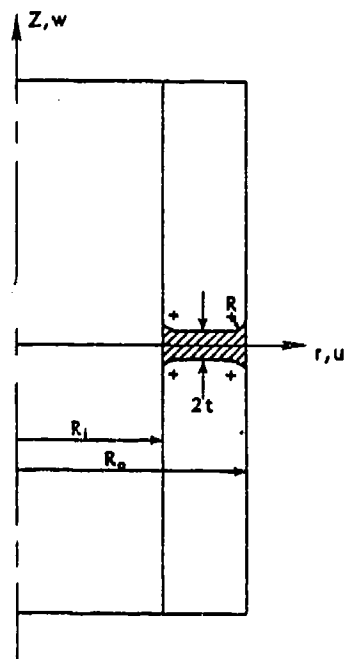e uniform shear stress than is produced by the standard radial thickness of the napkin ring geometry. Ratios of the moduli of structural metals to those of structural adhesives generally range from 50 to 120. Although it might be thought that rigidity of adherends would be a reasonable assumption, evidence of combined relaxation and creep phenomena in adhesively bonded joints indicates that it is not. If the adherends in the cone and plate specimen are not rigid then some accommodation must be made between the radial stresses in the adherends and the constant stress in the adhesive. A finite element stress analysis was therefore conducted for a specimen having radius $R_o = 12.7$mm and adhesive volume angle $\theta_o = 3°$.

Under torsional loading it can be seen (Fig. 6) that the shear stress in the adhesive is highly nonuniform for an aluminum/epoxy joint. The nonuniformity leads to normal stresses that are highly concentrated near the center of the specimen. Only when a steel/rubber combination is considered does the solution approach the closed form solution. By contrast, a bond-normal applied displacement of 25.4 μm produces a more uniform axial stress with a zero shear component over most of the bond radius (Fig. 7). The residual shear stress is similarly distributed (Fig. 8) although the axial stress is more nonuniform. The degree of uniformity could be increased by cutting out a central hole although there is still a substantial axial stress component under torsional loading [8].
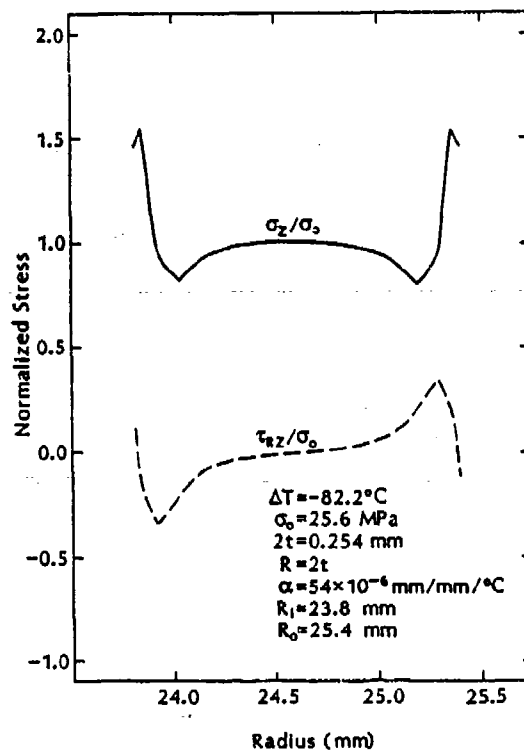
FIG. 4   Residual Stress State in a Napkin Ring Specimen
          With Rounded Adherends
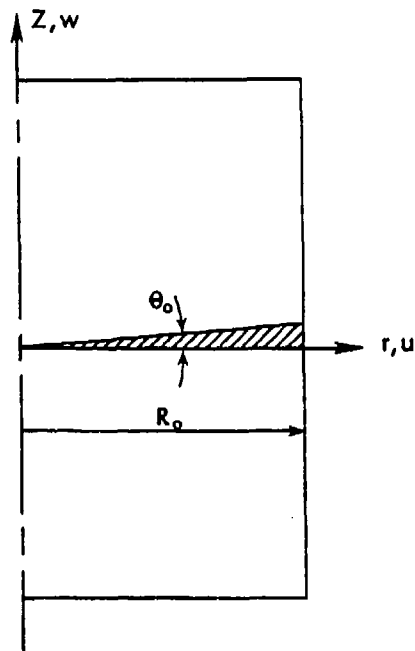
FIG. 5   Cone and Plate Specimen
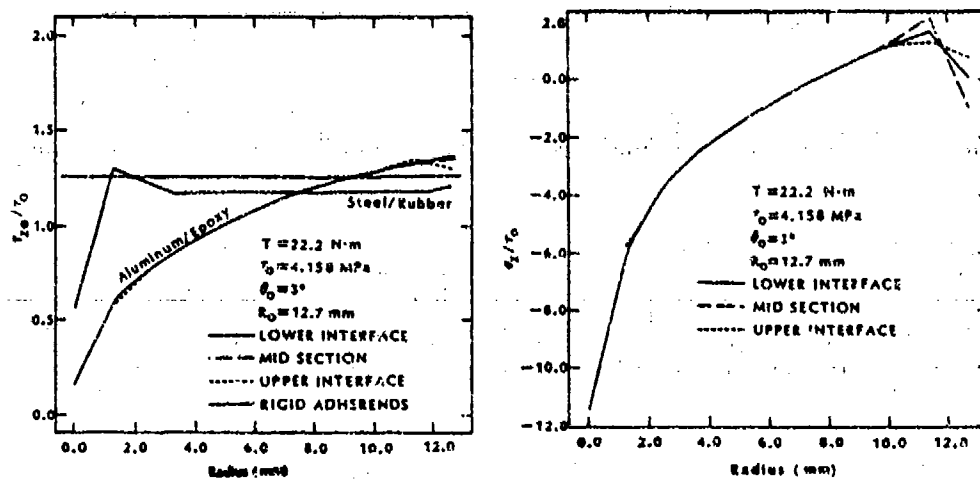
FIG. 6   Stresses in a Cone and Plate Specimen Under Torsion
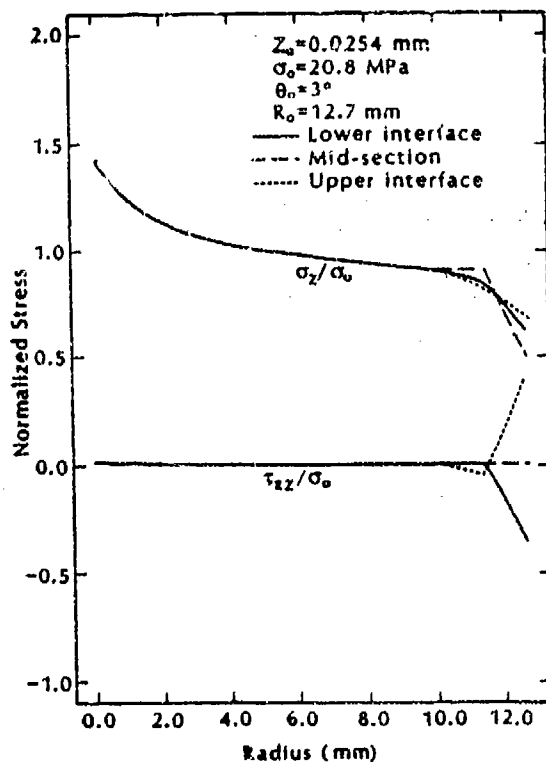
FIG. 7   Stress in a Cone and Plate Specimen Under Bond-Normal Loading

4-8
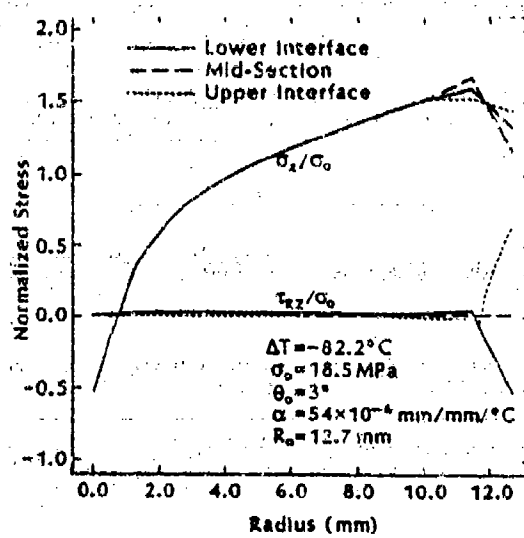
FIG. 8 Residual Stresses in a Cone and Plate Specimen

$\Delta T = -82.2°C$
$\sigma_o = 18.5\,MPa$
$\theta_o = 3°$
$\alpha = 54 \times 10^{-4}\,min/mm/°C$
$R_o = 12.7\,mm$

Grips and Specimen

Specimen Types

Straight Notch with
Sharp Adherends
(SNSA)

Straight Notch with
Rounded Adherends
(SNRA)

Rounded Notch with
Sharp Adherends
(RNSA)
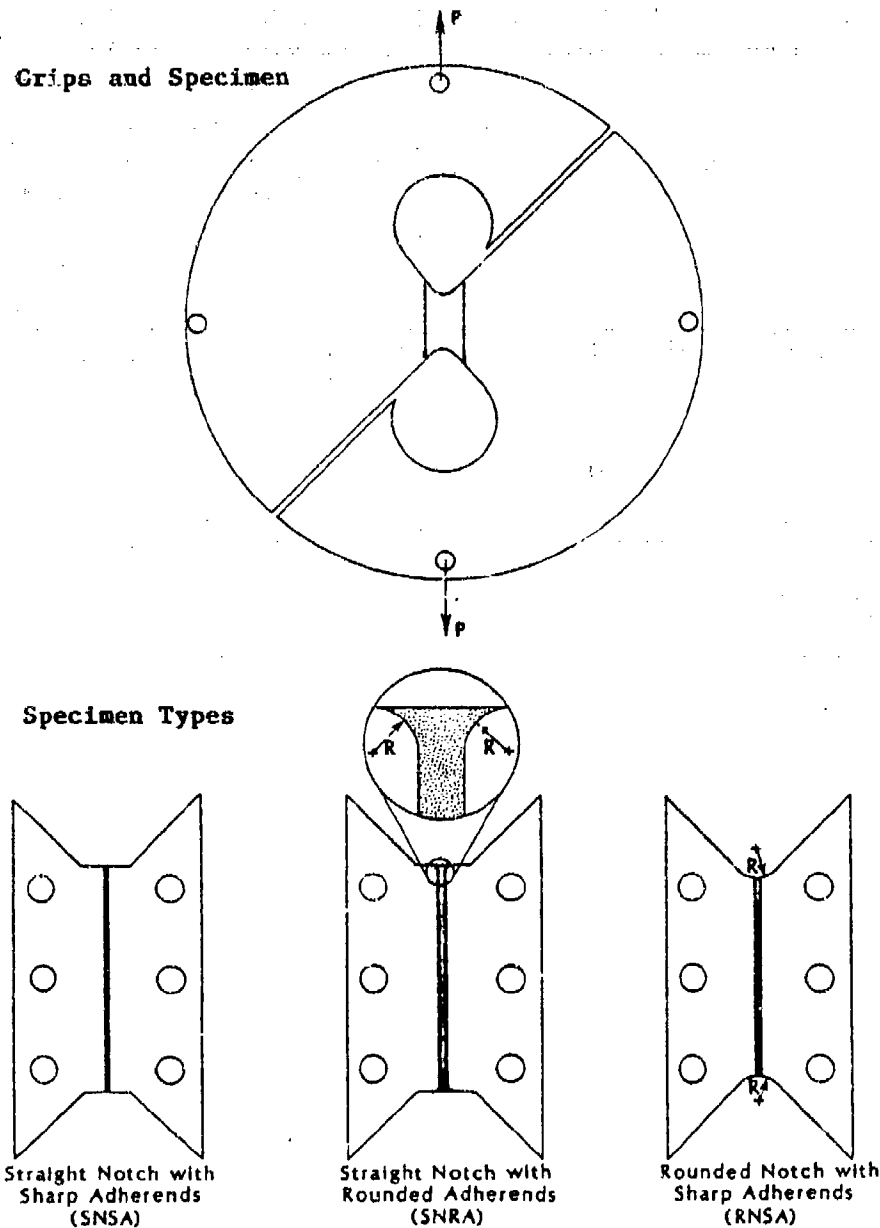
FIG. 9 Stiff Adherend Specimen

4-9
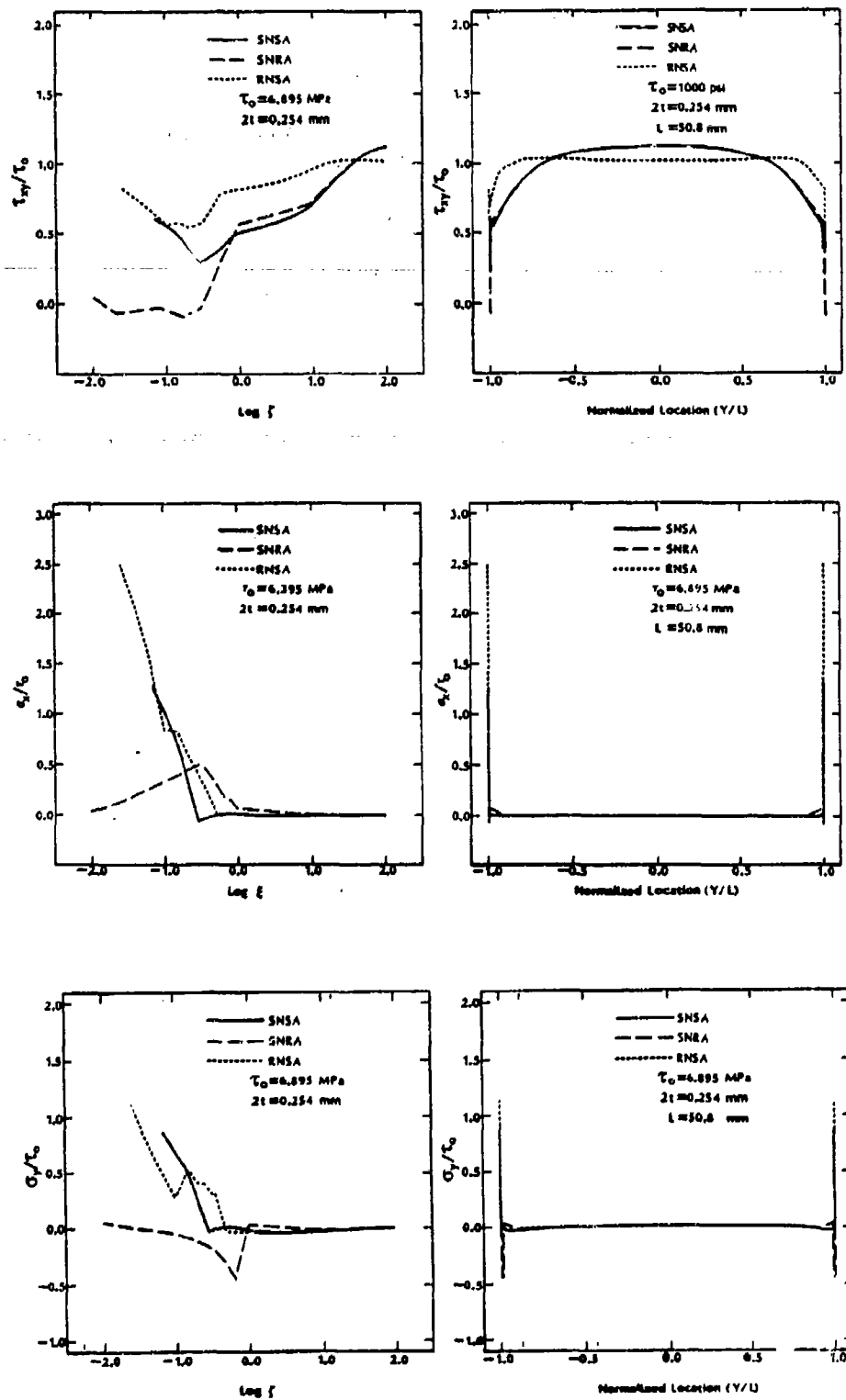
FIG. 10   Stresses in a Stiff Adherend Specimen Under Shear Loading
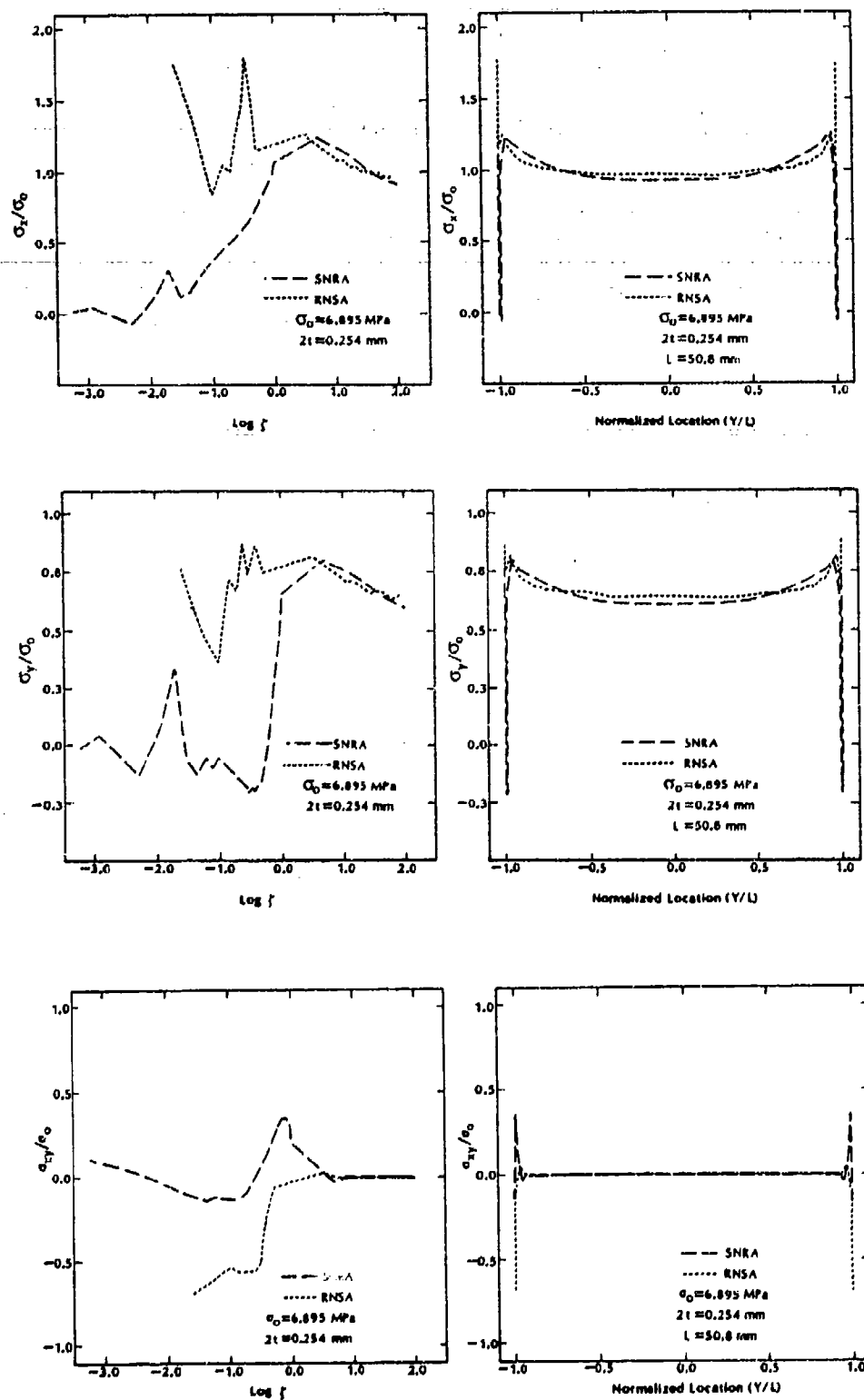
FIG. 11   Stresses in a Stiff Adherend Specimen Under Bond-Normal Loading
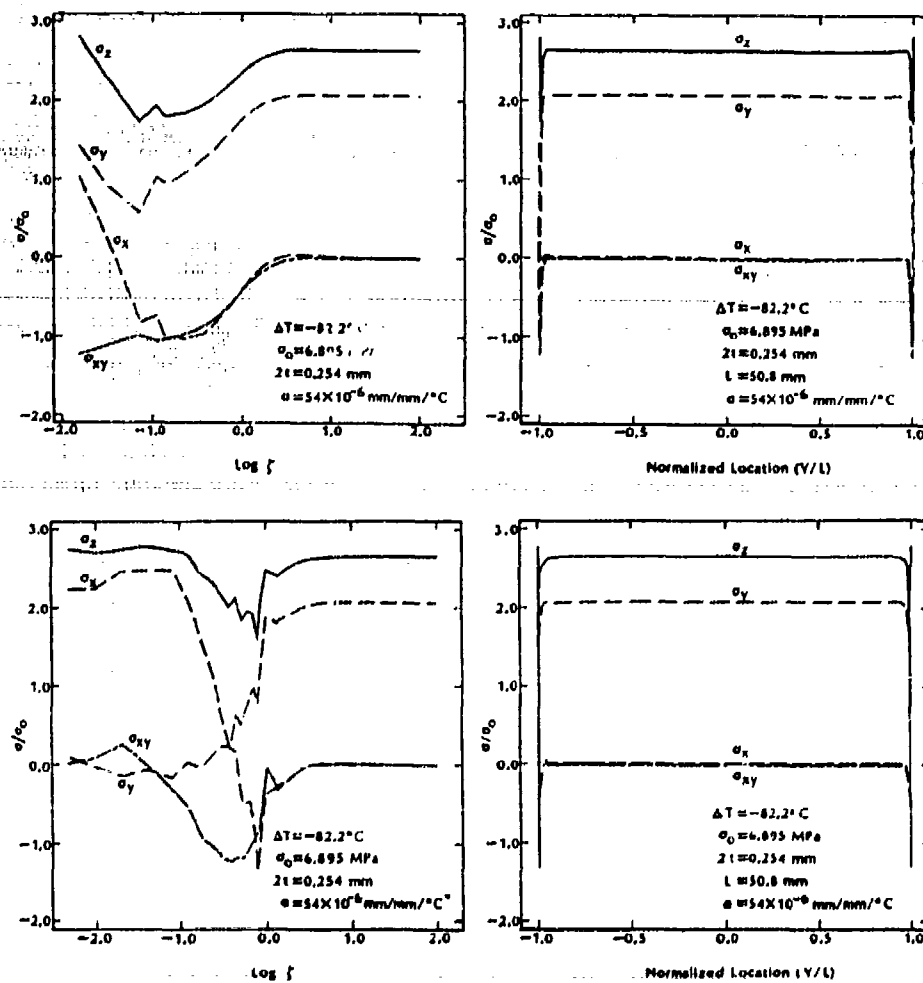
FIG. 12   Residual Stresses in a Stiff Adherend Specimen
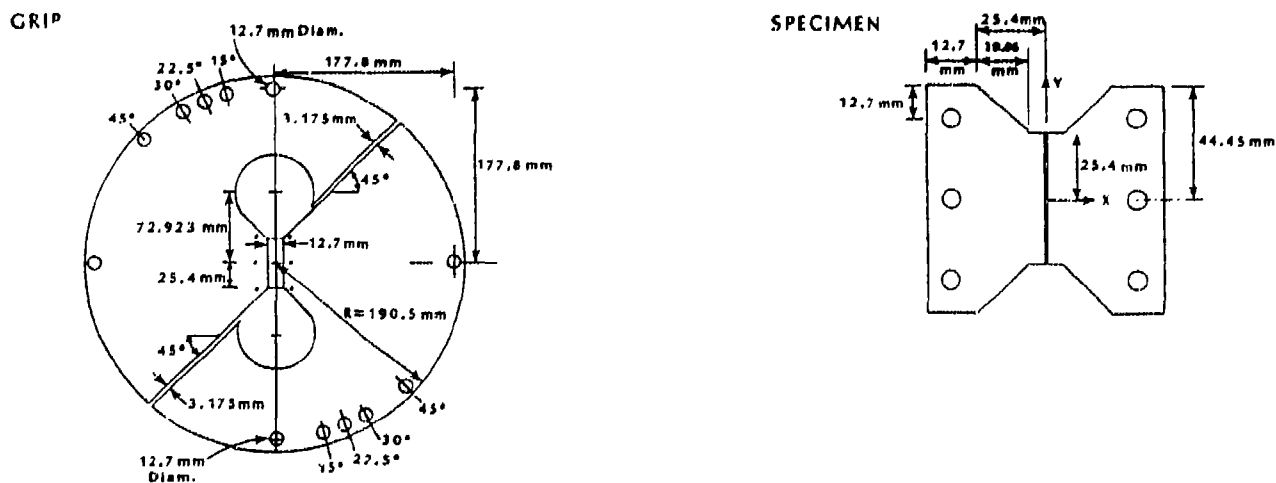
FIG. 13   Dimensions of Stiff Adherend Specimen and Grips

Stiff Adherend Specimen

The stiff adherend specimen is shown in Figure 9 and consists of S-shaped grips to which the butterfly-shaped specimens are attached. In homogeneous specimens, the notched region is supposed to modify the parabolic shear distribution that exists in unnotched beams [4] by providing the proper degree of concentration and thus producing a uniform shear stress in the test section. It was not clear what the effect of bimaterial corners in the notched region would be and so three notch configurations (Fig. 9) were examined: straight notch with sharp adherends (SNSA), straight notch with rounded adherends (SNRA) and rounded notch with sharp adherends (RNSA). Under tension shear loading, the shear stresses are reasonably uniform (Fig. 10) although there are signs of stress concentration for the sharp adherend cases in the semi-logarithmic plots of shear stress vs normalized (by adhesive thickness) distance from the bond edge. The purity of the shear stress state was confirmed, particularly for the rounded adherends, by the zero values for normal stresses. The rounded adherends also produce the most uniform stress state under bond-normal loading (Fig. 11) and thermal loading (Fig. 12). Test procedures were therefore developed for the SNRA specimen.

2.2 Test Procedures and Results

The bondline length was chosen (Fig. 13) to be 50.8mm to ensure a sufficiently large aspect ratio for bond-normal loading. In order to maintain the scaling established in previous work [3], the outer radius of the grips turned out to be 190.5mm, which is quite massive. In order to obtain a number of specimens having the same processing history, blocks of aluminum having the planform geometry of the specimens shown in Figure 13 were bonded together. The thickness of the blocks was such that 10 specimens having 6.34mm thickness could be sliced from the blocks. The rounding of the adherend edges was achieved by filing and checking the radius against a master under the microscope. Surface preparation consisted of various cleaning steps, a sodium dichromate/sulfuric acid etch and priming with BR 127* [6], the bonding of the adherends with FM-300 following standard manufacturer's procedures. The adherends were skimmed to obtain a bondline thickness of 0.254mm. The slicing out of specimens following cure was conducted by a circular cutter. The cut surface was smoothed by a milling step with a fly-cutter followed by a polishing step in order to facilitate microscopic observation of the bondline during testing.

Specimen gripping and alignment during testing turned out to be very critical. Once the grips were aligned, a blank specimen (no bolt holes) was inserted into the grips and alignment was checked using the microvideo system shown in Figure 14. The hole locations were then transfer-punched. In the original gripping procedure, after the holes had been drilled, the specimen was reinserted into the grip slots and was secured by bolts so that the specimen boundaries were essentially clamped. As will be shown later, slipping between the grips and the specimen usually occurred at some point during the loading, no matter how much clamping force was applied. As an alternative, the bolts were replaced by pins so that the loads were transferred from the grips to the specimen by bearing on pins rather than clamping. There were no signs of slipping in this procedure.

The shear strain across the adhesive was measured using the extensometer shown in Figure 15. Its legs were attached to bases that were themselves clamped to each adherend. A relative motion of one adherend with respect to the other therefore resulted in a relative movement between the left upper and lower legs of the extensometer, exciting a strain gage placed on the lower leg of the extensometer. The shear strain was taken to be the displacement measured by the extensometer divided by the bondline thickness. Any extension in the adherends between extensometer bases and the adhesive adherend interface was, in effect, very small. The load was measured by a load cell and divided by the 50.8 × 6.34mm bond area to yield the shear stress.

A typical shear stress strain curve for a specimen that was clamped to the grips is shown in Figure 16. The data for the plot of small values of strain was obtained by suitable magnification of the extensometer signal and was to be used for determining the shear modulus. In the magnified mode, it can be seen that there is a sharp increase in slope for a strain of approximately 1.5%. The change in slope was associated with a lateral movement of the adherends as observed by the micro-video system. Once the lateral movement stopped, the slope of the stress strain curve returned to an equal or slightly smaller value than was observed before lateral movement started. Furthermore it was noticed that for specimens for which the load was manually decreased, following the return to initial slope, the unloading path showed no signs of deviation and the same was true for subsequent reloading. It was therefore concluded that some realignment had taken place. The shear modulus obtained from the initial tangent was 318 MPa. The ultimate shear strength was 32.86 MPa and the strain to failure was 42.2%. Following the attainment of the maxiumum load, failure of the specimen seemed to take place in a gradual way, with microcracks opening up around scrims fibers as the load dropped. The fracture took place in the plane of the scrim cloth as can be
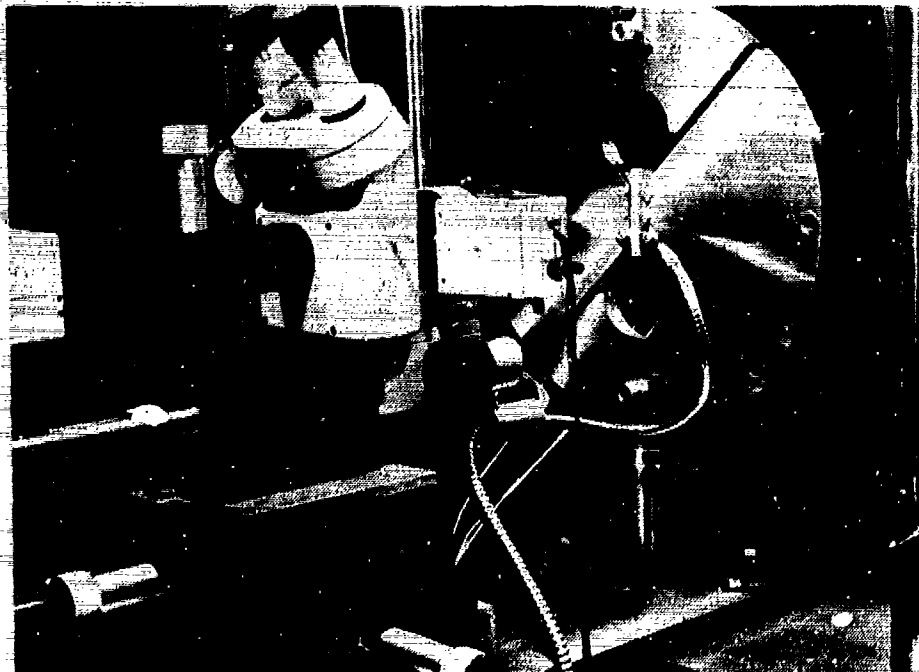
Figure 14: Specimen Mounting and Microvideo System
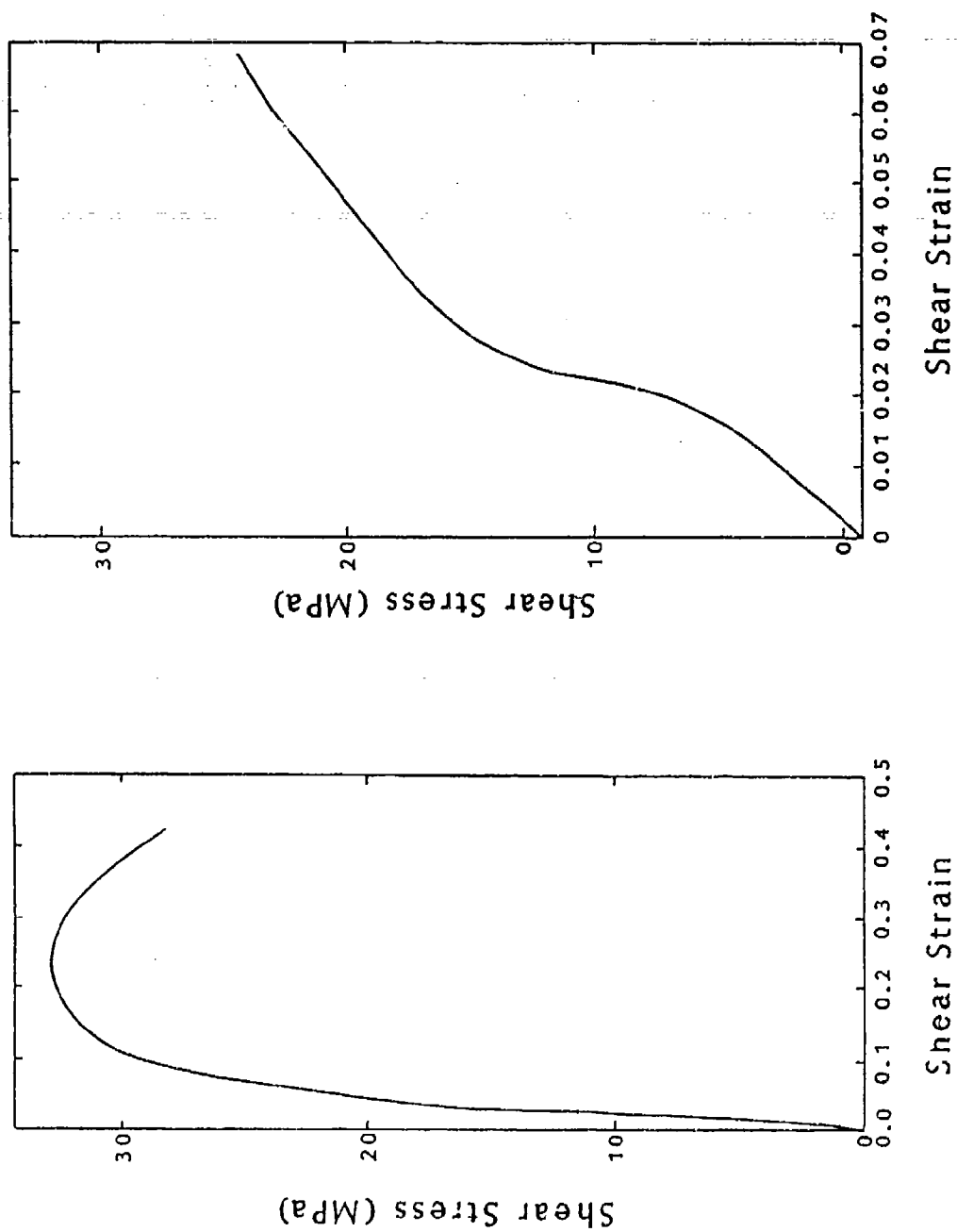

Figure 15: Extensometer Mounting

FIG. 16   Shear Stress-Strain Response of FM 300 Tested Under Clamped Boundary Conditions

seen (Fig. 17) from the optical micrographs of the fracture surfaces. The top picture shows both fracture surfaces under low magnification, whereas the bottom is a close-up and shows the former locations of the scrim fibers that were embedded in the adhesive. The overall stress strain curve for FM-300 obtained from a specimen that was pinned to the grips is shown in Figure 18. In these cases there was no increase in the initial slope of the stress strain curve in the magnified plots of strains up to 7% as had been seen for the clamped case. Furthermore, no noticeable lateral movement of the adherends was observed in the micro-video system. The modulus derived from this data was found to be 347 MPa. The ultimate shear strength was 45 MPa with a strain to failure of 41%. The fracture surface from the pinned specimen was quite different from those observed in specimens that had been tested under clamped conditions. They were much rougher (Fig. 19), having very regular ridges running perpendicular to the load direction. Scrim fiber markings could be seen on some of the ridges. When the bond line was viewed in profile (Fig. 20), it appears that the ridges were formed by microcracks that grew at 45° to the loading direction and then linked to cause final failure. The 45° orientation of the microcracks would imply that they grew perpendicular to the maximum principal stress direction. From the flatness of stress strain curve it appears that the microcrack growth was progressive in nature, but linkage did not occur until the failure strain approached. The microscopic observation with the video system also indicated that microcracks grew in a progressive manner, followed by a sudden parting of the specimen at the maximum strain.

Comparing the results from the two sets of data, it can be seen that the adhesive modulus differed by less than 10%. Since such variations can be encountered in tests conducted under similar conditions, it is unlikely that the noted difference can be attributed to gripping procedures. However, the ultimate strength of the adhesive that was tested under pinned conditions was 37% greater than the value obtained from specimens that had been clamped. The fracture surfaces were also quite different so that the shear strength was clearly affected by gripping procedure. The higher ultimate strength obtained under pinned conditions would suggest that pure shear was indeed attained because any bond-normal loading would reduce the strength in shear. The appearance of the fracture surfaces also suggests that pure shear was achieved under the pinned gripping conditions but not the clamped case. The rough ridges formed by microcracks aligned at 45° to the load axis suggest that pure shear existed when pinned gripping was used. The relatively flatter fracture surfaces that resulted from the clamped gripping indicate that tensile bond-normal stresses were also active. The strain to failure differed by less than 3% and did not appear to be affected by gripping condition.

500μm ⊢←→⊣

|←——500μm——→|

FIG. 17   Fracture Surfaces of a Modified Thick Adherend Specimen
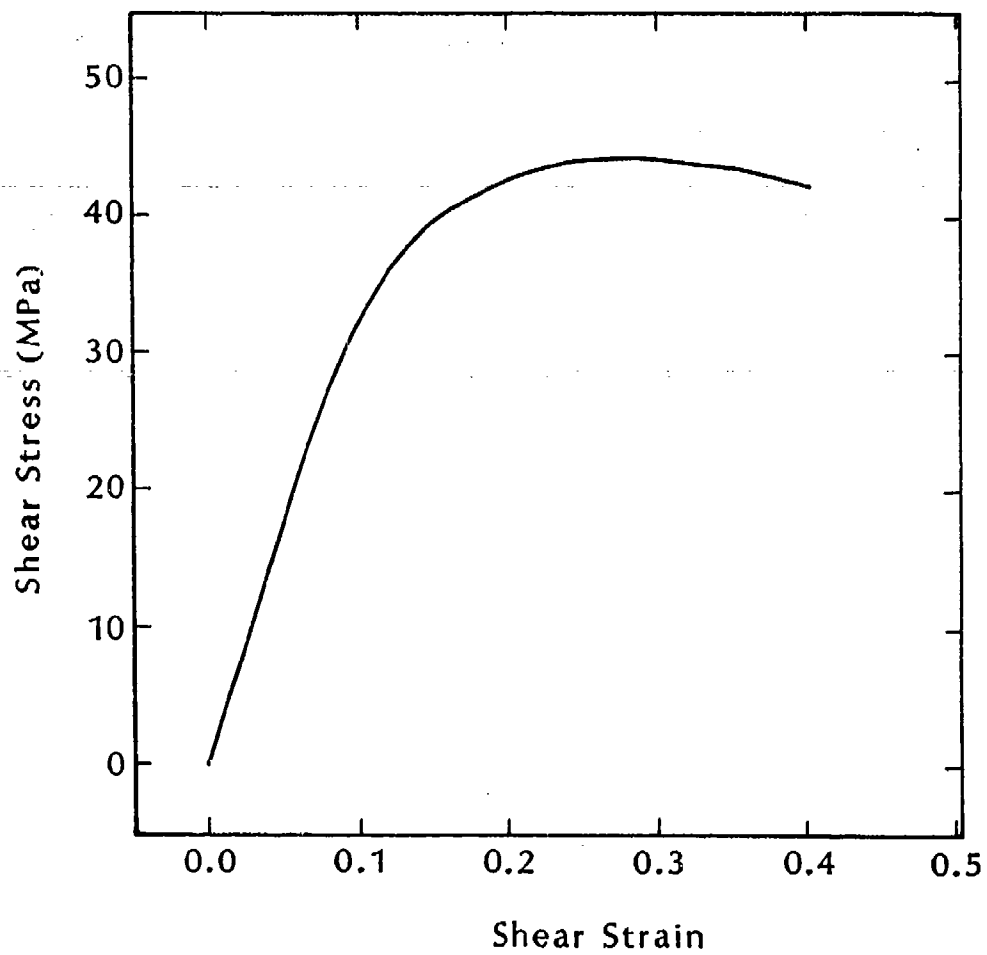(SNRA) Tested Under Clamped Boundary Conditions

4-18

FIG. 18   Shear Stress-Strain Response of FM 300 Tested Under Pinned
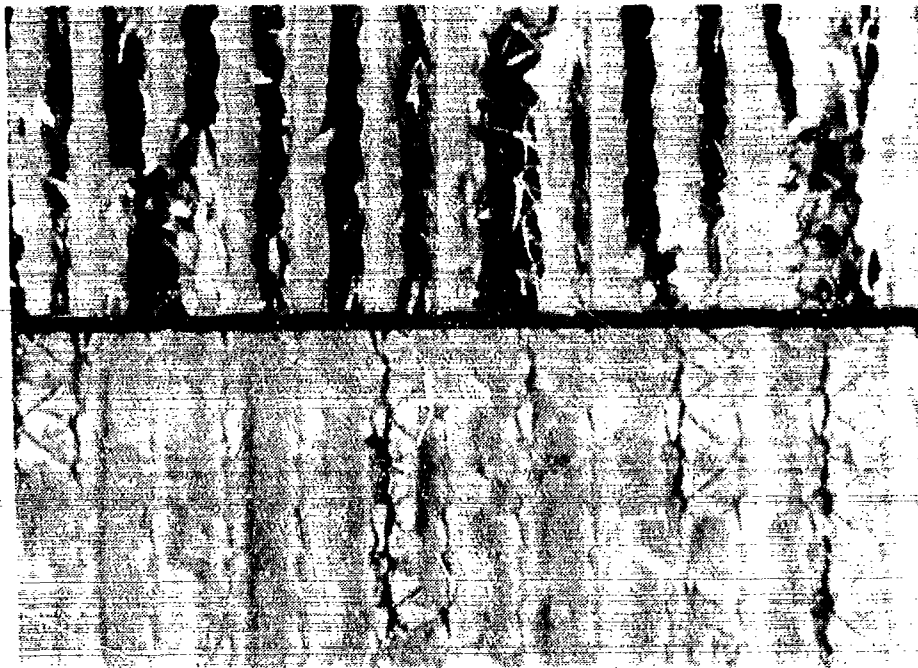Boundary Conditions

Figure 19: Fracture Surfaces of a Modified Stiff Adherend Specimen (SNRA)
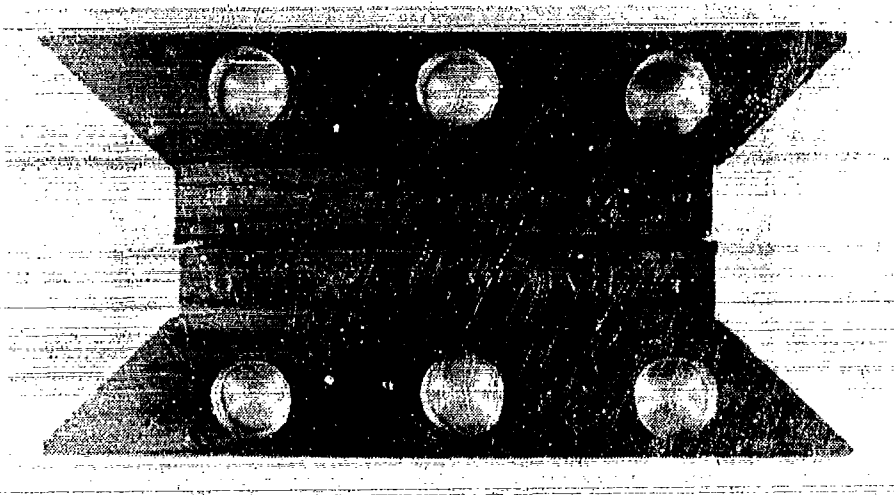Tested Under Pinned Boundary Conditions

Figure 20: Side View of Fracture Surfaces of a Modified-Stiff Adherend Specimen
Tested Under Pinned Boundary Conditions

The data can also be compared with existing data obtained from single lap shear and napkin ring tests. The manufacturer's listed value of lap shear strength is 35.5 MPa and falls between the strengths discussed above. The implication is that the pinned gripping condition gave rise to a purer state of shear and thus a higher strength. Following further on this line of thought, it would seem that the state of stress in the adhesive layer of the clamped specimens was less of a pure shear state than that produced by single lap shear tests. Stringer [9] used the napkin ring to compare the stress strain behavior of a number of structural adhesives. Among the compared adhesives was a supported rubber modified epoxy (adhesive D, [9]). The shape of the stress strain curve of the adhesive was quite similar to that of Figure 3.8, the stress strain behavior of the adhesive in the pinned specimens. The shear modulus, strength and strain to failure of adhesive D were 722±203 MPa, 46.3 MPa and 51%, respectively. The ultimate strength and strain were thus quite similar, although the FM-300 modulus derived here is about 50% lower.

An interesting comparison of the data can also be made with data obtained from neat films of FM-300 that were subjected to uniaxial tension [25]. The tensile modulus, ultimate strength and strain to failure were 2.285 GPa, 48.5 MPa, and 3.8%. The Poisson's ratio was 0.4, leading to a shear modulus of 815.9 MPa which is more than twice the shear modulus of the *in-situ* adhesive determined here. The neat film strength in tension was a bit higher than the *in-situ* shear strength, but there was a large difference in strains to failure—probably because more damage can be sustained for the *in-situ* case. In that case, an initial microcrack arrested by the adherends and other microcracks are forced to grow, whereas in tensile thin film tests one microcrack can result in final failure of the specimen.

The modified stiff adherend specimen (SNRA), when properly aligned and pinned to grips, has provided higher values of shear strength than have previously been measured. This would seem to indicate that a purer shear stress state does indeed exist. The values of shear modulus obtained were 50% less than values obtained from bulk specimens tested in tension. It is not clear at this time whether the difference can be attributed to the bulk vs. *in-situ* issue or to a consistent error in strain measurement on the stiff adherend specimen. Dolev and Ishai found that the shear modulus obtained from testing FM-73 *in-situ* was about 7% less than the value obtained from tests of the bulk material. Alternate methods for measuring shear strain based on optical methods are now being considered, not only as a check on the mechanical extensometry, but also to determine the uniformity of the strain field along and across the adhesive layer thickness.

2.3 Alternate Specimen Geometries

Although the stiff adherend specimen has performed well for the shear testing of adhesives, and shows promise for bond-normal loading and studies of the multiaxial strength of adhesives, it may be too complex a specimen for standard production testing. The adherend shape is more complex than lap shear or laminated beam geometries. Specimen alignment is also more crucial and time-consuming. A laminated beam specimen proposed by Moussiaux et. al. [12] is showing some promise in this regard and would be most compatible with the fracture property specimens already proposed in section 3. In [12], the authors present a strength of materials analysis to the problem of a cantilevered, laminated beam subjected to equal shear forces in each adherend (Fig. 21). The analysis indicated that the shear stress in the adhesive rose quickly from zero at the cantilevered end and maintained a constant value for as much as 90% of the bondlength for suitably chosen beam parameters. The results were compared with a finite element stress analysis, and surprisingly good agreement was obtained—even at the ends where stress singularities should have arisen. During the most recent reporting period, the finite element analysis has been checked and various modifications similar to the successful ones for the stiff adherend specimen have been considered in an attempt to eliminate stress concentrations.

The specimen considered in the analysis had the same dimensions as the fracture property specimens. The length was 4 inches, the aluminum adherend thicknesses were 0.25 inches and the FM-300 adhesive thickness was 0.010 inches. Each adherend was subjected to an end load $P = 1,000$ lbf. The adhesive layer thickness was subdivided into 5 layers for the finite element analysis, the lengthwise distribution (for the rounded adherend case) is shown in Figure 22. The stresses along the center of the adhesive layer and along the upper and lower interfaces are shown in Figure 23 for a specimen having sharp 90° corners at the ends. At the cantilevered end there are stress concentrations in all the stresses, particularly at the lower interface. At the loaded end there is a slight increase in the shear stress before it drops to zero. There are some oscillations in the axial stress before it becomes zero at the free edge. However, the interfacial peel stresses are singular and would most likely be a source of premature failure. Furthermore, the shear stress is only uniform over 70% of the bondline, making this configuration of the specimen unattractive. In the napkin ring and stiff adherend specimens considered earlier, rounding of the adherends had proved beneficial in eliminating stress concentrations. Similar rounding (Fig. 22) was considered for the LBAST specimen, and the resulting normal stresses are shown in Figure 24. There was essentially no change in the shear stress distribution and, if anything, larger oscillations and more concentration in the
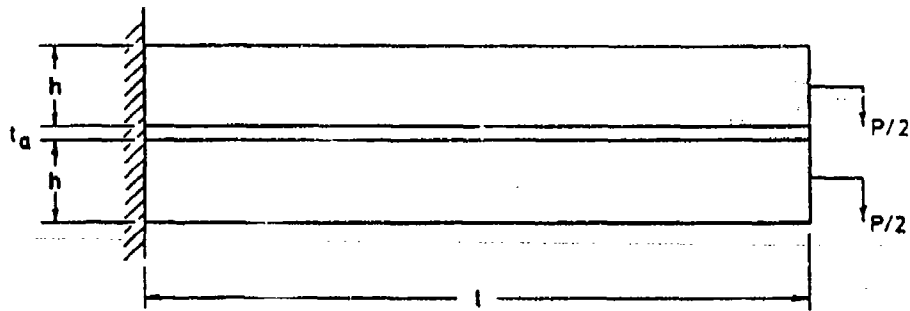
h = 0.25 in.   l = 4.0 in.
t_a = 0.01 in.   P = 1000 lb.
Adherend :   E = 10 × 10^6 psi
               ν = 0.32
Adhesive :   E = 4 × 10^5 psi
               ν = 0.4

FIG. 21   Bending Laminated Beam Adhesive Shear Test (LBAST) Specimen Geometry
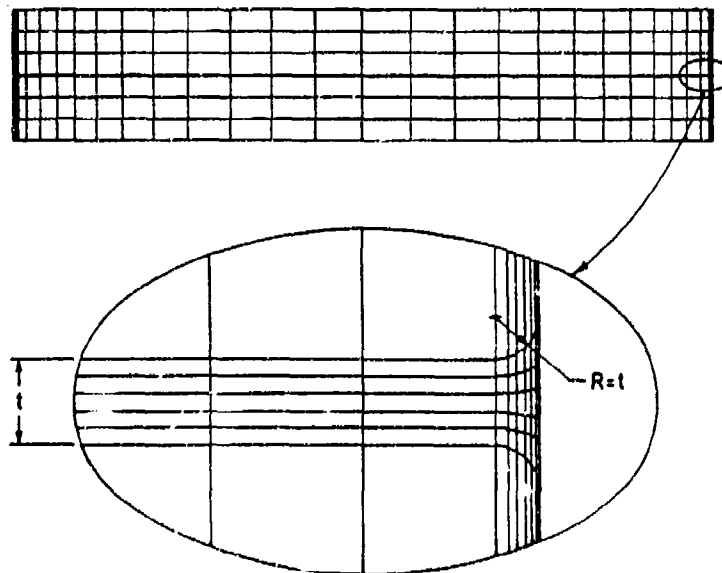

FIG. 22   Finite Element Mesh for LBAST Specimen with Rounded Adherends
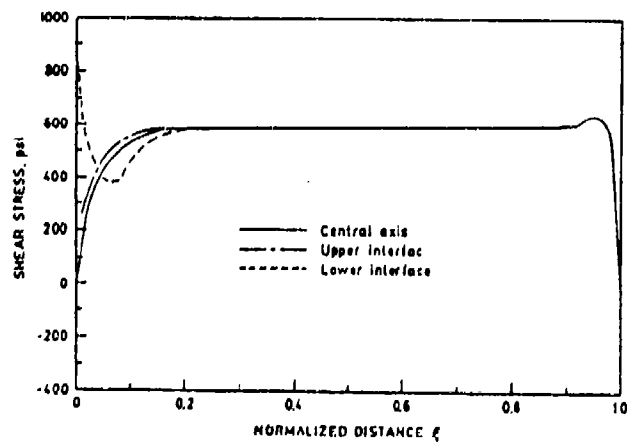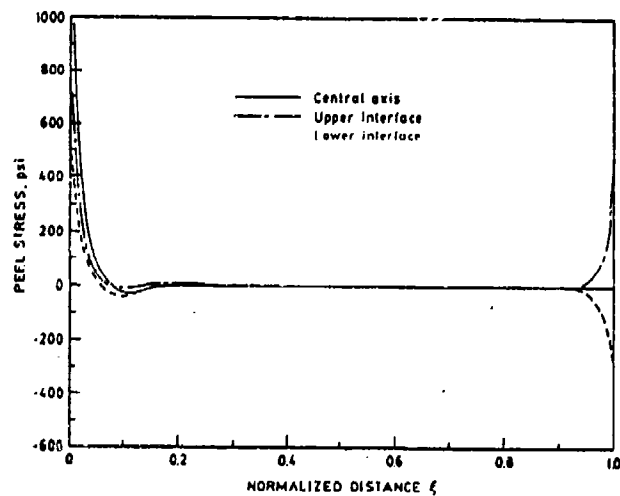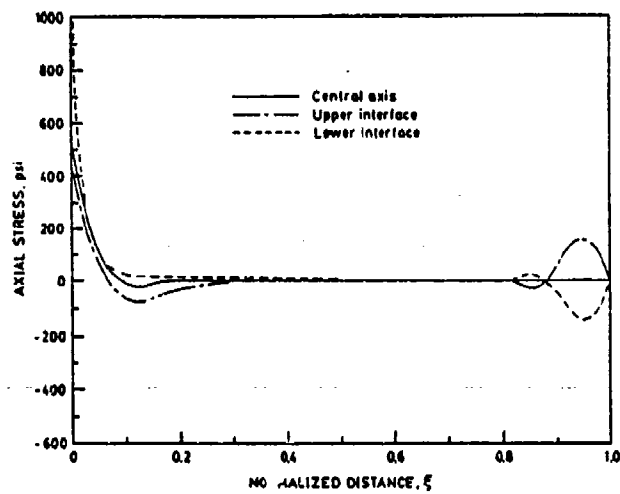
4-24

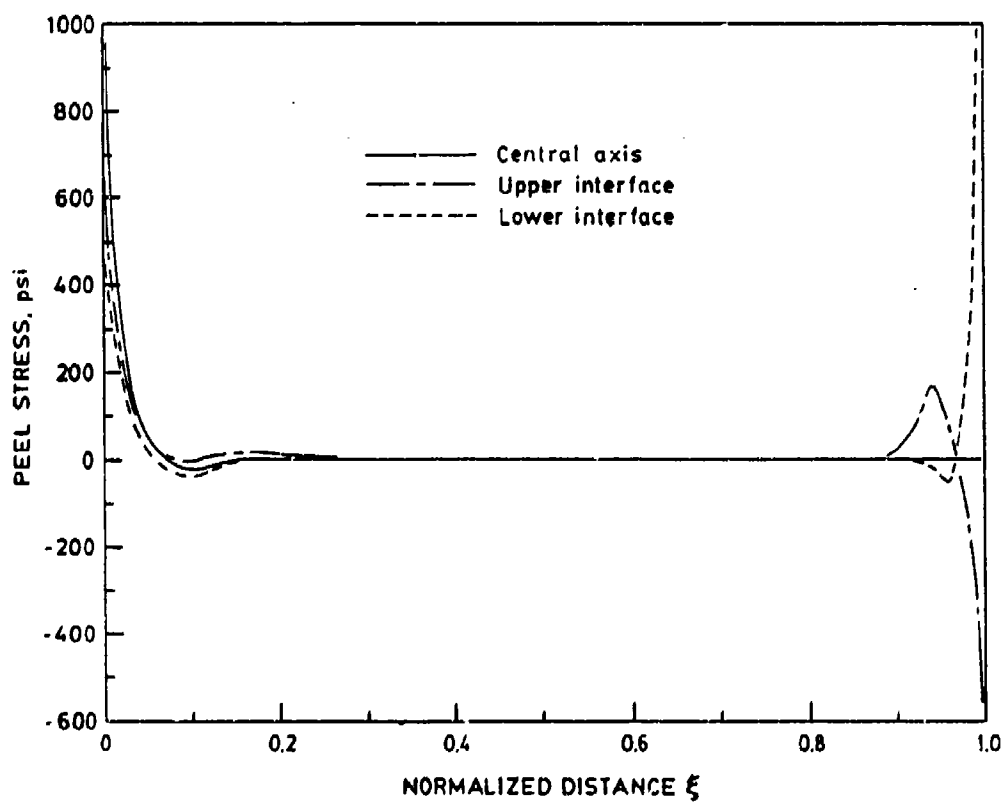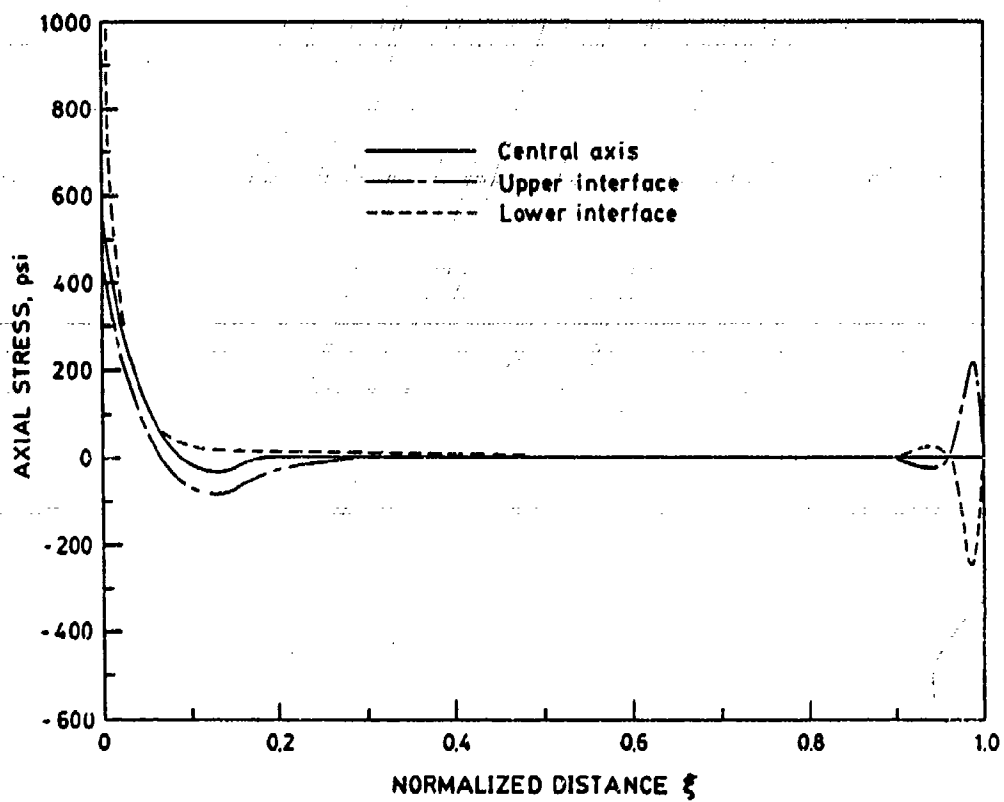FIG. 23   Stress Distributions in an LBAST Specimen with Sharp Adherends

4-25

FIG. 24   Stress Distributions in an LBAST Specimen With Rounded Adherends

normal stresses. With all the problems at the cantilevered and loaded ends, it was decided to shorten the bonded region to a central 2 inch length while maintaining the original adherend length of 4 inches (Fig. 25). In order to prevent differential bending in the adherends in the regions without adhesive, steel shims were placed between the adherends, 0.5 inches in from each end. In the finite element analysis, the adherends were allowed to slide (without friction) over the shims. The adhesive termination was originally considered to be sharp, i.e. forming a 90° angle with the adherends. As expected, stress singularities arose, and the adhesive was therefore rounded as shown in Figure 25. It was thought that such a rounding could be achieved by placing a folded teflon film between the adherends, using the fold radius to mold the adhesive radius. The resulting stress distributions are shown in Figure 26 where it can be seen that the shear stress has peaks at either end of the adhesive, with the peak closest to the loading end being larger. The magnitude of the peaks varied through the thickness, causing peaks in the axial stress at the interfaces. The sharp drop in shear stress following the peaks caused stress singularities in the peel stresses at the interfaces which would again probably cause premature failure in the adhesive.

The stiff adherend specimen still provides the most uniform stress state. Steps are therefore being taken to make the geometry more compatible with the fracture specimens and to simplify testing procedures.

3. Fracture Properties

Crack growth in adhesively bonded joints is an inherently mixed-mode process because of the constraint applied by the adherends. Depending on the particular adhesive system, the fracture toughness may vary with mode-mix, usually increasing with increasing mode II component [13,14]. It may not, therefore, be sufficient to determine the fracture toughness under pure mode I conditions using the double cantilever beam (DCB) specimen first proposed by Ripling et al. [12]. Over the years a number of specimen geometries have proposed for the determination of mode II and mixed-mode fracture toughness of adhesives. Such geometries include the prismatic shear specimen [15], the scarf joint [14,16], independently loaded mixed-mode specimen [16] and the cracked lap shear specimen [17,18]. In considering interlaminar delamination in laminated fiber reinforced composites the most recent emphasis has been on simplicity and multiple use of beam-like specimens. Vanderkley [19] demonstrated how the DCB geometry, by a simple modification of its loading, could be used to determine a range of mixed-mode interlaminar toughnesses. Along similar lines, the end-notched flex-
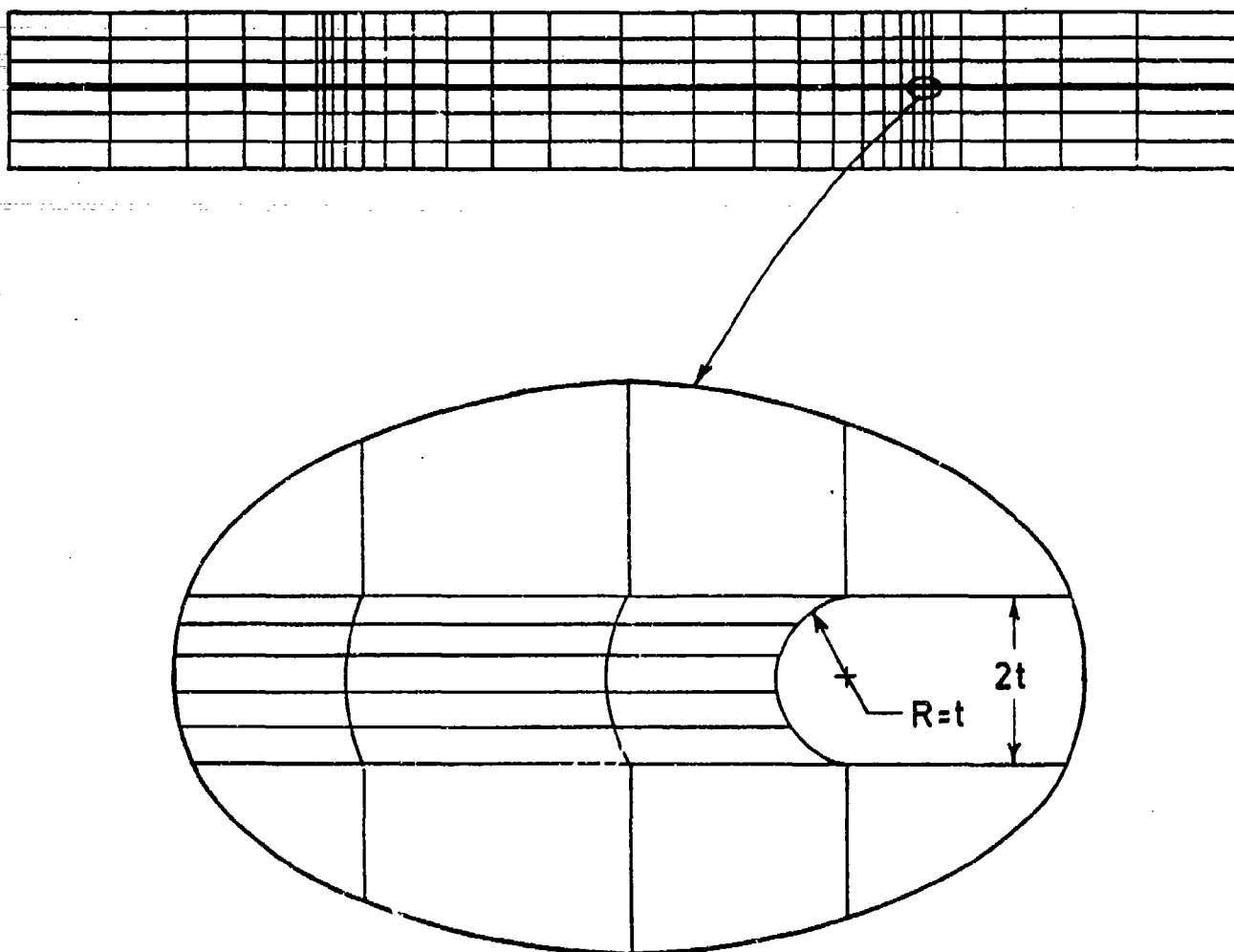
2t

R=t

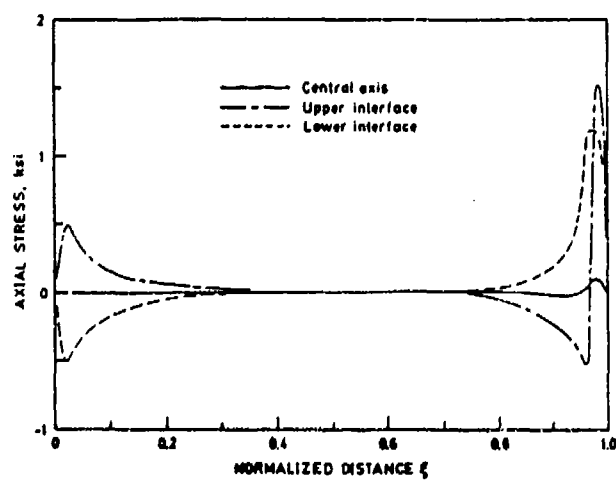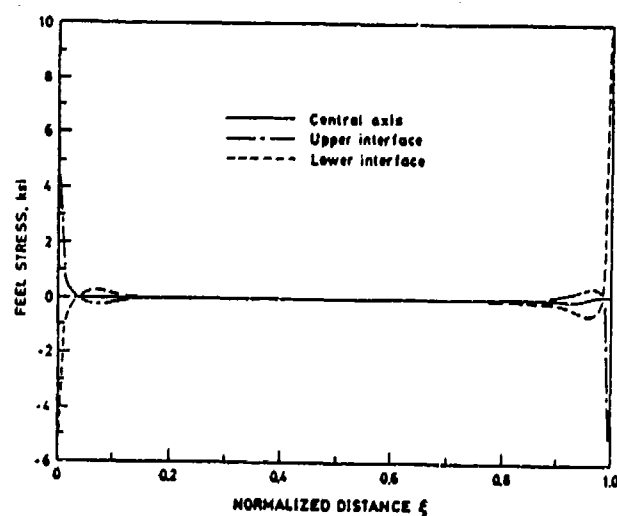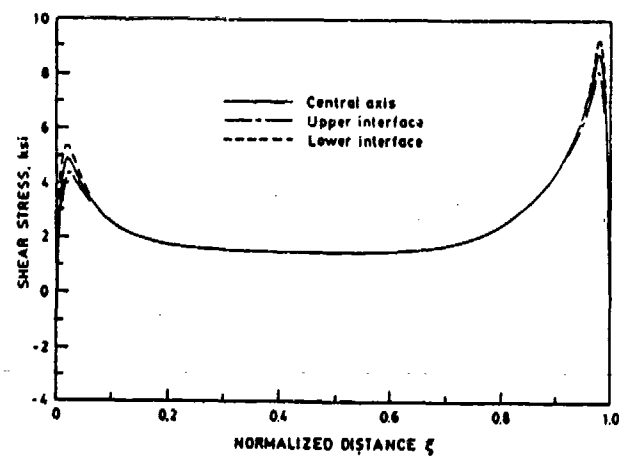FIG. 25   Short Adhesive LBAST Specimen Geometry

FIG. 26   Stress Distribution in a Short Adhesive LBAST Specimen

ure (ENF) [20,21,22] and mixed-mode flexure (MMF) [20] have also been proposed for the determination mode II and mixed-mode interlaminar toughnesses, respectively. The first application of the ENF specimen for the determination adhesive fracture toughness was recently presented by Mall [23,24] who considered the effects of friction between the crack faces and found that the fracture toughness of EC3445 bonded composite specimens had the same fracture toughness under the full range of mode-mixtures.

The purpose of the present work was to consider the feasibility of using simple laminated beams for the determination of pure and mixed-mode fracture toughnesses of adhesives with emphasis on high temperature applications. The wide range of mode mixtures was obtained by essentially similar geometries loaded in different ways. Such an approach allows specimens to be obtained from the same plate, thereby reducing scatter to variations in cure and surface preparation. A further objective in designing the specimens was to minimize size so that they could be used in adhesive development programs where the amounts of material available may be limited. In this way variations in adhesive formulation could be evaluated in terms of properties that are directly applicable to the structural design process rather than being limited to simple qualitative comparisons in tests in which failure mechanisms and loads are not really understood.

3.1 Specimen Fabrication and Testing

The specimens considered in this study were the double cantilever bea.n (DCB), end-notched flexure (ENF) and mixed-mode flexure (MMF) for pure mode I, pure mode I, pure mode II and mixed-mode fracture toughnesses, respectively. Pending the development of a new high temperature (700°F) adhesive, specimen analysis and development was based on aluminum adherends bonded to FM-300[†] under room temperature conditions. The specimen geometries are shown in Figure 27 and were essentially driven by the constraints of the ENF specimen for which the highest fracture toughnesses were anticipated. A nominal length of 10cm and a width of 12.7mm were chosen in order to limit the amount of adhesive per specimen. In view of the lower stiffness and strength of aluminum compared to fiber reinforced composites the adherend thickness was relatively large at 6.25mm. The eventual high temperature application and use of titanium would relax the thickness requirement which ensures that yielding in the adherends does not occur prior to crack growth in the adhesive.

The specimens were sliced from a 20 x 30cm bonded panel. The bonded surfaces of the plates making up the panel had been solvent wiped, vapor degreased, scrubbed with cleanser,

---

[†]Product of American Cyanamid whose furnishing of material is gratefully acknowledged
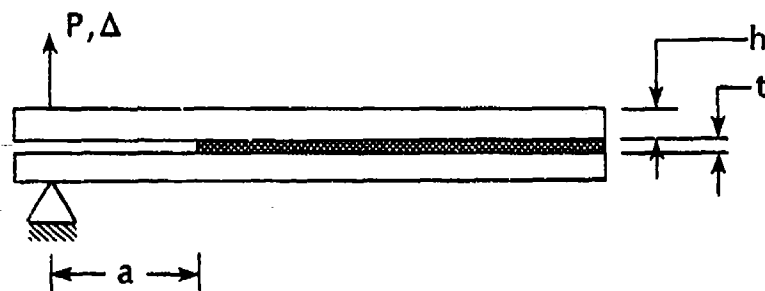
a) Double Cantilever Beam (DCB)
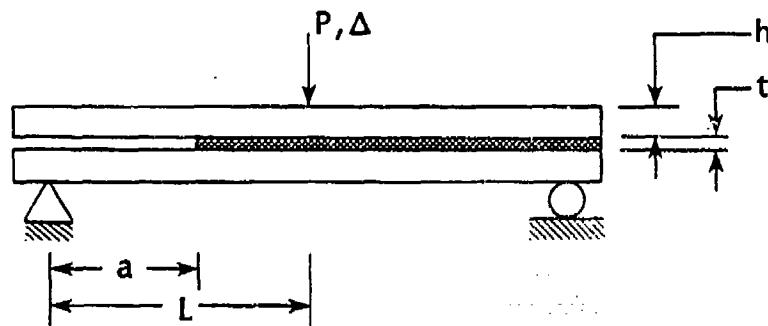
b) End-Notched Flexure (ENF)

c) Mixed-Mode Flexure (MMF)

L=50.8 mm, h=6.25 mm, t=0.20 mm

FIG. 27   Laminated Beam Fracture Specimens

rinsed with water and etched with a sodium dichromate/sulfuric acid paste. After a distilled water rinse the panels were oven dried and then primed with BR127[‡] The vacuum dried adhesive was then applied between the plates which were separated by spacers to ensure a uniform adhesive layer thickness of 0.20mm. Curing followed standard manufacturer's recommendations [25]. The sliced edges of the specimens were polished to aid in th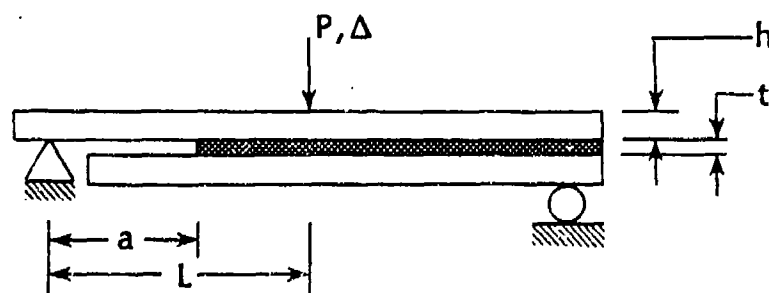e visual determination of crack length. Each specimen was then given a precrack of approximately 12-20mm by wedging a razor blade between the adherends so that the crack tip was beyond the edges of the razor. This gave each specimen an initial crack in mode I. In view of the different modes provided by the ENF and MMF specimens data from this initial crack was always disregarded.

As indicated in Figure 27, the DCB specimen was subjected to a tensile load in the usual manner while the ENF and MMF specimens were subjected to three point bending. The DCB adherends were connected to the loading device actuators through U-joints and aircraft-type rod ends that transferred the load in a direct manner, free from any measurable moment. The ENF and MMF specimens were supported by roller pins which allowed the support points on the specimen to move freely. Loads were measured by load cells attached to the stationary crosshead of the loading device and the load point displacement by a direct current differential transducer (DCDT). Crack length was measured optically using a microscope and a 0.127mm resolution scale attached to the specimen. A video camera, monitor and recorder were attached to the microscope so that the crack tip region could be monitored during loading.

Each specimen was loaded at a constant displacement rate until the onset of crack propagation. The displacement was then held constant while the crack arrested and the load dropped. Following arrest, the new crack length was measured and the specimen was partially unloaded before reloading so that compliance measurements could be made. This procedure was subsequently modified in light of plasticity effects associated with the arrested cracks that then became the starter cracks for the next test in a given specimen. In some of the data presented here the arrested cracks were extended in fatigue prior to reloading.

Each load-displacement record was used to determine specimen compliance as a function of crack length. In the DCB and MMF specimens crack initiation occurred at the maximum load. However, in the ENF specimen, the video recordings revealed that crack initiation

occurred prior to the attainment of maximum load and the critical load was therefore associated with deviation from the linear response. For each load arrangement, the compliance of the machine and fixturing was determined by substituting a much stiffer bar in the place of the specimen and was subsequently subtracted from the measured specimen compliance.

3.2 Analysis

Critical strain energy release rates were determined from the measured compliance, beam theory analysis and finite element analysis. No matter which method of analysis was used the critical strain energy release rate or fracture toughness, G_c, was determined from the rate of change of compliance, C, with crack length, a, and the critical load, P_c, through

$$G_c = \frac{P_c^2}{2b} \frac{\partial C}{\partial a} \tag{1}$$

where b was the specimen width.

The measured compliances could be used directly in equation (1). The compliances determined from beam theory included the effect of shear [25] due to the relative shortness of the specimens. The compliances are given in equations (2), (3) and (4) for the DCB, ENF and MMF specimens respectively.

$$C_I = \frac{8a^3}{Ebh^3} + \frac{3a}{Gbh} \tag{2}$$

$$C_{II} = \frac{2L^3 + a^3}{8Ebh^3} + \frac{1.2L + 0.9a}{4Gbh} \tag{3}$$

$$C_{I,II} = \frac{2L^3 + 7a^3}{8Ebh^3} + \frac{0.6L + 0.45a}{Gbh} \tag{4}$$

The finite element analysis was used to check the validity of the beam theory results and determine the particular mode-mix for each specimen. The analysis was conducted using the finite element code ABAQUS which could account for crack face contact in the case of the ENF specimen. Eight node isoparametric quadrilateral elements were used away from the crack tip which was itself modelled by triangular, collapsed quadrilaterals with quarter point nodes. The locus of failure was taken to be cohesive in the middle plane of the adhesive thickness and mode I and mode II energy release rates were determined from crack opening displacements in the crack tip region[25].

3.3 Results

Since fracture toughness was determined by compliance through equation (1), the measured and predicted compliances are first compared. In the measured compliances a distinction is made between starter cracks that were arrested cracks and those that had been extended in fatigue. The mode mixes and fracture toughness results are then presented. The results are presented on the basis of specimen type and compared in a fracture envelope.

Double Cantilever Beam

The variation of compliance with crack length for the DCB specimen is shown in Figure 28. The compliance from beam theory equation (2) is consistently lower than the measured values and those predicted by finite element analysis. This is to be expected because the cracked beam halves are assumed to be cantilevered at the crack tip. The latter are in fairly good agreement with the largest differences being noted for the longer crack lengths. The type of starter crack did not appear to have much effect on measured compliance. Finite element analysis confirmed that the energy release rates derived from equation (1) were pure mode I. The fracture toughness, G_{I_c}, determined from the measured compliance was found to be 1.2 kJ/m^2 with a standard deviation of 14%. The careful polishing of the specimen edges allowed the crack growth mechanisms to be clearly identified. The circular cross-sections of scrim cloth fiber pairs could be seen at regular intervals along the bond length. The extension of the main crack was preceeded by whitening of the adhesive around one or two fiber pairs ahead of the main crack. The whitening was then followed by the initiation and growth of microcracks which were generally parallel to the bondline. The extension of the main crack then occurred by a linking with the nearest microcrack. The scrim cloth fibers clearly acted as stress concentrators with the microcracks growing perpendicular to the plane of the maximum principal stress.

End-Notched Flexure

The compliance results for the ENF specimen are compared in Figure 29. The beam theory and finite element predictions are in fairly good agreement with one another with the beam theory values being lower for short cracks. The difference in the predictions decreases until the curves intersect and the beam theory values remain slightly larger for long cracks. The predictions are closer to the compliances of the specimens having fatigue mode II starter cracks. The compliances of the arrested mode II starter cracks were generally less than the
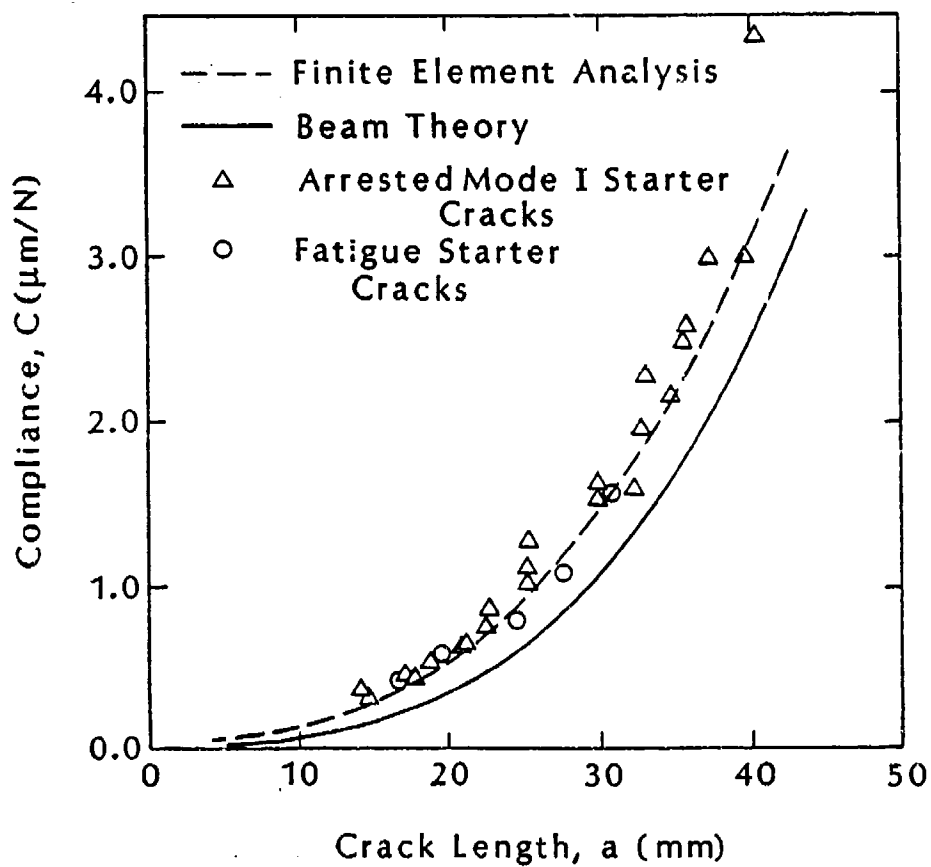
FIG. 28   Comparison of Measured and Predicted DCB Compliance
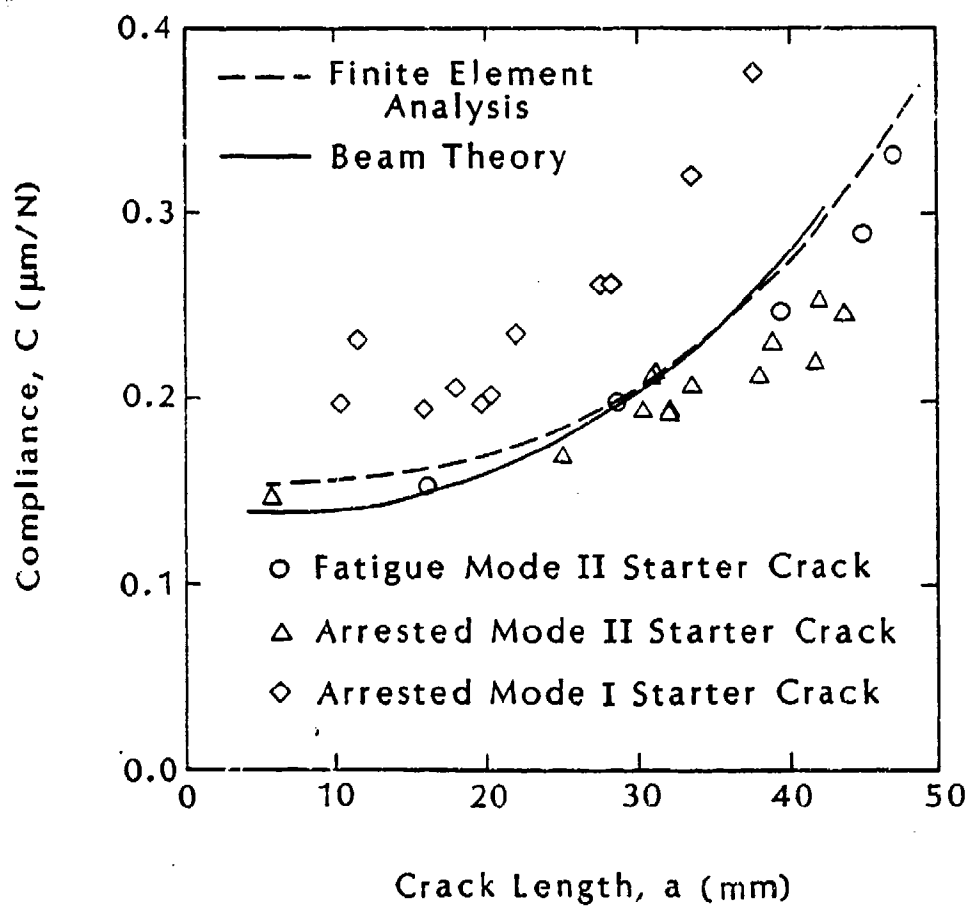
4-35

FIG. 29   Comparison of Measured and Predicted ENF Compliance

fatigue crack values. Also included in the compliance measurements is a set of data obtained from cracks that were generated under mode I loading (razor wedge) and then loaded in three point bending to a load level that was insufficient for crack initiation. The procedure was repeated for successively longer cracks which were grown by reinserting the razor wedge. When the fracture surfaces were examined under an optical microscope the surfaces of mode I cracks were much smoother than mode II cracks. It is likely that the rough surfaces of the mode II cracks interlocked under loading thus resulting in lower compliances. This supposition is further borne out by the fact that the compliance of the specimens containing fatigue mode II starter cracks was greater than those that contained arrested mode II starter cracks. Presumably the fatigue induced motion of the crack faces smoothed out asperities. The differences in measured compliances may, therefore, be linked to differences in frictional effects associated with the three types of fracture surfaces. However, they are inconsistent with the predictions shown in Fig. 29 which were obtained under the assumption of zero crack face contact (by specifying that each cracked adherend was rigidly supported in the vertical direction). On this basis the predictions should have been closest to the compliances of the mode I cracks. Finite element analyses were conducted in which the vertical restraint on the upper adherend was relaxed and crack face contact was allowed by the use of interface elements [25]. However, there was only a 2% difference in compliance when frictionless crack face contact was allowed. Frictional contact for coefficient values ranging 0.2 to 3.0 produced very little change in compliance. The predictions are in agreement with those of Mall and Kochhar [24] but do not account for the interlocking that must occur for the rough surfaces.

The finite element analyses with and without crack face contact all confirmed that the ENF specimen containing a smooth cohesive crack along the midplane of the adhesive produces pure mode II conditions. The fracture toughnesses derived from equation (1) were, therefore, considered to be G_{II_c} values. The average value of G_{II_c} obtained from measured compliances and fatigue starter cracks was 1.79 kJ/m^2 with a standard deviation of 45%. The high degree of variation was brought about by an increase in G_{II_c} with crack length for each specimen that may be due to the interaction of crack tip plastic zones and the region of compression below the central load point. The crack growth sequence of whitening around one or two scrim fiber pairs ahead of the main crack, followed by microcracking and then linkage with the main crack was the same as that observed in the DCB specimen except that the micro cracks grew at approximately 45° to the bondline. The path of the main crack was much more tortuous than was the case for the DCB specimen; a fact that was confirmed by the rougher appearance of the fracture surfaces under the optical microscope.

Mixed-Mode Flexure

The predicted compliances for the MMF specimen were in close agreement (Fig. 30) although it is surprising that the best agreement was for the shortest crack lengths. Both sets of measured compliances were consistently higher than the predictions. The effect of fatigue precracking was small but did result in slightly lower compliances. Finite element analyses indicated that the mode I energy release rate was 57% of the total and that the mode-mix was independent of crack length [25]. The measured compliance gave a mixed-mode fracture toughness of 1.10 kJ/m² with a standard deviation of 16%. Whitening of the adhesive and microcracking around scrim fibers ahead of the main crack were again observed. The microcracks tended to form at an angle to the bondline that was less than 45°.

Fracture Envelope

The pure and mixed-mode fracture toughnesses of FM-300 are compared in the fracture envelope depicted in Fig. 31. The shaded band represents the variation of one standard deviation above and below the quoted mean values. The scatter in G_{II_c} values is high and prevents conclusive statements from being made at this time. However, it does appear likely that $G_{II_c} > G_{I_c}$ and that the total energy release rate criterion

$$G = G_c = G_I + G_{II} \qquad (5)$$

does not apply. The criterion

$$\frac{G_I}{G_{I_c}} + \frac{G_{II}}{G_{II_c}} = 1 \qquad (6)$$

was more applicable. It should be remembered that the energy release rates were derived on the assumption that the cracks grew in a cohesive and coplanar fashion whereas observations indicated that the microcracks were oriented at different angles to the bondline, depending on the mode mix. If such details were accounted for the character of the envelope might change. Another point to note is that visible damage occurred two or three bond thicknesses ahead of the main crack. Initial estimates of plastic zone sizes indicate that they may extend up to forty bond thicknesses ahead of the main crack, under mode II conditions. The scrim cloth clearly plays a strong role in the fracture process. The validity of linear elastic fracture mechanics concepts can well be questioned under such conditions.
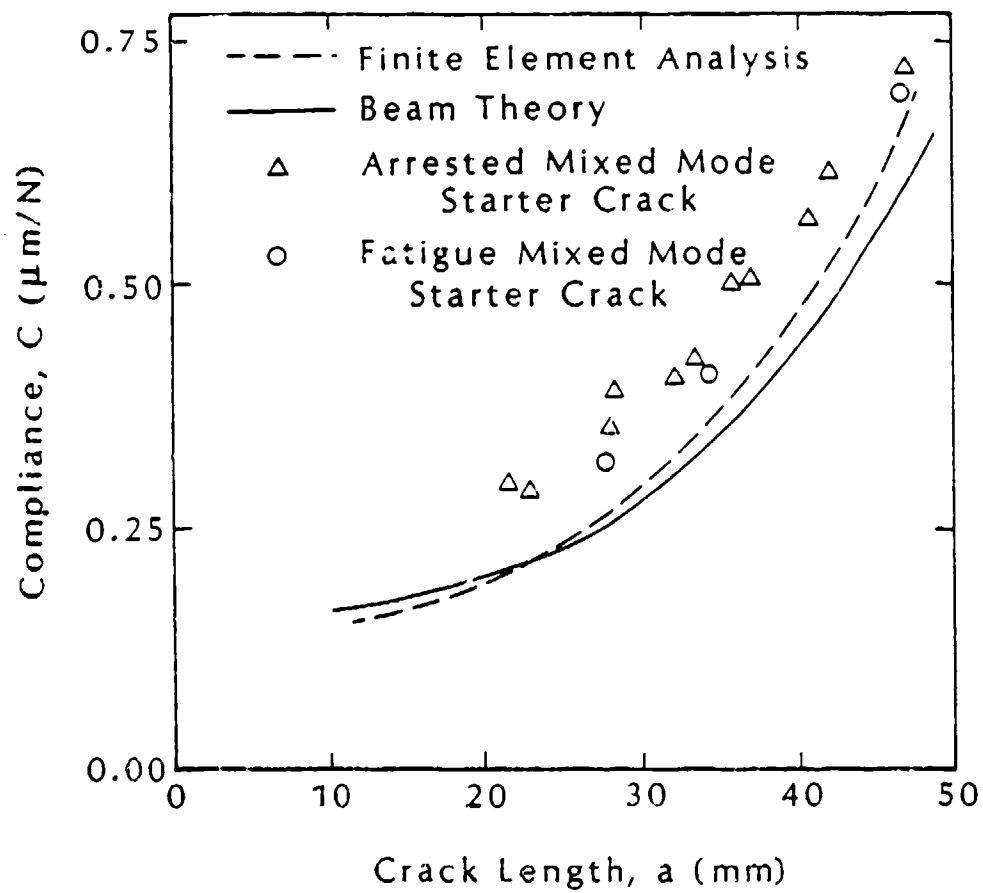
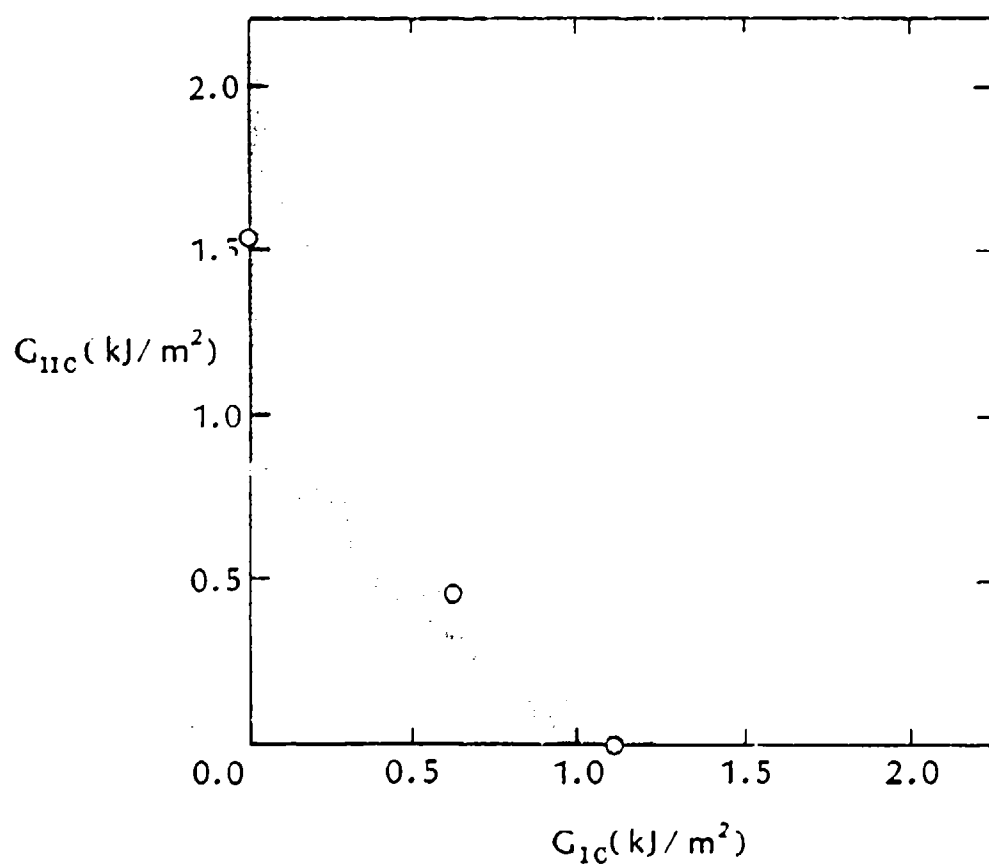**FIG. 30   Comparison of Measured and Predicted MMF Compliance**

FIG. 31   Fracture Envelope for FM 300

3.4 Elastoplastic Analysis of the ENF Specimen

In the ENF tests for mode II fracture toughness there was a notable increase in G_{II_c} with crack length [25]. It was suspected that, for the longer cracks, there was some interaction between crack tip fields and those set up by the central load point. Such interactions could not occur under linearly elastic conditions, and so the possibility of elastoplastic behavior giving rise to long plastic zones ahead of the crack was investigated. The constraint applied by the adherends has been shown in the past to elongate plastic zones for sufficiently thin adhesive layer thicknesses [26]. The problem was addressed experimentally and numerically using the micro-moiré method [27] and an elasto plastic finite element analysis.

The micro-moiré method proposed in [27] has a resolution in displacement of 5×10^{-4} inches, which is intermediate to the resolutions of classical moiré and the more recent moiré interferometry. A 5000 lines per inch phase grating was observed under the microscope and photographed in the undeformed and deformed states. The negatives were then superposed and the resulting moiré fringe patterns analyzed in the usual way. Since, in the present context a microscope is already used to determine the crack tip location, the method seemed readily adaptable. In order to extract the data in real time, the superposition of undeformed and deformed gratings would be carried out using a video subtractor. The main issue in the use of moiré methods in crack propagation studies is the ability of the grating to deform and fracture with the substrate. Photo-resist offers some promise in this regard and was therefore considered.

The specimen edges were first polished on a wet polisher with alumina powder to produce a smooth, reflective surface. The specimen was then cleaned with acetone and methanol and oven-dried. Primer and photoresist were then applied, using a spinner with a specially designed mount to hold the specimen in place. The details of photoresist application and curing are summarized in Figure 32. The thickness of the photoresist [red, #AF1350JSF] was approximately $1.5 \mu m$. Unfortunately, a 5000 lpi Master grating could not be obtained quickly, and so 1000 lpi Master was used instead. A photograph of the photoresist pattern is shown in Figure 33. The height of the grating reflects the adhesive thickness. The grating was of course applied to the adherends, but does not appear under the particular exposures and polarization used to bring out the adhesive. The apparatus used for the micro-moiré analysis is shown in Figure 34. The region of interest was observed through a microscope to which a video camera was attached. The video signal is then taken through a timer (for later synchronization with applied load) to the video subtractor which subtracts any incoming frame from a stored reference frame. In our case the reference frame is the
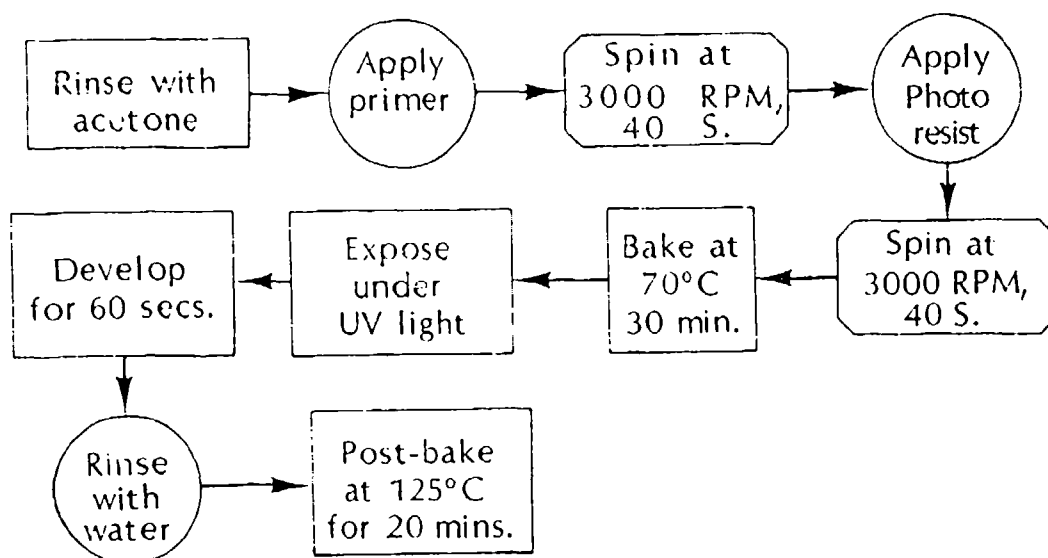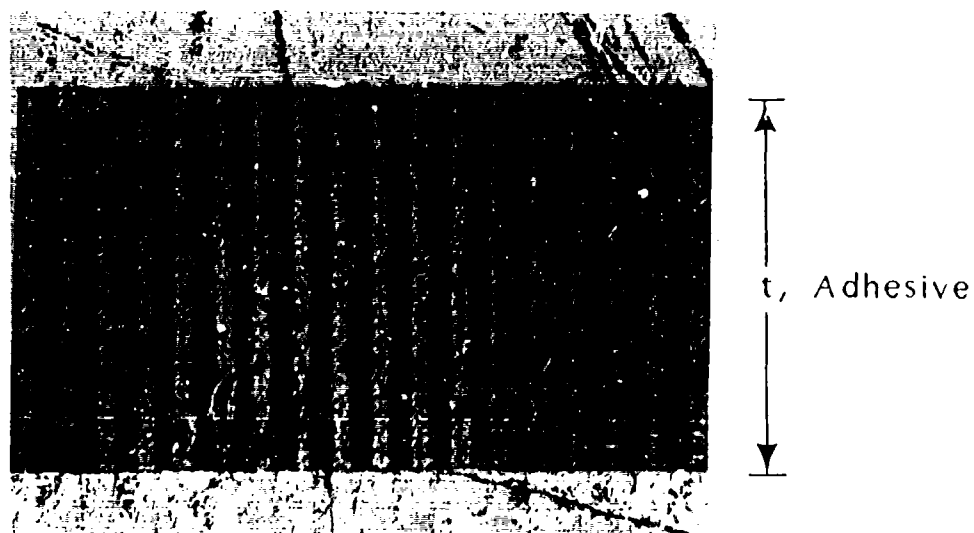
FIG. 32 Photoresist Process Flow Chart

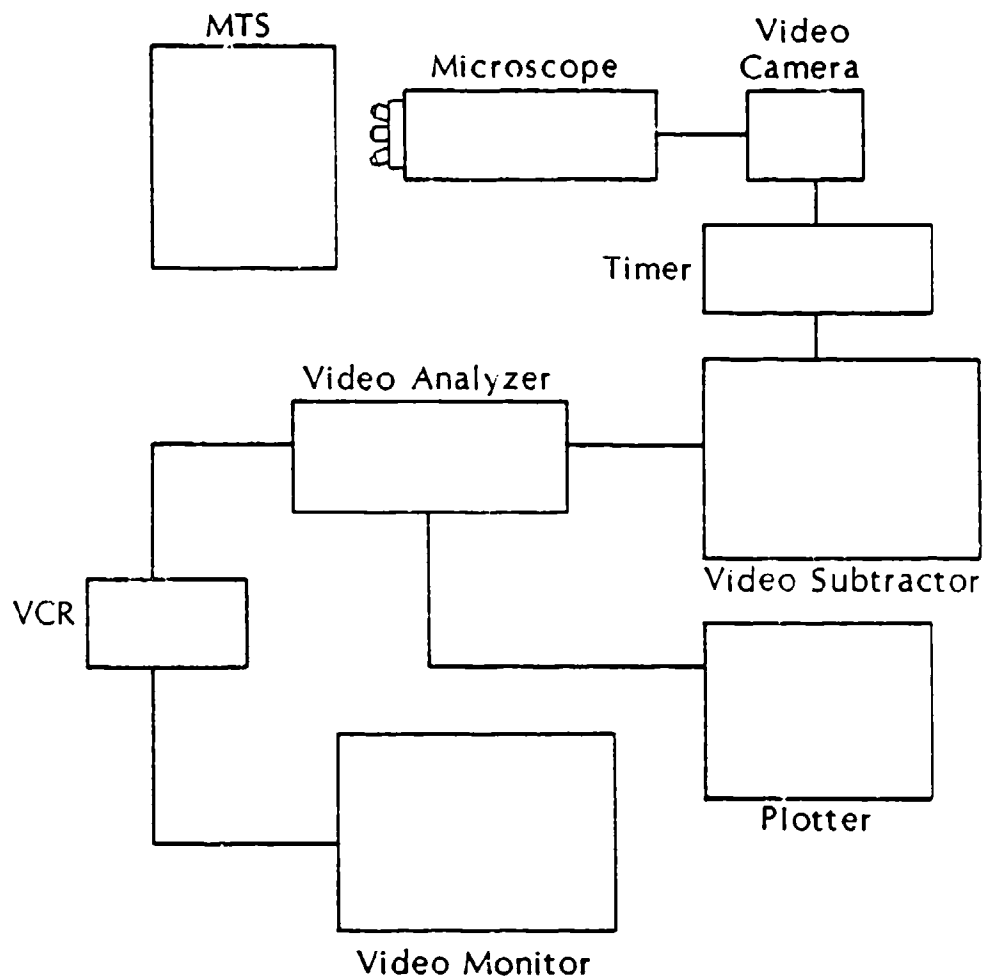FIG. 33 Photograph of Photoresist Grating

FIG. 34   Micro-Moiré Apparatus

undeformed grating, the incoming frame is the deformed grating, and the result of the subtraction is a series of moiré fringes which are contours of constant displacement. The particular component depends on the orientation of the grating. For the grating of Figure 33 the displacements parallel to the bondline, u, were extracted and can be determined through $u = Np$, where N is the fringe order at a particular location and p is the pitch (0.001 in.).

The ENF specimen was mounted in the standard three point bend loading fixture attached to a servohydraulic loading device. The contours of u-displacement were observed in real time and ran parallel to the bondline. However, because the pitch was relatively coarse, one fringe essentially occupied the 0.008 inch bond thickness. The displacement distribution over the adhesive thickness could not be easily discerned, although fractional fringe techniques could in principle be applied. In this regard, the video intensity at a particular point in the adhesive was extracted by an analog analyzer which gave the video intensity under a cross hair as a function of time. The signal varied in a reasonably regular manner, indicating that displacements could be extracted in this way. However, a tenth of a fringe would only yield a strain resolution of 1%, and higher frequency gratings are definitely required.

The photoresist did not respond well behind the crack tip. Although the adhesive clearly contained a crack, the crack length in the photoresist was smaller. A more brittle photoresist would be better. Ahead of the crack tip the shear deformation in the grid could be clearly seen without the use of a reference grating. Figure 35 is a sketch of the permanent deformation that remained in the adhesive ahead of a crack following a loading/unloading cycle. An interesting feature of the permanent deformations is that they were localized in the scrim plane. In this instance the region of permanent deformation could be seen up to 0.35 inches from the crack front. Such large plastic zones would interact with the local stress fields set up by the central load pin.

A stress analysis of a cracked ENF specimen was conducted with consideration being given to the plastic response of the adhesive. The Abaqus finite element code was employed for the analysis. The adhesive very close to the crack tip was assumed to behave in an elastic-perfectly plastic manner (Fig. 36a); further away, a piecewise approximation (Fig. 36b) to the tensile stress strain behavior was employed. The assumption of the elastic-perfectly plastic behavior was necessary in order to obtain convergence in the high strain region close to the crack tip. The analysis was conducted for a load level of 720 lbs. and crack length of 1.25 inches. The crack tip was therefore 0.75 inches from the central load point.

A stress contour plot of the Von Mises equivalent stress is shown in Figure 37. Level 4 $(3.30 \times 10^3$ psi$)$ corresponds to initial yielding, and so the plastic zone extends about 0.45
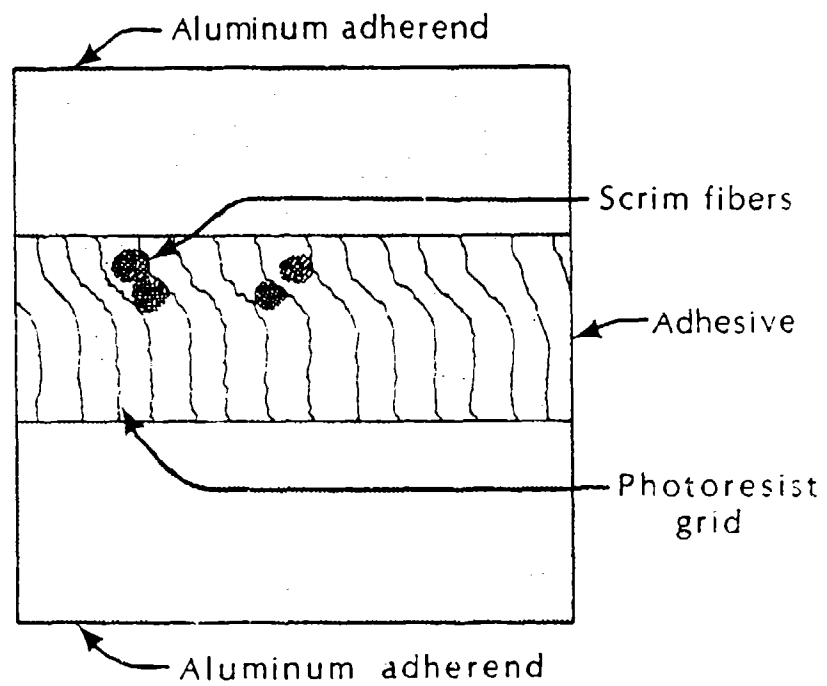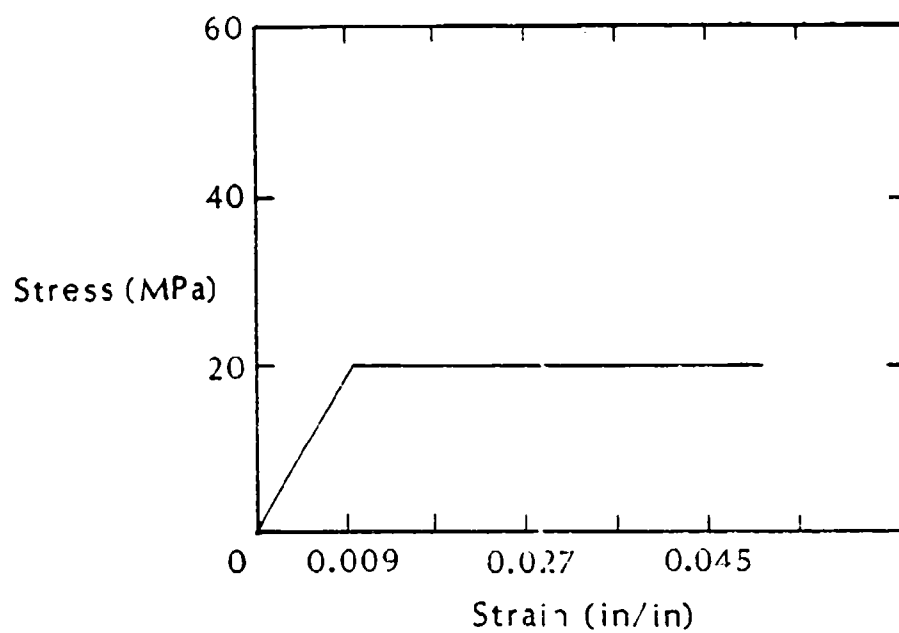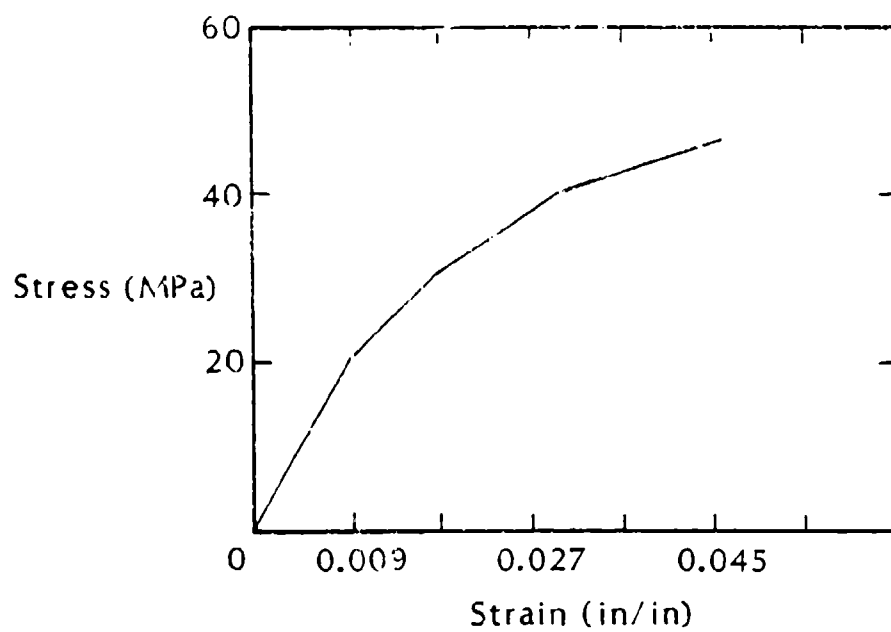
FIG. 35 Deformation of Photoresist Grating Far From Crack Front

FIG. 36   Idealized Stress Strain Behavior of FM-300

4-46

inches ahead of the crack (outside the field of view of Figure 37) to 0.007 inches behind the crack tip. Between these limits, the plastic zone was fully developed across the adhesive layer thickness. The J-integral for the elastic case was 6.92 in lb./in.^{2} and dropped to 2.2 in lb./in.^{2} for the elasto-plastic case. The length of the plastic zone ahead of the crack front was therefore in qualitative agreement with grid observations. In order to establish desirable resolution limits on moiré methods, the u-displacement contours were plotted in increments of 5×10^{-4} inches (Fig. 38). Indications are that a 2000 lpi grating would give rise to 10 fringes across the adhesive layer thickness at this load level. The resolution of the video system is currently being upgraded to achieve this, and alternative photoresists are being considered.

3.5 Effect of Zero Scrim

In observing the growth of cracks in FM-300 it was clear that the scrim cloth played a strong role in the initiation of microcracks ahead of the main crack. In this portion of the work the adhesive was obtained in unscrimmed form (FM-300U) and fracture toughness tests were conducted under mode I and mode II conditions using the DCB and ENF specimens, respectively. Specimen dimensions were the same as those given in Figure 27. The tests were carried out at the same rate as the previous tests on the scrimmed material.

The compliances of the DCB specimens are shown in Figure 39 where they are compared with beam theory and finite element analyses and previously measured values for the scrimmed specimens. The compliance of specimens having scrimmed or unscrimmed adhesive seemed to be very much the same. However, the mode I fracture toughness of the unscrimmed adhesive was higher at 2.108 kJ/m^2 with a coefficient variation of 5.8%. Cracks grew in a cohesive fashion, roughly along the mid plane of the adhesive with no signs of microcracking ahead of the main crack, except when voids were encountered.

The measured compliance of the ENF specimens without scrim was much closer to the predicted values than those containing scrim (Fig. 40). The mode II fracture toughness, based on measured compliance, was 10.5 kJ/m^2 with a coefficient variation of 7.78%. The scrim cloth decreased the mode II fracture toughness by a factor of 7. The specimens made with FM 300M contained many voids but they did not have as deleterious an effect as the scrim. Particularly in the ENF specimens, microcracks could be seen emanating from voids at the characteristic 45°angle.
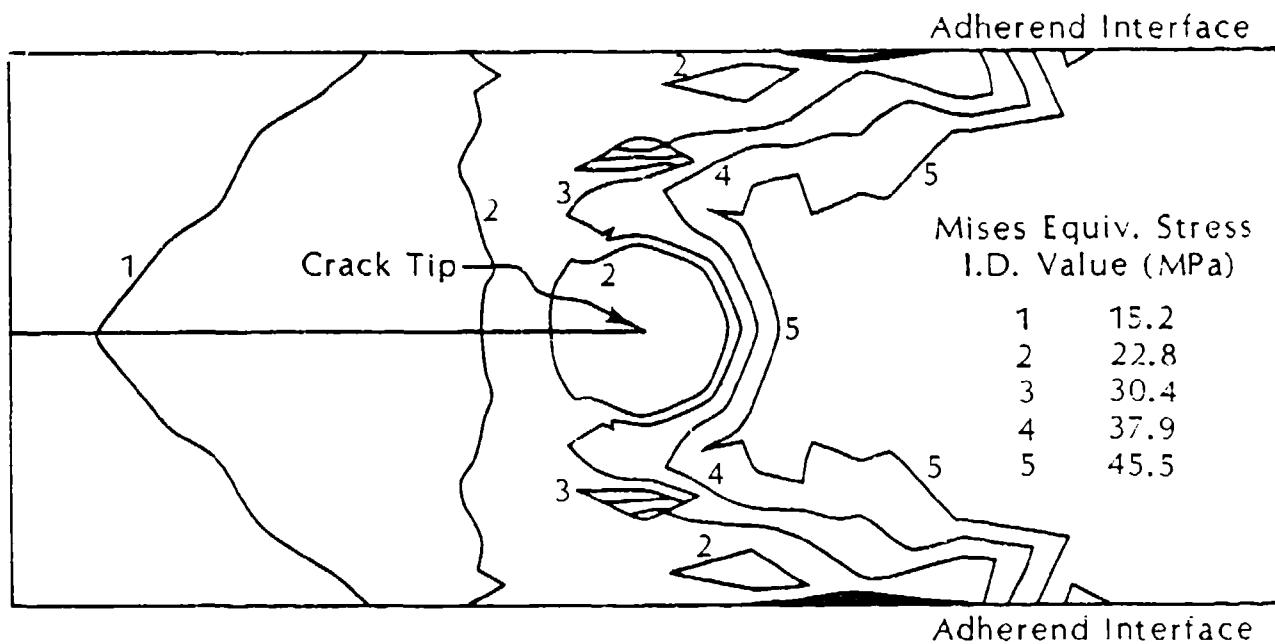
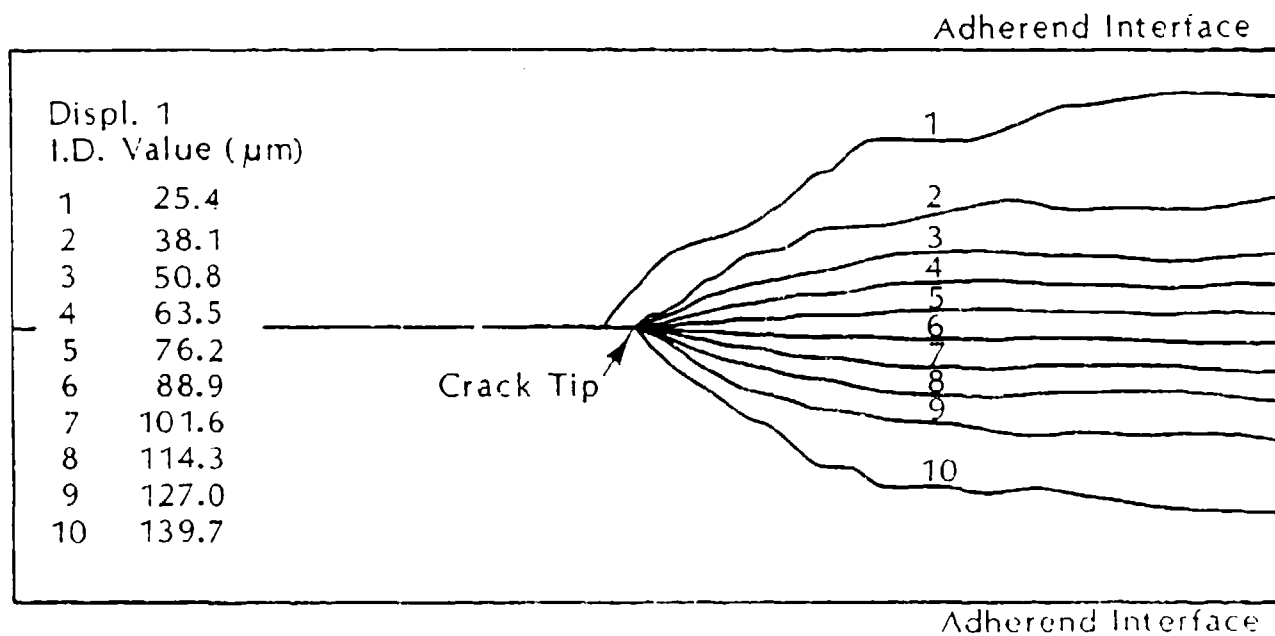FIG. 37 Von Mises Equivalent Stress Contours Near The Crack Front
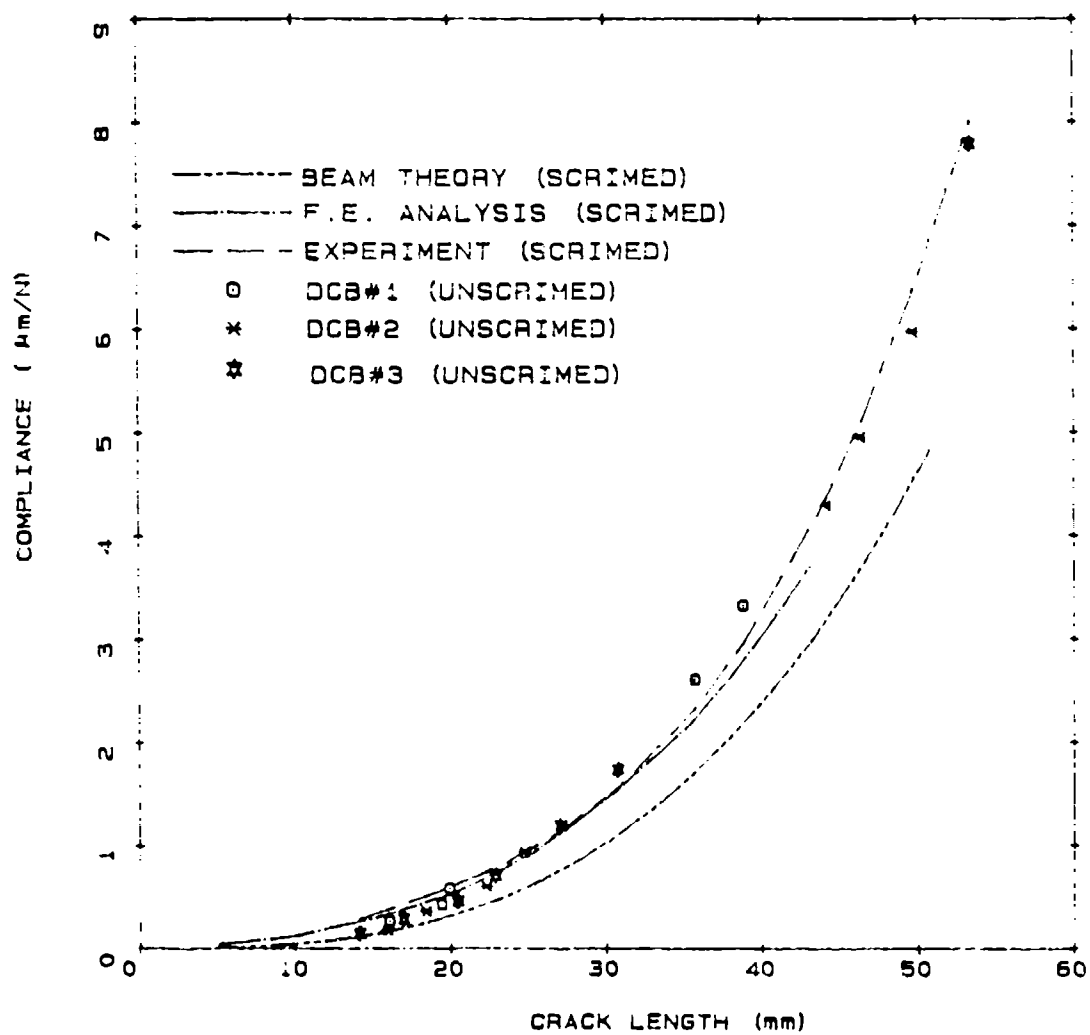

FIG. 38 U – Displacement Contours Near The Crack Front

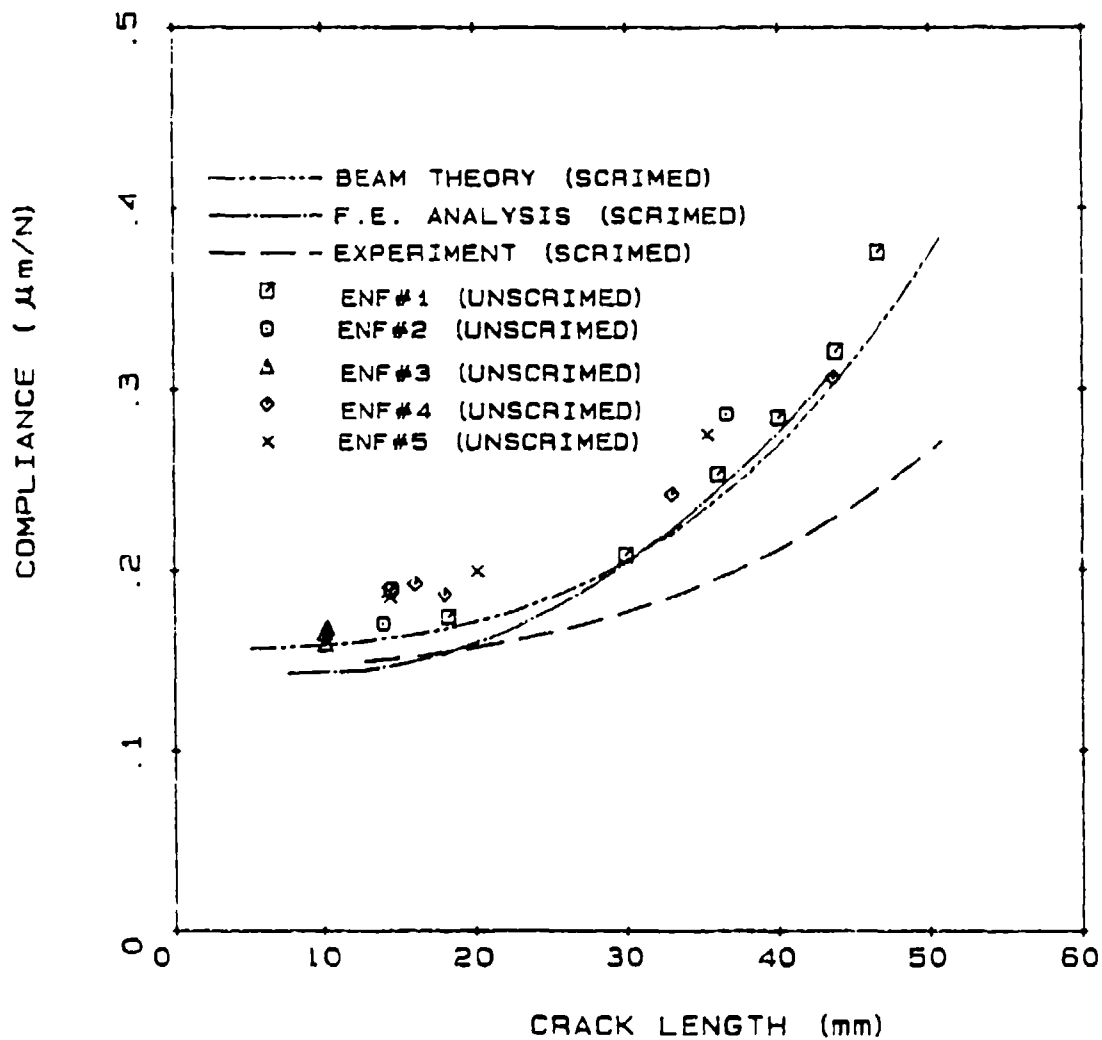Figure 39: Compliance of Aluminum/FM-300U DCB Specimens

Figure 40: Compliance of Aluminum/FM-300U ENF Specimens

3.6 Fracture Tests on High Temperature Adhesives

With test procedures essentially established for room temperatures, the next step was to conduct fracture toughness tests on high temperature adhesives at high temperature. Two adhesives, FM-36 and LARC TPI, were considered. They were used to bond 3.3mm thick plates of Titanium Ti-6Al-4V together, which was half the thickness of the Aluminum/FM 300 specimens. However, the higher yield strength of the Titanium was sufficient to prevent yielding in the adherends. The thinner adherends were easier to slice into fracture specimens. Specimens made with FM-36 had Chronic Acid Anodized (CAA) adherends. Some of the specimens with LARC-TPI were also subjected to Chromic Acid Anodization. Two cure temperatures were used (650°F and 750°F); only the 650°F curved specimens were tested at U.T. Other LARC TPI specimens had adherends whose surface preparation consisted of a plasma spray (PS), recently developed by Martin Marietta.

In all cases the test procedures consisted of mounting the specimen in the grips which were surrounded by a temperature controlled cabinet. The load was measured by a load cell mounted outside the chamber. The loadline displacement was measured by a clip gage with capacitive sensors for the high temperatures. The clip gage stiffness contributed to the load applied to the specimen and was accounted for in the load measurements. The crack length was measured remotely by means of a long working distance microscope mounted outside the environmental chamber. The specimen was illuminated from within the chamber using a high temperature fiber optic light source probe. A number of crack initiation experiments were conducted on each specimen by first bringing the specimen to temperature, loading to crack initiation, unloading to arrest the crack and then measuring the new crack length, prior to reloading.

The specimens made of FM 36 adhesive were tested at room temperature and 500°F. The measured compliances are compared (Fig. 41) with finite element and beam theory predictions based on room temperature properties of the adhesive. The measured compliances of the specimens tested at room temperature are reasonably close to the predictions. The compliances of the specimens tested at 500°F are greater, as would be expected, but are not as consistent at the room temperature values. In order to account for the changing properties, fracture toughnesses were derived from the measured compliances and the critical loads through equation (1). The results are shown in Figure 42 where it can be seen that G_{I_c} is higher at 500°F than at room temperature. Some of the Ti/FM 36 specimens were tested in mode II. However, it was vary hard to determine the crack length and there was a lot of scatter to the data. Time did not permit these matters to be resolved and so no G_{II_c} values
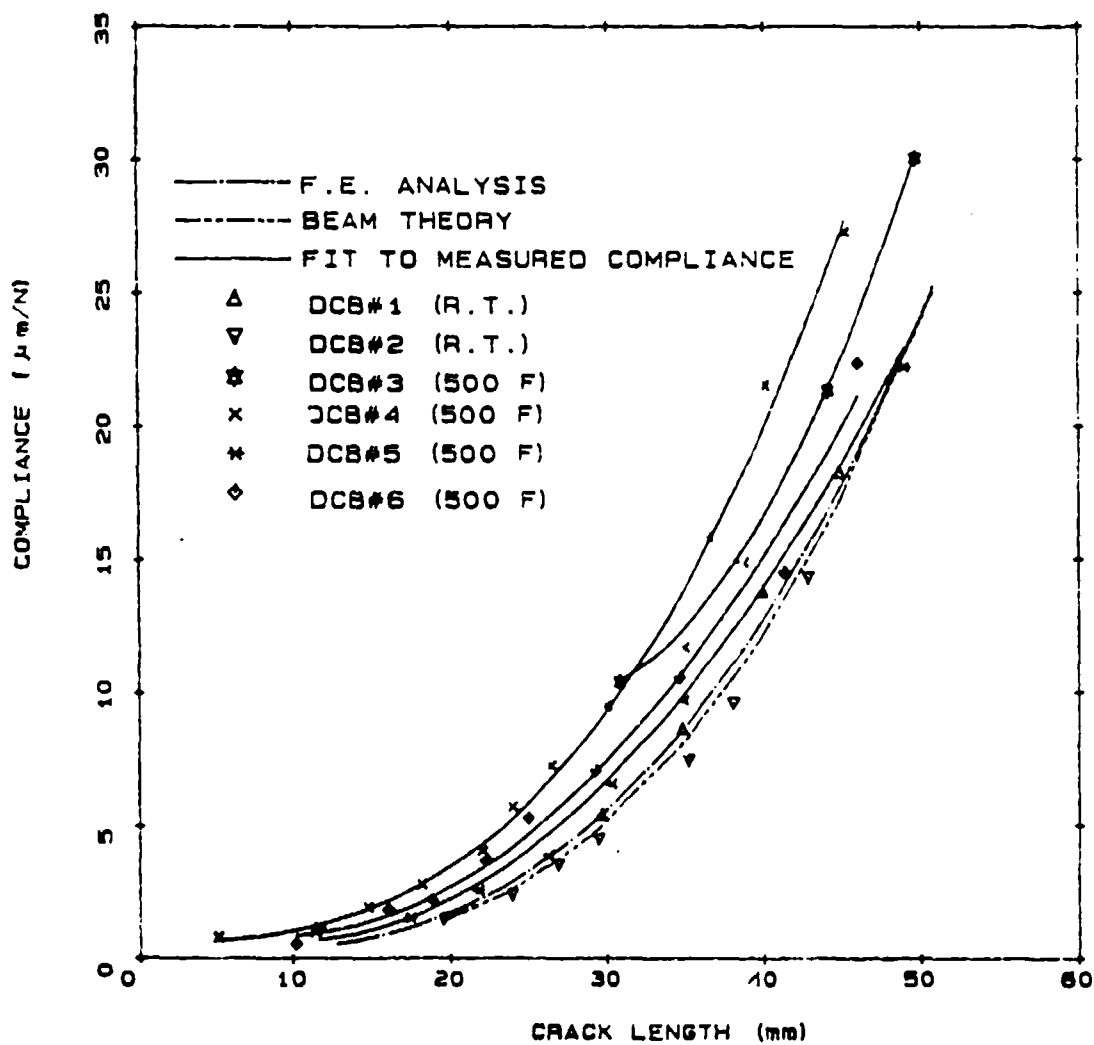
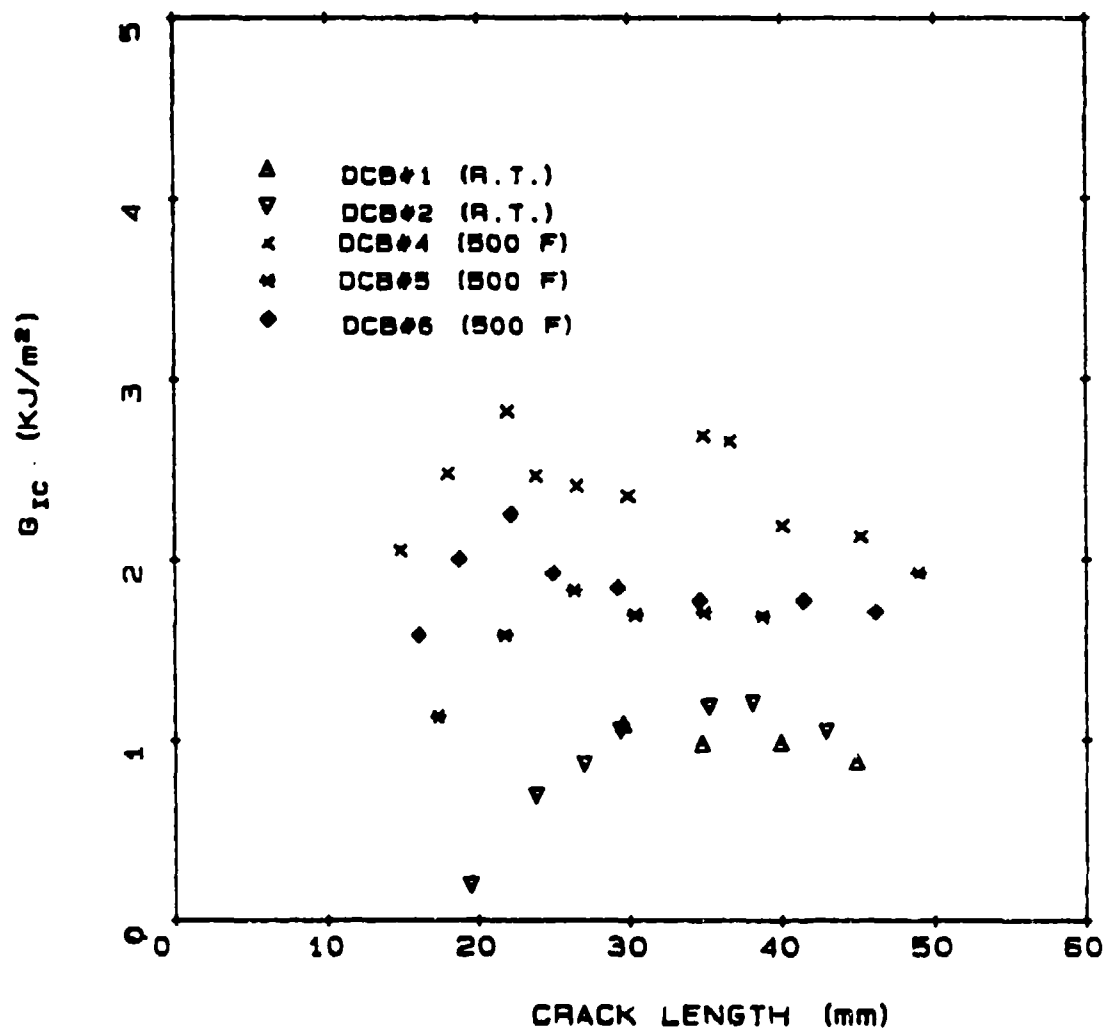Figure 41: Compliance of Titanium/FM36 DCB Specimens

Figure 42: Mode I Fracture Toughness of FM36 Based on Measured Compliance

can be reported at this time.

The Ti/LARC-TPI DCB specimens were tested at room temperature (CAA surface preparation) and at 450°F (CAA and PS surface preparation). The measured compliances are shown in Figure 43. Although the values are consistent within each specimen, there are inconsistencies from specimen to specimen especially between the CAA specimens where the compliance of the specimens tested at room temperature were higher than those that were tested at 450°F. The corresponding G_{I_c} values calculated from equation (1) are shown in Table 1.

Table 1: Mode I Fracture Toughnesses of LARC-TPI

SURFACE PREPARATION	TEST ID		G_{I_c} (J/m^2)
CAA	DCB1	(RT)	5C4.2
(650°F cure)	DCB1	(450°F)	787.0
	DCB2	(450°F)	499.0
	DCB2	(450°F)	387.1
	DCB3	(450°F)	747.8
PS	DCB2	(450°F)	228.6
(750°F cure)	DCB2	(450°F)	245.0

In all cases crack growth was cohesive with separation occurring entirely on one side of the scrim cloth. Nonetheless there were noticeable differences in mode I fracture toughnesses. Within the set of specimens having CAA surface preparation, it appears that the room temperature toughness was again lower at room temperature although the results from specimen #2 contradict this. All the CAA toughness values were higher than the threshold G_I values (100 J/m^2) determined by Martin Marietta through wedge tests of similarly prepared specimens. The same consistency was not observed in the specimens having the plasma spray surface preparation. Although G_{I_c} values obtained from two sets of tests were reasonably close they were less than the 375 J/m^2 threshold values measured by Martin Marietta. It is not clear at this time what the noted discrepancies are due to. However, some time-dependence was noticed in the loading and unloading response during the fracture toughness
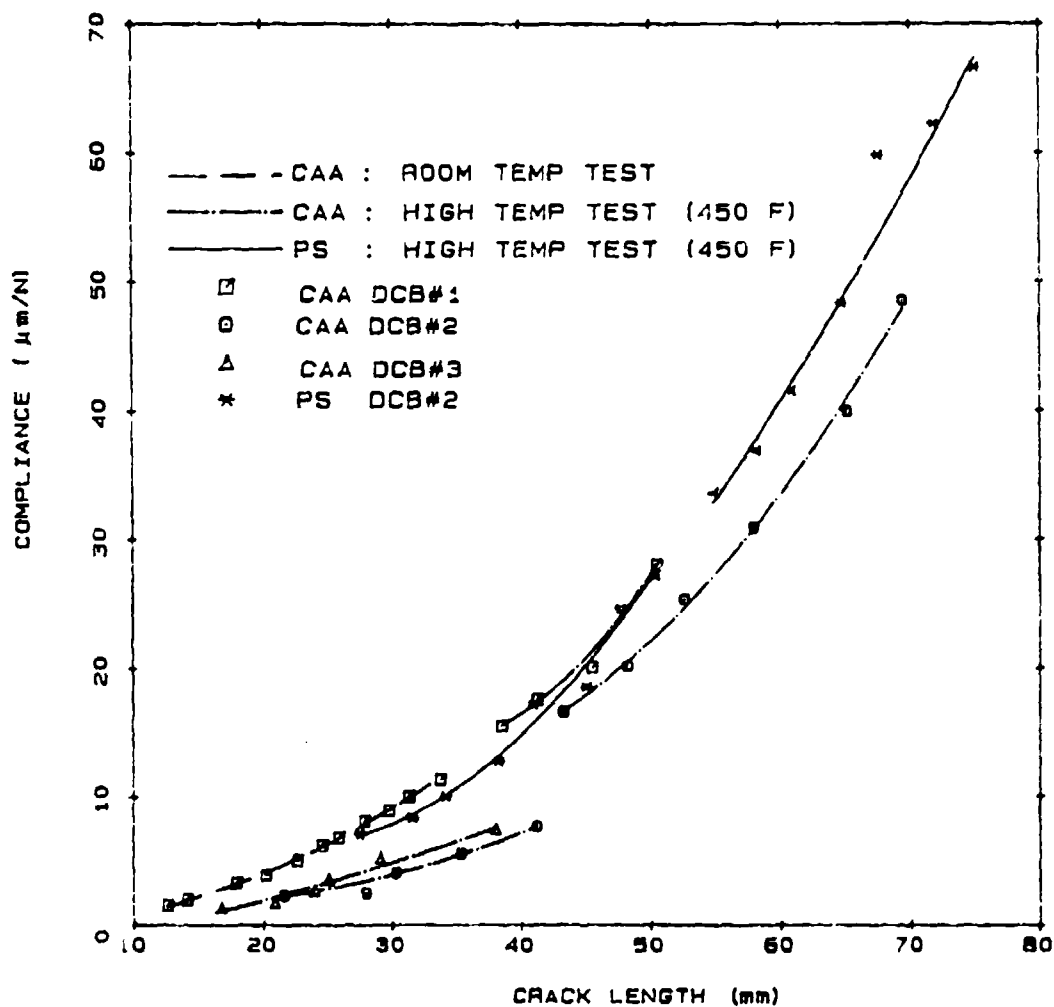
Figure 43:   Compliance of Titanium/LARC-TPI DCB Specimens

tests and this aspect is considered further in what follows.

Since no relaxation data was available for LARC-TPI, the adhesive was considered to be FM-73U for which shear relaxation [28] and Poisson ratio [29] data exist. The former is shown in Figure 44 and the Poisson ratio was found [29] to be constant at 0.4. The first temperature and loading history that was considered (Fig. 45) corresponds to the curing and testing of a wedge test specimen made of Aluminum/FM-73U. Temperature levels were chosen with respect to the cure temperature of FM-73U rather than those that were actually used for the FM-36 and LARC-TPI. Basically the specimen is cooled down from 250°F following cure and given a fixed displacement an hour before being placed in the environmental chamber at 200°F. Under this loading the load point reaction followed the response shown in Fig. 46. The initial constant reaction following cure cooldown arose because the specimen was considered to be fixed. A typical wedge test lasts 10^3 minutes and it can be seen that there is a considerable reduction in reaction over this period of time, even without considering the effects of crack extension. Thus, if we recall the simplest beam theory expression for the stress intensity factor of a DCB

$$K_I = 2\sqrt{3}Pa/h^{3/2}$$

we see that the stress intensity factor drops off as the load (reaction) drops off and any calculations of K_I that do not account for this (as is currently the case in the data reduction of wedge test data) will overestimate K_I values at long times. Thus threshold values will generally be overestimated, depending on the time dependence of the particular adhesive. For the particular example considered here, the error in threshold values is almost 50%. If one bears in mind that the actual tests conducted here were at 450°F, only 50°F below the glass transition temperature of LARC-TPI, then errors of similar magnitude may occur as have been noted for the FM-73U analysis This would make the CAA results even more reasonable and would also put the PS G_{I_c} values (marginally) above the threshold values. It is interesting to note that in this fixed grip experiment, while the load drops off, the crack opening displacement represented by "SINGVAL", the coefficient of the square root term in distance from the crack tip, (Fig. 47) increases following the load application.

In order to initially examine time dependent effects further, DCB specimens made of Ti and LARC-TPI were tested at IE-3 to IE-6 inches/sec. (25 to 0.025 μm/sec). A typical temperature and applied displacement history is shown in Figure 48 where the specimen is brought to uniform temperature prior to ramp loading and unloading. An analysis based on the properties of FM-73U indicate some possibility of time dependence in that the maximum reaction (Fig. 49) decreases with decreasing load rate and the hysterisis effect is larger.
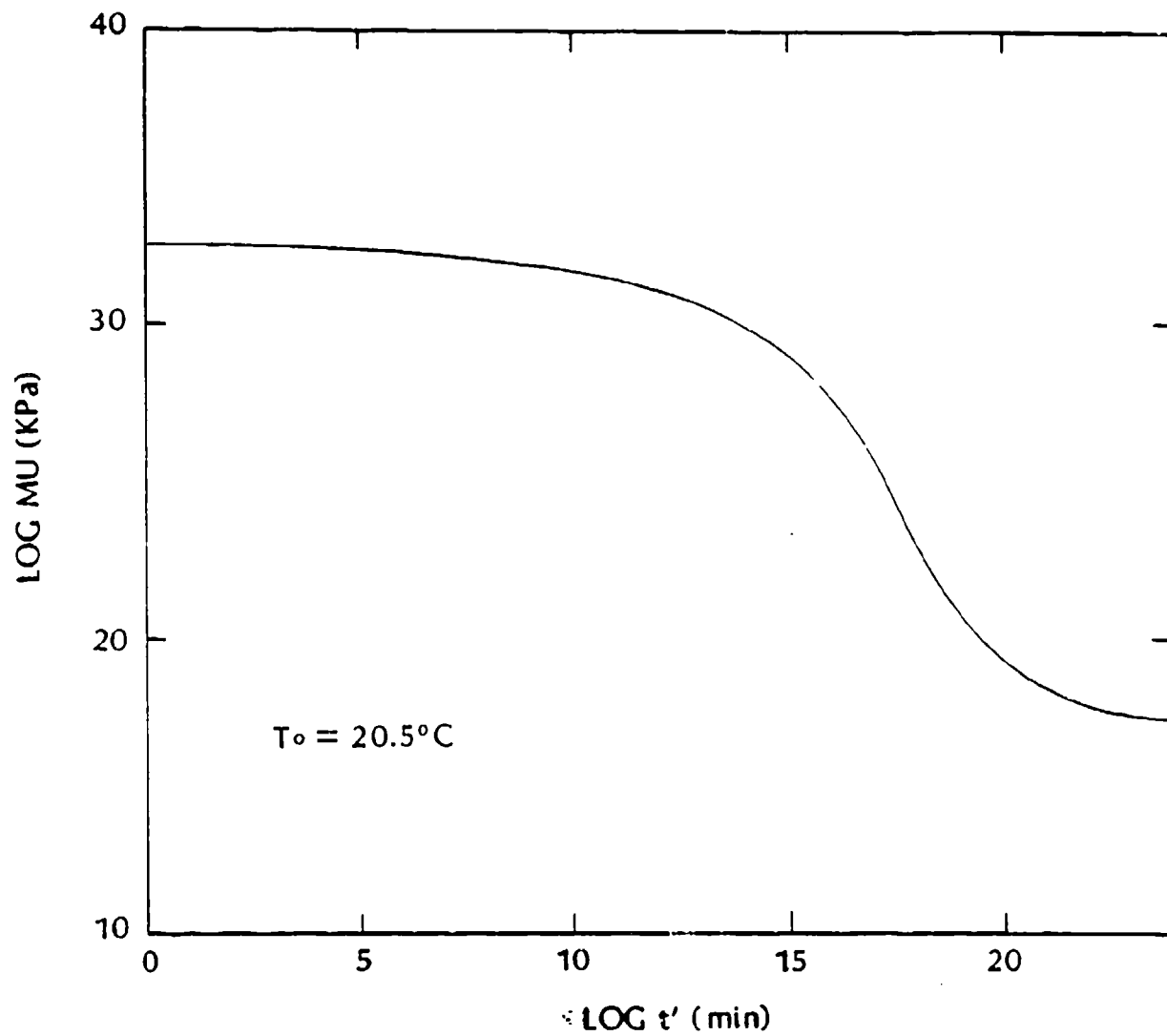
Figure 44:   Shear Relaxation Modulus of FM-73U
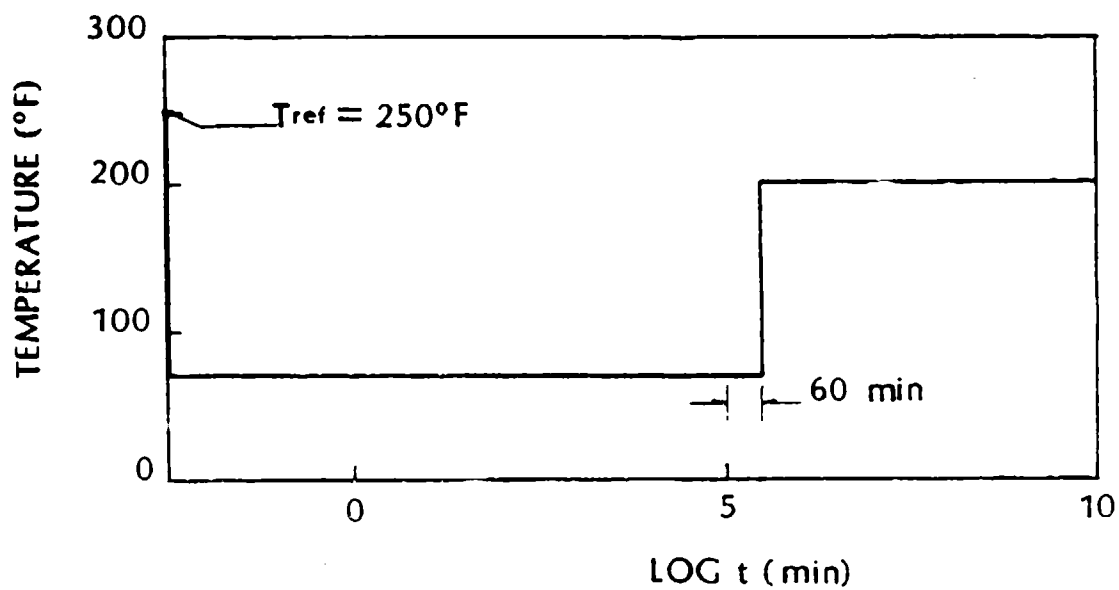
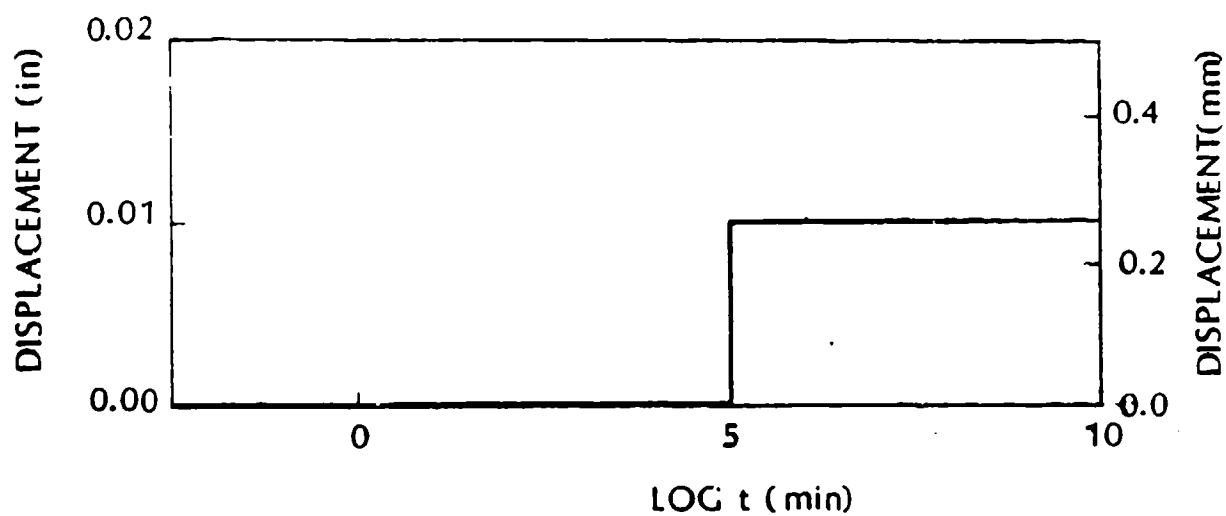TEMPERATURE HISTORY OF AL/FM73U WEDGE TEST

Figure 45: Temperature and Loading History for a Wedge Test of an Aluminum/FM-73U Specimen
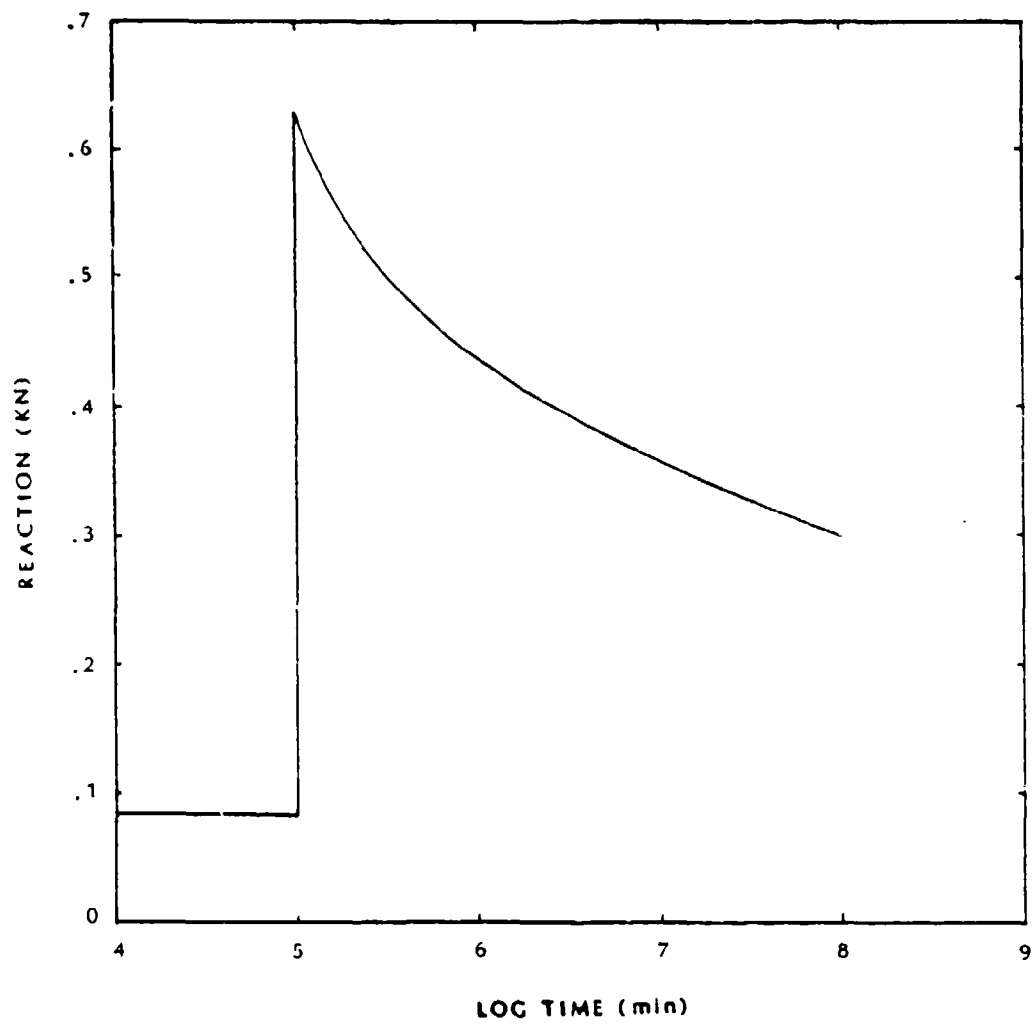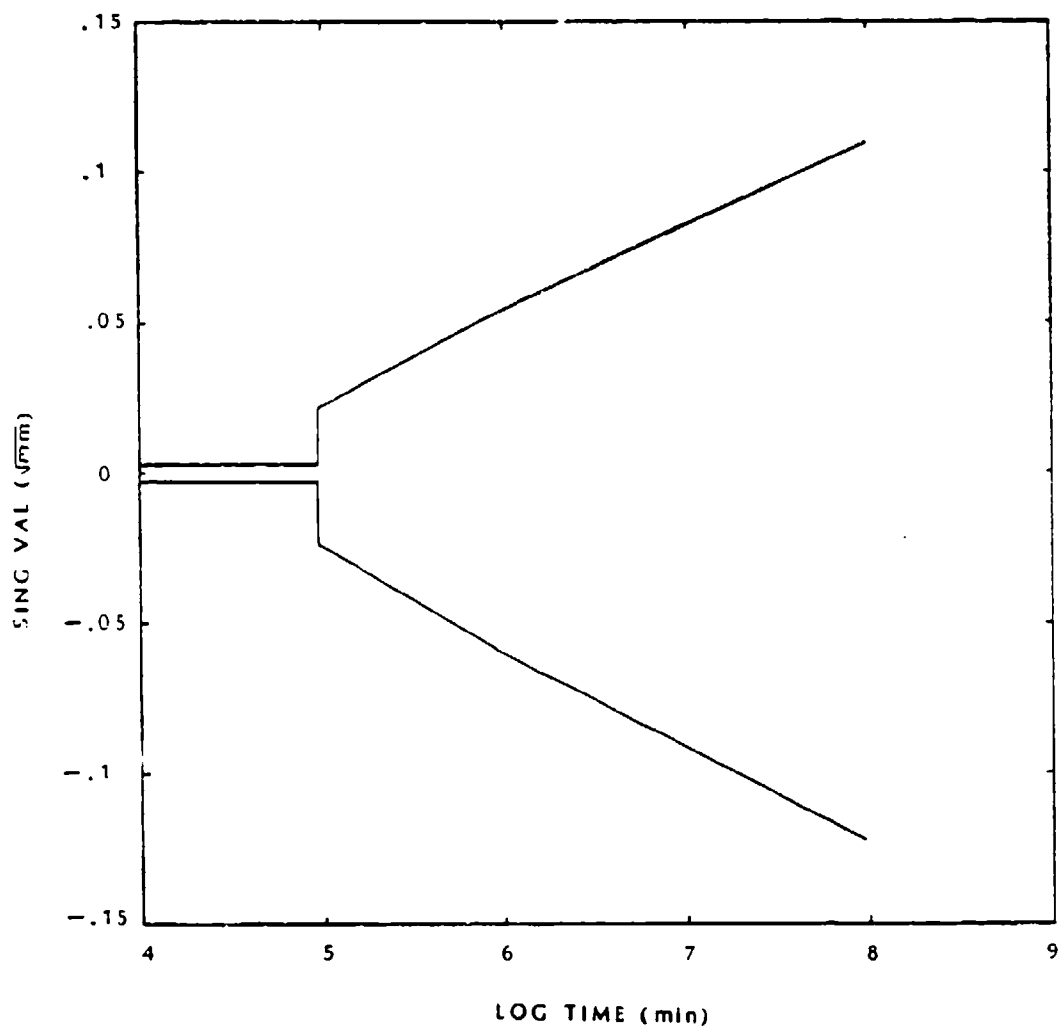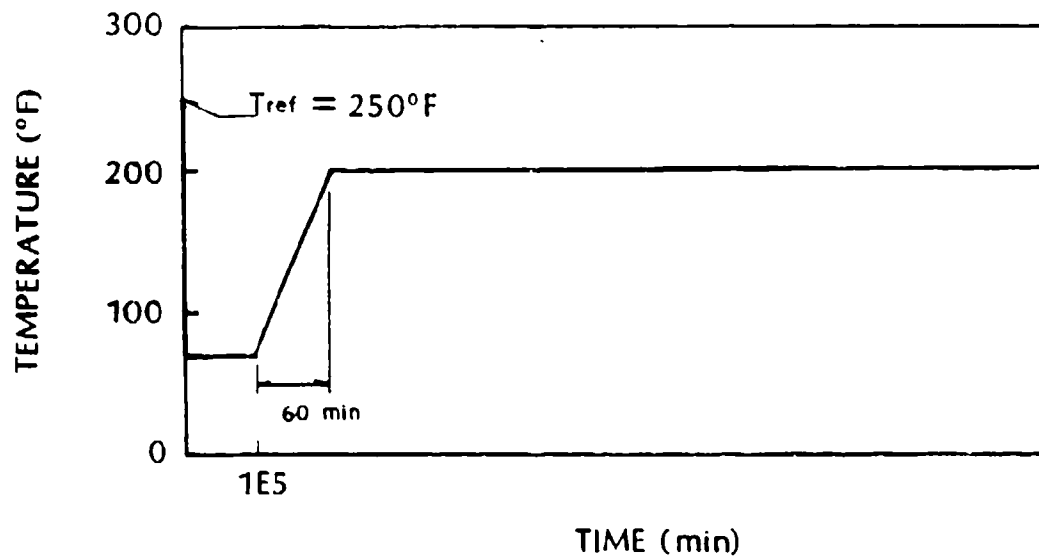
Figure 46:   Wedge Test Reaction

Figure 47:   Wedge Test Crack Opening Displacements

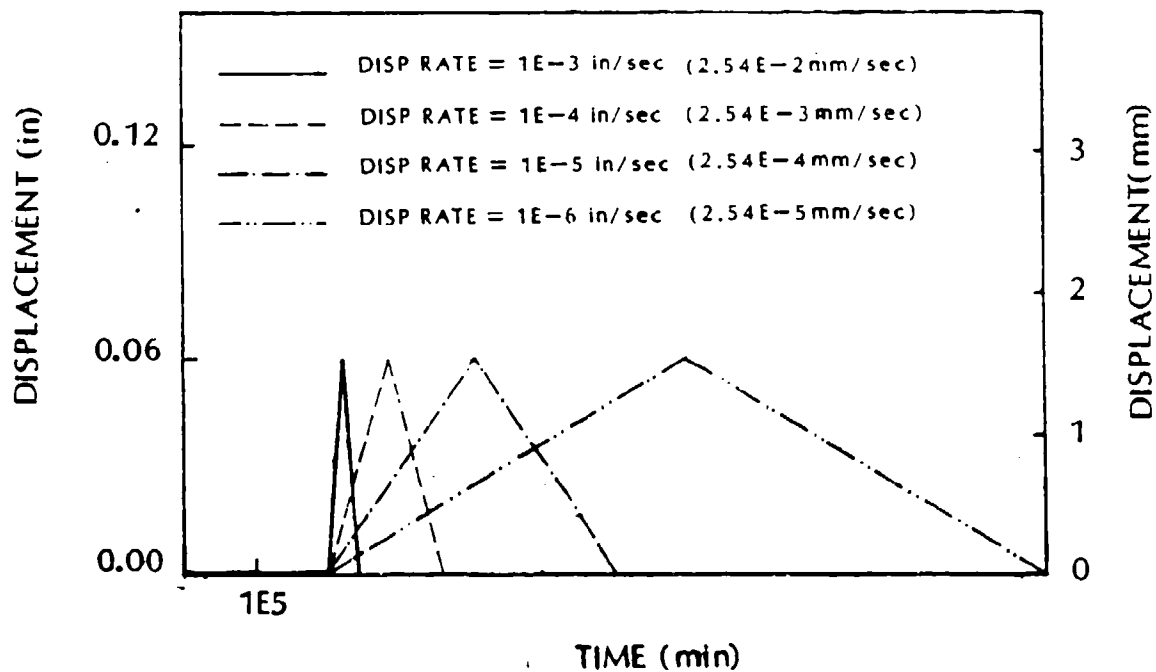TEMPERATURE HISTORY OF AL/FM73U MODE I TEST

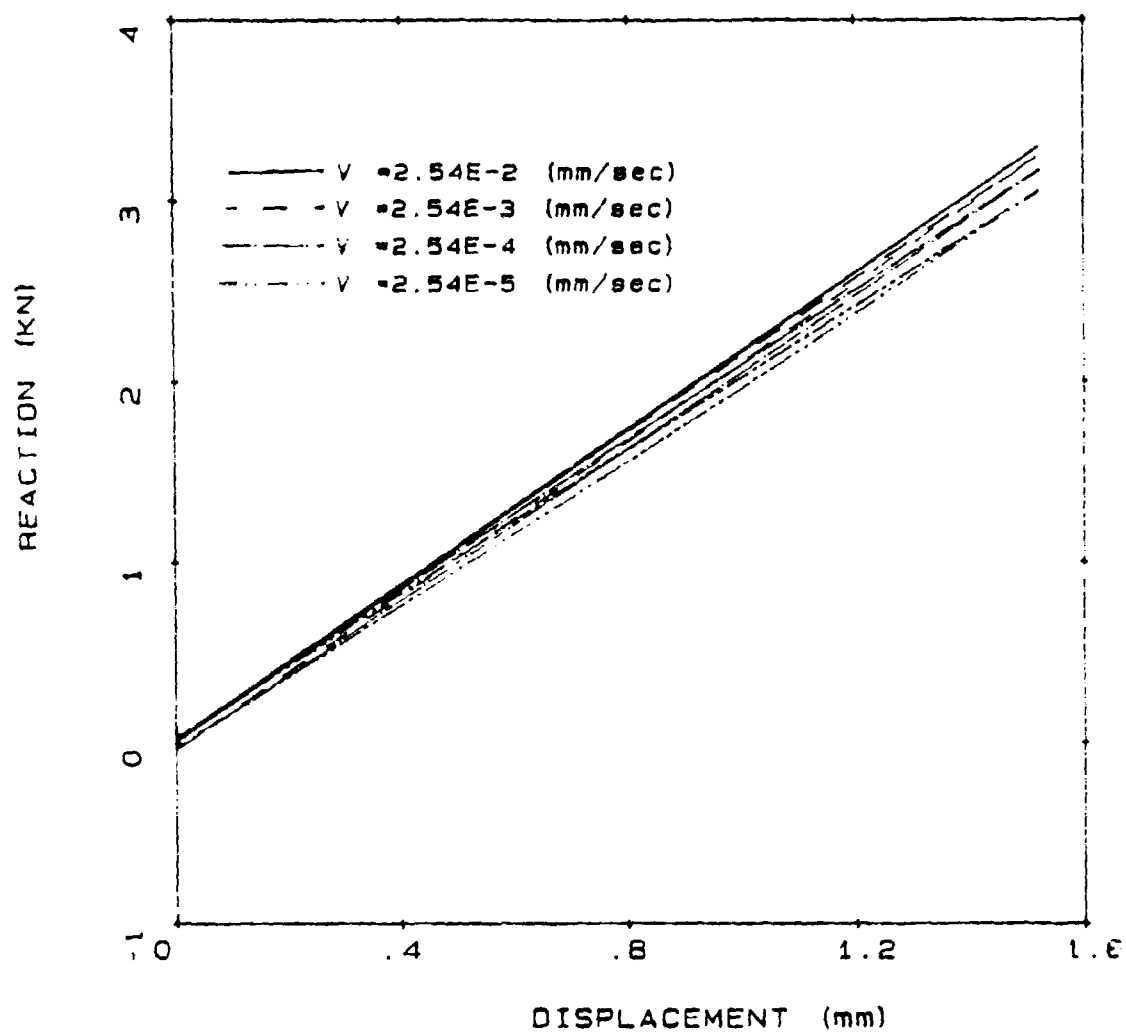Figure 48: DCB Ramp Loading and Thermal Histories

4-61

Figure 49: DCB Reaction *vs.* Applied Displacement Rate

The crack opening displacements of the upper and lower crack faces, again represented by "SINGVAL" are again larger at the lower loading rate (Fig. 50).

Crack initiation tests were conducted at the same rates as those just analyzed. As Figure 51 indicates, two tests were carried out at each rate and the compliance was measured. The tests were conducted at 450°F on the same specimen, whose adherends had been treated by plasma spray. The figure indicates that the compliance values are in reasonable agreement with those previously shown in Figure 43 where the applied displacement rate was 2.54 E-2 mm/sec. This result indicates that the change in compliance is due mainly to increases in crack length rather than rate effects in the material. The corresponding values of critical strain energy release rate are noted in Table II.

Table 2:   Mode I Fracture Toughnesses of LARC-TPI at Different Applied Displacement Rates at 450°F

DISPLACEMENT RATE (mm/s)	G_{Ic} (J/m^2)
2.54 E-2	120.8
2.54 E-3	129.0
2.54 E-4	78.2
2.54 E-5	101.3

Although there is some scatter in an admittedly small sample there is some suggestion that the G_{I_c} values are decreasing with decreasing applied displacement rate. The values obtained here are 50% lower than the already low values (Table 1) obtained for the plasma spray treated adherends and 750°F cured LARC-TPI. Fracture was again cohesive on one side of the scrim cloth, again suggesting that the 750°F cure temperature rather than the plasma spray surface treatment is responsible for the low toughness values.

A recent comparison of the fracture surfaces of the LARC-TPI specimens with plasma sprayed adherends indicated that the adhesive was darker in the specimens that were tested at Caltech and U.T. than those at MML, indicating a problem with curing procedures. This, more than anything, explains the inconsistent toughness values that were obtained here for the plasma sprayed specimens. Nonetheless, the viscoelastic stress analysis of the high temperature wedge test indicates a need for further work in that regard.
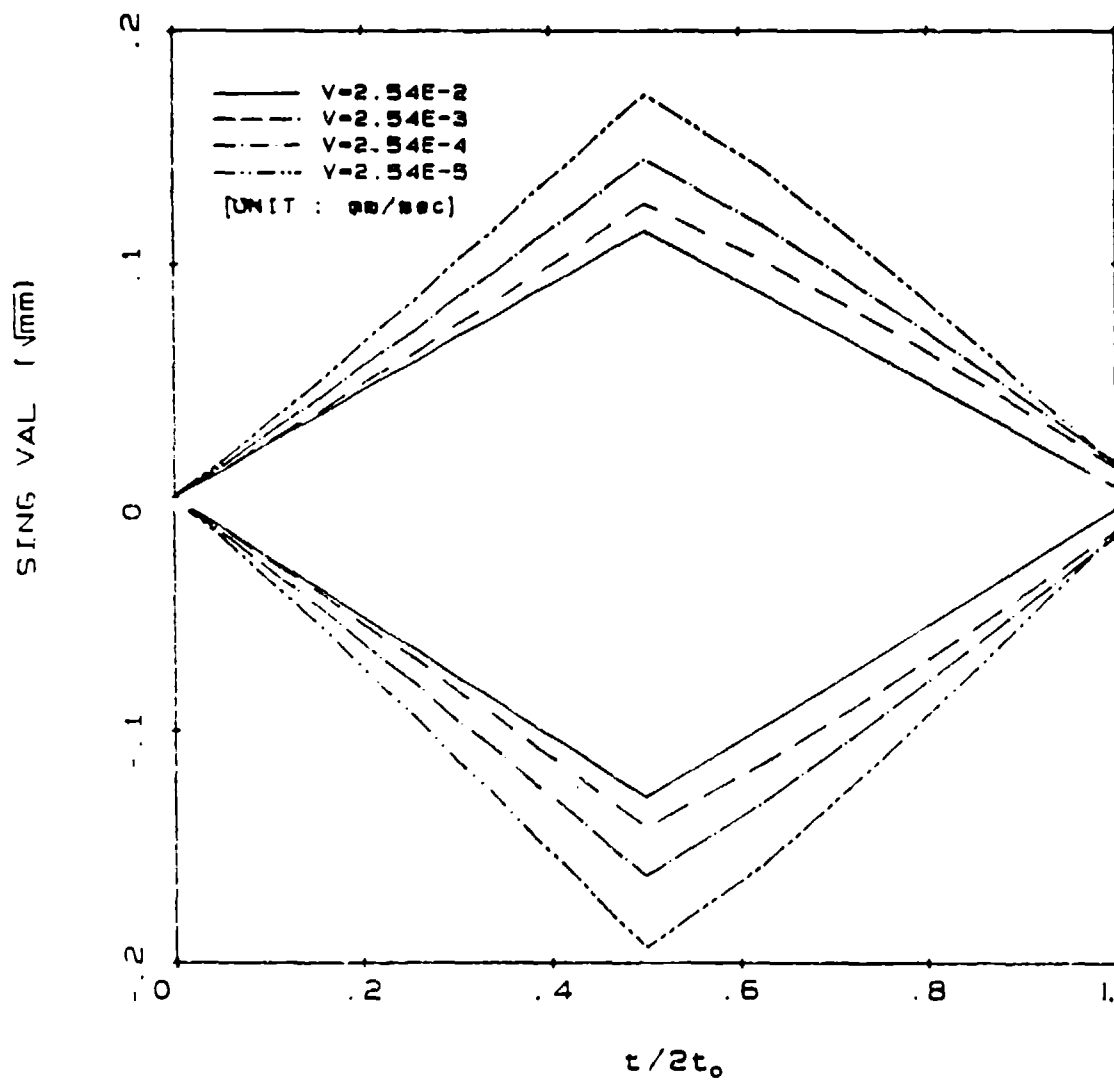
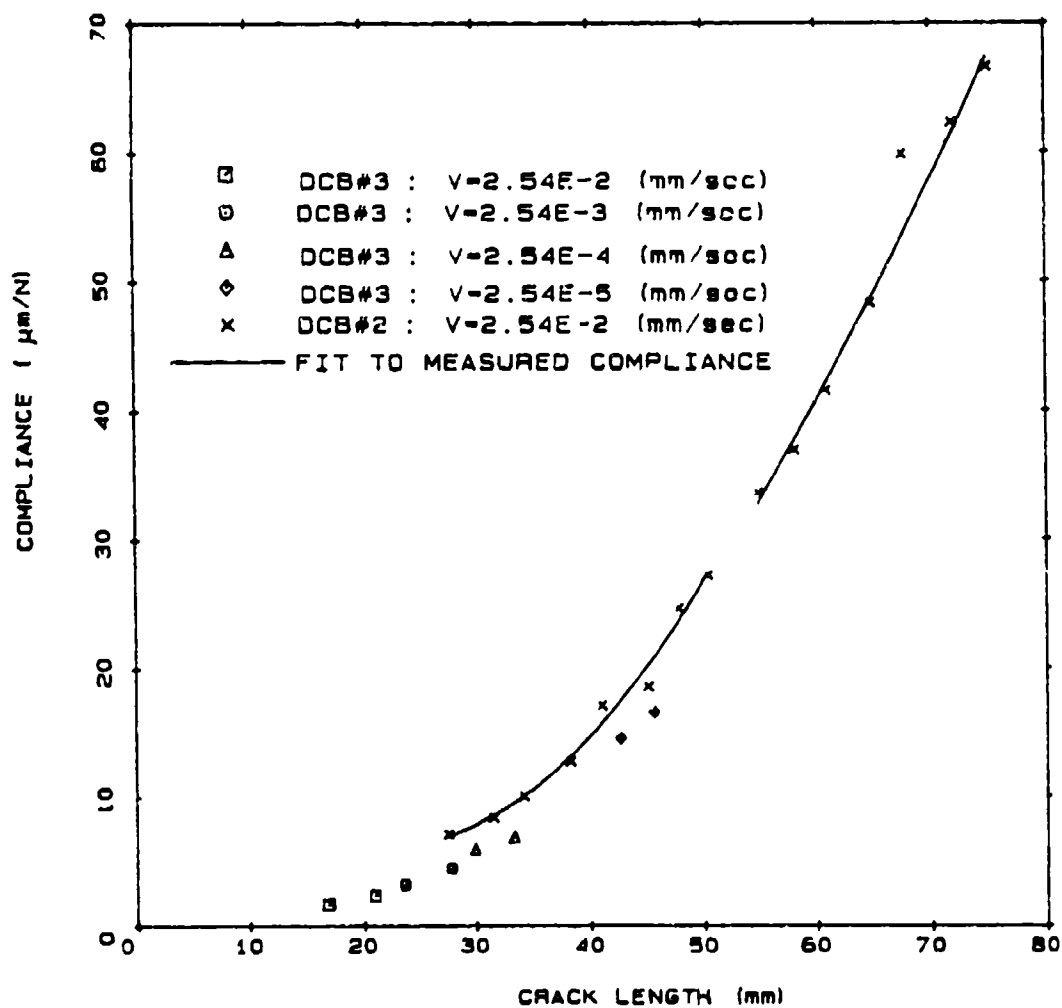Figure 50:   DCB Crack Opening Displacements Under Various Ramp Loadings

Figure 51: Compliance of Titanium/LARC-TPI DCB Specimens at Various Ramp Rates

4. Conclusions

In the portion of the work directed towards determining the stress strain behavior of the adhesive *in-situ*, finite element stress analysis of napkin ring, cone-and-plate stiff adherend and cantilever beam specimens revealed that the stiff adherend specimen provides most uniform stress states under shear, bond normal and thermal (cooldown) loads. This is especially true when the adherend edges are rounded in order to eliminate stress concentrations at bimaterial corners. Shear tests conducted on the stiff adherend specimens essentially confirmed the purity of the stress state by virtue of the higher strengths obtained and also from the appearance of the fracture surfaces. The specimen geometry is such that more machining steps are required to produce a specimen. Modifications to the specimen and grips are currently being considered with a view to simplifying the specimen geometry while retaining purity and uniformity of stresses.

Double cantilever beam, end-notched flexure and mixed-mode flexure specimens were used to determine mode I, mode II and mixed-mode fracture toughness of various adhesives at room and high temperatures. The specimens were cut from the same laminated plate. Limits were established for the range of crack lengths over which meaningful fracture toughness data could be obtained using elastic-plastic finite element analyses. The presence of scrim cloth in FM 300 adhesive reduced the mode I fracture toughness by a factor of two and the mode II value by a factor of 7.

The mode I toughnesses of FM-36 and LARC-TPI increased when the adhesives were tested at 500°F and 450 °F, respectively. However, time dependent effects were noticed at the high temperatures and should therefore be included in any further analysis of crack initiation tests or creep (wedge) growth tests.

5. Educational Benefits

To date, four graduate students have been supported by the program. Messrs. Freda [25] and Hayashi [8] graduated with MS degrees in 1987. Mr. K.T. Yun is currently pursuing a Ph.D. degree. Mr. J.N. Cooper provided some assistance. Their work is greatly appreciated. Two archival papers from this work will be published and four proceedings papers have been published.

References

1. Frazier, T.B., "A Computer Assisted Thick Adherend Test to Characterize the Mechanical Properties of Adhesives," in Proceedings of National SAMPE Technical Conference, Vol. 2, Aerospace Adhesive and Elastomers, Dallas, Tx, Oct. 1970, p. 71.

2. Guess, T.R., Allred, R.E., and Gerstle, F.P., Jr., "Comparison of Lap Shear Test Specimen," *Journal of Testing and Evaluation*, JTEVA, Vol. 5, No. 3, March 1977, pp. 84-93.

3. Goldenberg, N., Arcan, M. and Nicolau, E., "On the Most Suitable Specimen Shape for Testing Shear Strength of Plastics," ASTM STP 247 (1958), pp. 115-121.

4. Weissberg, V. and Arcan, M., "A Uniform Pure Shear Testing Specimen for Adhesive Characterization," Proc. Int. Symp. on Adhesively Bonded Joints: Testing, Analysis and Design, Sept. 1986. To appear as ASTM STP XXX (1987) W.S. Johnson, Ed.

5. Lin, C.J. and Bell, J.P., "The Effect of Polymer Network Structure Upon the Bond Strength of Epoxy-Aluminum Joint," *J. of Applied Polymer Science*, Vol. 16, (1972), pp. 1721-1733.

6. Grant, J.W. and Cooper, J.N., "Cone-and-Plate Shear Stess Adhesive Test," *J. Adhesion*, No. 21, (1987), pp. 155-167.

7. Williams, M.L., "Stress Singularities Resulting from Various Boundary Conditions in Angular Corners of Plates in Extension," *J. Applied Mechanics*, (1952), pp. 526-528.

8. Hayashi, T., "Pure Shear Testing of Adhesives," Master's Thesis, Department of Aerospace Engineering and Engineering Mechanics, The University of Texas at Austin, Engineering Mechanics Laboratory, Report Number EMRL #87/7.

9. Stringer, L. F., "Comparison of the Shear Stress-Strain Behavior of Some Structural Adhesives," J. Adhesion, Vol. 18, 1985, pp. 185-196.

10. Freda, T., "The Use of Laminated Beams for the Determination of Pure and Mixed-Mode Fracture Properties of Adhesives," M.S. Thesis, University of Texas at Austin, Department of Aerospace Engineering and Engineering Mechanics, Engineering Mechanics Research Laboratory Report #EMRL 87/5, 1987.

11. G. Dolev and O. Ishai, "Mechanical Characterisation of Adhesive Layer in-situ and as Bulk Material," J. Adhesion 12 (1981), 283-294.

12. E. Moussiaux, H. F. Brinson and A. H. Cardon, "Bending of a Bonded Beam as a Test Method for Adhesive Properties," VPI & SU, Center for Adhesion Science Report CAS/ESM-87-2.

13. Ripling, E.J., Mostovoy, S. and Patrick, R.L., "Measuring Fracture Toughness of Adhesive Joints," Materials Research and Standards, No. 4, (1964) pp.129-134.

14. Trantina, G.C., "Combined Mode Crack Extension in Adhesive Joints," *J. Comp. Matls.*, No. 6, (1972), pp. 371–385.

15. Ripling, E.J., Mostovoy, S. and Corten, H. T., "Fracture Mechanics: A Tool for Evaluating Structural Adhesives," *J. Adhesion*, No. 3, (1971), pp. 107–123.

16. Bascom, W.D., Cottington, R.L. and Timmons, C.O., "Fracture Reliability of Structural Adhesives," *J. of Applied Polymer Science*, No. 32, (1977), pp. 165–188.

17. Mall, S., Johnson, W.S. and Everett, R.A., Jr., "Cyclic Debonding of Adhesively Bonded Composites," NASA TM-84577 (1982).

18. Brussat, T.R. and Chiu, S. T., "Fatigue Crack Growth of Bondline Cracks in Structural Bonded Joints," *J. Eng. Mat. and Tech.*, No. 100, (1978), pp. 39–45.

19. Vanderkley, P.S., "Mode I - Mode II Delamination Fracture Toughness of a Unidirectional Graphite/Epoxy Composite," Master's Thesis, Texas A&M University, Mechanics and Research Center, Report Number MM3724-81-15.

20. Russell, A.J. Street, K.N., "Moisture and Temperature Effects on the Mixed-Mode Delamination Fracture of Unidirectional Graphite/Epoxy," Delamination and Debonding of Materials, ASTM STP 876, American Society for Testing and Materials, Philadelphia, (1985), pp. 349-370.

21. Carlsson, L.A., Gillespie, J.W. and Pipes, R.B., "On the Analysis and Design of the End Notched Flexure (ENF) Specimen for Mode II Testing," *J. of Composite Materials*, (1985).

22. Murri, G.B. and O'Brien, T.K., "Interlaminar G_{II_c} Evaluation of Toughened Resin Matrix Composites Using the End-Notched Flexure Test," Presented at the 26th AIAA/ASME/ASCE/AHS Structures, Structural Dynamics, and Materials Conference, Orlando, Florida, (April, 1985).

23. Mall, S. and Kochhar, N.K., "Finite-Element Analysis of End-Notched Flexure Specimens," *J. of Composites Technology and Research*, Vol.8, No. 2, (1986), pp. 54–57.

24. Mall, S. and Kochhar, N.K., "Criterion for Mixed Mode Fracture in Composite Bonded Joints," Proceedings of the Institution of Mechanical Engineers, IMechE, No. 6, (1986), pp. 71–76.

25. Freda, T., "The Use of Laminated Beams for the Determination of the Pure and Mixed-Mode Fracture Properties of Adhesives," Master's Thesis 1987, The University of Texas at Austin, Engineering Mechanics Research Laboratory, Report Number EMRL 87/5, (1987).

26. Bascom, W.D., Cottington, R.L. and Timmons, G.O., "Fracture Reliability of Structural Adhesives". J. Appl. Poly. Sci., 32 (1977), 165-188.

27. Link, R.E. and Sanford, R.J., "Micro-Moiré — A High Sensitivity Moiré Technique for Determining Displacement Fields by Using Phase Gratings as Amplitude Gratings," Proc. S.E.M. Spring Meeting, Las Vegas (1985).

28. Becker, E. B., Chambers, R. S., Collins, L. R., Knauss, W. G., Liechti, K. M., and Romanko, J., "Viscoelastic Stress Analysis of Adhesively Bonded Joint Including Moisture Diffusion". AFWAL-TR-84-4057, August, 1984.

29. Romanko, J. and Knauss, W. G., "On the Time Dependence of the Poisson's Ratio of a Commercial Adhesive Material," *J. Adhesion*, 10, pp. 269-277 (1980).